Radium isotopes as tracers of element cycling at ocean boundaries

Dissertation

zur Erlangung des akademischen Grades eines Doktors der Naturwissenschaften

– Dr. rer. nat –

an der Mathematisch-Naturwissenschaftlichen Fakultät

der Christian-Albrechts-Universität zu Kiel

vorgelegt von

Lúcia Helena Vieira

Kiel, 2019

1. Gutachter: Prof. Eric P. Achterberg

2. Gutachter: Dr. Walter Geibert

Tag der mündlichen Prüfung: 21.06.2019

Abstract

Trace elements (TEs) play crucial roles in regulating ocean processes including marine biogeochemical cycles, and are therefore vital to support marine life. Understanding the biogeochemical cycling of TEs requires knowledge of their sources/ sinks and transport in the oceans. Radium isotopes (^{223}Ra, ^{224}Ra, ^{226}Ra, and ^{228}Ra) have shown to be suitable tools to study inputs of elements from the continental margins, as they are produced by the decay of particle-bound thorium isotopes in sediments, and are soluble in seawater. As Ra isotopes present a range of half-lives varying from days to thousands of years, and have relative conservative behaviors in the oceans, they can be applied to study oceanographic processes which occur within this time scale. Therefore, in this Ph.D. thesis, I used Ra isotopes to determine boundary TE fluxes from two diverse environments that constrain the major TE sources, including shelf sediments in an Arctic shelf region and in an eastern boundary system off the western African coast, as well as rivers such as the River Congo.

First, the distributions of the dissolved and total dissolvable TEs (cadmium (Cd), iron (Fe), nickel (Ni), copper (Cu), zinc (Zn), lead (Pb), manganese (Mn), and cobalt (Co)) were investigated in the Chukchi Sea during spring, and ^{228}Ra isotope was applied as tracer of benthic TE inputs. The results show that elevated benthic TE inputs on the Chukchi shelf provided suitable conditions for phytoplankton blooms, and 10-25% of dFe from the Chukchi shelf sediments is transported to the central Arctic Ocean. Radium-228 fluxes from Chukchi shelf sediments are some of the largest in the world. Seasonal variability of Ra is observed, as the ^{228}Ra activities in spring appear to be 2-fold higher than in summer, which was a surprising observation and requires further investigation.

Next, ^{228}Ra was used to investigate the influence of the Congo River, the world's second largest river by discharge volume, on surface ocean TE concentrations in the South Atlantic Ocean. The results show that the Congo River plume constitutes a large and unexpected input of bio-essential TEs (e.g., dissolved Fe, Mn, and Co) into the South Atlantic. Limited removal of dFe is observed on the shelf linked to the Congo River outflow, which is in contrast to all other major river systems globally, where dissolved Fe

is rapidly removed from the water column upon entering the ocean. Yet, ^{228}Ra distributions suggest that there must be an unknown Ra and TE source, which may be submarine groundwater discharge, that likely balances dFe removal in the Congo estuary. Radium-228 was used to quantify the fluxes of TEs from the Congo River plume into the Southeast Atlantic Gyre. As the supply of these elements into the Southeast Atlantic is dominated by the Congo discharge, the factors constraining marine primary production in this region will be sensitive to future climate change associated shifts in wind patterns and rainfall across the Congo Basin and western African shelf.

Finally, Ra isotopes were used to investigate a number of key ocean boundary processes in the Southeast Atlantic Ocean, including Ra supply by the shelf, abyssal and slope sediments, the influence on Ra isotope distributions of the subantarctic waters, Benguela upwelling, and oxygen minimum zone along western Africa. The results show elevated ^{228}Ra activities in the upper 300 m extending >1000 km from the African continental margin into the South Atlantic Ocean, indicating recent contact of water masses with shelf and slope sediments. Upwelling in the Benguela region is visible in the Ra distributions, and elevated Ra isotopes, Fe (II) and silicate concentrations were observed in the Benguela oxygen minimum zone, possibly due to inputs from the reducing shelf sediments as a result of silica dissolution, or submarine groundwater discharge along the Namibian shelf.

This Ph.D. thesis was developed in the framework of the SUBICE (Study of Under Ice Blooms in the Chukchi Ecosystem) and the international GEOTRACES programs.

Zusammenfassung

Spurenelemente spielen eine zentrale Rolle in der Regulation ozeanischer Prozesse einschließlich des marinen biogeochemischen Kreislaufs und sind dadurch eine zentrale Voraussetzung für das Leben im Meer. Das Verständnis der biogeochemischen Kreisläufe der Spurenelemente basiert auf dem Wissen um deren Quellen, Senken und Transportwege innerhalb des Ozeans. Die Radiumisotope (^{223}Ra, ^{224}Ra, ^{226}Ra, and ^{228}Ra), welche als Zerfallsprodukt von partikulär gebundenem Thorium in Sedimenten entstehen, sind wasserlöslich und haben sich als nützliche Werkzeuge herausgestellt, die den Input von solchen Elementen aus den kontinentalen Hängen nachvollziehen lassen. Generell haben Radiumisotope eine Bandbreite von Halbwertszeiten, die zwischen Tagen und Tausenden von Jahren liegen. Im Ozean selber verhalten sie sich konservativ, auch zueinander, und können deshalb für ozeanographische Studien, abhängig vom erwünschten Zeitfenster, verwendet werden. Diese verwende ich in der vorliegenden Dissertation, um die bedeutendsten Spurenelementquellen zu beleuchten, die den Austausch zwischen Schelfsedimenten und dem angrenzenden Ozean vornehmen. Dies geschieht anhand zweier kontrastierender Umgebungen, dem arktischen Schelf und des östlichen „Grenzsystems“ vor der Küste Westafrikas, das auch Flusseinträge wie zum Beispiel aus dem Kongo beinhaltet.

Zunächst wurde die Verteilung der gelösten und säurelöslichen Spurenelemente (Cadmium (Cd), Eisen (Fe), Nickel (Ni), Kupfer (Cu), Zink (Zn), Blei (Pb), Mangan (Mn) und Cobalt (Co)) in der Tschuktschensee zum Frühling untersucht. Als Tracer zur Bestimmung benthischen Eintrags wurde dort ^{228}Ra verwendet. Die Ergebnisse zeigen, dass sich der erhöhte Spurenelementeintrag vom Tschuktschenseeschelf für die Algenblüte eignet und 10–25 % des aus dem Tschuktschenseeschelfsediment gelösten Eisens in den Zentralen Arktischen Ozean transportiert wird. Die dortigen ^{228}Ra-Durchflussmengen sind eine der größten der Welt. Auch wurden saisonale Schwankungen beobachtet. Im Vergleich zum Sommer scheinen die ^{228}Ra-Aktivitäten im Frühling um das Doppelte erhöht zu sein; eine überraschende Erkenntnis, die es weiter zu untersuchen gilt.

Des Weiteren wurde ^{228}Ra verwendet, um den Einfluss des Kongo, der gemessen an dem Ausflussvolumen der weltweit zweitgrößte Fluss ist, auf die im oberen Ozean befindlichen Spurenelemente im Südatlantik zu untersuchen. Die Ergebnisse zeigen, dass die Flusswasserfahne des Kongo einen unerwartet großen Eintrag bioessentieller Spurenelemente (z. B. gelöstes Fe, Mn und Co) in den Südatlantik ausmacht. Im Gegensatz zu anderen großen Flusssystemen der Welt, wo die Abscheidung des Eisens aus der Wassersäule schnell nach Kontakt mit dem Ozean erfolgt,

ist nur eine begrenzte Abtrennung auf dem vom Kongo beeinflussten Schelf ersichtlich. Dennoch weist die Verteilung des ^{228}Ra auf eine weitere, unbekannte Radium- und Spurenelementquelle hin, die möglicherweise unterseeisch als Grundwasseraustritt existiert und eventuell der Eisenabscheidung in der Mündung des Kongo entgegenwirkt. Weiterhin wurde ^{228}Ra verwendet, um den Eintrag an Spurenelementen aus der Kongoflussfahne hin zum Südatlantischen Wirbel zu quantifizieren. Da die Zuführung dieser Elemente in den Südost-Atlantik vom Eintrag des Kongo dominiert wird, sind die Faktoren, die die marine Primärproduktion in dieser Region begrenzen, – Regen- und Windverhältnisse im Kongo-Becken und auf dem westafrikanischen Schelf – empfindlich gegenüber dem zukünftigen Klimawandel.

Mit Hilfe der Radiumisotope wurden abschließend eine Reihe von Schlüsselprozessen im Grenzflächenaustausch des Südost-Atlantiks untersucht. Dies beinhaltet deren Freisetzung von Schelf-, Tiefsee- und Kontinentalhangsedimenten und deren Einfluss auf die Radiumisotopenverteilung im Subantarktischen Wasser, dem Benguela-Auftriebsgebiet sowie der Sauerstoffminimumzone entlang der westafrikanischen Küste. Die Ergebnisse zeigen erhöhte ^{228}Ra-Aktivität in den oberen 300 m, welche mehr als 1000 km von der afrikanischen Kontinentalküste in den Südatlanischen Ozean hinein reicht. Dies deutet auf vorherigen Kontakt der Wassermasse mit Sedimenten des Kontinentalschelfs bzw. des Kontinentalhangs hindeutet. Der Auftrieb der Benguela-Region ist ebenfalls in der Radiumverteilung ersichtlich. Gleichzeitig weisen erhöhte Konzentrationen der Radiumisotope, Fe (II) und Kieselsäure in der Benguela-Sauerstoffminimumzone auf Zufuhr aus reduzierenden Schelfsedimenten als Resultat der Auflösung von Kieselgesteinen oder aus unterseeischem Grundwasseraustritt entlang des Namibianischen Schelfs hin.

Diese Doktorarbeit ist im Rahmen des SUBICE (Study of Under Ice Blooms in the Chukchi Ecosystem) und des internationalen GEOTRACES Programms entstanden.

Translated from the English version by Stephan Krisch

Acknowledgments

Firstly, I would like to express my sincere gratitude to my supervisor Eric P. Achterberg and co-supervisors Jan Scholten and Martha Gledhill for the guidance and support, for giving me the opportunity to conduct interesting research and for helping me to grow into an independent scientist.

I would like to thank the 'Conselho Nacional de Desenvolvimento Científico e Tecnológico' (CNPq, Brazil), for the financial support (grant number 239548/2013-2), as well as ISOS and the CAU Graduate Centre for the opportunity to participate at international conferences by providing travel financial support.

I will be forever grateful to Aaron J. Beck for his support, thoughtful feedback and insights that improved my thesis. No matter how busy he was Aaron always found time to discuss my work, help me with proof reading and with whatever I needed. I am also grateful to Mark J. Hopwood for his meaningful comments and advices during my PhD.

I thank Michiel Rutgers van der Loeff for the personal training to conduct Ra isotope analysis and Volker Liebetrau for letting me use the gamma spectrometer at GEOMAR.

I would like to thank the Captains and crew from RV Healy for their assistance on the cruise (HYLY 1401) to the Arctic. A special thanks to Joaquin for his extensive help with trace element sampling, and the crew of the HYLY 1401 cruise for their effort on fighting the extremely cold weather that froze my seawater samples inside pumps and barrels. I also would like to thank the crew and cruise participants from RV Meteor on the GEOTRACES GA08 cruise (M121) who helped me to turn the extensive work during the cruise into an amazing experience. I am also grateful to the chief scientists Kevin Arrigo and Mathew Mills (HYLY 1401) and Martin Frank (M121).

I thank Tim Steffens for the training on the ICP-MS, Andre Mutzberg, Dominik Jasinski, and Birgit Reiner for all the technical and administrative support I needed during my PhD. Thanks to all the great people of my working group, in particular my office mates JC and Stephan, and my friends Jean, Maria, and Müne. Thanks to Christian, Pablo, Tom,

Ruifang, Mario S., Insa, Ali, Felix, Eva, Kechen, Jan-Lukas, Dagmara, and many more great people I met during my time in Kiel.

Finally, I would like to thank my parents Alécio and Heliane, my siblings Danielle and Junior, and my nephews Luiz R. and Miguel, as they always believed in me and stood right my side giving me all the support and encouragement I needed. “Eu gostaria de agradecer minha família - meus pais Alécio e Heliane, meus irmãos Danielle e Junior, meus sobrinhos Luiz R. e Miguel, e meus amigos ‘Caminheiros’ - que sempre acreditaram em mim e estiveram sempre ao meu lado dando-me todo o apoio e encorajamento que eu precisei.”

I dedicate this thesis to my family,

the solid foundation that sustains my life.

Contents

List of figures

Supplementary Materials

List of tables

Supplementary Materials

1 Introduction

The supply of macro-nutrients (nitrate (NO^{3-}), phosphate (PO_4^{3-}) and silicate (SiO_4^{-})) and bio-essential trace elements (hereafter, TEs) to the oceans is vital for supporting marine life, as they play an important role in a range of metabolic processes in marine organisms and are essential for phytoplankton growth (Morel and Price, 2003). It is well established that in regions of high nitrate and low chlorophyll-a (HNLC), the major factor that restricts the growth of phytoplankton is inadequate iron (Fe) supply. Recent studies suggest that other than Fe, trace elements such as cadmium (Cd), copper (Cu), zinc (Zn), manganese (Mn) and cobalt (Co), may also be (co-) limiting factors for phytoplankton growth (Moore et al., 2013; Morel and Price, 2003). Nonetheless, our understanding of the biogeochemical cycles of trace elements and their influence on ocean productivity is still limited, and sources, sinks and boundary processes that control the distributions of these elements are poorly constrained.

Radionuclides from the uranium (U) and thorium (Th) decay series (Fig. 1.1) have been used as tracers and chronometers of processes in the oceans (Bourdon et al., 2003). Because the radionuclides have distinct chemical properties and half-lives ranging from seconds to millions of years, they can provide valuable information about a variety of processes which occur within this time scale. Thus, radionuclides can be used to investigate the cycling of TEs that have similar geochemical behavior or similar sources/ sinks, and can provide a time constraint on the biogeochemical processes of these TEs in the oceans. For example, Th and polonium (Po) are particle-reactive in seawater and can be useful for quantifying scavenging rates of carbon and TEs onto particles in the water column (e.g., Buesseler, 1998; Nozaki et al., 1997). In contrast, Th daughters, i.e., radium

(Ra) isotopes, do not interact strongly with particles in seawater, and can therefore be suitable tracers for ocean mixing processes (Ku and Luo, 2008), and powerful tools to investigate exchange rates between the ocean boundaries (Moore et al., 2000 a; Dulaiova et al., 2009; Charette et al., 2016).

The complex links between the biological, physical and geochemical processes at the land-ocean interface control the distribution of TEs and radionuclides in coastal environments. Understanding the factors that control the export of Ra isotopes to the oceans helps to evaluate physical and chemical processes that regulate inputs of other dissolved elements in the coastal and open ocean. Therefore, the main objective of this study was to apply the naturally occurring radium isotopes (^{223}Ra ^{224}Ra, ^{226}Ra, and ^{228}Ra) to provide insights into the distribution and behavior of TEs and quantify their boundary inputs into the ocean (see section 1.3). Trace elements reported in this Ph.D. thesis are Cd, Fe, Cu, Zn, Co, Mn, nickel (Ni), and lead (Pb). This introductory chapter presents an overview of the sources/ sinks, biogeochemical behavior, and distributions of both TEs and Ra isotopes in the oceans.

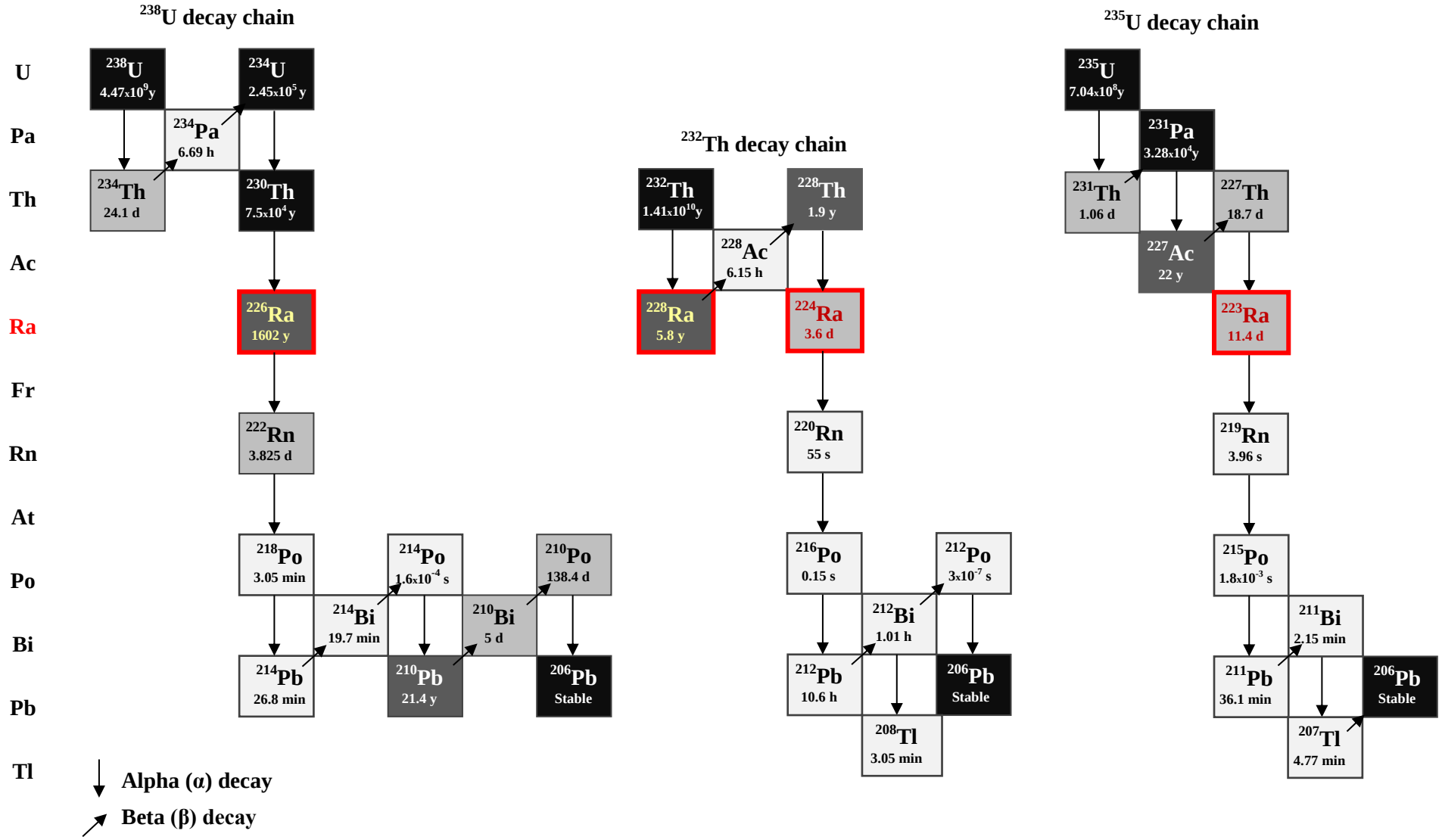

Figure 1.1: Scheme of the ^{238}U, ^{232}Th, and ^{235}U decay series. The grayscale reflects half-life, with darker shades corresponding to longer half-lives (modified from Ivanovich and Harmon, 1992). Ra isotopes are highlighted.

1.1 Trace elements and Ra isotopes in the oceans

Some of the most common elements in the Earth's crust (e.g. Fe) are found in the present ocean as traces, with very low concentrations of a few pmol L^{-1} to nmol L^{-1}, and higher concentrations near the continental margins (Bruland and Lohan, 2003). The concentrations of TEs and Ra isotopes in the worlds' oceans are controlled by their input and removal balance. Both Ra isotopes and TEs may be supplied to the ocean through river discharge, shelf and abyssal sediment release, atmospheric deposition and hydrothermal venting (Libes, 2009; Bruland et al., 2014; Krishnaswami and Cochran, 2008). Trace elements undergo biogeochemical cycling in the oceans that are mediated by redox reactions and formation of particulate matter. Thus, the removal of TEs can occur by biological uptake, and incorporation into or onto organic and inorganic settling particles (Chester and Jickells, 2012; Bruland and Lohan, 2003). While biological activity strongly affects the distributions of biogenic TEs in the oceans, Ra isotopes are much less affected by biological processes; therefore inputs, mixing, and decay are the major factors controlling Ra distributions. Because Ra isotopes present a range of half-lives (t ½) between 3.66 days to 1600 year (Fig. 1.1), and behave essentially conservatively in the oceans, they can be applied to study the age of water masses (Moore, 2000 b; Charette et al., 2001), shelf-ocean mixing processes (Moore and Dymond, 1991; Moore et al., 1995; 2000 a; Knauss et al., 1978), ocean circulation (Ku and Luo, 2008; Chung and Craig, 1980), mixing across the thermocline and between the benthic boundary layers (Sarmiento et al., 1990; Sarmiento et al, 1982; Moore, 1972), and more recently as traces of TE fluxes in the oceans (Vieira et al., 2019; Sanial et al., 2018; Charette et al., 2016; Dulaiova et al., 2009).

1.1.1 Biogeochemistry and distribution of TEs and Ra isotopes in the oceans

Trace elements

Trace elements in the ocean are typically classified as (i) nutrient-type elements (Cd, Cu, Ni, and Zn), whose distribution is controlled by biological activity and decomposition of organic matter; (ii) scavenged elements (aluminum (Al), Pb and Mn) which are removed from the water column through particle adsorption processes (Bruland et al., 2014); (iii) "hybrid-type" trace elements, i.e., a combination of nutrient-type and scavenging-type behaviors; and (iv) conservative-type (e.g., U, molybdenum (Mo) antimony (Sb), tungsten (W), rhenium (Re), cesium (Cs), and rubidium (Rb)), whose concentrations present a nearly constant ratio to salinity in the oceans, and their long residence time (on the order of 10^5 years) is greater than the vertical mixing (Bruland and Lohan, 2003).

Nutrient-type elements are depleted in surface waters due to biological uptake and enriched in deep waters owing to remineralization and dissolution of sinking organic matter (Fig. 1.2). Iron and Co display nutrient-like depletion in surface waters, but they are often referred to as hybrid-type trace elements since their distribution is controlled by both biological uptake and scavenging processes (Bruland et al., 2014). In contrast, Mn usually exhibits a surface enrichment due to the photochemical reduction of Mn oxides to soluble Mn (II), although it is also considered to be a hybrid-type element at high latitudes, where nutrient drawdown occurs (Bruland and Lohan, 2003). In addition, like Ra isotopes, Mn can be used as a tracer of lateral transport from continental margins (Aguilar-Islas and Bruland, 2006), whilst Pb is a good tracer of anthropogenic inputs to surface seawater through aerosol deposition (Maring and Duce, 1990). Moreover, elements such as Cd, Cu, Ni, and Zn follow the profiles of the

major macronutrients, nitrate, phosphate, and silicate, indicating their involvement in biological cycles (Boyle and Edmond, 1975; Bruland, 1980). Figure 1.2 shows an example of vertical profiles of 3 types of elements.

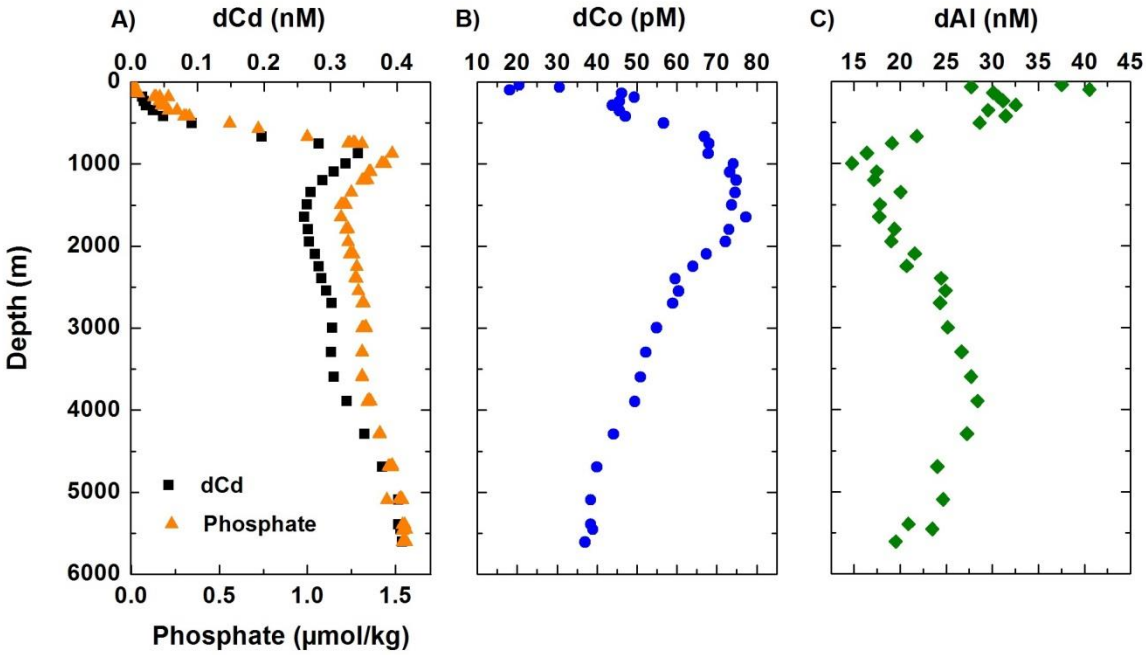

Figure 1.2: Profiles of dissolved cadmium and phosphate (A), dissolved cobalt (B) and dissolved aluminum (B) representing the nutrient-type, hybrid-type, and scavenged-type elements, respectively. Data taken from IDP 2017 data base (Schlitzer et al., 2018); GEOTRACES section GA03 in the North Atlantic Ocean, station 12 (56°81 W, 29°70 N).

The bioavailability and solubility of TEs in the oceans are governed by their redox-speciation in seawater and their aggregation into organic and inorganic complexes. The redox potential of a specific trace element and redox conditions of seawater dictate the oxidation state of this element in the ocean. Iron, Co, and Mn, for example, are typically present in seawater as trivalent cations as Fe (III), Co (III) and Mn (III), which are less soluble and more thermodynamically stable than their reduced form, Fe (II), Co (II), and Mn (II) (Stumm and

Morgan, 1981, 1995). When the reduced TEs undergo oxidation process, they can subsequently bind to particles forming, for example, colloidal Fe and Mn, and particulate Fe oxyhydroxide and Mn oxides, which can remove TEs by particulate scavenging and sinking (Lohan and Bruland, 2008). Moreover, oxidizing bacteria may also play an important role in biotic Mn (II) (and Co (II)) oxidation (Sunda and Huntsman, 1988; Moffett and Ho, 1996).

Radium isotopes

There are no stable isotopes of Ra, and each Ra isotope is derived from the decay of a corresponding isotope of Th (see Fig. 1.1). Radium-226 (t ½= 1600 years) and ^{223}Ra (t ½ = 11.4 days) are member of the ^{238}U and ^{235}U decay series, respectively; ^{224}Ra (t ½= 3.66 days) and ^{228}Ra (t ½ = 5.75 years) derive from the ^{232}Th radioactive decay series. The decay energies and percentage of emission of each Ra isotope are shown in Table 1.1. The most abundant Ra isotope is ^{226}Ra. As an alkaline earth metal, with atomic number Z = 88, all Ra isotopes, as well as the other alkaline earth metal (e.g. Be, Mg, Ca, Sr, and Ba), are only present in the environment in the +2 oxidation state.

Table 1.1: Energies (E) and emission percentage (*I*) of the natural occurring Ra isotopes. Values reported in: https://www.nndc.bnl.gov/nudat2/ (accessed 14. March 2019)

Radionuclide	**Half-life (t ½)**	**Alpha (α)**		**Beta (β)**		**Gamma (γ)**	
		E (keV)	***I* (%)**	**E (keV)**	***I* (%)**	**E (keV)**	***I* (%)**
^{223}Ra	11.43 days	5539.8	9.2			114.232	3.22
		5606.73	25.7			154.21	5.62
		5716.23	52.6			269.459	13.7
		5747	9.2			323.871	3.93
^{224}Ra	3.66 days	5448.6	5.06			240.986	4.1
		5685.37	94.92				
^{226}Ra	1602 years	4601	5.55			186.211	3.59
		4784.34	94.45				
^{228}Ra	5.75 years			12.83	30		
				25.71	20		
				39.23	40		
				39.62	10		

Radium is present in the environment, manly in seawater, at very low molar concentration (Broecker et al., 1967, Kaufman et al., 1973). The distribution of each isotope in the ocean varies significantly from one isotope to another and within ocean basins. For example, ^{226}Ra activities in the surface Atlantic Ocean are around 7.8 dpm 100 L^{-1} (Broecker et al., 1976), much lower than the surface activities in the Southern Ocean (>13 dpm 100 L^{-1}; Ku and Lin, 1976), due to upwelling of the ^{226}Ra enriched deep waters in the Antarctic region. The lowest surface ^{226}Ra activities are found in the Pacific Ocean (6.69 - 7.2 dpm 100 L^{-1}; Sanial et al., 2018; Chung, 1980), likely due to dilution in this larger size basin.

Radium-228 activities in surface waters of the Atlantic Ocean (1-3 dpm 100 L^{-1}) and Indian Ocean (2.6 - 10.7 dpm 100 L^{-1}) are generally an order of magnitude higher than the Pacific

and Southern Oceans (Li et al., 1980; Kaufman et al., 1973; Moore 1969). This is a result of inputs from the larger Atlantic/ Indian continental margins (Moore et al., 2008; Kwon et al., 2014), due to decay and mixing in the significantly larger Pacific basin, and due to low ^{228}Ra levels in upwelled Antarctic waters (see Okubo et al., 1979; Moore, 1969; Kaufman et al., 1973; Sanial et al., 2018; van Beek et al., 2007). Unlike ^{226}Ra, whose surface activities are relatively uniform within the basins, surface ^{228}Ra activities vary significantly across the same basin, due to its much shorter half-life relative to ^{226}Ra. Because of their very short half-life of few days, ^{223}Ra and ^{224}Ra are only found in regions close to their sources, such as continental margins and abyssal sediments. For this reason, the short-lived Ra isotopes are not typically detected beyond 50-100 km offshore (Levy and Moore, 1985; Moore, 2000 a, 2000 b), and 100 m above the seafloor (Charette et al., 2015).

Radium-226 is depleted in surface layers relative to deep waters (Fig. 1.3). However, the fact that Ra is present in the ocean at very low molar concentration makes direct precipitation of Ra phases difficult. Radium export from the water column may therefore occur by co-precipitation of phases in which Ra can be incorporated as solid form. The Ra removal rate is only relevant for the longest-lived and most abundant isotope (^{226}Ra) and is negligible relative to the loss through decay for ^{223}Ra, ^{224}Ra, and ^{228}Ra. Due to the similarity of Ra and barium (Ba) ionic radii, their chemical behavior is similar. Indeed, the linear relationship between Ba and ^{226}Ra in the global ocean, with a slope of 2.2 ± 0.2 dpm μmol^{-1} (Roy at al., 2018 and reference therein) lead scientists to hypothesize that barite ($BaSO_4$) formation plays an important role in the marine ^{226}Ra cycle, as barite can incorporate Ra as $Ba(Ra)SO_4$. A linear correlation has also been reported between ^{226}Ra and silicate (Si) from the surface ocean to about 2000 m, which suggests that ^{226}Ra is scavenged by marine diatoms, which are

siliceous organisms (see Chung, 1980; Moore and Dymond, 1991; Ku and Lin, 1976; Ku et al., 1970; Broecker et al., 1967; Charette et al., 2015). As a result, ^{226}Ra exhibits a nutrient-like profile. Below 2000 m, ^{226}Ra and Si relationship is more variable owing to the enrichment of ^{226}Ra relative to Si in deep waters, most likely due to diffusion of ^{226}Ra from abyssal sediments (Chung, 1980) (see Fig. 1.3 and 1.4). Because the mean life of ^{228}Ra is much shorter than the vertical ocean mixing, little ^{228}Ra penetrates into the thermocline (Moore, 1969); in addition, the rates of biological uptake and export are small compared to the ^{228}Ra supply to the oceans. As a result, a decrease in ^{228}Ra activities with depth is typically observed (Moore, 1972; Kaufman et al., 1973; Li et al., 1980) corresponding with an increase in water density that likely precludes vertical mixing. An example of the distributions of ^{226}Ra, ^{228}Ra, Si, and Ba in the ocean is shown in Figure 1.3 and Figure 1.4.

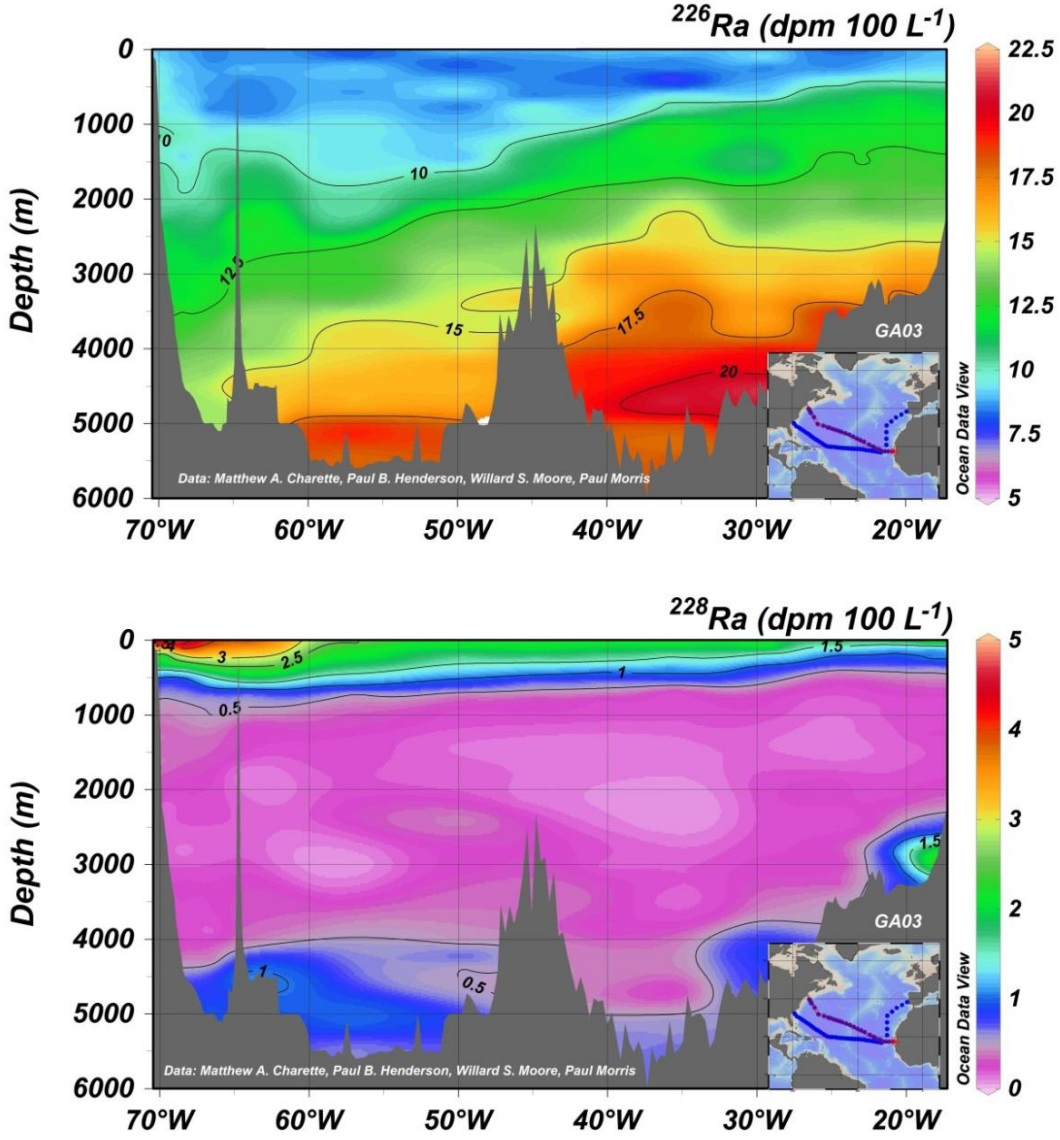

Figure 1.3: Radium-226 and ^{228}Ra distributions along a GEOTRACES section GA03 in the Atlantic Ocean (IDP 2017 data base (Schlitzer et al., 2018). This data is published in Charette et al. (2015).

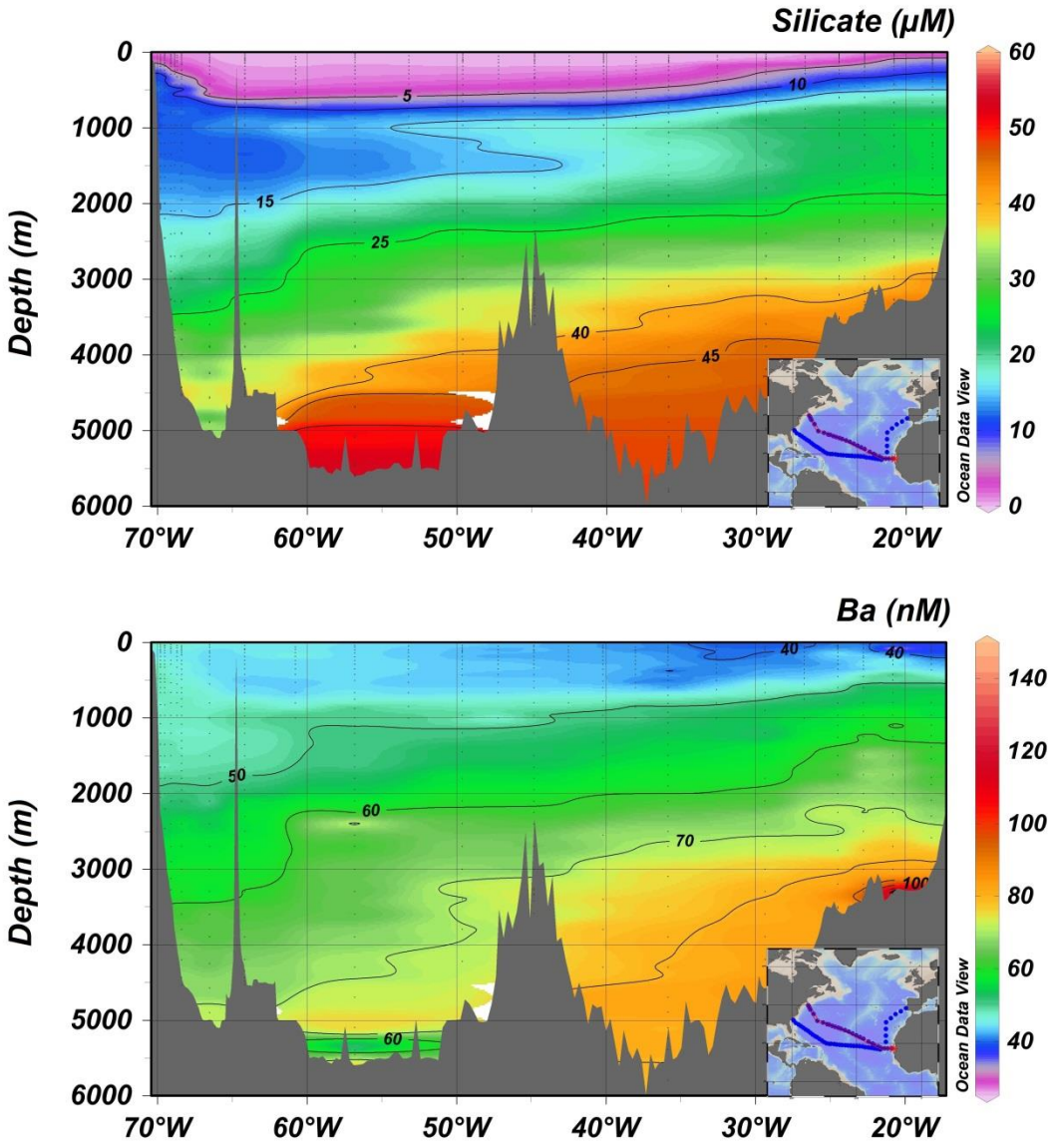

Figure 1.4: Silicate and barium along a GEOTRACES section GA03 in the Atlantic Ocean (IDP 2017 data base (Schlitzer et al., 2018). This data is published in Charette et al. (2015) and Roy et al. (2018).

.

1.1.2 Sources of TEs and Ra isotopes to the ocean

1.1.2.1 Rivers

Rivers are major sources of dissolved and particulate materials to the oceans (Bruland et al., 2014). The delivery of terrestrial materials from rivers to the oceans depends on the river water composition, as well as on the biogeochemical changes that occur preferentially in the mixing zone between the river and ocean waters (Macias et al., 2014; Tovar-Sanchez et al., 2016). Although dissolved TEs (dTEs) (e.g., Mn and Fe) are present in rivers, in colloidal form (defined by < 0.02 – 0.2 μm filtration), at micromolar concentrations (Gaillardet et al., 2003), their concentrations tend to decrease with increasing ionic strength in the river-ocean interface, due to particle scavenging, rapid aggregation of colloids and complexes in saline waters (Boyle et al., 1977; Sholkovitz et al., 1978; Johnson et al., 1999). Whilst a transfer of river-derived TEs from the dissolved to particulate phase does not necessarily result in its immediate removal from the water column (Gustafsson et al., 2000; Hong and Kester, 1985), settling of these particles on the shelf diminishes the role of rivers in supplying TEs to the offshore ocean. Nonetheless, TE concentrations derived from rivers are often augmented by interactions with shelf sediments in estuaries (see sections 1.1.2.2 and 1.1.2.3). Moreover, TEs can be stabilized by organic material, which keeps TEs in solution. In this way, the total TE supply from rivers/ estuaries may be significant, regardless of removal in estuaries.

In contrast to TEs, dissolved Ra concentrations in rivers are generally low, with activities ranging between 3 and 120 dpm 100 L^{-1} for both ^{226}Ra and ^{228}Ra (Vandenhove et al., 2010). Amongst the largest rivers in the world (Fig. 1.5), the long-lived Ra activities lie within a narrow range, with ^{226}Ra and ^{228}Ra varying from 3.3 to 20 dpm 100 L^{-1} and 3.2 to 16.3 dpm

100 L^{-1}, respectively. Radium desorption from riverine particle surfaces occurs as the particles enter the high ionic strength waters of the estuary (Li et al., 1977; Elsinger and Moore, 1980; Key et al., 1985; Moore, 1986). Consequently, unlike TEs, Ra activities in the river-ocean mixing zone increase compared to the riverine levels (Fig. 1.5). Furthermore, large fluxes of Ra from coastal sediments and submarine groundwater discharges contribute significantly to enhance Ra activities in estuaries (Moore et al., 1996; Shaw et al., 1998; Cai et al., 2003).

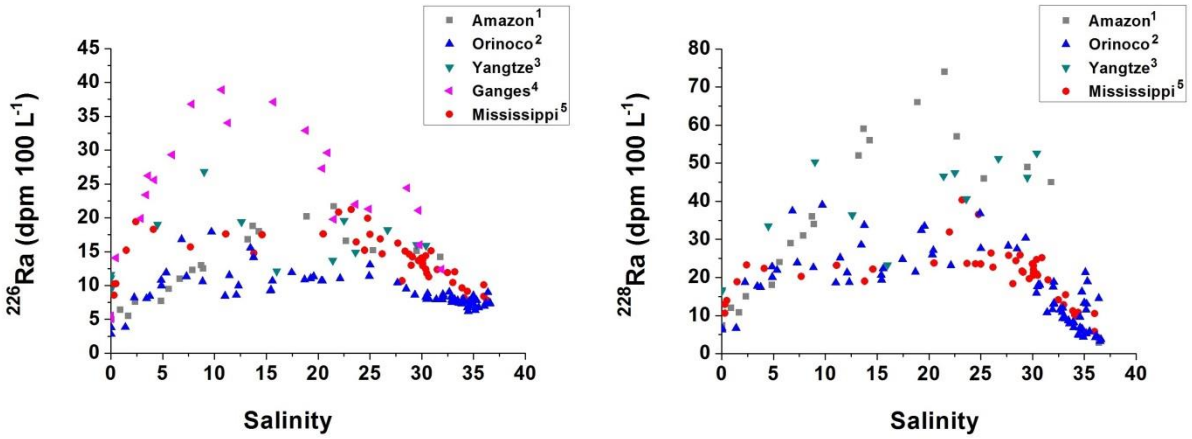

Figure 1.5: Activities of ^{226}Ra (A) and ^{228}Ra (B) across the estuarine salinity gradient in the Amazon[1], Orinoco[2], Yangtze[3], Ganges[4] and Mississippi[5] estuaries. [1] Key et al., 1985; [2] Moore and Todd, 1993; [3] Elsinger and Moore, 1984; [4] Carroll et al.,1993; [5] Krest et al., 1999.

1.1.2.2 Submarine Groundwater Discharge

Submarine groundwater discharge (SGD) has received considerable attention over the last two decades, as it appears to be a source of nutrients, TEs and radionuclides to coastal environments (e.g., Valiela et al., 1990; Windom et al., 2006; Moore, 1996). Burnett et al. (2003) defined SGD as "any and all flow of water on continental margins from the seabed to the coastal ocean, regardless of fluid composition or driving force". Most of the

groundwaters have high levels of Fe (II) and Mn (II) (Clark, 2015) which are turned into Fe (III) and Mn (III) under oxidizing conditions. As mentioned previously, this process leads to the formation of solid phase Fe-oxyhydroxides and Mn-oxides, in which other TEs tend to be incorporated through co-precipitation. Thus, the extent to which TEs are transported via groundwaters, as well as the biogeochemical behavior of TEs in coastal regions influenced by SGD are likely dependent on the TE solubility and sorption capacity, on the hydraulic conductivity, presence of Fe oxyhydroxide, Fe-sulfides and Mn oxides, and groundwater flow rates (Tang and Johannesson, 2006; Burnett et al., 2003, 2006).

Radium presence in groundwater results from the interaction of groundwater with U- and Th-bearing phases (e.g., soils, rocks, and ores). Radium isotopes have shown to be effective tracers of groundwater inputs to coastal regions (e.g., Rodellas et al., 2017; Moore, 1996). This method is based on the principle that Ra is strongly adsorbed to particles in freshwaters, while in brackish-saline waters they are primarily dissolved, due to rapid desorption resulted from ion exchange competition with the major constituents of seawater (Li et al., 1977; Key et al., 1985; Elsinger and Moore, 1984; Webster et al., 1995). In this way, Ra isotopes are valuable tools to study groundwater and regions influenced by SGD, where mixing of fresh and salty waters occur. As Ra isotopes are produced according to their decay constants, a short-time scale (day to months) seawater recirculation through permeable sediments only allows the in-growth of the short-lived Ra isotopes (^{223}Ra and ^{224}Ra). On the other hand, SGD are also commonly enriched in long-lived Ra isotopes in large seawater recirculation cells and long groundwater flow paths. Moore et al. (2008) suggested that SGD is the primary source of ^{228}Ra in the upper layer of the Atlantic Ocean, with flux of 1.9 ± 0.8 x 10^{23}atoms yr^{-1} corresponding to 54% of the total ^{228}Ra input to the Atlantic basin. They also

suggested that SGD fluxes may exceed the riverine nutrient fluxes. More recently, Kwon et al. (2014) estimated that the SGD contribution on the global ^{228}Ra budged was 5.6 ± 1.4 x 10^{23} atoms yr^{-1}, corresponding to 58% of the total ^{228}Ra input to the global ocean.

1.1.2.3 Sediments

Continental shelf sediments are important sources of TEs to the oceans (Elderfield and Hepworth, 1975; Elrod et al., 2004; Heggie and Lewis, 1984). Trace elements derived from river and atmosphere are deposited in sediments by settling particles, but they can eventually return back to the water column by diffusion (Elderfield and Hepworth, 1975) upon reductive/ non-reductive dissolution (Homoky et al., 2016; Lohan and Bruland, 2008), sediment resuspension, and submarine groundwater discharge (SGD) (Homoky et al., 2012; Chase et al., 2007; Windom et al., 2006). When organic matter is remineralized in the sediments, oxygen is consumed and upon full oxygen removal, nitrate is used as electron acceptor followed by TE reduction (e.g., Fe (III) and Mn (III)) (Lohan and Bruland, 2008). As reduced Fe and Mn are more soluble than their oxidized forms, they can diffuse back to the overlying waters. Thus, the TE supply from the sediments will depend on several factors including the organic matter and oxygen concentrations in the sediments, oxygen concentration in porewaters/ bottom waters and sediment type (Lohan and Bruland, 2008). Further discussion on the processes and the magnitude of benthic TE fluxes can be found in chapter 3.

Sediments also form a major source of Ra isotopes to the oceans (e.g., Moore, 1969; Cochran and Krishnaswami, 1980; Koczy, 1958) and represent, for example, the source of 25% of ^{228}Ra present in the global ocean (Kwon et al., 2014). As Ra parents (Th isotopes) are highly

insoluble and particle-reactive in seawater, they strongly adsorb onto mineral surfaces, and are complexed by humic acids and other organic ligands, and can be subsequently exported to the sediments (Langmuir and Herman, 1980; Buesseler, 1998), where Ra is produced. From sediment pore waters Ra is transported through advective and diffusive processes into the water column. Several factors control the Ra fluxes from the sediment, including: (i) the production rates governed by the specific Ra isotope decay constants (Moore, 1996); (ii) the concentrations of Ra parents and the nature of the sediment, e.g., non-carbonate sediments are enriched in ^{232}Th, and therefore may represent a significant source of ^{228}Ra and ^{224}Ra (Hancock et al., 2006); black shales and marine phosphates are commonly rich in ^{238}U (Bourdon et al., 2003) and may therefore be source of ^{226}Ra to the oceans; (iii) sedimentation rates; (iv) diffusive pore water transport; and (v) bioturbation (Cochran, 1980; Rutgers van der Loeff et al., 1984). Radium-228 flux from the sediment is discussed in detail in chapter 3, where a comparison between several systems is presented.

1.1.2.4 Atmospheric deposition

Atmospheric dust has been recognized as a major source of bioactive TEs (e.g. Fe, Mn, Cd, Co, Zn, and Ni) to the surface ocean (e.g. Duce et al., 1991), where phytoplankton grow. Volcanic ashes can also be an important TE source to the oceans (Achterberg et al., 2013). Aerosol transport is particularly important to primary productivity in remote regions of the ocean, where the influences of continental margins are limited. However, atmospheric deposition flux can vary significantly from one region to another by over two orders of magnitude (Mahowald et al., 2005), which suggests that the influence of aerosol inputs on TE biogeochemistry in surface oceans differs significantly over global scales (Boyd et al., 2010).

For example, in the Arctic region atmospheric dust fluxes to the ocean is the lowest with <0.5 g m^{-2} yr^{-1} due to absence of proximal dust sources (Jickells et al., 2005; Mahowald et al., 2005); whereas atmospheric dust deposition is the major source of TEs to the surface of the North and Equatorial Atlantic (Rijkenberg et al., 2014) due to inputs from the Sahara desert (>5 g m^{-2} yr^{-1}) (Jickells et al., 2005).

Radium isotopes are present in the air as soil dust. Moore et al. (2008) and Kwon et al. (2014) estimated the ^{228}Ra release from fine grained sediments contributes less than 1% of the total ^{228}Ra to the Atlantic Ocean.

1.1.2.5 Hydrothermal vents

Hydrothermal vents are fissures on the seafloor through where seawater can penetrate, be heated (up to 500°C) and chemically modified, as seawater-rock interaction enriches the circulating fluid with TEs, gases, and radionuclides (e.g., Resing et al., 2015; Kadko and Moore, 1988). The circulating fluid can rapidly be expelled back into the overlying waters in the form of black or white smoke. Elevated Ra activities were observed in the vicinity of hydrothermal vents (Kadko, 1996; Kadko and Moore, 1988), as the low pH and high temperature of the hydrothermal fluids may release Ra when the circulating fluid interacts with basalt. Once released from the hydrothermal vents, TEs can be rapidly scavenged onto particles, form sulfide and metal-oxides (e.g. Fe oxyhydroxides and Fe-sulfide and Mn oxides) and precipitate (Bruland and Lohan, 2003). In this way, hydrothermal vent form an important source (and sink in the case of TEs) for TEs and Ra in the deep ocean.

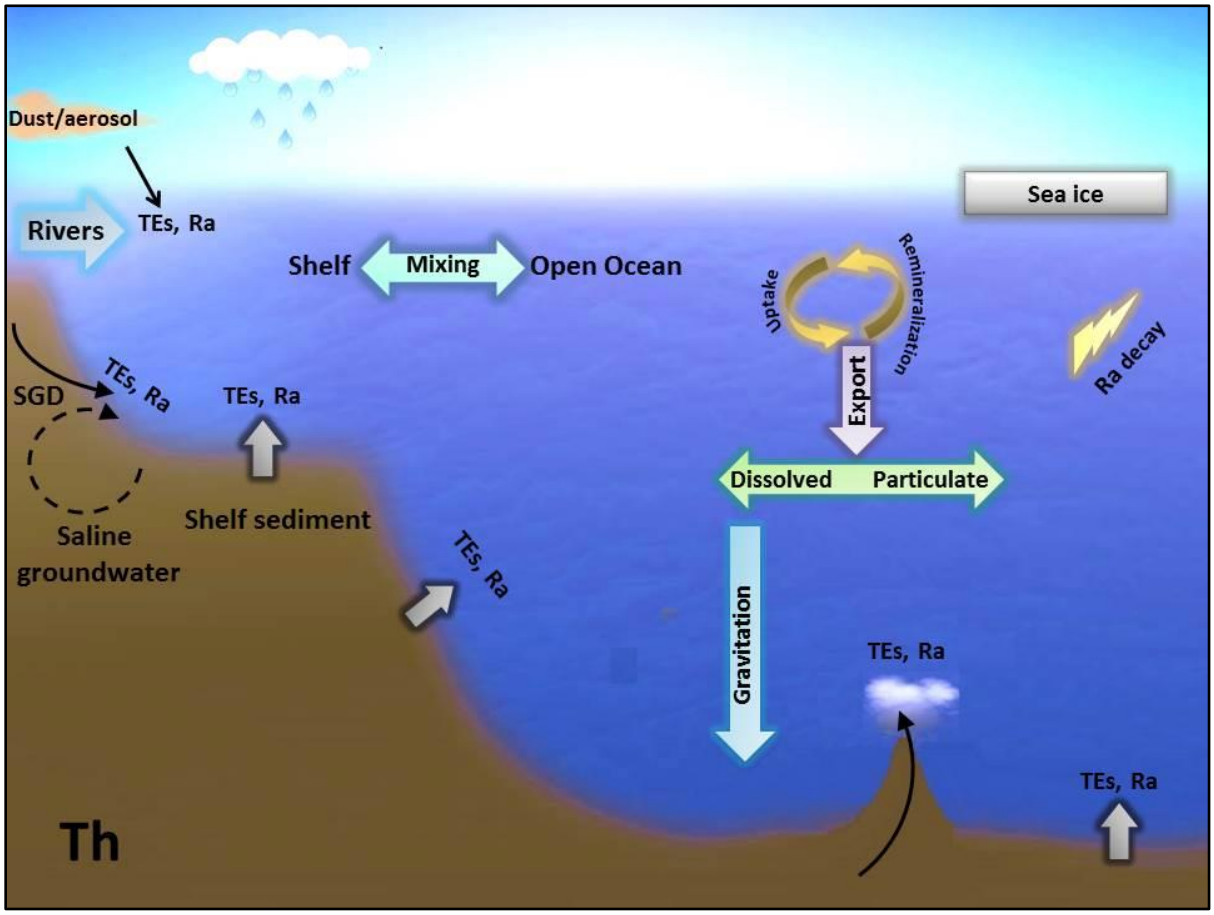

Figure 1.6: Schematic representation of the main TE and Ra sources, sinks, transport mechanisms, and processes that affect their distributions. Gravitation implies the sink terms (sorption and settling/ scavenging). The term "Th" represent thorium isotopes present in sediments.

1.2 Characteristics of the study regions

In order to study TE boundary fluxes in diverse ocean environments, this Ph.D. project focused on two regions with different oceanographic features that constrain the major sources and transport mechanisms controlling TE distributions, such as shelf sediments and rivers. One of these regions is the Chukchi Sea, the Pacific gateway to the Arctic and an important source of nutrients to the Arctic Ocean productivity. Pacific-origin waters that reach the Arctic basin through the Bering Strait are modified on the large Chukchi shelf before entering the Arctic Ocean, due to interaction between sediment and near-bottom water, ice

formation and melting, and primary production (Cooper et.al., 1997). The importance of the Chukchi shelf sediments in contributing TEs to primary productivity in the Arctic Ocean has been pointed out (Taylor et al., 2013; Nakayama et al., 2011). However, few studies focused on TEs other than Fe in the Chukchi Sea (Cid et al., 2012; Kondo et al., 2016); in addition, they focused on regions beyond the slope boundary between Chukchi Sea and Canada Basin. Before this Ph.D. project, an extensive TE and Ra isotope sampling over the Chukchi shelf had never been conducted, and TE data for the spring period was not available. As this region is unique because of its susceptibility to climate change (see chapter 3), the study of TE biogeochemical processes in the Chukchi Sea, as well as the comprehension of the role of shelf sediment in delivering TEs to the central Arctic basin, are crucial in the evaluation of the potential response of the biogeochemical cycles to future changes in the Arctic Ocean.

The second study region is the Southeast Atlantic Ocean, an important eastern boundary region that not only receives the discharge of one of the major world's rivers (Congo River), but is also influenced by the Benguela Upwelling system and the associated high biological productivity and low oxygen levels in subsurface waters. The Congo River is the world's second largest river by discharge volume of water (1.3×10^{12} m^3 yr^{-1}) and drainage basin size ($\sim 3.7 \times 10^6$ km^2) (Hopkins et al., 2013; Spencer et al., 2014), after the Amazon River. The Congo canyon is directly connected to the river mouth, which makes the bathymetry drop abruptly to 100 m still in the estuary. The Congo River plume can reach over 800 km offshore during the austral summer (Hopkins et al., 2013). Despite of the importance of the Congo River waters in the SE Atlantic, its influence on the TE biogeochemistry and chemical oceanography of the SE Atlantic has not been yet investigated comprehensively and there is far less information available than for other ocean regions. For example, it has been reported

that about 15% of the ^{228}Ra in the Atlantic Ocean is derived from the Amazon River (Moore et al., 1995) with most of the Ra originating from desorption from suspended particles in the estuary (Key et al., 1985); before this Ph.D. project however, comparable data for the Congo River was not available. Several studies have investigated the biogeochemical implications on nutrient and carbon cycling of the Congo River inputs in the coastal discharge region (e.g., Spencer et al., 2012; Vangriesheim et al., 2009; Braga et al., 2004), but little is known about fluxes of dissolved TEs from the Congo River and their influence on the primary productivity of the coastal and open (oligotrophic) waters of the southeastern Atlantic Gyre. Thus, to address this knowledge gap, this thesis evaluated the fate of the Congo River inflow in its far field in the SE Atlantic Ocean, and TE inputs from the Congo River waters and continental margin into the SE Atlantic Ocean were quantified by using Ra isotopes.

The southern portion of the study domain in the SE Atlantic Ocean is influenced by the Benguela Upwelling system. Benguela is one of the four major systems located on an eastern boundary of the worlds' oceans, and its oceanographic characteristics are somewhat similar to those found in the northwest of the Canaries in Africa, on the coast of California to the west of the USA, and in the current of Humboldt off Peru and Chile (Shannon and Nelson, 1996). However, the Benguela region is unique, as it constrains the boundaries of the 3 major oceans, such as the Atlantic, Indian, and Southern Oceans. The Benguela Current is therefore formed by three components: the South Atlantic Current as the southern limb of the South Atlantic subtropical gyre; the subantarctic water from the Antarctic Circumpolar Current (ACC); and the Agulhas Current, which is responsible for a leakage of Indian Ocean water masses into the Atlantic Ocean (Garzoli and Gordon, 1996). Waters from the Indian Ocean enter the Atlantic through relatively warm and salty eddies from the Agulhas retroflection,

while subantarctic surface waters from the ACC enter the South Atlantic Current through exchange processes across the Subtropical Front (Stramma and Peterson, 1989). In addition, like in the other named eastern boundary systems, the Benguela region is characterized by wind-driven offshore surface water drift resulting in strong upwelling episodes that extent along the SW African margin, adjacent to the coasts of Angola, Namibia and South Africa (Shannon and Nelson, 1996). The permanent upwelling results in a high input of TEs into the photic zone, thereby inducing an increase in primary productivity and consequently a formation of an intense oxygen minimum zone. All these features make of this region a critical environment for understanding the cycling of TEs in the ocean, and an important site for examining land-ocean export.

1.3 Objectives and structure of the thesis

The major objective of this thesis was to investigate the source and fate of TEs in the ocean, and to quantify boundary TE inputs to coastal and open ocean, in order to better understand their biogeochemical cycling and evaluate how that might change in response to a changing climate. To this end, the naturally occurring Ra isotopes (^{223}Ra ^{224}Ra, ^{226}Ra, and ^{228}Ra) were applied as tracers of TE fluxes from different ocean boundaries (shelf-sediments and rivers). The specific objectives included: (i) improve our understanding on the TE (i.e., Cd, Fe, Ni, Cu, Zn, Mn, Pb, and Co) distributions in shelf regions and their transport off-shelf; (ii) investigate and quantify the release of TEs from the shelf-sediments; (iii) identify the driving factors of the TE and Ra distributions along the western African coast, which includes the Benguela Upwelling System and the Congo River outflow; (iv) apply a novel technique by

using Ra isotopes to quantify TE fluxes from a river plume (Congo River) into the open ocean.

The study conducted in the Chukchi Sea was part of the SUBICE program (Study of Under Ice Blooms in the Chukchi Ecosystem). The major aim of SUBICE was to investigate the driving factors of the under-ice phytoplankton blooms observed in the Chukchi Sea, as an increase in light penetration associated with the loss of sea ice has led a dramatic increase in primary productivity in this region. The current study may therefore shed light into the role of TE inputs in the formation of large phytoplankton blooms that occur beneath the sea ice. The study conducted in the Southeast Atlantic Ocean was part of the GEOTRACES international program (section GA08). The GEOTRACES program succeeds the GEOSECS (Geochemical Ocean Sections Study) and TTO (Transient Tracers in the Ocean) programs, and has the mission to "identify processes and quantify fluxes that control the distributions of key trace elements and isotopes in the ocean, and to establish the sensitivity of these distributions to changing environmental conditions." The current study in the Southeast Atlantic therefore helps to fulfill the major objective of the GEOTRACES program.

To address the aims of this Ph.D. project, the thesis is structured with 6 chapters, including this introductory section. Chapter 2 has been written to provide a detailed description of the sampling and analytical methods used in this study. A succinct method section has been provided in each of the following chapters; therefore, chapter 2 only describes details that have been omitted in chapters 3, 4, and 5. Chapter 3 presented a discussion about the biogeochemical processes controlling the distribution of TEs in the shelf regions of the Bering and Chukchi Seas. The long-lived Ra isotopes (^{226}Ra and ^{228}Ra) were used as tracers

of TE fluxes from shelf sediments and the subsequent TE export to the Arctic Ocean. In chapter 4, the influence of the Congo River plume on the TE (Fe, Mn and Co) biogeochemistry and distributions is investigated. The processes governing the distributions of TEs in the river-ocean interface are discussed. Radium isotopes (^{224}Ra and ^{228}Ra) were applied to identify TE sources and to determine TE fluxes into an oligotrophic region of the South Atlantic Gyre. In chapter 5, the dominant sources of Ra isotopes along the western African coast and their inputs to the South Atlantic are discussed in detail. A comparison has been made between the northern region influenced by the River Congo and the southern region influenced by the Benguela Upwelling System. Chapter 6 finalizes this thesis with a summary of the main findings, their implications on the oceanographic studies; future recommendations are given in order to fill the gaps in the current knowledge on TE cycling and boundary exchange.

2 Methods

This chapter will describe the analytical methods and sampling procedures that are not already discussed within later chapters of the thesis.

2.1 Trace elements

2.1.1 Sample preparation and collection

Seawater samples are highly susceptible to contamination during sampling, filtration, storage and analysis procedures, due to the ubiquitous presence of trace elements, mainly Fe, on research vessels, working materials, and laboratories. To prevent contamination, strict clean working procedures must be adopted, from the initial bottle cleaning through the final analysis procedure. Therefore, before usage, all bottles, manufactured-laboratory materials, such as tubing, filters, hoses, were rigorously acid-cleaned (section 2.1.1.1).

In this study, dissolved trace element (dTE) samples, defined as anything which pass through a 0.2 - 0.45 μm pore sized filter, were collected by filtering seawater through an acid washed inline filter (0.2 μm pore size filter, Sartobran-Sartorious P-300). Total dissolvable trace element (TdTE) samples were collected without filtration. After collection, the samples were immediately acidified to pH 1.9 using concentrated HCl (OPTIMA, Fisher Scientific); samples were stored double-bagged for >12 months for further land-based analysis.

2.1.1.1 Cleaning procedure

Trace element samples were collected at sea in low-density polyethylene (LDPE, Nalgene) 125 mL bottles, which had been acid-cleaned following three main steps: (i) soaking for 24 hours in Mucasol Universal detergent (e.g., Sigma-Aldrich), in order to remove any residual grease on the bottle walls, rinsing with warm tap water to remove the soap, and subsequently rinsing three times with de-ionized water (18.2 MΩ cm^{-1}, Milli-Q, Millipore) (ii) soaking for a week in 20% v/v Hydrochloride acid (6.7 M - HCl) bath (e.g., Sigma-Aldrich, reagent grade 37%) and rinsing three times with de-ionized water, (iii) soaking for a week in 20% v/v Nitric acid (8.3 M - HNO_3) bath (e.g., Sigma-Aldrich, reagent grade 37%), and (vi) rinsing five times with de-ionized water and stored double-bagged until usage at sea.

New bottles used in the laboratory for trace element analysis (fluorinated ethylene propylene (FEP), Nalgene) (section 2.1.2.1) passed through the same cleaning process described above; additionally, the bottles were soaked for a day in 1 M HCl (e.g. Sigma-Aldrich, analytical grade) at 50°C, UV irradiated for 4 h and rinsed five times with de-ionized water. After this first cleaning step and the first usage, the FEP bottles were acid-cleaned after every usage by rising them three times with de-ionized water and completely filled with ~ 0.3 M (Ultra-pure Acid grade, Romil), UV- irradiated for 4 h, or heated at 45°C overnight and left aside for a week. This cleaning procedure showed to be efficient, as no contamination was observed when re-using the bottles.

Polypropylene (PP) 4 ml vials used in the last part of the analysis, described in section 2.1.2.2, were cleaned prior to use as follows: (i) soaking in Mucasol detergent (Sigma Aldrich) for a day and rinse 3 times with warm tap water and deionized water; (ii) heating in

a HCl bath (analytical grade as described for bottles) at 50°C for 24 hours and rinse 3 times with deionized water; (iii) heating in a HNO_3 bath (analytical grade as described for bottles) 50°C for 24 hours and rinsing 5 times with deionized water. After cleaning, the vials were stored double-bagged until the preconcentration procedure.

2.1.2 Analytical methods

Trace element analyses described in this section correspond to the study conducted in the Chukchi Sea. Trace element data from the GEOTRACES GA08 cruise (used in chapter 4 and 5) was provided by Stephan Krisch and Mark J. Hopwood.

2.1.2.1 Sample preconcentration in the SeaFAST

The ultra-low concentrations (nM-pM) of TE species in seawater require analytical techniques with appropriate detection limits. Thus, TE analysis started with offline preconcentration using an automated system SeaFAST (Sc-4 DX SeaFast pico; Elemental Scientific Inc. (ESI)), equipped with a TE chelating Wako resin (Wako Pure Chemical Industries, Japan). After the preconcentration step, the samples were subsequently analyzed in an inductively coupled plasma mass spectrometry (ICP-MS, Element-XR, Thermo Fisher Scientific).

The automated system SeaFAST consists of 6 reservoirs;(i) de-ionized water; (ii) a fresh ammonium acetate buffer solution (NH_4Ac, 1.5 M) prepared at pH 8.5 ± 0.05 and used to adjust the pH of the samples from 1.9 to the optimal pH of the chelating process of the resin (pH 6.4); (iii) elution acid (1 M sub-boiled HNO_3, SpA – Romil, purified by single distillation in a sub-boiling perfluoroalkoxy-polymer (PFA) distillation unit (DST-1000,

Savillex)); this solution was spiked with indium (In) solution (1µg L^{-1}) for correction of any instrumental drift during ICP-MS analysis and TE elution from the preconcentration column; (iv) 1 M HNO_3 (sub-boiled) used to clean up the resin; (v) and (vi) two additional 4 L reservoirs containing 1 M HNO_3 (rinsing solutions) used to rinse the valves, the tubing, and the autosampler needle.

The functioning principle of automated system SeaFAST is described as follows: First, the sample is loaded into a coil (10 mL) by a vacuum pump, and mixed with buffer in a 5 mL mixing column until the mixture reaches the pH 6.4 ± 0.05; whilst this mixture passes through the preconcentration column, trace elements are loaded onto the resin. The resin is then rinsed with de-ionized water to remove the seawater matrix and subsequently eluted with 1 M sub-boiled HNO_3 (spiked with In) to release the trace elements into a 4 mL Polypropylene (PP) vial for further analysis in the ICP-MS. The resin is then cleaned with 1 M sub-boiled HNO_3. The valves, the tubing, and the autosampler needle are finally rinsed with 1 M HNO_3 (rising solutions).

For TE preconcentation, sub-samples were prepared containing 15 mL and 9 mL of seawater samples for dTE and TdTE analysis, respectively. Less volume of seawater samples was used in the preconcentration of TdTEs since the unfiltered samples were highly enriched in TEs (see chapter 3). The concentrations of dTEs and TdTEs (i.e., Cd, Fe, Ni, Cu, and Zn) were determined by isotope dilution, whereas the method of standard addition was used for Pb and the monoisotopic elements Mn and Co (see section 2.1.3). Prior to preconcentration, the sub-samples were spiked (100 µL) with an isotope dilution spike solution (ID_{spike1}) and a multielement standard solution ($ME_{standard}$). The first contains isotopically-enriched multi-

elements (^{111}Cd, ^{57}Fe, ^{62}Ni, ^{65}Cu and ^{68}Zn, ISOFLEX USA). These enriched isotopes were initially in a solid form, but were dissolved in concentrated HNO_3 (sub-boiled); the resulting solution was externally calibrated by ICP-OES and reverse ID-ICP-MS (Rapp et al., 2017), and subsequently diluted several times in 1 M HNO3 (sub-boiled) until the desired concentration of my isotope dilution spike solutions. As the TdTE (e.g., TdFe and TdMn) concentrations of my samples were high (see chapter 3), isotope spike solutions (ID_{spike1}) with different concentrations had to be used for dTEs and TdTEs. Therefore, for the dTE analysis, the concentrations of ^{111}Cd, ^{57}Fe, ^{62}Ni, ^{65}Cu, and ^{68}Zn in my isotope dilution spike were respectively: 46.9 nM, 133 nM, 48.5 nM, 140 nM, and 92.3 nM; while for the TdTE analysis their concentrations were 462 nM, 1312 nM, 477 nM, 1404 nM, and 908 nM, respectively. The final concentrations of Td- and d-Cd, Fe, Ni, Cu, and Zn were calculated as in section 2.1.3.

For analysis of Mn, Co and Pb, I prepared a multielement standard solution by serial dilution of individual stock standards (CertiPur, Merck) in 0.45 M sub-boiled HNO_3, with concentrations of 110 nM, 17.8 nM, and 9.30 nM for dMn, dCo, and dPb respectively; whereas for TdTE analysis their concentrations were respectively, 1006 nM, 161 nM, and 84.6 nM. After spiking the sub-samples, they were UV irradiated for 4 h in a home-made box equipped with four low-pressure mercury vapor lamps (25 Watt, Phillips), in order to increase TE recovery, in particular, Co and Cu, that are strongly complexed to organic compounds (Milne et al., 2010). Their calibrations were performed by standard additions to every 10th sample, and concentrations were calculated based on linear regressions of the sequentially-spiked samples, i.e. the mean slope, from one standard addition run before and

one after the sample, was used to calculate the concentrations of Co, Mn, and Pb (section 2.1.3).

The accuracy and precision of the method were evaluated by analyzing SAFe (D1) reference seawater treated in exactly the same way as the seawater samples (see supplementary material of chapter 3).

2.1.2.2 Analysis in the ICP-MS

Inductively coupled plasma mass spectrometry not only offers extremely low detection limits (pM) with good precision but has also a multielement capability and provides fast analysis. The sample, collected from the 4 mL PP vials by the autosampler needle, is pumped into a nebulizer where it is transformed into droplets of aerosol with argon. Subsequently, fine and large aerosol droplets are separated in a spray chamber. When the fine aerosol exits the spray chamber, it is transported to the inductively coupled plasma (ICP) at a very high temperature (6000 – 10000 °C) where it is converted into positively charged ions. The ions are directed into the interface of the mass spectrometer (sampler and skimmer) under high vacuum (1 x 10^{-7} mbar). The interface consists of metallic cones with tiny orifices where the ions pass through to reach the ion optics. The lenses in the ion optics are used to focus the ion beam through a 1 mm gap into the electrostatic and magnetic sectors and separate the ions by their mass to charge ratio. The ion separation is done by alternating AC and DC voltage before the ions reach the detector. Subsequently, the ions are detected in a Faraday detector combined with a dual mode Secondary Electron Multiplier (SEM) detector where an electrical signal is produced proportional to the number of ions reaching the detector surface.

Three more solutions were prepared and analyzed together with the preconcentrated samples in the ICP-MS. These solutions are: (i) a spike solution (ID_{spike2}) containing the artificial isotope ratios of the elements (i.e., $^{110}Cd/^{111}Cd$, $^{56}Fe/^{57}Fe$, $^{60}Ni/^{62}Ni$, $^{63}Cu/^{65}Cu$, and $^{66}Zn/^{68}Zn$), prepared by diluting the concentrated isotope dilution spike (described in the previous section) in 1 M sub-boiled HNO_3; (ii) a multielement spike solution (ME_{spike}) containing the natural ratio of isotopes of the elements analyzed (i.e., Cd, Fe, Ni, Cu and Zn), prepared by dilution of individual stock standards (CertiPur, Merck) in1 M sub-boiled HNO_3; and (iii) a solution of 1 M sub-boiled HNO_3 used as acid blank (AB). These solutions were measured 10 times at the beginning and at the end of each ICP-MS run and every 10^{th} samples. They were used to obtain the natural (ME) and enriched (spike) isotope ratios in order to calculate trace element concentrations as described in the following section.

2.1.3 Trace element concentration estimates

Trace element concentrations using the isotope dilution technique (Cd, Fe, Ni, Cu, and Zn) were determined as follows:

$$C_{sample} = C_{spike} (R_{sample} - R_{ID\_spike})/(R_{ME\_spike} - R_{sample})/x \qquad \text{(Equation 2.1)}$$

where C_{sample} is the TE concentration in the sample before the buffer correction; C_{spike} is the TE concentrations in the ID_{spike1} added to the sample; R_{sample} is the isotopic (natural) ratio measured in the sample; R_{ID_spike} is the artificial isotopic ratio of the isotope dilution spike (ID_{spike2}) prepared for the ICP-MS analysis; R_{ME_spike} is the natural isotopic ratio of the multielement spike (ME_{spike}) prepared for the ICP-MS analysis; and x is the natural abundance of the isotope.

Blank contributions were corrected for the final TE concentrations. They were determined from the manifold and the NH_4Ac buffer blanks obtained in the preconcentration procedure, as well as the acid blank prepared for the ICP-MS analysis and used to dilute the ID_{spike} and ME_{spike}. The manifold blank (MB) contribution accounts for the TEs present in the elution acid and any component of the preconcentration procedure and was determined as the concentration of TEs in 1 M HNO_3 (spiked with In) after processing through the first three steps from the sample preconcentration method described in section 2.1.2.1. Five manifold blanks were collected at the beginning and at the end of the preconcentration and two were collected every 10^{th} samples. Therefore, the isotope ratios of equation 2.1 were determined by taking into account the manifold and acid blanks contributions as follows:

$$R_{sample} = (n_1 - MB_1)/(n_2 - MB_2) \qquad \text{(Equation 2.2)}$$

where n_1 and n_2 are the number of counts in the sample for isotope 1 and isotope 2, respectively; MB_1 and MB_2 are the number of counts in the manifold blank for isotope 1 and isotope 2, respectively. After the sample was analyzed, trace element concentrations were corrected by the average of counts of one manifold blank before and two manifold blanks.

$$R_{ID\_spike} = \text{Average } [(spike_1 - AB_1)/(spike_2 - AB_2)] \qquad \text{(Equation 2.3)}$$

where $spike_1$ and $spike_2$ are the number of counts in the ID_{spike2} for isotope 1 and 2, respectively (measured every 10^{th} sample before and after the sample); AB_1 and AB_2 are the number of counts in the acid blank for isotope 1 and 2, respectively. Similarly, R_{ME_spike} was determined by replacing the ID spike in equation 2.3 by the multielement spike (both

measured every 10^{th} sample before and after the sample). Final concentrations were determined after the correction of the buffer blank.

The NH_4Ac buffer blank was determined using two batches of filtered (0.2 µm) South Atlantic seawater diluted 1:10 with de-ionized water and acidified to pH 1.9 and 1.6 with HCl (UpA, Romil). Seawater was diluted in order to reduce the concentration of TEs in the solutions. The solutions were treated as the samples and preconcentrated in replicates of 5. Different amount of buffer had to be added to these solutions during the preconcentration in order to increase the pH from 1.9 or 1.6 to pH 6.4. Therefore, buffer contribution in the samples (C_{buffer}) was determined as the difference between the mean TE concentrations in these solutions as follow:

$$C_{buffer} = V_{sample} \text{ x } C_{solution}/V_{solution} \qquad \text{(Equation 2.4)}$$

where V_{sample} is the volume of buffer added to samples collected at sea, $V_{solution}$ is the difference in volume of buffer added to the different solutions described above; and $C_{solution}$ is the difference of TE concentrations in the two solutions. The final trace element concentrations (C_{final}) were obtained as follows:

$$C_{final} = C_{sample} - C_{buffer} \qquad \text{(Equation 2. 5)}$$

The final TE concentrations determined by the standard addition method (Mn, Co, and Pb) were calculated as follows:

$$C_{final} = (n_{sample}/n_{Indium})/slope \qquad \text{(Equation 2. 6)}$$

where n_{sample} is the number of counts in the sample; n_{Indium} is the number of counts of Indium in the sample (from the elution acid); and the average slope of the linear regressions (every 10^{th} samples).

2.2 Radium isotopes

Radium sampling and analysis during SUBICE and GEOTRACES GA08 research cruises discussed in this thesis were performed in similar ways, and differences are described where appropriated.

2.2.1 Sample collection and preconcentration

Radium isotopes (e.g., ^{226}Ra, ^{228}Ra, ^{224}Ra, and ^{223}Ra) are present in open ocean waters at very low concentrations; therefore, large volumes of water (200-1000 L) are required to preconcentrate Ra and to obtain measurable quantities for the analytical methods used.

Surface samples were collected by pumping ca. 200-260 L of seawater into a barrel using (i) the ship's seawater intake and Niskin bottles of the CTD rosette frame (SUBICE cruise); and (ii) a high flow submersible and in-line booster pump (12 V d.c., Whale) that was lowered to about 3 m depth (GEOTRACES GA08 cruise). In order to check if the seawater collected from the ship's intake during the SUBICE cruise was not contaminated by thorium isotopes and the pipes did not contribute additional Ra to the sampled seawater (Charette et al., 2007), we compared samples collected from the intake line with water collected from the CTD at selected stations (see details in chapter 3). Subsequently, Ra isotopes were preconcentrated by pumping (<1 L min^{-1}; Solinst Peristaltic Pump, 410) from the barrel through a single PVC column loaded with 18 g of MnO_2-coated fibers (hereafter Mn-fiber), which were then rinsed

and partially dried for further analysis (chapter 3). In order to check the extraction efficiency of the Mn-fibers, two identical columns filled with 18 g of Mn-fiber were used in line (in 4 stations). The extraction efficiency of 95% ± 3% during the GEOTRACES cruise was obtained (using ^{224}Ra and ^{223}Ra), while during the SUBICE cruise the extraction efficiency was 94 ± 4% (using ^{228}Ra and ^{226}Ra). The extraction efficiencies (E) were determined using the activity ratios of column 1 and column 2 as follows:

$$E = 1 - (\text{column 2}/\text{column 1}) \qquad \text{(Equation 2.7)}$$

Deep seawater samples were collected during the GEOTRACES GA08 cruise by using five in-situ Stand-Alone Pumping Systems (SAPS; Challenger Oceanic) equipped with a membrane filter (1 μm pore size, polycarbonate Whatmann) to collect suspended particles; the filtrate then passed through MnO_2-coated polypropylene filter cartridges (1μm grooved Micro-Klean G Series cartridges, 3 M; hereafter Mn-cartridges) to extract the Ra isotopes (see Moore et al., 1985; Charette et al., 2015; Henderson et al., 2013). The in-situ pumps were fixed on steel wire of the CTD-Rosette and lowered to the desired depths (100 m, 200 m, 300-400 m; 500-650 m, and 1000-1250 m). The pumps operated for approximately 1 h, pumping around 1000 L of seawater through the Mn-cartridges at a mean flow rate of approximately 15 L min^{-1}. Before every deployment, the Mn-cartridges were first cut in half (~15 cm each piece), and a plastic spring was placed below each Mn-cartridge inside the holder in order to avoid seawater bypass through the cartridge, hence improving the Ra extraction efficiency on the Mn-cartridges (Sanial et al., 2018). The scavenging efficiency of radium on the MnO_2 cartridges (65% ± 12%) was determined by measuring Ra-226 in a discreet water sample (1 L), via co-precipitation of Ra with $BaSO_4$ (Moore et al., 1985),

using high purity, well-type germanium detectors (HPGe) for a period of 55 days (see section 2.2.2); and by placing two cartridges in series in the in-situ pump at certain stations, and applying equation 2.7. Our extraction efficiency is consistent with reported values (Sanial et al., 2018; Charette et al., 2015).

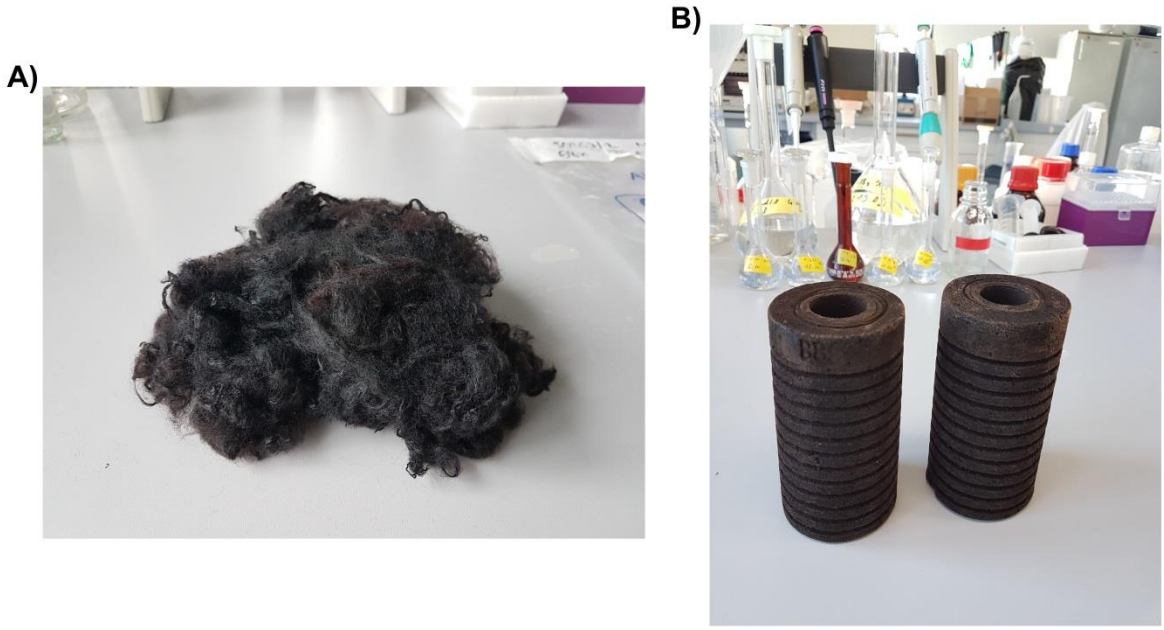

Figure 2.1: Photography of the MnO_2-coated fibers (A) and the MnO_2-coated cartridges (B).

2.2.2 Analytical methods

Several techniques for Ra isotope analysis are available, for example: (i) the RaDeCC system (Radium Delayed Coincidence Counter), developed by Moore and Arnold. (1996) can be used to measure both short-lived (Moore, 2008; Garcia-Solsona et al., 2008) and long-lived Ra isotopes such as ^{226}Ra via ^{222}Rn ingrowth (e.g., Geibert et al., 2013) and ^{228}Ra via ^{228}Th ingrowth; (ii) γ-spectrometry for all radium isotopes (e.g., Michel et al., 1981; Charette et al., 2001 van Beek et al., 2010; Moore et al., 1995; Reyss et al., 1995); (iii) a radon-in-air

monitor (e.g. RAD-7, Durridge) for ^{226}Ra determinations (Kim et al., 2001); (iv) mass spectrometry for ^{226}Ra and ^{228}Ra (e.g., Foster et al., 2004, Bourquin et al., 2011; Varga, 2008; Hsieh and Henderson, 2011); (v) Lucas cell (^{226}Ra, e.g. Key et al., 1979). In this research work, the RaDeCC system was applied to measure the short-lived Ra isotopes, while the long-lived ^{228}Ra and ^{226}Ra were analyzed by γ-spectrometry.

2.2.2.1 Short-lived Ra isotope analysis by the RaDeCC

The RaDeCC system offers a fast and precise analysis of ^{224}Ra and ^{223}Ra in water samples (Moore, 2008) and consists in (i) a scintillation cell; (ii) a photomultiplier tube; (iii) a pump used to pump helium through the samples (a column filled with Mn-fibers/ Mn-cartridges). The system is based on the measurement of alpha particles from the decay of ^{223}Ra and ^{224}Ra daughters (i.e. ^{219}Rn and ^{220}Rn, respectively), and their decay products (^{215}Po and ^{216}Po, respectively). First, helium (He) circulates through the Mn-fibers/ Mn-cartridges (5-7 L min^{-1}), where ^{219}Rn and ^{220}Rn produced by the decay of Ra isotopes are swept into the alpha scintillation cells. The alpha particles generated by the decay of Rn and Po-daughters produce a signal that is directed to a delayed-coincidence system composed of three different counter channels: two distinct channels that record the counts of the ^{219}Rn-^{215}Po and ^{220}Rn-^{216}Po pairs (219 and 220 channels) and one channel that records all decay events. The delayed-coincidence system uses the differences in decay constants of ^{215}Po and ^{216}Po to detect the alpha particles corresponding to the ^{219}Rn and ^{220}Rn decay, and hence to determine the ^{223}Ra and ^{224}Ra activities in the sample. The principle of the RaDeCC system is described in details in Moore and Arnold (1996).

Activities of ^{223}Ra and ^{224}Ra were determined using 4 radium RaDeCC systems (Fig. 2.2). The fibers and cartridges were first counted on-board the ship to determine the total activities for the short-lived Ra isotopes. The total activity of a daughter (e.g., ^{224}Ra) consists in a component which is supported by secular equilibrium with its parent (i.e. ^{224}Ra activity is equal the activity of its parent ^{228}Th) and an "excess" component which decays with time. The Mn-fibers/ cartridges were aged for 6 weeks in order to allow initial excess ^{224}Ra to equilibrate with ^{228}Th, which is also adsorbed to the Mn-fibers/ cartridges. The samples were then recounted to determine ^{228}Th activities and thus correct for ^{224}Ra supported by dissolved ^{228}Th. Thus, ^{224}Ra in excess ($^{224}Ra_{ex}$) can be obtained as follows:

$$^{224}Ra_{ex} = {}^{224}Ra_{total} - {}^{224}Ra_{supported} \qquad \text{(Equation 2.8)}$$

Before every sample counting, a background measurement was performed for the correction of the results and uncertainties according to Garcia-Solsona et al. (2008). In order to avoid counts build up in the total channel due to the ingrowth of ^{222}Rn from the ^{226}Ra decay, the measurement of every sample was split in two measurements of 3 h each (Garcia-Solsona et al., 2008). The system was flushed with air for 10 minutes, then with helium for 5 minutes before every measurement.

The calibration of the detectors for analysis of ^{224}Ra was performed by adsorbing known activities of ^{232}Th to Mn-fibers as described in Scholten et al. (2010). Three standards were prepared and counted periodically when the samples were analyzed. The standard material (^{232}Th) was provided by the International Atomic Energy Agency (IAEA) (Jan Scholten, pers. comm.). The RaDeCC detector efficiency for ^{223}Ra was calibrated with ^{224}Ra, taking

into account the different isotope half-lives, the time the counting gates are open, and detector volume (Moore and Cai, 2013).

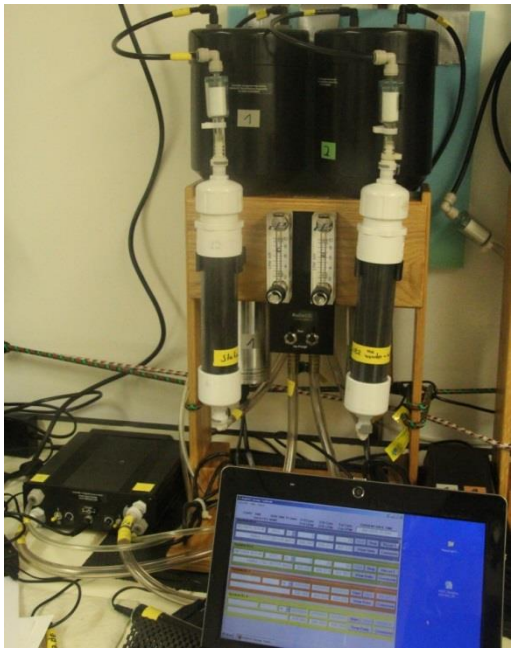

Figure 2.2: RaDeCC system on board the GEOTRACES GA08 cruise.

2.2.2.2 Sample preparation for the long-lived Ra isotope analysis

Two different sample preparations for Ra analyses were applied for SUBICE and GEOTRACES GA08 cruises. During the SUBICE expedition, only surface samples were collected and therefore only Mn-fibers were used to preconcentrate radium from seawater. Radium-228 and ^{226}Ra were extracted from the Mn-fibers via chemical leaching followed by co-precipitation with $Ba(Ra)SO_4$. Details of this procedure are given in the method section of chapter 3 and therefore there will be no further discussion at this point here. The blanks were determined from acids and solutions used in the leaching procedure, as well as from the Mn-fibers: the same amount of fiber as used for the sample collection were leached and analyzed

as described for the samples. The recovery of this method is described in details in chapter 3. Blank and background contributions were considered in the calculation of final Ra activities. The analyses of the samples were then performed by gamma spectrometry using a single high-purity, well-type germanium detector (HPGe; Canberra, EGPC 150) (see section 2.2.2.3).

Samples obtained during the GEOTRACES GA08 cruise were first analyzed for the short-lived Ra isotopes by the RaDeCC. Then the Mn-cartridges and Mn-fibers used to preconcentrate Ra were ashed at 600°C for 16 h (muffle oven Nabertherm, LE14/11/B150); after cooling, the cartridges were turned over and ashed again at 600°C for 16 h. The Mn-fibers were ashed only once. This procedure reduced the volume of the Mn-fibers by 90% with a final mass of about 2 g. The final mass of the cartridges ranged between 5 g to 25 g. The remaining amount of ash of the cartridges was too large to fit inside the well of the HPGe detector (Canberra Eurisys GMBH, EGPC 150) (see Fig. 2.3). Therefore, the Mn-fibers/ cartridges ashes were subsequently leached followed by co-precipitation with $BaSO_4$ as described below.

The leaching procedure consisted in boiling the ashes in 3.5 M hydroxylamine (e.g., VWR Chemicals) until all the ash was totally dissolved. Subsequently, concentrated HCl (e.g., Carl Roth, reagent grade 37%) was added until completely discoloring the solution. Radium present in the solution was co-precipitated with $BaSO_4$ when the solution was still warm. After precipitation, the solution was kept warm (60°C) and stirred with a magnetic stirring bar for > 1 h, in order to increase the crystal sizes of $Ba(Ra)SO_4$. After removing the stirring bar, the solution was left to settle overnight. The supernatant was then discharged and the

precipitated matter washed with de-ionized water three times. After drying at 105°C (8 h) (Heratherm Oven, Thermo Scientific), the precipitate was transferred to a 1 mL vial sealed with Parafilm (Moore et al., 1985), in order to avoid loss of sample material (Michel et al., 1981). The precipitate was stored for at least 3 weeks before analysis to allow ^{222}Rn to grow into equilibrium with ^{226}Ra, and analyzed by gamma spectrometry. In order to check the recovery of this method, Mn-cartridges and Mn-fibers were spiked with known ^{226}Ra and ^{228}Ra activities followed by the same purification procedure as described above. The recovery of Ra from Mn-cartridges was 93% ± 3%, while the recovery on Mn-fibers was 94% ± 6%.

2.2.2.3 Long-lived Ra isotope analysis by Gamma Spectrometry

Gamma-ray spectrometry has been widely used for qualitative and quantitative analysis of natural radioactivity in environmental samples. In a well-type germanium detector, such as used during this research work (Fig. 2.3), the samples are virtually surrounded by active detector material, which provides good detection efficiency. The gamma photons emitted by the sample with known energies interact with the germanium crystals and emits signals corresponding to the energy of the incoming photons. The signals are displayed as a spectrum plotted as the number of counts versus the radionuclide energy (Fig. 2.4). Each radioisotope emits gamma-rays with specific energies. Radium-226, for example, emits a single measurable line in 186 keV with an intensity of 4%. However, interference is caused by the 185.7 keV line emitted by the ^{235}U. Therefore, ^{226}Ra activities are determined by the energies of its daughters lead-214 (^{214}Pb, 352 keV) and bismuth-214 (^{214}Bi, 609 keV). As ^{228}Ra has no significant gamma emission (see Table 1.1), actinium-228 (^{228}Ac, t ½ = 6.15 h; 911 keV),

which is in radioactive equilibrium with ^{228}Ra, is used to determine ^{228}Ra. The peaks were analyzed by the software Gamma Acquisition & Analysis (Gennie 2000, v.3.2.1, Canberra Industries).

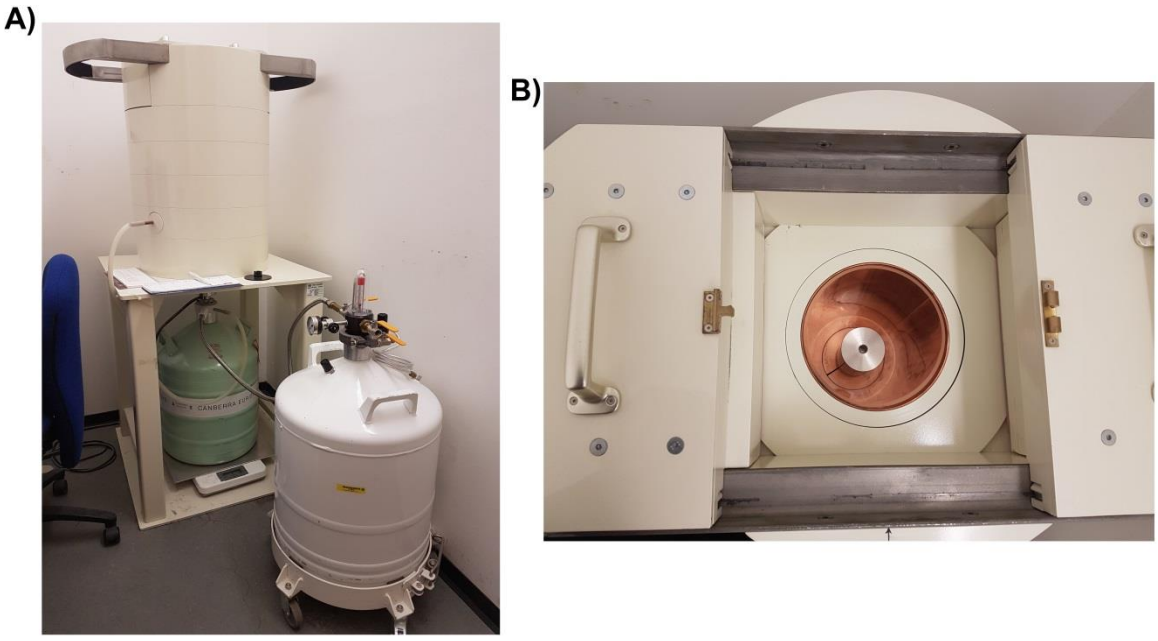

Figure 2.3: (A): Photography of the well-type germanium detector (HPGe; Canberra, EGPC 150), used during this research work, based in Kiel at GEOMAR (Helmholtz Centre for Ocean Research Kiel). (B): The well inside the detector (5.5 cm height and 1.5 cm diameter).

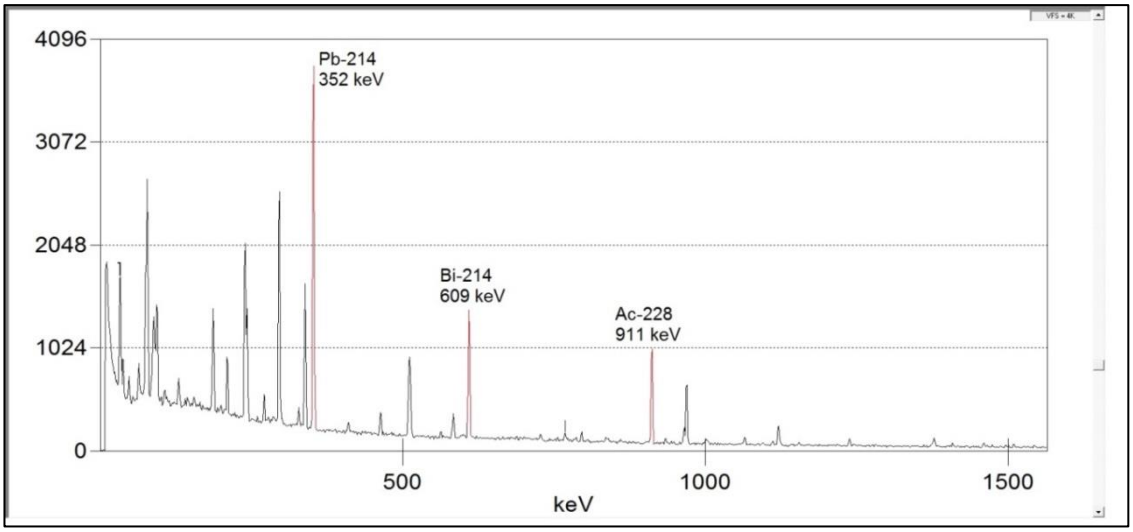

Figure 2.4: Example of spectra for long-lived Ra isotope analysis. Red peaks represent ^{214}Pb peak at 352 keV and ^{214}Bi peak at 609 keV used for ^{226}Ra analysis and ^{228}Ac peak at 911 keV for ^{228}Ra analysis.

The detector counting efficiency was calibrated by measuring Mn-fibers spiked with increasing amounts of ^{228}Ra and ^{226}Ra, with activities varying between 2 and 35 dpm 100 L^{-1} for ^{228}Ra and 5 to 50 dpm 100 L^{-1} for ^{226}Ra. The calibration curves obtained for each peak analyzed is shown in figure 2.5. The standards were prepared in the same $BaSO_4$ matrix and geometry as per samples in order to avoid different gamma photon adsorption. The Ra spike solutions were provided by the International Atomic Energy Agency (IAEA) (Jan Scholten, pers. comm.) and have a reported activity accuracy of 6% for ^{226}Ra and 5% for ^{228}Ra.

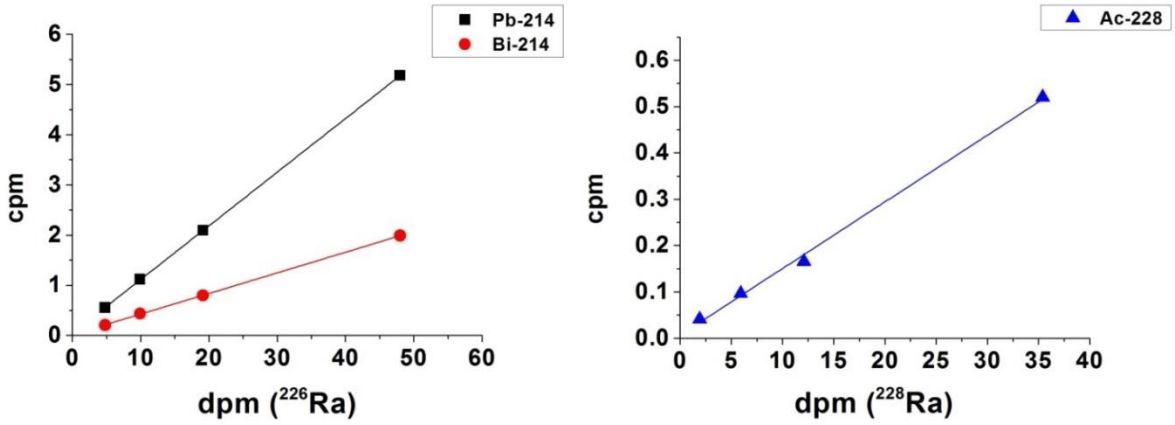

Figure 2.5: Calibration curves for each peak analyzed, as ^{214}Pb, ^{214}Bi used to determined ^{226}Ra and ^{228}Ac used to determined ^{226}Ra activities in the samples.

3 Benthic fluxes of trace elements in the Chukchi Sea and their transport into the Arctic Ocean

Lúcia H. Vieira[1], Eric P. Achterberg[1], Jan Scholten[2], Aaron J. Beck[1], Volker Liebetrau[1], Matthew M. Mills[3] and Kevin R. Arrigo[3]

Published in *Marine Chemistry*

https://doi.org/10.1016/j.marchem.2018.11.001

1 Marine Biogeochemistry Division, GEOMAR Helmholtz Centre for Ocean Research Kiel, Kiel 24148, Germany

2 Institute of Geosciences, Christian-Albrecht University Kiel, Kiel 24118, Germany

3 Department of Earth System Science, Stanford University, 473 Via Ortega, Stanford, CA, 94035

Abstract

The Chukchi Sea is a primary site for shelf-ocean exchange in the Arctic region and modifies Pacific-sourced water masses as they transit via the Bering Strait into the Arctic Ocean. The aim of this study was to use radium and trace element distributions to improve our understanding of biogeochemical cycles in the Bering and Chukchi Seas, and evaluate their potential response to future changes in the Arctic. We investigated the distributions of dissolved and total dissolvable trace elements (Cd, Fe, Ni, Cu, Zn, Mn, Co, and Pb) in the Bering and Chukchi Seas during spring. In addition, the long-lived radium isotopes (^{226}Ra and ^{228}Ra) were measured as tracers of benthic trace element inputs. Trace element concentrations, especially Fe and Mn, were highly elevated in Chukchi shelf waters compared with the open Arctic Ocean and Bering Strait. Trace element, nutrient, and Ra patterns suggested that Fe, Mn, and Co concentrations were predominantly controlled by reductive benthic inputs, whereas the other trace elements were influenced by biological uptake and release processes. We propose that Fe, Mn, and Co in the Chukchi Sea are supplied from shelf sediments during winter overturning, and we combine the ^{228}Ra fluxes with the distributions of Fe, Mn, and Co to provide a first estimate of their benthic fluxes in the region. The average benthic flux of ^{228}Ra was 1.49 x 10^{8} atoms m^{-2} d^{-1}, which is among the highest rates reported globally. Estimated dissolved Fe (dFe) flux from the sediments was 2.5 µmol m^{-2} d^{-1}, whereas dMn and dCo fluxes were 8.0 µmol m^{-2} d^{-1} and 0.2 µmol m^{-2} d^{-1}, respectively. The off-shelf transport of dFe to the Arctic Ocean is estimated to be about 10-25% of the benthic Fe flux, with the remainder retained on the shelf due to scavenging and/or phytoplankton uptake. Our results highlight the importance of the Chukchi Sea as a major source of the micro-nutrients to the Arctic Ocean, thereby supporting primary production.

Long-term changes in factors that affect cross-shelf mixing, such as the observed reduction in ice cover, may therefore enhance shelf nutrient inputs and primary productivity in the Arctic.

3.1 Introduction

Pacific water inflow forms an important source of freshwater, heat, and nutrients to the Arctic Ocean (Aagaard and Carmack, 1989; Woodgate and Aagaard, 2005; Shimada et al., 2006). Pacific water helps ventilate the Arctic halocline, determine nutrient budgets, and maintain the stratification of the Arctic Ocean (Woodgate et al., 2005). As Pacific-sourced waters pass through the Bering Strait and enter the Arctic Ocean, they are modified by biogeochemical processes in the Chukchi Sea (Brown et al., 2015; Mills et al., 2015). Remineralized nutrients and resuspended sediment particles from the Bering and Chukchi shelves are entrained in dense bottom water as it flows northward (Cooper et al., 1997; Mathis et al., 2007), contributing to the development of an Arctic nutrient maximum (Jones and Anderson, 1986; Moore et al., 1983; Aagaard et al., 1981), which forms the main source of nutrients for primary productivity in the Arctic Ocean. Since the Bering and Chukchi Seas are along the only pathway of Pacific water to the Arctic, changes in the Bering and Chukchi Seas have profound impacts on the physical and chemical states of Arctic Ocean ecosystems.

Long term climate effects are driving changes in the Bering and Chukchi Seas, such as reduced ice cover (Serreze et al., 2007) and an increase in primary productivity (Arrigo et al., 2008; Arrigo and Van Dijken, 2015), changes in runoff (Peterson et al., 2002; Yang et al., 2002), permafrost thawing (e.g. Hinzman et al., 2005; Romanovsky et al., 2002), increases in groundwater inputs to streams (Walvoord and Striegl, 2007) and increased inflow of Pacific water through the Bering Strait to the Chukchi Sea and wider Arctic Ocean (Woodgate, 2018). These changes may alter chemical budgets and biogeochemical cycles in the Chukchi Sea, with subsequent consequences for Arctic ecosystems. Although changes to the climate

are becoming better understood, little is still known about their consequences for the biogeochemical cycles of trace elements in the oceans. The vertical flux of particulate carbon from surface waters to sediments increases substantially upon phytoplankton blooms in the Arctic, whilst the surface water is still cold and zooplankton growth rates are low (Michel et al., 2006). Increases in carbon export, in turn, stimulate denitrification rates in sediments due to reduced sediment redox potentials, resulting in decreased nitrate concentrations in the water column of the Chukchi Sea (Arrigo et al., 2008). Moreover, the sedimentary trace element release (e.g. iron (Fe)) into the overlying water column of a North Pacific shelf region was proportional to the input flux of particulate organic matter to the sediments (Elrod et al., 2004). Therefore, climate change effects may be altering Arctic biogeochemistry, and a thorough study of trace element and nutrient dynamics on the shelf is needed to access potential impacts throughout the region.

A number of studies have evaluated the distributions of dissolved trace elements, chiefly Fe, in the Arctic Ocean. The concentrations of Fe varied considerably between the Arctic basins, with the lowest concentrations observed in the central basin (e.g. Klunder et al., 2012a, 2012b; Thuróczy et al., 2011; Moore, 1983). The few studies in the western Arctic Ocean (Chukchi Sea and Canada Basin), argued that high trace element concentrations in surface waters were due to input from Chukchi shelf sediments, melting sea-ice, and river waters (Cid et al., 2012; Kondo et al., 2016; Aguilar-Islas et al., 2013). However, because these studies focused on regions beyond the slope boundary between Chukchi Sea and Canada Basin, they may not have captured biogeochemical processes occurring on the Chukchi shelf. A better knowledge of the processes controlling the distributions and cycling of trace

elements on the Chukchi Sea shelf, one of the most productive Arctic shelves, is therefore fundamental for our understanding of trace element export to the Arctic Ocean.

Organic matter-rich, reducing sediments of the Chukchi Sea shelf (Mathis et al., 2014; Grebmeier et al., 2006) appear to be a major source of trace elements to the water column, mainly Fe, manganese (Mn), cobalt (Co), and aluminum (Al) (Cid et al., 2012). The importance of sedimentary trace elements to primary production relies on their transfer to surface waters, as well as the extent to which they are transported offshore into the halocline layer of the Arctic Ocean. Reducing conditions in the sediments and frequent sediment resuspension events, such as those found in the Chukchi Sea, may influence the magnitude of benthic trace element fluxes. Subsequent delivery of these elements to the Arctic Ocean is controlled by physical transport processes such as advection, wind-driven upwelling, and slow ventilation, and the extent to which each element is retained on the shelf is determined by biological uptake and/or scavenging. Similar to trace elements, Ra isotopes (e.g. ^{228}Ra, half-life = 5.75 yr, and ^{226}Ra, half-life = 1600 yr) have a strong benthic source because they are constantly produced by radioactive decay of particle adsorbed thorium isotopes in sediments (^{232}Th → ^{228}Ra, and ^{230}Th → ^{226}Ra). In contrast to thorium, Ra is soluble in seawater and is released, together with trace elements, from the sediments into the water column by processes such as diffusion, advection, and convective mixing. Radium-226 is regenerated very slowly in sediments due to its long half-life; in contrast, more ^{228}Ra is produced and released to the overlying waters, related to its shorter half-life. Thus, high ^{228}Ra/^{226}Ra activity ratios indicate recent shelf sediment inputs to the water column. The geochemical behavior and radioactive nature of these nuclides make them powerful tools to

investigate the inputs of trace elements to the oceans (e.g. Charette et al., 2007, 2016; Dulaiova et al., 2009; Sanial et al., 2018).

The present study was part of the "Study of Under Ice Blooms in the Chukchi Ecosystem" (SUBICE) program, whose objectives were to investigate the key determinants of under-ice phytoplankton blooms in the Chukchi Sea. Our study aimed to investigate the processes that control trace element and Ra distributions in the Bering and Chukchi Seas, and quantify shelf trace element fluxes and transport to the Arctic Ocean, in order to better understand potential effects of future changes in the Arctic Ocean. First, we describe the distributions of the dissolved and total dissolvable trace elements (cadmium (Cd), Fe, nickel (Ni), copper (Cu), zinc (Zn), Mn, Co, and lead (Pb)), and the radium isotopes ^{226}Ra and ^{228}Ra. Then, we estimate sedimentary fluxes of ^{228}Ra, and, combine these fluxes with the distributions of the redox-sensitive elements Fe, Mn, and Co to estimate their benthic fluxes. To our knowledge, this is the first study to present data of both trace elements and Ra isotopes in the Chukchi Sea during the spring season and to determine their benthic fluxes in the Chukchi Sea.

3.2 Methods

3.2.1 Hydrography of the study region

The shelf of the Bering Sea is highly productive (Walsh et al., 1989) and commonly divided into 3 main domains based on seafloor depth: inner (~50 m), middle (50 – 100 m), and outer shelf (100 – 180 m) (Fig. 3.1). During the spring-summer period, the water column structure on the inner shelf is well mixed or weakly stratified, while the middle shelf is two layered; on the outer shelf, the upper and lower-mixed layers are separated by a subtle density interface

(Stabeno et al., 1998 and references therein). The surface waters on the continental shelf of the Bering Sea have high Fe and low nitrate concentrations, with sediments forming an important source of micronutrients to the productive area along the continental slope known as the "Green Belt" (Springer et al., 1996; e.g. Aguilar-Islas et al., 2007, 2008, 2013; Hurst et al., 2010; Tanaka et al., 2015; Cid et al., 2011). Phytoplankton in surface waters of the deep basin of the Bering Sea are Fe-limited under high-nitrate low-chlorophyll (HNLC) conditions (Aguilar-Islas et al., 2007).

On their way to the Arctic Ocean, Pacific waters flow through the Bering Strait and the Chukchi Sea. In general, the current flow is from south to north across the study region and this transport occurs along three main pathways (Coachman et al., 1975; Weingartner et al., 2005; Corlett and Pickart, 2017). On the eastern side of the inflow is Alaskan Coastal Water (ACW), which is warm, fresh and nutrient-depleted water that flows to the northeast from the Bering Strait into Barrow Canyon, predominantly in summer. On the western side of the inflow is Anadyr Water (AW), cold, salty and nutrient-rich water from the Gulf of Anadyr. The middle branch that passes through the Central Channel contains Bering Sea Shelf Water that is intermediate between ACW and AW in temperature and salinity characteristics. In summer, the Bering Shelf Water and AW combine north of the Bering Strait on the southern portion of the Chukchi shelf to form Bering Summer Water (BSW). Additionally, other water masses are found on the Chukchi shelf such as the cold winter water (near freezing point) known as Newly Ventilated Winter Water (NVWW), and the warmer Remnant Winter Water (RWW) which is the NVWW modified by heating via solar radiation or lateral mixing with summer waters on the shelf. A comprehensive description of the hydrography in our study

area during the SUBICE field campaign is given in Lowry et al. (2018) and further details are provided in Arrigo et al. (2017).

Salt rejection during ice formation creates dense brine-enhanced waters that sink to the seafloor in the Chukchi Sea before flowing off the continental shelf into the Arctic Ocean. This surface water is replaced by nutrient-enriched bottom water through convection, thereby mixing the water column. Remineralization in organic-rich Chukchi Sea sediments leads to high benthic nutrient fluxes (Mathis et al., 2014), and convective mixing leads to the formation of a relatively uniform and nutrient-rich water mass throughout the Chukchi Sea (Arrigo et al., 2017), known as the NVWW described above. The water column mixing that occurs throughout the winter (Woodgate and Aagaard, 2005) makes the Chukchi Sea one of the most productive Arctic shelves when the sea ice retreats in late spring and early summer (Hill and Cota, 2005).

3.2.2 Sample collection and analysis

Seawater samples for trace element (TE) and Ra isotope analyses were collected during the SUBICE field campaign, from 13 May to 24 June 2014, onboard the research vessel U.S.C.G.C. *Healy*. For TE profiles, 44 hydrographic stations were sampled in the Chukchi Sea and 7 surface water samples in the Bering Sea (Fig. 3.1; see supplementary material Table S 3.1); in addition, a total of 69 surface water samples for Ra isotopes were collected (Fig. 3.2). The sampling and analytical methods are described below.

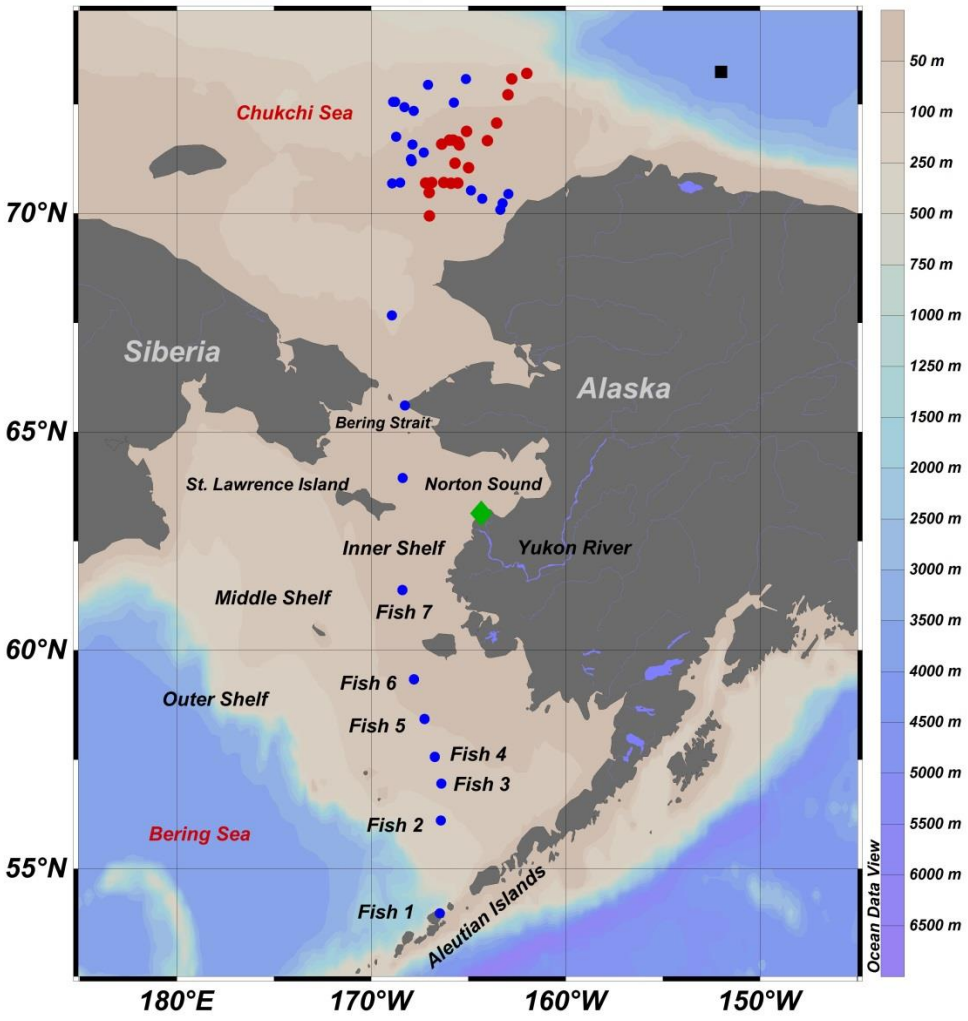

Figure 3.1: Stations in the Bering and Chukchi Seas sampled for trace elements. The stations sampled in the main flow path discussed in Figure 3.3 are indicated by red circles. The black square indicates the location of the station S3 in Nakayama et al. (2011) used to estimate the off-shelf dFe flux into the Canada Basin. Fish 1-7 represent the stations sampled using a trace element clean towed fish. Water depth (m) is indicated by color coding.

3.2.2.1 Trace elements

In the open waters of the Bering Sea, we conducted surface water sampling up to the sea ice edge using a trace element clean towed fish. In the ice-covered area, mostly in the Chukchi Sea, the samples were obtained using acid-cleaned PVC hose that was manually deployed at

the starboard side of the vessel, lowered to specific depths (12-15 m, 20-25 m, 35 m, and 40-50 m, preferentially). Seawater was transferred using a Teflon diaphragm pump (ALMATEC A15) into a shipboard clean laboratory container. Trace element samples were collected in low-density polyethylene (LDPE) 125 mL bottles that had been rigorously acid-cleaned as described in Achterberg et al. (2001). Dissolved trace element (dTE) samples were filtered through an acid washed inline filter cartridge (0.2 µm pore size filter, Sartobran-Sartorious P-300), whereas total dissolvable TE (TdTE) samples were collected without filtration. Immediately after sample collection, the samples were acidified to pH 1.9 (0.01 M) using concentrated HCl (OPTIMA, Fisher Scientific). All sample preparation was conducted in a HEPA-filtered Class 100 laminar flow clean area inside a clean laboratory container. The samples were stored double-bagged for >12 months. The TdTE concentrations measured in acidified unfiltered samples include both the dissolved fraction and a leachable fraction of the particulate pool.

The concentrations of dissolved and total dissolvable TEs (i.e. Cd, Fe, Ni, Cu, Zn) were determined by isotope dilution, whereas the method of standard addition was used for Mn, Co, and Pb. Elements were preconcentrated using an automated system (SeaFAST, ESI) with subsequent analysis using a high resolution inductively coupled plasma-mass spectrometer (HR-ICP-MS; Thermo Fisher Element XR) (Rapp et al., 2017). For the preconcentration step, we used 10 mL of sample for dTE analysis and 4 mL for TdTE analysis. Briefly, the samples were spiked with an isotopically-enriched multi-element solution containing ^{111}Cd, ^{57}Fe, ^{62}Ni, ^{65}Cu, and ^{68}Zn. The concentrations of Cd, Fe, Ni, Cu, and Zn were calculated following the standard isotope dilution equation described in de Jong et al. (2008). Similarly, a standard addition working solution containing Co, Mn, and Pb was prepared by dilutions of

individual stock standards (CertiPur, Merck), and calibrations were performed by standard additions to every 10th sample. Their concentrations were calculated based on linear regressions of the sequentially-spiked sample, i.e. the mean slope, from one standard addition run before and one after the sample, was used to calculate the concentrations of Co, Mn, and Pb. The accuracy and precision of the method were evaluated by analyzing SAFe (D1) reference seawater (Bruland, 2009) (see supplementary material Table S 3.2).

3.2.2.2 Radium isotopes

The long-lived Ra isotopes (^{228}Ra and ^{226}Ra) were extracted from 200 L of surface seawater collected from 7 m depth either from the ship's seawater intake or from Niskin bottles attached to the CTD rosette frame. We ensure that the seawater collected from the ship's intake was not contaminated by thorium isotopes and the pipes did not contribute additional Ra to the sampled seawater (Charette et al., 2007), as we compared samples collected from the intake line with water collected from the CTD at selected stations (n = 4, see supplementary material Table S 3.3). After collection, seawater was slowly pumped from the drums over a single column filled with MnO_2-coated acrylic fiber (Mn-fiber) at a flow rate of <1 L min^{-1}. The Mn-fiber was then rinsed with Ra-free tap water, dried, and stored for land-based isotope analysis.

In the laboratory, ^{226}Ra and ^{228}Ra were removed from the Mn-fiber via a chemical leach followed by co-precipitation with $BaSO_4$. Briefly, the fiber was boiled in 6 M HCl, until bleached white but otherwise intact, then rinsed with 1 M HCl, and vacuum-filtered through a glass fiber filter (Whatman GF/F 47 mm). Radium present in the filtrate was co-precipitated with $BaSO_4$ and stored in a 1 mL vial sealed with Parafilm (Moore et al., 1985). Since Ra is

tightly bound in the crystal lattice of $BaSO_4$, Parafilm is only used to avoid loss of sample material (Michel et al., 1981). Precipitates were stored at least 3 weeks before analysis to allow ^{222}Rn to grow into equilibrium with ^{226}Ra. Radium activities were then measured by gamma spectrometry using a high-purity, well-type germanium detector (HPGe). The ^{226}Ra activities were determined using the ^{214}Pb peak (352 keV) and ^{214}Bi peak (609 keV), and ^{228}Ra activities were determined using the ^{228}Ac peak (911 keV). To confirm that the leaching procedure quantitatively removed Ra from the fibers, six leached bulk fiber remains were ashed at 600°C for 48 h and analyzed by gamma spectrometry. Ra activities close to the background and blank values in the leached fiber ash confirm ~ 95 % (1-σ) extraction efficiency of Ra using this leaching procedure (Table S 3.4). Blank fibers (the same amount of fiber as used for the sample collection) were leached and analyzed as described for the samples. Sample activities were corrected for detector backgrounds and fiber blank activities. The detector efficiency was determined by measuring Mn-fibers spiked with known amounts of ^{228}Ra and ^{226}Ra. The Ra spike solution was provided by the International Atomic Energy Agency (IAEA) and had a reported activity accuracy of 6% for ^{226}Ra and 5% for ^{228}Ra.

3.3 Results and Discussion

3.3.1 Distribution of trace elements and radium isotopes in the Bering Sea

During the study period, the Bering Sea was ice-free up to the vicinity of St. Lawrence Island (north of station Fish 7; Fig. 3.1). Further north, the study domain was ice-covered (see Fig. S 3.1). Surface water temperature and salinity decreased from Fish 1 (T = 6.73°C and S = 31.2) to Fish 7 (T = 1.22°C and S = 30.3). In the Bering Strait surface temperature was ~ -0.47°C

and salinity 31.4. Details on water column stratification and other hydrographic data are not available for those stations.

In the Bering Sea, Fe, Mn, Zn, and Pb existed mainly in the leachable particulate phase (LP-) (calculated here as the difference between TdTE and dTE concentrations), while Cd, Ni, Cu, and Co were largely found in the dissolved phase. Trace element concentrations and Ra activities were low close to the Aleutian Islands (e.g. dMn = 4.69 nM and TdMn = 7.69 nM). The dFe concentrations at the outer shelf stations, Fish 1 (0.77 nM) and Fish 2 (1.8 nM), were somewhat higher in comparison to 0.1 – 0.9 nM reported by Aguilar Islas et al. (2007), Aguilar Islas et al. (2008) and Hurst et al. (2010) during the summer. However, the current study was conducted in mid-spring, when the phytoplankton communities had likely not yet depleted micronutrients.

Concentrations of trace elements and Ra isotopes increased northwards to the Bering Strait (e.g. dMn = 15.2 nM and TdMn = 31.4 nM). This is likely due to the shallower water depths, with benthic derived trace elements and Ra reaching surface waters through turbulent mixing, and the influence of frontal processes at the shelf-breaks between outer/middle and middle/inner shelves causing vertical mixing of TE-and Ra-enriched deeper waters.

Enhanced dZn (1.99 nM), dCd (0.53 nM), dNi (8.55 nM), and dCu (8.21 nM) concentrations were observed in surface waters of the northern middle shelf/inner shelf boundary region (Fish 5; Fig. 3.1), relative to the southern stations Fish 1-4. The lowest Ra activities in the Bering Sea were found on the middle shelf (4.75 dpm 100 L^{-1} for ^{226}Ra and 1.64 dpm 100 L^{-1} for ^{228}Ra; Fish Ra 1). On the northern inner shelf between Fish 6 and the station in the Bering Strait, trace element concentrations were relatively high and variable (dFe: 2.66 – 6.87 nM;

dNi: 3.65 – 6.71 nM; dCu: 3.24 – 7. 17 nM; dMn: 4.67 – 15.2; dCd: 0.22 – 0.30 nM; dPb: 0.002 – 0.009 nM; dCo: 0.34 – 0.45 nM).

The highest concentrations of trace elements were observed in inner shelf ice-free waters (Fig. 3.1 and Table S 3.1; Fish 7) with dFe and TdFe concentrations of 6.87 nM and 707 nM, respectively. The station 70 km from St. Lawrence Island (Fish Ra 3; Fig. 3.2) was located near Norton Sound (Fig. 3.1) and 200 km off the Yukon River delta, where the highest ^{228}Ra activity (11.8 dpm 100 L^{-1}) was observed. The Yukon River plume is unlikely to be the source of trace elements and Ra at those stations at the time of our sampling, as our sample collections in the Bering Sea occurred in May, prior to peak discharge (Yang et al., 2014)

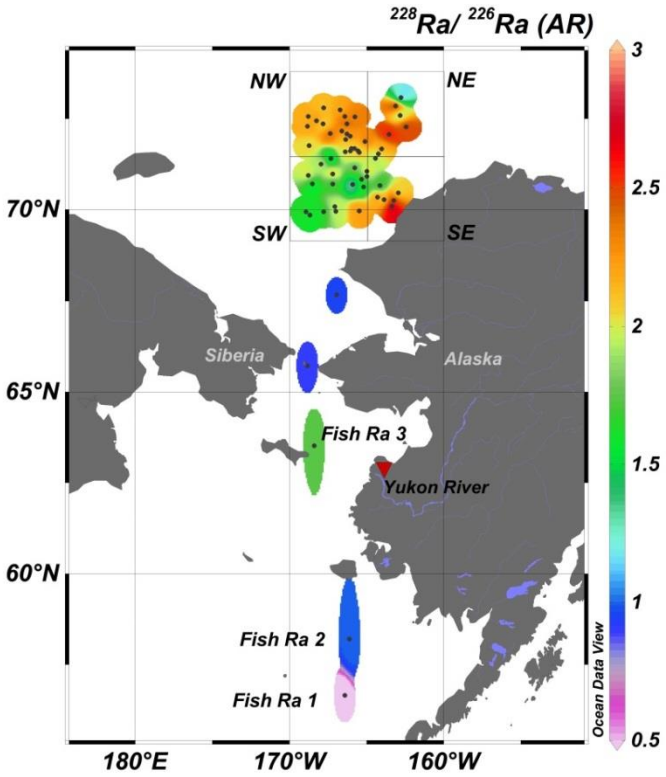

Figure 3.2: Distribution of ^{228}Ra/^{226}Ra activity ratio (AR) in surface waters of the Bering and Chukchi Seas and Bering Strait. Fish Ra 1-3 represent the stations sampled for Ra using a trace element clean towed fish.

3.3.2 Distribution of trace elements and radium isotopes in the Chukchi Sea

The weakly stratified water column of the Chukchi Sea was almost exclusively composed of near freezing NVWW (excluding the stations beyond the shelf-break and those north of the Bering Strait), with a mean temperature of -1.65°C and salinity of 32.2. In the incoming waters, north of the Bering Strait, the Bering Summer Water (BSW) was prevalent. Beyond the shelf-break, the water column was composed mostly of RWW, which was highly stratified due to a shelf-break front separating the NVWW on the shelf from the warmer and fresher water over the slope (Lowry et al., 2018) (see isopycnals in Fig. 3.3). Sample collection (May-June 2014) in the Chukchi Sea occurred prior to the major phytoplankton bloom and melt pond formation, within extensive sea ice coverage where leads of open water in the sea ice were prevalent (Lowry et al., 2018).

Dissolved Fe ranged from 1.45 to 46.3 nM (average: 4.71 nM), and dMn varied from 2.94 to 59.6 nM (average: 15.5 nM). For TdFe and TdMn, the concentrations ranged from 6.05 nM to 4.71 μM (average: 552 nM) and 7.23 to 123 nM (average: 38.2 nM), respectively (Table 3.1). These elements existed mainly in a leachable particulate form, which represented >98% of TdFe and ~60% of TdMn (Table 3.1). TdPb was also predominantly in the leachable particulate form, which accounted for ~80% of TdPb. In contrast, Cd, Ni, Co, and Cu existed mainly in the dissolved form, and 50% of TdZn was found as leachable particulates.

Table 3.1: Minimum and maximum concentrations of dissolved and total dissolvable trace elements (standard deviations 1 σ), with average percentage of the leachable particulate phase (L.P.) observed in the Bering Strait and Chukchi Seas. All samples and depths are included.

Bering Sea				**Chukchi Sea**			
Trace element	**Dissolved (nM)**	**T. Dissolvable (nM)**	**LP (%)**	**Trace element**	**Dissolved (nM)**	**T. Dissolvable (nM)**	**LP (%)**
Cd	0.22 ± 0.03 0.53 ± 0.04	0.25 ± 0.03 0.56 ± 0.01	13	Cd	0.11 ± 0.03 0.79 ± 0.06	0.18 ± 0.01 0.80 ± 0.01	9
Co	0.25 ± 0.02 0.50 ± 0.05	0.27 ± 0.02 0.76 ± 0.06	18	Co	0.27 ± 0.02 0.73 ± 0.07	0.32 ± 0.04 1.98 ± 0.15	28
Cu	2.70 ± 0.29 8.21 ± 0.17	2.75 ± 0.05 8.91 ± 0.96	4	Cu	0.22 ± 0.03 8.79 ± 0.18	1.91 ± 0.04 9.77 ± 1.13	26
Fe	0.77 ± 0.01 6.87 ± 0.40	20.7 ± 1.13 707 ± 42.1	97	Fe	1.45 ± 0.03 46.8 ± 0.66	6.38 ± 0.34 4715 ± 231	98
Mn	4.02 ± 0.42 15.2 ± 1.57	7.69± 0.65 42.7 ± 3.59	62	Mn	2.94 ± 0.32 59.6 ± 1.71	7.23± 0.60 123 ± 9.70	59
Ni	3.65 ± 0.12 8.55 ± 0.26	4.58 ± 0.10 8.73 ± 0.48	5	Ni	3.75 ± 0.36 8.31 ± 0.19	4.35 ± 0.27 9.24 ± 0.66	14
Pb (pM)	1.86 ± 0.18 13.1 ± 0.78	14.0 ± 0.93 109 ± 7.32	80	Pb (pM)	2.51 ± 0.24 83.1 ± 5.93	12.6 ± 0.94 516 ± 32.1	83
Zn	0.29 ± 0.02 1.99 ± 0.08	0.97 ± 0.08 5.87 ± 0.40	64	Zn	0.75 ± 0.06 7.19 ± 0.33	2.51 ± 0.20 33.7 ± 2.97	49

The Pacific water entering the Chukchi Sea as the BSW and the RWW beyond the shelf-break were depleted in trace elements (and Ra), while over most of the Chukchi shelf their concentrations were elevated at all depths. Dissolved Fe, dCd, dCo, dNi, dCu, and dMn were ~1.5 – 2 fold higher on the Chukchi shelf, while dPb and dZn were ~4 times higher than in the Bering Sea. Sections of dissolved TE concentrations are shown in Fig. 3.3 for stations in the Central Chukchi Sea to the shelf-break parallel to the dominant currents (stations in red in Fig. 3.1). A depletion of all TE at stations beyond the shelf-break (except dPb, which shows some elevated concentrations off-shelf) is shown in Fig. 3.3. Elevated levels of trace

elements were found in near-bottom waters, (5-7 m above the seafloor) suggesting a sediment source.

Sediment and pore water resuspension is likely to occur in the shallow Chukchi Sea due to convective mixing caused by winter overturning. Thus, pore water release and desorption from resuspended sediment particles are likely sources of trace elements to bottom waters. Furthermore, refreezing leads were found throughout the study area and, as a result of brine rejection, the water column can become fully mixed in less than 9 hours (in some cases in less than 1 hour) (Pacini et al., 2016; Lowry et al., 2018), stirring trace elements, Ra and nutrients from the bottom waters into the surface layers. The enhanced ^{228}Ra activities, and consequently high ^{228}Ra/^{226}Ra ARs ($1.1 < AR < 2.8$; Fig. 3.2) indicate benthic inputs to the water column. Furthermore, remineralization of organic matter in sediment consumes oxygen first, followed by nitrate and then Fe and Mn reduction (Lohan and Bruland, 2008). Reduced Fe (II) and Mn (II) produced in sediments are mobile and diffuse into to the oxygenated bottom water, where they are oxidized to their less soluble forms, Fe (III) and Mn (IV). Oxidized colloidal Fe and Mn, and particulate Fe oxyhydroxide and Mn-oxides, can be removed from the water column by particulate scavenging and sinking (Lohan and Bruland, 2008). Oxidizing bacteria play an important role in Mn oxidation (Sunda and Huntsman, 1988). The oxidation processes are consistent with the low dTE/TdTE ratios measured in the current study for Fe (0.00067 – 0.22) and Mn (0.14 – 0.81), indicating that these elements were mainly in leachable particulate phases. Cobalt, in turn, is readily scavenged by Fe or Mn-oxide phases and is released into solution when the oxides undergo reductive dissolution (Moffet and Ho, 1996).

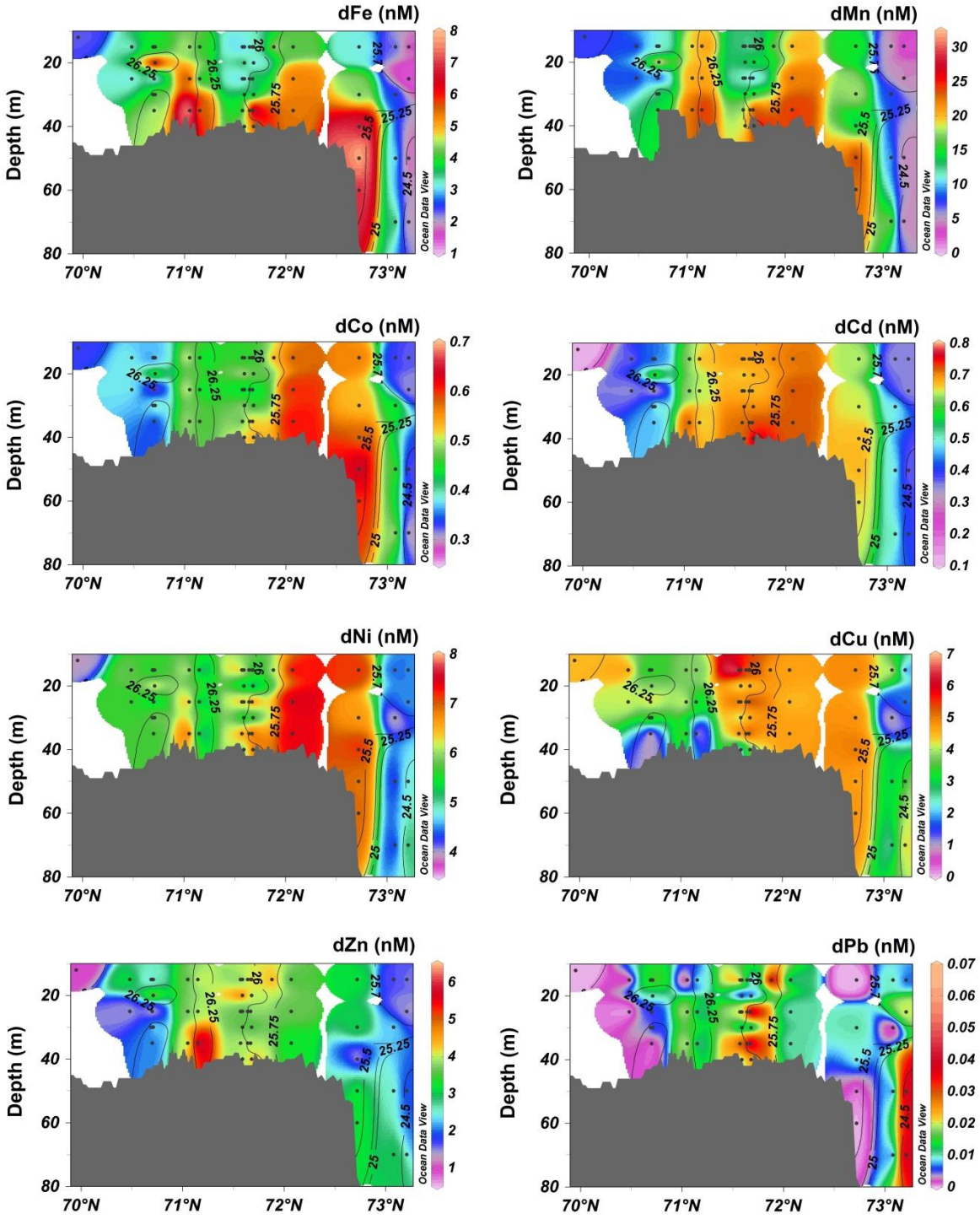

Figure 3.3: Sections of dissolved trace elements (in nM) along main flow path of Pacific-origin waters. Iso-contours represent potential density (kg m^{-3}). Stations along this transect are marked in red in Figure 3.1.

In addition to the reductive supply of Fe (II) and Mn (II) from shelf sediments, resuspended sediments tend to have elevated Fe and Mn content. Strong negative correlations were observed between transmission and the TdFe ($r = 0.86$; $n = 34$) and TdMn ($r = 0.74$ $n = 34$) (data not shown), suggesting coinciding Fe and Mn inputs from particle resuspension. Trefry et al. (2014) observed Fe/Mn ratios in surface sediments of the Chukchi Shelf of 82.6 ± 33.5 (their Table 3); in near-bottom waters, we found a similar LP-Fe/LP-Mn ratio of 44 ± 9.6. The difference in ratios between sediment (dashed line in Fig. 3.4A) and suspended particles in bottom waters (black line in Fig. 3.4A) indicates an excess of LP-Mn relative to LP-Fe in near-bottom waters. This could be because Fe and Mn are released from pore water and resuspended sediment particles, likely in their dissolved form, but they are transferred to their leachable particulate forms and/or are removed from the water column at different rates. Because the Fe/Mn ratio is so much lower in the dissolved phase (0.19 ± 0.04) than in the leachable particulate phase (44 ± 9.6) (Fig. 3.4A and B), there is likely preferential precipitation of Fe. It is possible that more Fe (II) is being released from the sediment relative to Mn (II), but Fe oxidizes faster to Fe (III) in the well-oxygenated bottom waters (O_2 ~355 μmol kg^{-1}) and precipitates rapidly; while Mn, because of its slower oxidation rate, persists longer in the dissolved phase (Stumm and Morgan, 1981). Indeed, the slow oxidation kinetics of Mn greatly reduces the net formation of Mn oxides (Sunda and Huntsman, 1988). This is consistent with the lower dFe/dMn (0.07 ± 0.03) and LP-Fe/LP-Mn (12.2 ± 3.17) ratios found in surface waters relative to bottom waters (0.19 and 44, respectively). A recent study reported that, during periods of sediment resuspension, the dFe released from sediment pore water via diffusive processes rapidly adsorbs onto particles, and that inputs of suspended particles to overlying waters lead to rapid scavenging of dFe into its leachable particulate

phases (Homoky et al., 2012). This is consistent with the large amount of LP-Fe found in our study (Table 3.1) and the frequent sediment resuspension episodes observed during the SUBICE campaign.

The high concentrations of dissolved and leachable particulate Fe found in surface waters of the shallow shelf of the Bering Sea (see Table 3.1) are also related to the benthic supply processes. Hurst et al. (2010) showed that LP-Fe averaged 81% of the total particulate Fe in the bottom waters of the Bering Sea, and suggested that elevated flux of reduced Fe at the sediment-bottom water interface and its subsequent oxidation and precipitation could lead to the formation of elevated concentrations of LP-Fe.

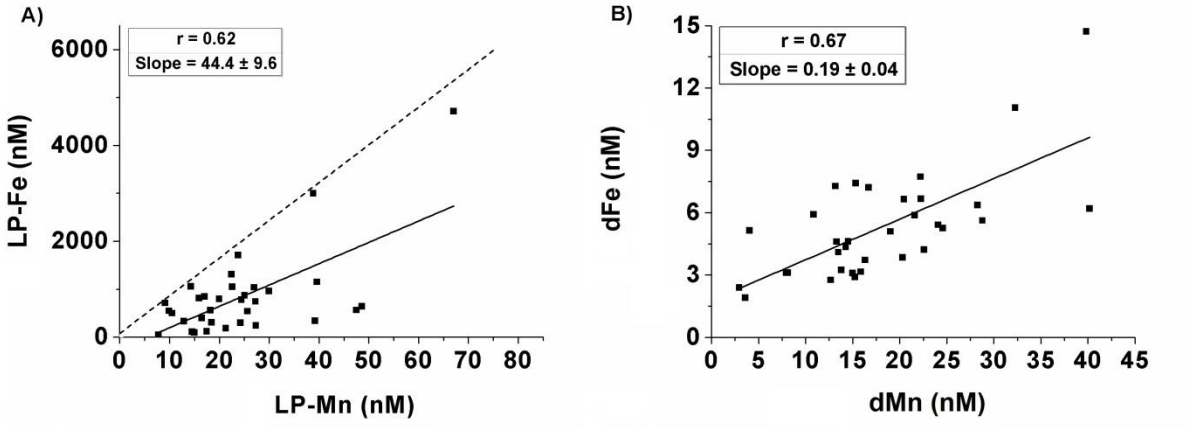

Figure 3.4: Plots of Mn versus Fe in deep waters of the Chukchi Sea in their leachable particulate (LP) form (A) and dissolved (d) form (B). The dashed line in (A) presents Fe/Mn ratio in the sediments of the Chukchi Shelf found in Trefry et al. (2014).

Interestingly, we observed a strong positive correlation between LP-Fe and LP-Pb in near-bottom waters (r = 0.97, n = 34) (Fig. S 3.2A) as well as between LP-Fe and LP-Co (r = 0.92; n = 34) (Fig. S 2B), while there was no close correlation between their dissolved forms (Fig. S 3.2C and D). In contrast, the relationships between LP-Mn and LP-Pb, as well as between

LP-Mn and LP-Co, were weaker ($r = 0.67$ $n = 34$ and $r = 0.81$ $n = 34$, respectively) (Fig. S 3.2E and F), suggesting that Pb and Co are preferentially scavenged by Fe-oxides, although Co is considered to be incorporated into Mn-oxides through the co-precipitation by manganese oxidizing bacteria (Moffet and Ho, 1996). The enhanced dPb and LP-Pb concentrations observed near the seafloor may indicate a sedimentary Pb source to the overlying waters (Noble et al., 2015). Although the biogeochemical processes that control benthic Pb release are poorly known, studies have suggested that anthropogenic Pb supplied to the water column may be scavenged onto Fe-Mn oxides to the sediments, and their subsequently reductive dissolution allows the diffusive benthic input of Pb into the water column (Noble et al., 2015; Rusiecka et al., 2018).

Copper existed mainly in dissolved form, unlike Fe, Mn, and Pb. Dissolved Cu may also have a benthic source under moderately reducing conditions (Heggie, 1982), but in highly reducing shelf sediments, such as found in the Chukchi Shelf, Cu may form inorganic sulfide compounds and precipitate, limiting its benthic source under very low O_2 conditions (Biller and Bruland, 2013). This could explain the distinct distribution of Cu relative to Fe, Mn, and Co in our study (see Fig. 3.3 and PCA results, below).

Principal Component Analysis (PCA) was performed to clarify relationships among the different constituents in the Chukchi Sea (Fig. 3.5). Only data from the surface waters of the Chukchi Sea were considered in the PCA to allow the inclusion of Ra isotopes, as they were collected only in surface waters. The PCA shows that the TEs, nutrients, and Ra fall clearly into two separate groupings. The TEs such as Cu, Pb, Zn, Ni, Cd in surface waters were associated with the major macronutrients (Fig. 3.5), suggesting that phytoplankton

uptake/surface adsorption and remineralization were the main factors controlling their distribution in this region. Fe, Mn, Co, Ra, and NH_4^+ grouped separately, suggesting that their distributions were strongly influenced by a common source, most likely sediments, as discussed above for Fe and Mn. See supplementary material (Table S 3.5) for details of the variance on the principal components. Previous studies also reported enhanced NH_4^+ in bottom waters of the Chukchi Sea shelf and slope regions (Wang et al., 2006; Connelly et al., 2014). The high primary production over the shallow shelf of the Chukchi Sea likely leads to a high flux of organic carbon to the seafloor (Grebmeier et al., 2006), and NH_4^+ produced by remineralization in sediments is released to the overlying waters (Brown et al., 2015).

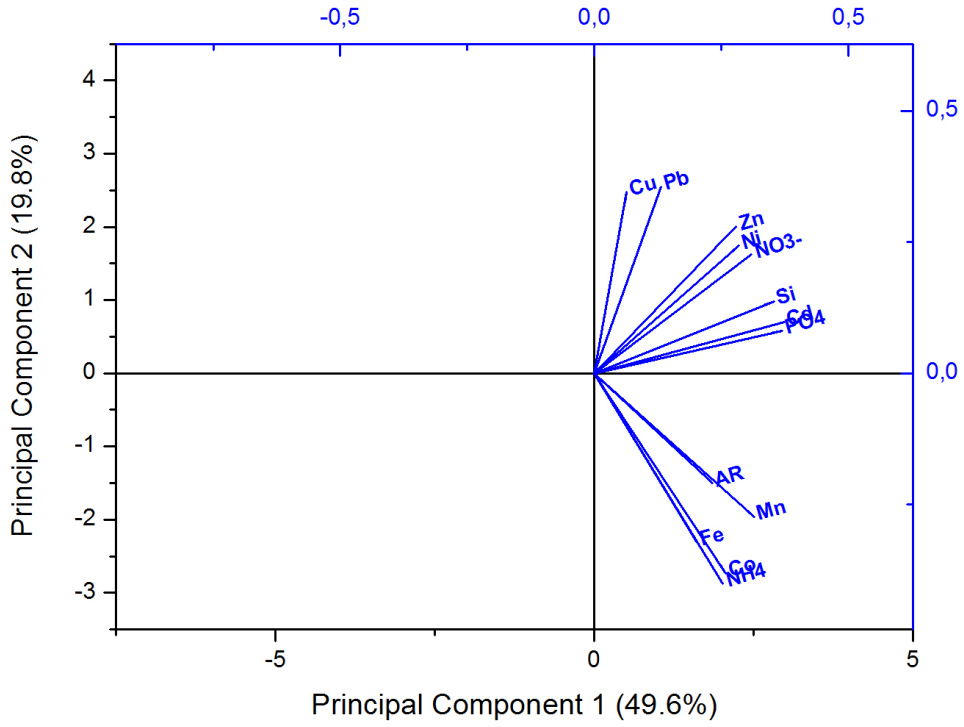

Figure 3.5: Principal component analysis (PCA) plot that characterizes the trends exhibited by dissolved trace elements, nutrients and $^{228}Ra/^{226}Ra$ ratios in surface waters of the Chukchi Sea. $^{228}Ra/^{226}Ra$ ratios are referred here as Activity Ratios (AR).

Dissolved Cd and phosphate showed a moderate correlation (r = 0.77; Fig. S 3.3A) with the following equation: [dCd nM] = 0.36 [PO_4 µM] - 0.038, n = 97. This agrees closely with previous work in the Chukchi and Beaufort Seas (Cid et al., 2012) and the North Pacific (Bruland, 1980). In those studies, dissolved Cd and phosphate were related according to: [dCd nmol kg^{-1}] = 0.33 [PO_4 µmol kg^{-1}] + 0.050, r = 0.62 (Cid et al., 2012); and [dCd nmol kg^{-1}] = 0.347 [PO_4 µmol kg^{-1}] - 0.068, r = 0.99 (Bruland, 1980). The observed Cd/phosphate relationship is consistent with replete levels of dFe that are not limiting primary production (Cullen, 2006). Dissolved Zn and silicate showed no correlation (Fig. S 3.3B). Dissolved TE involved in biological cycles (Cd, Cu, Ni, and Zn) typically follow the profiles of the major macronutrients in the open ocean, but showed a nearly uniform vertical distribution in the current study (Fig. 3.3), due to a vertically well-mixed water column. The dCo distribution appears visually similar to the latter elements, but the PCA results (Fig. 3.5) shows that its distribution matches better with dFe and dMn. The more uniform Co distribution may be because Co is transported farther from the sediments than reduced Fe and Mn before it is removed by particulate scavenging and precipitation (Heggie and Lewis, 1984; Moffet and Ho, 1996). The PCA suggests that, like dMn and dFe, dCo is released from the sediments, but it remains longer in the water column and can be easily transported to surface waters, which could explain its nearly uniform distribution.

The ^{226}Ra activities measured in in the Chukchi Sea varied from 4.68 ± 0.41 to 10.9 ± 0.94 dpm 100 L^{-1} (average: 7.83 ± 1.69 dpm 100 L^{-1}), while ^{228}Ra activity presented a broad range of 4.49 ± 0.22 to 24.4 ± 1.16 dpm 100 L^{-1} (average: 15.6 ± 4.39 dpm 100 L^{-1}). The distribution of the $^{228}Ra/^{226}Ra$ activity ratios (AR) (Fig. 3.2) shows high AR over most of the shelf, where stratification was weak or nonexistent due to convective mixing. Because of the

shallow bathymetry of the Chukchi Sea, convective mixing can also lead to sediment and pore water resuspension, with subsequent supply of ^{228}Ra. Furthermore, sediment type plays an important role in the amount of ^{228}Ra delivered to the water column, and variations in water column Ra activities may reflect differences in the underlying sediments (see section 3.3.4).

Based on the spatial distribution of ^{228}Ra/^{226}Ra, the Chukchi Sea shelf can be divided into four sections (Fig. 3.2). The northwest and southeast sections (NW and SE) presented high ^{228}Ra/^{226}Ra ratios ranging from 2.0 to 2.8 (average = 2.25; n = 27). The lowest ^{228}Ra/^{226}Ra ratios, ranging from 1.1 to 2.5 (average = 1.91; n = 26), were observed in the southwest section (SW), as well as beyond the shelf-break in the northeast sections (NE). The SW section in our study was mostly sampled at the end of the cruise when the NVWW water mass was being replaced by Pacific summer water containing low ^{228}Ra. The cross-shelf station in the NE section appeared to be composed mostly of the highly stratified RWW. The low ^{228}Ra value beyond the shelf-break is consistent with low activities previously observed in surface water at this site and further north (Kadko and Muench, 2005). The ^{228}Ra gradient observed in the NE section may indicate Ra removal (see section 3.3.5) or mixing between the ^{228}Ra enriched NVWW and RWW within the shelf-break front. Furthermore, the water that exits the Chukchi Shelf is denser relative to the near-surface water on the slope in the boundary between the Chukchi Sea and Canada Basin, and tends to sink below the surface slope water (Stabeno et al., 2018). Enhanced Ra activities were observed by Kadko and Muench (2005) at depth from 75 to 200 m compared to the surface waters on their cross-shelf transects. Moreover, due to the stratification of the water column, the absence of newly injected ^{228}Ra from bottom waters to the surface could also explain the lower activities in

surface waters in this region. In contrast, within the same NE section, stations located on the shelf exhibited high $^{228}Ra/^{226}Ra$, elevated trace element concentrations (Fig. 3.3) and a fully mixed water column, suggesting that convection likely increased ^{228}Ra activities and trace element concentrations in the surface waters of these stations. Furthermore, a strong shelf-break signal was observed at these stations (Fig. 3.3), where the difference in density at the edge of the shelf between the NVWW and RWW supports a bottom-intensified shelf-break jet (Mathis et al., 2007).

3.3.3 Other potential sources and sinks of trace elements and Ra isotopes in the Chukchi Sea

Melting ice has been identified as an important source of trace elements, especially Fe, to polar surface ocean waters (Lannuzel et al., 2007; Aguilar-Islas et al., 2008; Measures, 1999; Tovar-Sanchez et al., 2010). Sediment resuspension events are rather common in the Chukchi Sea, and sediment particles can be incorporated into the ice during frazil ice formation (Eicken et al., 2005). Release of sediment and brines from the melting ice may consequently contribute TE to surface waters in spring. Most of the study region was covered by 1.0 – 1.5 m of sea ice and 0.02 – 0.15 m of snow (Arrigo et al., 2017), with ice concentrations around 80 – 95% (Fig. S 3.1). The high ice cover suggests that melting sea ice was unlikely to be a major source of trace elements for most of the study region, although some dissolved TE release can begin during early ice melt (van der Merwe et al., 2011). In the coastal ice zone, however, melting ice might have contributed additional trace elements to surface waters, since enhanced sediment entrainment into the sea ice and advanced melting at the end of sampling period were observed in this region (Fig. S 3.1). The station nearest to shore

presented the highest concentrations of trace elements, especially dFe, dMn, and dNi. This region was occupied twice, once on 19-21 May and again on 8 June. During the first occupation, sea ice covered ~80% of the coastal area and trace elements in surface waters were lower than those observed during the second occupation. The mean dissolved Fe, Mn, and Ni concentrations on the first occupation were 4.38 nM, 12 nM, and 7.02 nM, respectively, while ^{228}Ra activity was 11.6 dpm 100 L^{-1}. On the second occupation, the sediment-laden ice had mostly melted, and ice concentration decreased to ~25% (Fig. S 3.1); the water column was stratified and dFe, dMn, and dNi concentrations and ^{228}Ra activity in the surface layer had increased to 46.3 nM, 59.6 nM, 8.31 nM, and 24.4 dpm 100 L^{-1}, respectively. After the ice melt, dMn was five times higher and dFe increased by an order of magnitude. Indeed, sea ice can accumulate Fe at concentrations one to two orders of magnitude higher than the under-ice seawaters, and release Fe to surface waters during its melting in a matter of weeks (Breitbarth et al., 2010 and reference therein). Activities of ^{228}Ra varied by 12.8 dpm 100 L^{-1} in this region. The ^{228}Ra content of melting ice of the Chukchi Sea is on the order of 0.55 dpm L^{-1} (Kipp et al., 2018). Given the observed salinity decrease from 32.7 to 29.9 at this station, an input of ^{228}Ra from the melting waters using the Kipp et al. (2018) numbers would have been only 4.72 dpm 100 L^{-1}, or about 20% for the most nearshore station, suggesting that melting ice was not a significant source of ^{228}Ra. However, the reported value of 0.55 dpm L^{-1} from Kipp et al. (2018) may be underestimated, as they estimated ^{228}Ra activity using sediment in melted sea ice collected late in the season, when sea ice had warmed and may have already lost chemical- and particle-rich brines. Nonetheless, Ra behavior during brine formation would likely mirror that of sea salts and would be enriched in brines proportional to seawater salinity (Loose et al., 2017). Thus, it

seems unlikely that such processes could enhance the ice source sufficiently to explain the increase in dissolved Ra, and a substantial portion of the Ra and trace element increase is therefore due to benthic input.

Atmospheric deposition and river runoff can represent important sources of trace elements to the ocean. However, extensive ice-cover during the current study would have prevented appreciable aerosol deposition reaching the surface waters. The major contribution of riverine water in the Chukchi Sea comes from the Yukon River on the northern Bering Sea shelf (Fig. 3.1). Its freshwater and terrestrial materials are transported by the Alaskan Coastal Current northward into the Chukchi Sea (Iken et al., 2010; Baskaran and Naidu, 1995; Stabeno et al., 2016). However, no clear low salinity signal from the Yukon was observed and the lower concentrations of trace elements found in the southern portion of our study domain (Fig. S 3.4) suggest a limited contribution of the Yukon River in the Chukchi Sea at the time of our sampling. This may be because the peak discharge occurs from early to late June (spring flood period) (Yang et al., 2014), i.e. one month after our sampling in the Bering Strait. Moreover, because of the lower Ra activities found in the Bering Sea (in the vicinity of the Yukon River mouth), the Bering Strait, and southern portion of the Chukchi Sea (Fig. 3.2), it is also unlikely that the Yukon River contributed to the elevated Ra signals observed on the Chukchi shelf.

3.3.4 Trace element fluxes derived from ^{228}Ra

Benthic inputs on the Chukchi shelf supplied dissolved ^{228}Ra to the inflowing waters from the Bering Sea, increasing activities by approximately a factor of two to three. In order to determine the magnitude of the fluxes that are required to sustain the observed enrichment,

excess ^{228}Ra activities were obtained at each station on the Chukchi shelf by subtraction of the average activities found in the Bering Strait and in the southern portion of our study domain (7.35 dpm 100 L^{-1}) from the observed activities. The inventory of excess ^{228}Ra (*I*, atom m^{-2}) was determined using the water depth (m) at each station. A uniform distribution of ^{228}Ra in the water column was assumed given the observed extensive vertical mixing and lack of stratification (Lowry et al., 2018), and these inventories therefore represent lower limit estimates. The stratified station localized beyond the shelf-break, as discussed in section 3.3.2, was excluded from our calculations. The excess ^{228}Ra inventory (*I*) ranged from 0.40 ± 0.09 x 10^{10} to 3.87 ± 0.18 x 10^{10} atoms m^{-2} (average = 1.81 ± 0.82 x 10^{10} atoms m^{-2}). However, the inventory determined here based on surface ^{228}Ra activities does not consider seasonal variations in the Ra supply to surface waters. Nonetheless, as the water column was actively overturning during our survey and experienced convective mixing throughout the winter, we assume that the inventory of ^{228}Ra was relatively constant over the months prior to our sampling.

Assuming sediments are the primary source of Ra to the water column, a steady state flux of Ra from sediments (J_{seds}) was balanced by loss due to exchange with low Ra waters off-shelf ($J_{exchange}$) and radioactive decay (J_{decay}) (e.g., Moore et al., 1995). The residence time (τ) of Pacific water in our study domain is ~4 months (Arrigo et al., 2017; Woodgate, 2018), giving a water exchange rate (K) of 0.008 d^{-1}. Hence, the flux of ^{228}Ra is therefore given by:

$$J_{seds} = J_{decay} + J_{exchange} = \lambda I + KI \qquad \text{(Equation 3.1)}$$

where λ is the decay constant of ^{228}Ra. However, because the half-life of ^{228}Ra is long relative to the residence time of water in the Chukchi Sea, no significant decay occurs and the

term J_{decay} can be neglected. The ^{228}Ra flux is then the inventory multiplied by the water exchange rate (K).

$$J_{seds} = J_{exchange} = KI \qquad \text{(Equation 3.2)}$$

The sediment ^{228}Ra flux estimated from equation 2 using the average inventory is 1.49 ± 0.71 x 10^8 atoms m^{-2} d^{-1}. The mean flux estimated here ranks among the highest reported globally and is similar to that reported for shelf systems such as the Amazon (3.01 x 10^8 atoms m^{-2} d^{-1}; Moore et al., 1995); Bega River, Australia (2.27 x 10^8 atoms m^{-2} d^{-1}; Hancock et al., 2000); Long Island Sound, USA (1.56 x 10^8 atoms m^{-2} d^{-1}; Cochran, 1984); and Narragansett Bay (1.42 x 10^8 atoms m^{-2} d^{-1}; Santschi et al., 1979) (Fig. 3.6). Moore et al. (2008) compiled estimates of sedimentary ^{228}Ra flux and showed that ^{228}Ra fluxes from fine-grained sediments are 1 – 2 orders of magnitude higher than those found in coarse-grained sediments. They suggested a global average flux of 50 ± 25 × 10^9 atoms m^{-2} yr^{-1} (1.37 x 10^8 atoms m^{-2} d^{-1}) for fine-grained sediments and 1.0 ± 0.5 × 10^9 atoms m^{-2} yr^{-1} (0.03 x 10^8 atoms m^{-2} $d^{-1)}$ for coarse shelf sediments. These literature values were used to calculate benthic fluxes at each station in the current study using the sediment type maps in Trefry et al. (2014) (see supplementary materials Fig. S 3.5). Calculated fluxes ranging from 0.4 - 1.3 × 10^8 atoms m^{-2} d^{-1} show that a completely independent estimate of benthic fluxes matches well with the average ^{228}Ra flux derived from the water column Ra inventory (1.49 ± 0.71 x 10^8 atoms m^{-2} d^{-1}), reinforcing the argument that benthic input is the primary source of ^{228}Ra to the system.

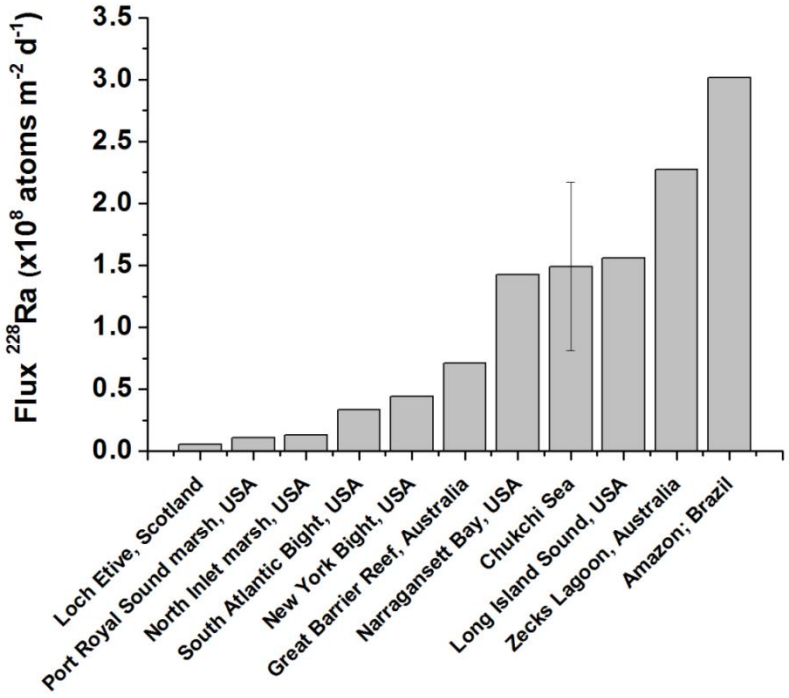

Figure 3.6: Shelf sediment ^{228}Ra fluxes. Values reported by: Li et al. (1979); Moore et al. (1987); Moore et al. (1995); Cochran (1984); Santschi et al. (1979); Rama and Moore (1996); Crotwell and Moore (2003); Hancock et al. (2000); Hancock et al. (2006); Hsieh et al. (2013). Most of the data are summarized in Moore et al. (2008).

Several factors can control sedimentary ^{228}Ra fluxes in the marine environment, such as diffusive pore water transport, bioturbation, sediment grain size and mineralogy (particularly non-carbonate sediments contain an enhanced abundance of ^{232}Th (Moore et al., 2008)). Although the sediment texture is quite variable in the Chukchi Sea shelf, silt and clay are dominant in the central Chukchi Basin (Trefry et al., 2014 and references therein). Overall, muds dominate (64%), with a substantial contribution from sands (31%) and gravel (5%) (Trefry et al., 2014). Marine clays are often enriched in ^{232}Th series radionuclides in comparison to quartz and carbonate-rich marine sediments (Hancock et al., 2006), which could explain the high sedimentary ^{228}Ra flux observed in the Chukchi Sea. Sediment resuspension and Ra desorption contribute to the benthic source. However, assuming a

sediment ^{228}Ra activity of 1.1 dpm g^{-1} and a 32% desorbable fraction (Kipp et al., 2018), a bulk density of 1.5 g cm^{-3} and 12% annual ingrowth rate, resuspension of sediment to a depth of 1 cm across the entire shelf could support only ~5% of the measured flux. Given that ^{210}Pb profiles in Chukchi Sea sediments indicate that mixing is limited below 1 – 2 cm (Lepore et al., 2009; Baskaran and Naidu, 1995), it is unlikely that sediment resuspension can represent more than 10% of the benthic ^{228}Ra flux in the Chukchi Sea, suggesting that diffusive release from shelf sediment is the major source of ^{228}Ra to the system.

Because dFe, dMn, and dCo in the Chukchi Sea have a benthic source similar to Ra (see section 3.3.2; Fig. 3.5), the ^{228}Ra flux can be used to estimate the sedimentary fluxes of these trace elements on the shelf (Table 3.2). Trace elements fluxes from the sediments were estimated by multiplying the average ^{228}Ra flux from the shelf sediments (derived from equation 2) by the shelf-averaged ratio between dTE concentrations observed in the near-bottom waters (5-7 m above the bottom) and ^{228}Ra activity (dTE/^{228}Ra). Trace element fluxes for the Chukchi Sea derived in this way are within the range of the sedimentary fluxes observed elsewhere (Table 3.2). For example, the estimated Fe flux in the current study is about 2.5 ± 2.4 µmol m^{-2} d^{-1}. This compares well with the global range of 2.5 –7.4 µmol m^{-2} d^{-1} (Tagliabue et al., 2014; Elrod et al., 2004; Dale et al., 2015). Our estimated Mn and Co fluxes were 8.0 ± 7.1 µmol m^{-2} d^{-1} and 0.2 ± 0.1 µmol m^{-2} d^{-1}, respectively. Benthic Mn fluxes reported elsewhere range between 0.4 (Monterey Shelf, Landing and Bruland, 1987) and 7.9 µmol m^{-2} d^{-1} (Oregon/California shelf, McManus et al., 2012). However, unlike Ra, trace elements are taken up by phytoplankton, oxidized and precipitate, and/or are scavenged onto biogenic or lithogenic/sediment particles. Sediment resuspension during the current study may have increased LP-Fe transport on the shelf (section 3.3.2). Suspended particles

may have scavenged a fraction of the dFe supplied from reducing sediment as LP-Fe, buffering the concentrations in the water column (Homoky et al., 2012; Milne et al., 2017). Therefore, if a significant amount of dFe released from the sediments was lost by scavenging, our sedimentary dFe fluxes may be underestimated given that they were calculated from near-bottom water dFe concentrations. This may also explain why the dMn flux estimates were much higher than dFe fluxes. Mn removal rates from the water column are slower than for Fe, so the original Mn/Ra ratio is more likely to be preserved in bottom waters (see section 3.3.2). Dale et al. (2015) argued that Fe scavenging rates as inorganic particulates and colloidal aggregates in bottom waters are far higher than previously thought, and the fraction of dFe that is scavenged close to the seafloor may be poorly estimated.

Nonetheless, regardless of the dFe removal processes described above, dFe fluxes in the Chukchi Sea appear to be sufficient to allow for complete consumption of macronutrients, i.e., the replete dFe concentrations do not limit primary productivity. The net primary production (NPP) during SUBICE varied from 76.7 to 104 mg C m^{-2} d^{-1} (Arrigo et al., 2017). Following the argument of Tanaka et al. (2015), who estimated the Fe consumption in the Green Belt, and equally using Fe:C uptake ratios of 3 – 33 μmol Fe/mol C for coastal diatoms, biological Fe uptake in the Chukchi Sea can be estimated as 76.7 (mg C m^{-2} d^{-1})/ 12000 (mg C/mol C) x 3 (μmol Fe/mol C). This gives an estimate of NPP Fe consumption in the Chukchi Sea of ~ 0.02 – 0.27 μmol Fe m^{-2} d^{-1}, which is well below the mean sedimentary dFe flux of 2.5 μmol m^{-2} d^{-1} (Table 3.2). However, this estimate of Fe consumption was based on the NPP rate before the spring phytoplankton bloom, and it may be higher during bloom periods.

3.3.5 Trace element and radium transport to the Arctic Ocean

A recent study suggested that the shelf ^{228}Ra fluxes to the Arctic Ocean have risen sharply over the period 2007-2015, and most of the increase was ascribed to shelf sediment inputs (Kipp et al., 2018). Their surface water ^{228}Ra activities on the Chukchi shelf in summer appeared low (<10 dpm 100 L^{-1}) compared to our observations, and they suggested that the ^{228}Ra activities in the Chukchi Sea did not increase during that period. In contrast, the current study observed ^{228}Ra activities in the winter waters of the Chukchi Sea as high as 24 dpm 100 L^{-1}, levels similar to those reported for the central Arctic (Kipp et al., 2018), Kara and Laptev Seas (Rutgers van der Loeff et al., 1995). Further field observations in the Chukchi Sea in the summer, two months after our SUBICE cruise (Li et al., 2017), also found lower ^{228}Ra activities (average 9.18 dpm 100 L^{-1}), supporting the notion that ^{228}Ra activities are lower in summer than in the winter waters. Given a water residence time of four months, by the time of their sampling in the summer season, up to 50% of the Ra-enriched shelf surface water we observed would have been transported off the shelf. As a result, instantaneous water sampling collection may miss (or coincide with) important transport periods, i.e. seasonal and interannual variability in ^{228}Ra inventories may lead to different conclusions about the Chukchi Sea contribution to the overall Ra budget in the Arctic, depending on when samples are collected. One reason for the discrepancy could be because, with the progress of the melting season and consequent stabilization of the water column, convective mixing ceases, diminishing the input of benthic derived Ra to the surface waters. Another reason would be due to biological or scavenging removals of Ra that may play an important role on the Arctic shelves (Rutgers van der Loeff et al., 2012). This is also reflected in the ^{226}Ra activities, which varied by 6.2 dpm 100 L^{-1} with a minimum activity of 4.68 dpm 100 L^{-1}, well below

that expected for Pacific surface waters (7-10 dpm 100 L^{-1}) (Chung and Craig, 1980). This suggests a strong potential Ra control by biological cycling and may be closely linked to the cycling of Ba as observed in other Arctic shelves (Rutgers van der Loeff et al., 2012), and in the Bering Sea (W.S. Moore, personal communication). If the biological removal is indeed important, the Ra benthic fluxes calculated in section 3.3.4 represent conservatively low values.

The importance of the Chukchi Sea in the off-shelf export of nutrients and trace elements to the Arctic Ocean has recently been reported (Nakayama et al., 2011; Cid et al., 2012; Kondo et al., 2016; Taylor et al., 2013; Aguilar-Islas et al., 2013). The concentrations of dFe (1.45 - 46.3 nM) and TdFe (6.05 nM – 4.71 μM) observed in our study in the western Arctic Ocean are substantially higher than in the eastern Arctic Ocean. On the shelves of the Barents and Kara Seas, for example, TdFe ranged between 6 and 60 nM (Thuróczy et al., 2011), whereas dFe concentrations (0.4 – 0.54 nM) were close to that for the slope and open ocean regions (Klunder et al., 2012a, 2012b). The Laptev Sea, although being as shallow as the Chukchi Sea (~50 m) and containing high suspended particle concentrations, has levels of Td and dFe reaching only 20 to 40 nM (Klunder et al., 2012b). Nakayama et al. (2011) suggested that high concentrations of dFe observed within the halocline waters of the shelf, slope and basin regions of the western Arctic Ocean were due to transport from the shallow shelves (≤~100 m depth) of the Chukchi Sea and Canada Basin (see also Aguilar-Islas et al., 2013). Furthermore, the elevated Ni, Zn and Cd concentrations within the halocline layer in the western Arctic Ocean are reported to come from the Chukchi Sea shelf (Cid et al., 2012; Kondo et al., 2016).

In section 3.3.4, we determined the areal trace element flux from sediments (mean dFe flux = 2.5 µmol m^{-2} d^{-1}). However, as the ecosystem in the central Arctic Ocean strongly depends on the surface water exchange between shelves and central basins, it is important to quantify the off-shelf transport of trace elements into the interior basin. Previous studies have combined the ^{228}Ra flux with trace elements to determine off-shelf fluxes of trace elements in a range of global ocean regions (see Charette et al., 2016; Dulaiova et al., 2009; Sanial et al., 2018). The shelf dFe flux from the Chukchi Sea to the Arctic Ocean (Flux dFe) can then be determined using the ^{228}Ra flux and shelf-enriched dFe/Ra ratios, according to Charette et al. (2016).

$$\text{Flux dFe} = \text{Flux Ra} \times \left[\frac{\text{dFe}_{\text{shelf}} - \text{dFe}_{\text{offshelf}}}{\text{Ra}_{\text{shelf}} - \text{Ra}_{\text{offshelf}}}\right] \qquad \text{(Equation 3.3)}$$

where Flux Ra is the ^{228}Ra flux over the Chukchi Sea derived from equation 2 (taken as the average flux of 1.49 ± 0.71 x 10^8 atoms m^{-2} d^{-1}). dFe_{shelf} and $dFe_{offshelf}$, as well as $^{228}Ra_{shelf}$ and $^{228}Ra_{offshelf}$, are the concentration of dFe and ^{228}Ra of the shelf and off-shelf endmembers, respectively. Given that trace elements concentrations in surface waters can be affected by melting ice and river runoff, these shelf and off-shelf values were calculated using the depth-interval weighted average of dFe between the surface and 70 m (this study) and 75 m (Nakayama et al., 2011; black square in Fig. 3.1), respectively. The dFe/Ra ratio in equation 3 takes the difference between the weighted average of dFe at the shelf-edge station and (i.e. dFe_{shelf} = 1.55 nM) and the off-shelf Arctic basin ($dFe_{offshelf}$ = 0.66 nM; Nakayama et al., 2011). The dFe concentration ranges observed at the shelf-edge station between 15 m and 70 m (1.62 – 1.91nM) matches well with the results of Nakayama et al. (2011) at the same location (their S3 station) and similar depth range (1.08 – 2.24 nM). Furthermore, the upper

halocline waters in the Canada Basin are an extension of the Pacific Winter Water that exits the Chukchi Sea shelf. The excess ^{228}Ra activities are calculated as the difference between the mean shelf ^{228}Ra activity (Ra_{shelf} = 15.8 dpm 100 L^{-1}) and off-shelf values ($Ra_{offshelf}$ = 3.3 dpm 100 L^{-1}; Kadko and Muench, 2005). We considered our initial ^{228}Ra value as the mean activity found on the shelf assuming that ^{228}Ra radioactive decay and particle removal are negligible within the short residence time of water in the Chukchi Sea. Hence, these considerations give a shelf dFe input to the Arctic Ocean of ~ 2.5 x 10^4 mol d^{-1} (considering our sampling area over the Chukchi Shelf as 400 x 250 km). Given the mean benthic dFe flux of ~ 25.2 x 10^4 mol d^{-1}, this implies that approximately 10% of dFe produced on the Chukchi shelf is transported to the Arctic Ocean and the remainder is retained on the shelf by scavenging and/or phytoplankton consumption. This is consistent with previous estimates that 10 to 50% of the shelf sediment-derived Fe flux is transported off the shelf (Siedlecki et al., 2012). However, if there is substantial Ra removal, the shelf-edge may be a more accurate ^{228}Ra endmember, rather than the average of ^{228}Ra activities. In that case, it would suggest 25% export. It is not clear which is the most appropriate endmember, and the phenomena on Ra removal certainly requires further investigation, as the assumption that Ra behaves conservatively has a large impact on the estimates of the trace element fluxes. Regardless, whilst the Chukchi shelf is not limited by Fe, the input of dFe from the shelf to the basin is rapidly attenuated (Aguilar-Islas et al., 2013), and may therefore be an important source for the phytoplankton that accumulate in the nutricline of the Canada Basin during the growing season (Taylor et al., 2013). Dissolved Mn and dCo concentrations at the edge of the shelf in the current study were similar to or lower than off-shelf concentrations reported by

Cid et al. (2012) and Kondo et al. (2016), suggesting that, unlike Fe, the elements Mn and Co are mostly not retained on the shelf.

The benthic trace element and Ra fluxes on the shelf and their off-shelf export to the central Arctic Ocean are likely to increase in response to climate change. The annual mean transport and velocity of Pacific waters through the Bering Strait are increasing (Woodgate, 2018), which may increase coastal erosion in the Bering Strait and Chukchi Sea regions, and consequently increase the input of trace elements and Ra to the system. Coastal erosion is accelerating along the Alaskan coast, for example, in the vicinity of Barrow and along the North Slope coastal region due to changes in climate (Peckham et al., 2001), and recent warming of permafrost in Alaska has been reported (Osterkamp, 2007). All these changes may increase the input of trace elements and Ra to coastal zones. Furthermore, changes in the redox chemistry in the sediments may also cause an increase in fluxes of redox-sensitive trace elements (including Fe, Mn, Co) to the water column in the Chukchi Sea. Reduced ice cover and longer open-water seasons drive increases in primary production and are expected to subsequently increase the vertical carbon export in the Chukchi Sea (Grebmeier et al., 2006; Arrigo and Van Dijken, 2015). Increased export of labile carbon to the sediments will change the redox potential by creating a more reducing sedimentary environment, which in turn, may lead to an increase in diagenetic mobilization of redox-sensitive TEs (Trefry et al., 2014). An increase in benthic fluxes to the water column may result in higher shelf trace element fluxes to the central Arctic in future, as an increase in off-shelf water transport due to a reduction in ice cover (Woodgate, 2018) will result in a shorter residence time of the water in the Chukchi Sea and consequently less nutrients and TEs will be retained on the shelf.

Table 3.2: Mean sedimentary fluxes of dissolved iron (dFe), dissolved manganese (dMn) and dissolved cobalt (dCo) from the Chukchi Sea shelf, and off-shelf transport of dFe into the Canada Basin. * No removal, off-shelf flux is equal to benthic flux. ** Considering the area of our sampling region (400 x 250 km) over the Chukchi Shelf.

	Benthic TE flux (μmol m^2 d^{-1})	**Off-shelf TE flux (x 10^4 mol d^{-1})****	**TE flux retained on the shelf (x 10^4 mol d^{-1})****
Fe	2.5	2.5 - 6.0	19.2 - 22.8
Mn	8	*	
Co	0.2	*	

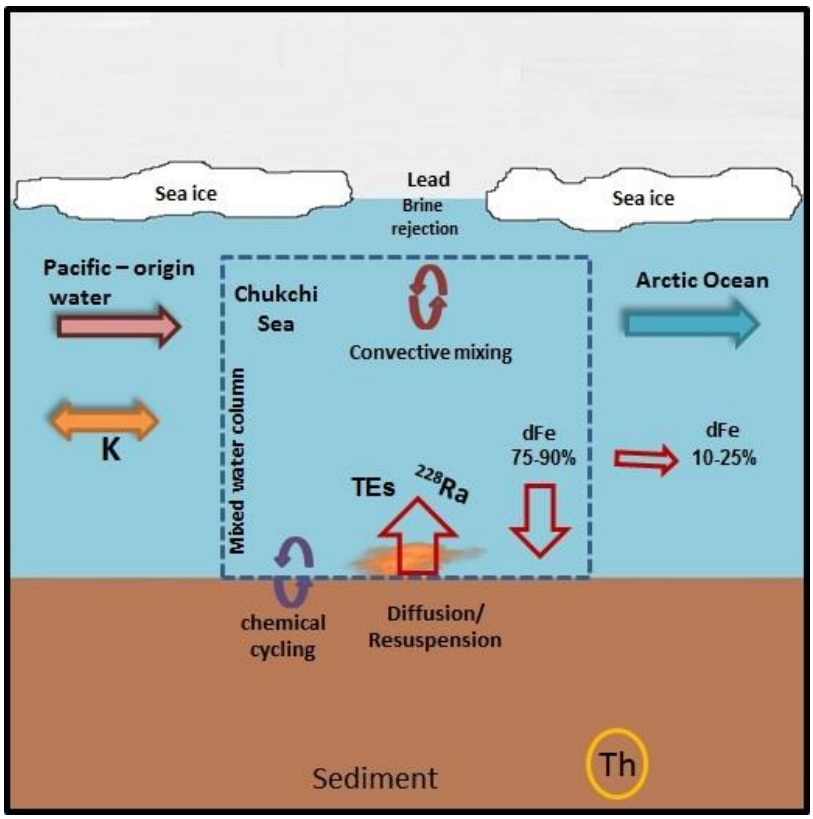

Figure 3.7: Schematic of trace element (TE) and ^{228}Ra enrichment in the Chukchi Sea. Brine rejection during ice formation leads to convective mixing of the water column. Pacific water entering the Chukchi Sea is depleted in trace elements and ^{228}Ra, but is enriched by benthic inputs in the Chukchi Sea as waters move northward to the Arctic Ocean. Given the mean benthic dFe flux over the Chukchi Shelf of ~ 25.2 x 10^4 mol d^{-1} (Table 3.2), approximately 19.2 – 22.8 x 10^4 mol d^{-1} (75-90%) is retained on the shelf, and 2.5 – 6.0 x 10^4 mol d^{-1} (10-25%)

is transported to the Arctic Ocean. The water exchange rate in the Chukchi Sea is represented by K, and Th represents the thorium isotopes present in the sediments.

3.4 Conclusion

This study is unique because it represents the only TE dataset for spring in the Chukchi Sea, a time when sea ice presence over the Chukchi shelf inhibits stratification and summer production has not yet substantially altered water column TE inventories. Thus, we were able to show that trace elements were considerably elevated throughout the Chukchi Sea shelf relative to open ocean waters, especially Fe and Mn, and that ^{228}Ra fluxes from the Chukchi Sea sediments are one of the highest reported in the literature. High concentrations of LP-Fe and the frequent sediment resuspension episodes observed during the SUBICE campaign suggest that dFe supplied by diffusive inputs from sediment pore water are scavenged by suspended particles and thereby form labile particulate phases. Trace element sedimentary fluxes of dFe (2.5 μmol m^{-2} d^{-1}), dMn (8.0 μmol m^{-2} d^{-1}), and dCo (0.2 μmol m^{-2} d^{-1}) were determined using ^{228}Ra fluxes.

Geochemical enrichment of inflowing Pacific waters highlights the importance of the Chukchi Sea as one of the major sources of (micro-) nutrients to the Arctic Ocean, which sustains Arctic primary productivity. The ^{228}Ra-derived shelf dFe input to the Arctic Ocean was about 10-25% of dFe produced on the Chukchi shelf, with the remainder retained on the shelf due to scavenging and/or phytoplankton consumption.

The predicted future increase in primary productivity due to sea ice loss and a longer open-water season is likely to increase the benthic source of trace elements in the Chukchi Sea. Even with rising temperatures, the shallow northern Bering and Chukchi Seas are expected to

continue to freeze in winter (Hunt et al., 2013), and consequently, brine rejection during ice formation will continue to drive convective overturning, likely supplying nutrients and trace elements from bottom to surface waters. An increase of the Pacific inflow and primary productivity will likely have a profound impact on the future carbon budget and behavior of redox-sensitive elements in the sediments, altering the biogeochemical cycles of trace elements supply in the Chukchi Sea and, consequently, their transport to the Arctic Ocean. Longer ice-free season increases primary productivity and off-shelf transport. The increase of the vertical carbon export on the shelf, due to the higher primary productivity will drive changes in the denitrification rates and redox potential in the sediments, consequently enhancing nutrient inputs to the water column. Consequences of climate change for sea ice cover may not directly affect the magnitude of benthic chemical fluxes, but timing of sea ice cover does control how benthic derived elements are mixed within the water column and transported off the shelf. This effect likely has a major impact on primary productivity in coastal Arctic seas, and increased carbon export may stimulate further positive feedbacks in benthic-pelagic chemical cycling in the Arctic Ocean.

Acknowledgments

The authors gratefully acknowledge the Captain and crew members of the research vessel U.S.C.G.C. Healy. We are especially grateful to Joaquin Pampin Baro for helping with trace element sample collection. We thank Michiel Rutgers van der Loeff for the personal training to conduct Ra isotope analysis. Constructive comments of the reviewers are appreciated and have led to significant improvements of the manuscript. Figures 3.1, 3.2, and 3.3 were made using Ocean Data View, version 5.1.0 (Schlitzer, R., Ocean Data View, https://odv.awi.de,

2018). Lúcia H. Vieira received a doctoral scholarship from the Conselho Nacional de Desenvolvimento Científico e Tecnológico (CNPq - grant number 239548/2013-2), Brazil. The work was supported by GEOMAR and US National Science Foundation Office of Polar Programs (award number PLR-1304563 to Kevin Arrigo).

Author contributions

Lúcia H. Vieira and Eric P. Achterberg designed this study. **Lúcia H. Vieira** carried out the sampling, analyzed samples, wrote the first draft of the manuscript. **Lúcia H. Vieira** and Aaron J. Beck discussed and edited subsequent drafts. Volker Liebetrau provided analytical assistance for Ra analysis. Eric P. Achterberg and Jan Scholten supervised the project. All authors gave detailed comments on a later version of the manuscript.

3.5 Supplementary material

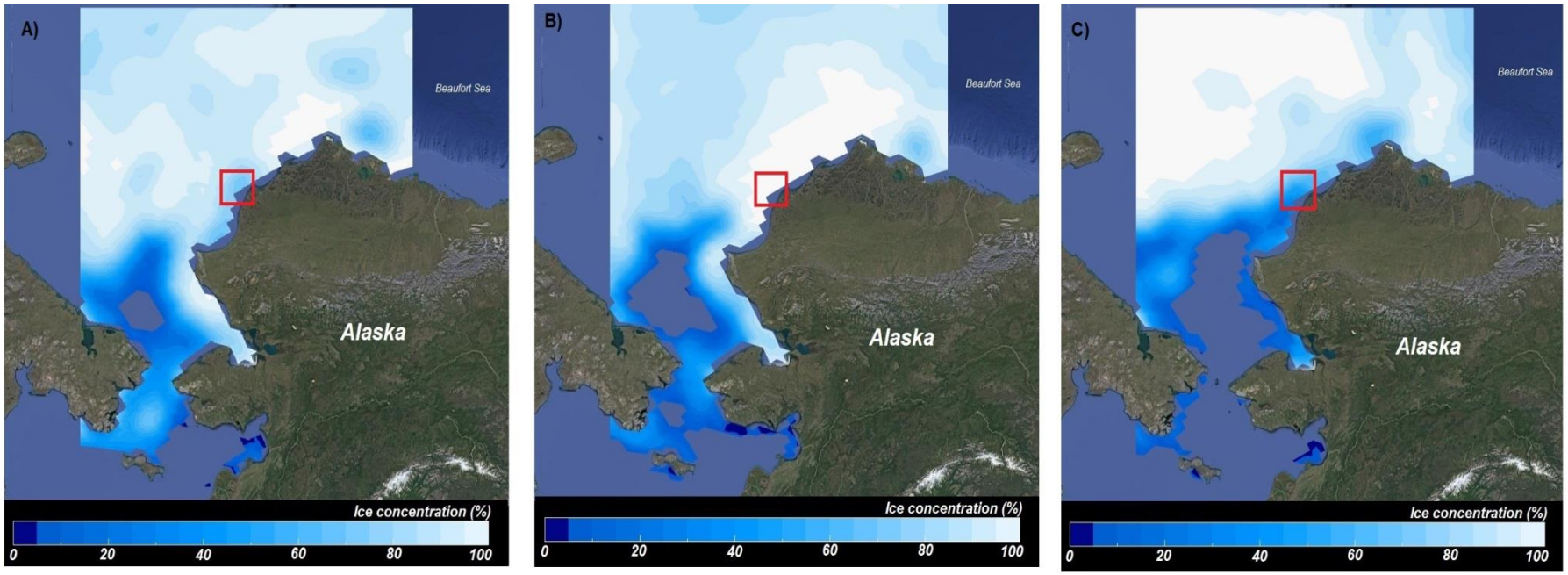

Figure S 3.1: Sea ice concentration on A) 14 May 2014; B) 25 May 2014 and C) 08 June 2014. Imagery from the NASA MODIS instrument - courtesy of the National Snow & Ice Data Center (NSIDC) DAAC. The red square represents the coastal ice zone discussed in section 3.3. National Snow & Ice Data Center (NSIDC). https://nsidc.org/data (accessed 14 May 2018).

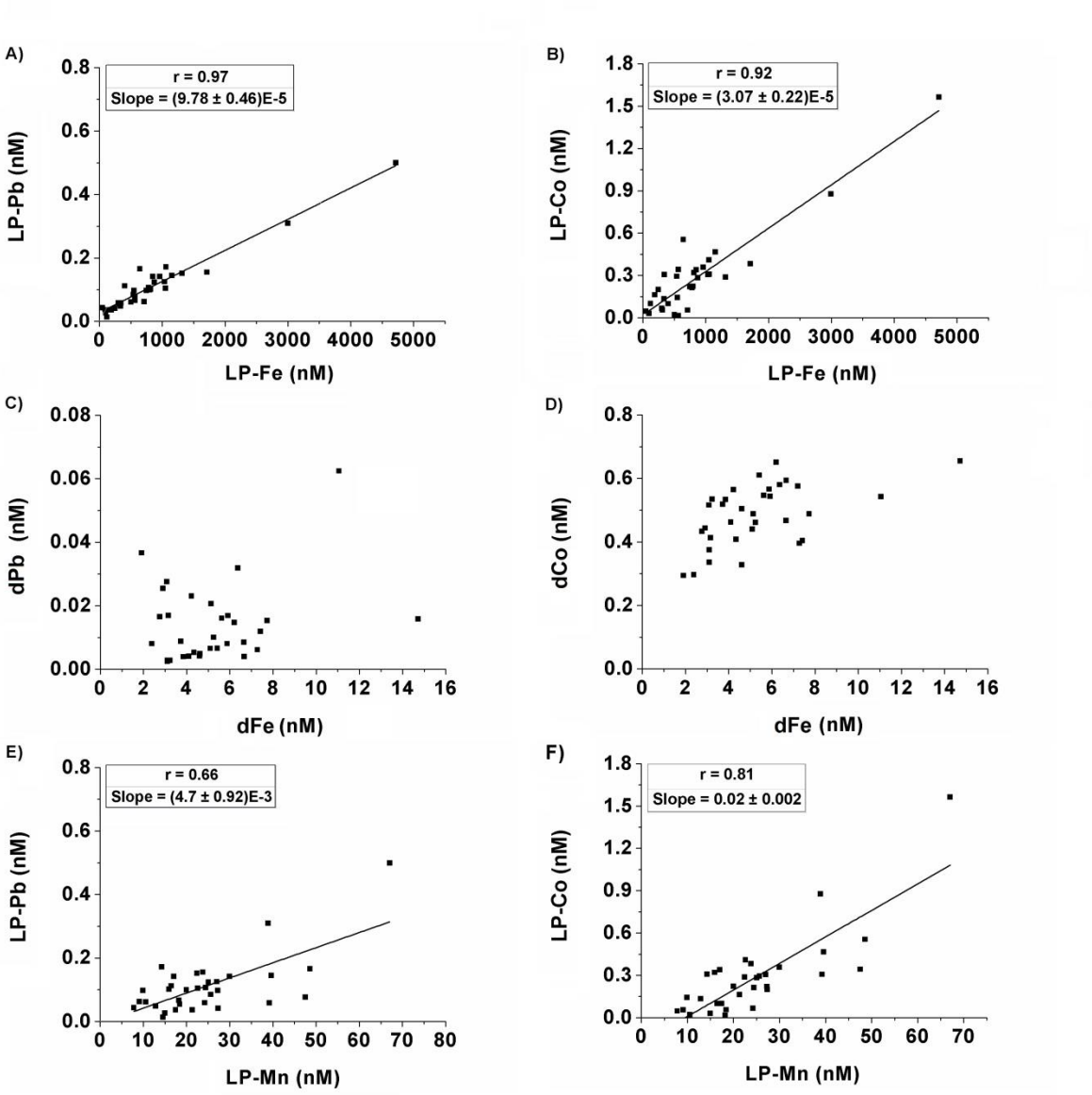

Figure S 3.2: Relationships between Fe, Mn, Co, and Pb for deep samples of the Chukchi Sea in their leachable particulate forms and their dissolved forms

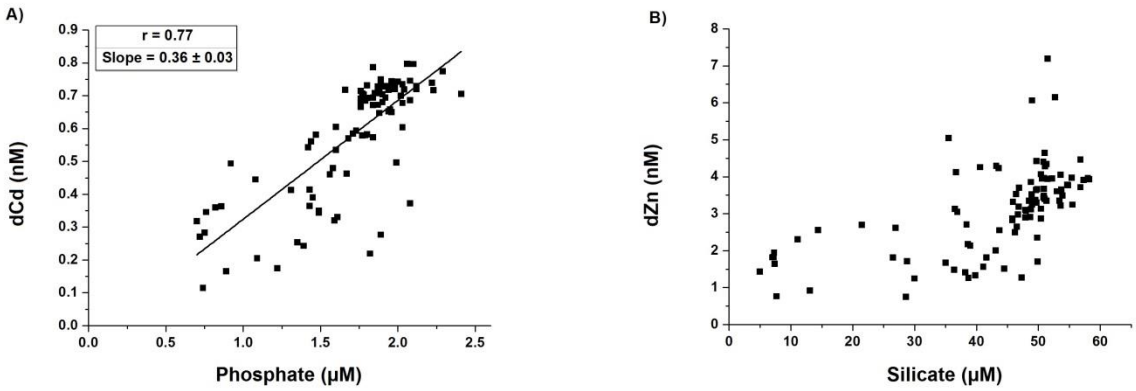

Figure S 3.3: Scatter plots of dCd versus Phosphate (A) and dZn versus Silicate (B). The plots include all samples and depths in the Chukchi Sea.

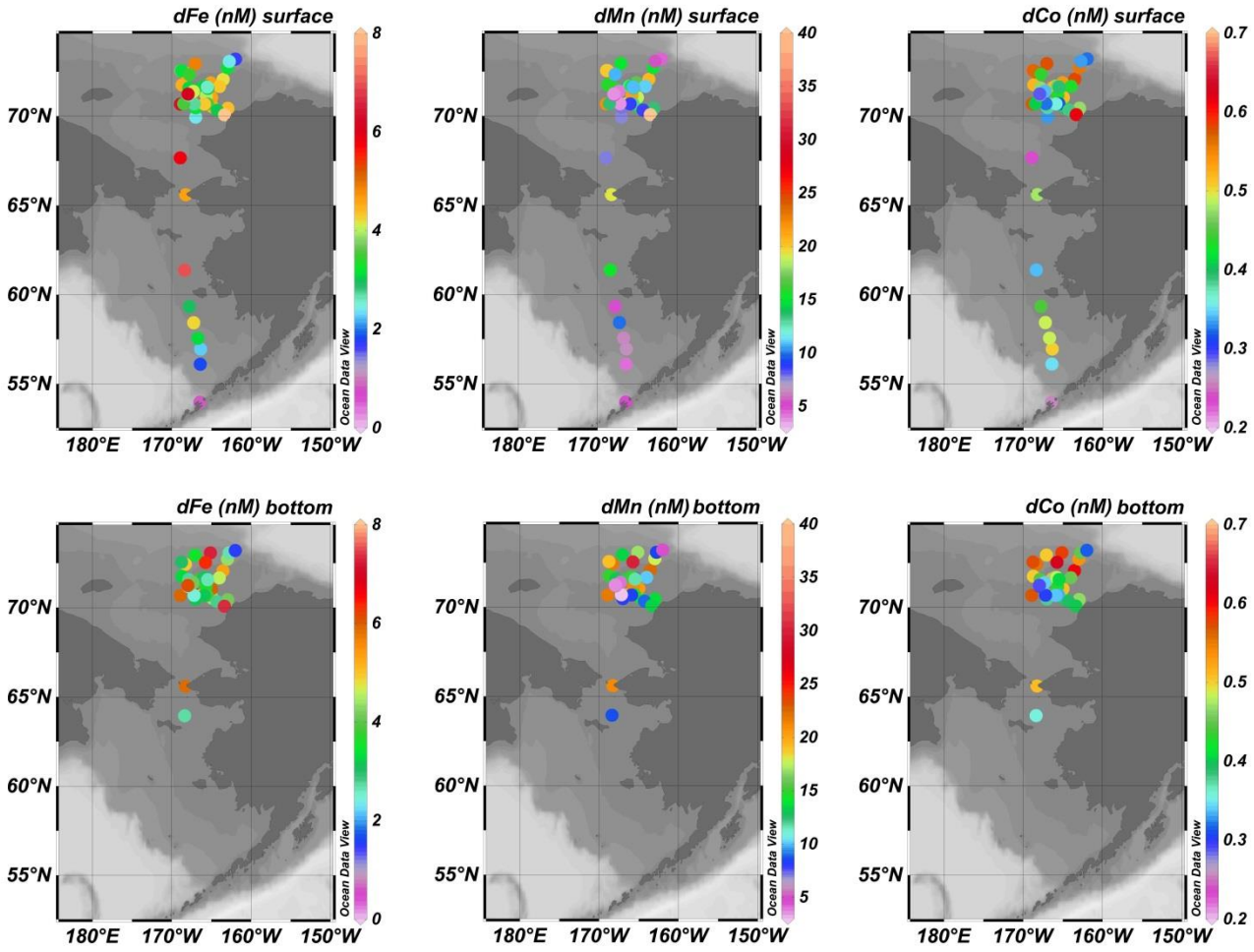

Figure S 3.4: Distributions of dFe, dMn, and dCo in surface and bottom waters (5-7 m above the seafloor). Maximum values of 46 nM for dFe and 59 nM for dMn in surface waters were excluded.

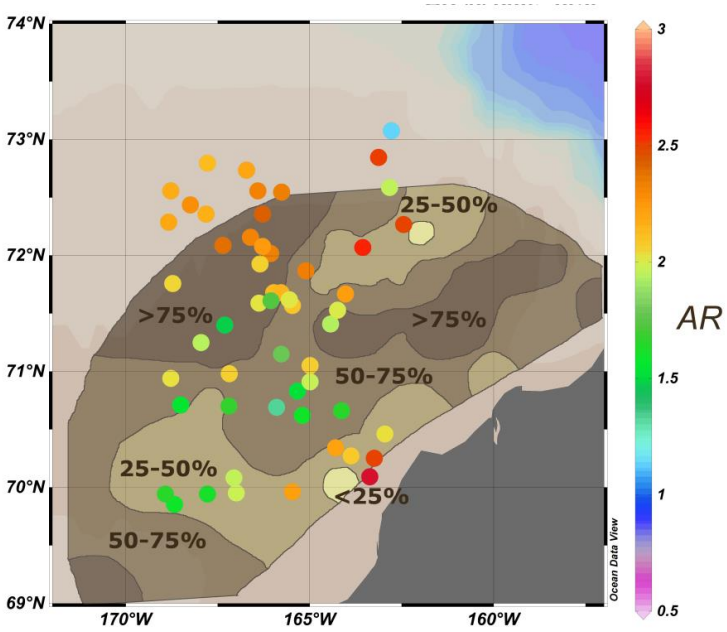

Figure S 3.5: Contour map of sediment type. The color dots represent $^{228}Ra/^{226}Ra$ activity ratios (AR) and tan-brown contours and numbers represent the percentage of silty + clay, redrawn after Trefry et al. (2014). The depth contours are also shown.

Table S 3.1: Concentration of dissolved trace metals in the Bering Sea (Fish 1-7) and Chukchi Sea.

Station	Depth (m)	Latitude	Longitude	dCd (nM)	dFe (nM)	dNi (nM)	dCu (nM)	dZn (nM)	dPb (pM)	dMn (nM)	dCo (nM)
Fish 1	0	53.98	-166.48	0.43 ± 0.01	0.77 ± 0.01	4.85 ± 0.15	3.15 ± 0.06	0.99 ± 0.10	6.78 ± 0.41	4.69 ± 0.49	0.25 ± 0.02
Fish 2	0	56.11	-166.43	0.37 ± 0.01	1.79 ± 0.05	4.34 ± 0.20	2.70 ± 0.29	0.29 ± 0.02	1.86 ± 0.15	4.02 ± 0.42	0.35 ± 0.03
Fish 3	0	56.95	-166.40	0.39 ± 0.04	2.23 ± 0.04	4.84 ± 0.19	3.56 ± 0.39	0.31 ± 0.02	3.03 ± 0.18	6.26 ± 0.65	0.50 ± 0.05
Fish 4	0	57.56	-166.74	0.35 ± 0.03	3.08 ± 0.04	5.11 ± 0.12	4.57 ± 0.50	0.75 ± 0.07	6.98 ± 0.46	6.13 ± 0.63	0.49 ± 0.04
Fish 5	0	58.43	-167.26	0.53 ± 0.04	4.19 ± 0.06	8.55 ± 0.26	8.21 ± 0.17	1.99 ± 0.08	2.33 ± 0.18	9.70 ± 1.00	0.49 ± 0.04
Fish 6	0	59.34	-167.81	0.30 ± 0.01	2.91 ± 0.06	6.71 ± 0.14	7.17 ± 0.18	0.77 ± 0.03	2.45 ± 0.15	4.68 ± 0.48	0.45 ± 0.04
Fish 7	0	61.38	-168.40	0.22 ± 0.00	6.87 ± 0.40	3.65 ± 0.12	3.24 ± 0.09	0.59 ± 0.04	4.02 ± 0.24	15.19 ± 1.57	0.34 ± 0.03
1	20	63.95	-168.39	0.25 ± 0.00	2.66 ± 0.07	5.26 ± 0.30	3.33 ± 0.37	1.71 ± 0.14	13.09 ± 0.78	8.46 ± 0.88	0.35 ± 0.03
2	10	65.61	-168.27	0.27 ± 0.01	4.56 ± 0.06	5.92 ± 0.12	4.43 ± 0.48	0.76 ± 0.01	8.77 ± 0.53	19.09 ± 1.98	0.48 ± 0.04
2	25	65.61	-168.27	0.06 ± 0.01	5.85 ± 0.13	2.28 ± 0.10	0.41 ± 0.05	1.94 ± 0.06	5.02 ± 0.32	20.97 ± 2.17	0.51 ± 0.05
9	15	67.67	-168.95	0.33 ± 0.01	5.76 ± 0.20	4.48 ± 0.08	2.77 ± 0.06	1.26 ± 0.10	9.71 ± 0.67	7.51 ± 0.78	0.23 ± 0.02
10	15	70.69	-168.93	0.72 ± 0.05	6.26 ± 0.09	6.94 ± 0.13	4.64 ± 0.09	4.28 ± 0.10	12.28 ± 0.76	22.03 ± 2.29	0.57 ± 0.05
10	30	70.69	-168.93	0.73 ± 0.06	5.88 ± 0.10	7.03 ± 0.21	4.30 ± 0.12	3.43 ± 0.09	8.06 ± 0.49	21.59 ± 2.24	0.57 ± 0.05
16	20	70.71	-166.89	0.65 ± 0.04	6.65 ± 0.13	6.30 ± 0.20	3.79 ± 0.14	3.95 ± 0.07	8.48 ± 0.51	20.45 ± 2.12	0.47 ± 0.04
19	15	70.71	-166.27	0.64 ± 0.04	5.18 ± 0.11	6.34 ± 0.14	3.68 ± 0.06	3.51 ± 0.15	5.98 ± 0.36	19.08 ± 1.97	0.47 ± 0.04
19	30	70.71	-166.27	0.63 ± 0.05	5.10 ± 0.11	6.12 ± 0.10	3.42 ± 0.08	3.12 ± 0.24	6.53 ± 0.40	19.00 ± 1.97	0.44 ± 0.04
24	15	70.53	-164.88	0.56 ± 0.04	4.42 ± 0.06	5.98 ± 0.13	*	2.82 ± 0.12	42.01 ± 2.50	14.47 ± 1.49	0.41 ± 0.04
24	25	70.53	-164.88	0.58 ± 0.01	4.37 ± 0.05	5.78 ± 0.25	6.40 ± 0.16	2.65 ± 0.10	18.51 ± 1.12	13.95 ± 1.44	0.41 ± 0.04
24	35	70.53	-164.88	0.57 ± 0.01	7.42 ± 0.08	5.79 ± 0.09	4.81 ± 0.09	2.49 ± 0.09	11.94 ± 0.71	15.33 ± 1.58	0.40 ± 0.04
30	15	70.24	-163.25	0.41 ± 0.02	5.81 ± 0.36	8.01 ± 0.57	6.57 ± 0.68	1.25 ± 0.12	5.01 ± 0.47	11.91 ± 1.31	0.73 ± 0.07
30	25	70.24	-163.25	0.58 ± 0.01	4.60 ± 0.06	8.04 ± 0.57	6.20 ± 0.12	1.67 ± 0.13	4.12 ± 0.29	13.28 ± 1.37	0.50 ± 0.05
31	15	70.45	-162.95	0.58 ± 0.01	4.33 ± 0.07	7.01 ± 0.17	5.32 ± 0.09	4.30 ± 0.20	4.18 ± 0.25	13.29 ± 1.37	0.47 ± 0.04
31	25	70.45	-162.95	0.59 ± 0.02	4.10 ± 0.08	6.68 ± 0.16	4.43 ± 0.48	2.55 ± 0.17	4.10 ± 0.27	13.47 ± 1.39	0.46 ± 0.04
36	15	71.05	-164.99	0.61 ± 0.05	4.55 ± 0.06	6.19 ± 0.32	3.74 ± 0.40	3.49 ± 0.31	4.50 ± 0.31	18.55 ± 1.91	0.51 ± 0.05
36	25	71.05	-164.99	0.62 ± 0.05	5.93 ± 0.09	6.57 ± 0.29	4.22 ± 0.07	3.63 ± 0.34	21.89 ± 1.32	20.19 ± 2.09	0.51 ± 0.05
36	35	71.05	-164.99	0.73 ± 0.06	7.73 ± 0.12	7.08 ± 0.11	3.87 ± 0.09	3.67 ± 0.12	15.30 ± 0.91	22.21 ± 2.30	0.49 ± 0.04
44	15	71.88	-165.10	0.70 ± 0.06	4.56 ± 0.06	6.12 ± 0.43	4.66 ± 1.07	4.40 ± 0.07	36.73 ± 2.18	16.72 ± 1.73	0.54 ± 0.05
55	15	72.95	-167.08	0.68 ± 0.05	4.85 ± 0.09	6.75 ± 0.76	4.54 ± 0.53	4.12 ± 0.20	10.03 ± 0.71	15.07 ± 1.56	0.57 ± 0.05
55	25	72.95	-167.08	0.69 ± 0.02	3.48 ± 0.08	6.57 ± 0.10	4.13 ± 0.10	2.87 ± 0.21	3.38 ± 0.21	13.21 ± 1.37	0.50 ± 0.05
55	35	72.95	-167.08	0.69 ± 0.02	3.23 ± 0.08	6.33 ± 0.17	4.05 ± 0.11	2.86 ± 0.07	2.76 ± 0.22	13.78 ± 1.42	0.54 ± 0.05
57	15	72.56	-168.88	0.66 ± 0.05	3.69 ± 0.44	6.43 ± 0.29	4.20 ± 0.46	3.88 ± 0.28	11.12 ± 0.96	19.82 ± 2.86	0.67 ± 0.06

59	15	72.44	-168.30	0.69 ± 0.02	4.47 ± 0.18	6.80 ± 0.20	4.22 ± 0.15	3.53 ± 0.19	4.35 ± 0.32	22.25 ± 2.32	0.57 ± 0.05
59	30	72.44	-168.30	0.69 ± 0.06	4.90 ± 0.13	6.71 ± 0.18	4.18 ± 0.07	3.19 ± 0.11	5.87 ± 0.35	21.64 ± 2.25	0.55 ± 0.05
59	40	72.44	-168.30	0.66 ± 0.02	5.36 ± 0.08	6.37 ± 0.07	3.87 ± 0.08	3.03 ± 0.11	6.54 ± 0.41	23.86 ± 2.47	0.57 ± 0.05
59	50	72.44	-168.30	0.34 ± 0.02	14.72 ± 0.20	6.57 ± 0.09	4.22 ± 0.11	3.95 ± 0.19	15.84 ± 0.95	39.82 ± 4.12	0.65 ± 0.06
70	15	72.07	-163.55	0.71 ± 0.05	4.15 ± 0.07	7.35 ± 0.40	4.66 ± 0.10	3.48 ± 0.14	8.77 ± 0.55	20.40 ± 2.11	0.58 ± 0.05
70	25	72.07	-163.55	0.72 ± 0.03	5.31 ± 0.15	7.45 ± 0.18	4.53 ± 0.16	3.61 ± 0.10	6.41 ± 0.38	22.19 ± 2.30	0.60 ± 0.05
70	35	72.07	-163.55	0.72 ± 0.05	5.42 ± 0.09	7.39 ± 0.23	4.71 ± 0.10	3.22 ± 0.12	6.55 ± 0.40	24.08 ± 2.49	0.61 ± 0.06
78	15	72.72	-162.97	0.64 ± 0.05	3.15 ± 0.07	7.15 ± 0.27	4.87 ± 0.14	3.10 ± 0.13	3.75 ± 0.25	14.93 ± 1.54	0.56 ± 0.05
78	30	72.72	-162.97	0.65 ± 0.05	4.31 ± 0.07	6.65 ± 0.39	4.79 ± 0.51	3.07 ± 0.42	7.29 ± 0.53	17.67 ± 1.47	0.53 ± 0.04
78	40	72.72	-162.97	0.67 ± 0.05	6.71 ± 0.38	7.20 ± 0.23	5.05 ± 0.54	1.25 ± 0.12	7.53 ± 0.61	12.62 ± 1.40	0.57 ± 0.05
78	50	72.72	-162.97	0.68 ± 0.01	8.14 ± 0.20	6.87 ± 0.42	4.66 ± 0.14	3.35 ± 0.09	4.39 ± 0.33	25.23 ± 2.74	0.66 ± 0.06
78	60	72.72	-162.97	0.65 ± 0.05	6.66 ± 0.24	6.96 ± 0.22	4.81 ± 0.17	3.13 ± 0.06	3.95 ± 0.32	22.25 ± 2.43	0.59 ± 0.08
81	15	73.08	-162.77	0.35 ± 0.03	2.35 ± 0.06	4.42 ± 0.29	4.24 ± 0.98	1.65 ± 0.08	5.58 ± 0.46	5.29 ± 0.57	0.33 ± 0.04
81	30	73.08	-162.77	0.49 ± 0.01	2.62 ± 0.06	3.95 ± 0.27	0.93 ± 0.22	2.31 ± 0.09	4.30 ± 0.30	8.23 ± 0.89	0.45 ± 0.06
81	50	73.08	-162.77	0.51 ± 0.04	3.25 ± 0.05	4.14 ± 0.28	2.96 ± 0.68	2.62 ± 0.07	3.52 ± 0.25	10.27 ± 1.11	0.49 ± 0.06
81	70	73.08	-162.77	0.53 ± 0.06	3.85 ± 0.10	4.15 ± 0.28	2.32 ± 0.53	3.04 ± 0.09	3.94 ± 0.32	20.29 ± 2.20	0.53 ± 0.07
83	15	73.21	-162.00	0.35 ± 0.01	1.62 ± 0.04	4.47 ± 0.32	1.78 ± 0.50	1.55 ± 0.08	6.70 ± 0.45	2.20 ± 0.25	0.32 ± 0.02
83	25	73.21	-162.00	0.35 ± 0.01	1.45 ± 0.03	4.49 ± 0.32	1.74 ± 0.40	1.43 ± 0.08	20.95 ± 1.47	4.34 ± 0.47	0.31 ± 0.02
83	50	73.21	-162.00	0.36 ± 0.01	1.69 ± 0.03	4.80 ± 0.32	*	1.83 ± 0.09	39.03 ± 2.68	4.13 ± 0.45	0.32 ± 0.03
83	70	73.21	-162.00	0.39 ± 0.01	1.91 ± 0.05	5.14 ± 0.35	4.31 ± 0.99	*	36.64 ± 2.51	3.59 ± 0.39	0.29 ± 0.04
91	50	73.08	-165.14	0.67 ± 0.06	7.21 ± 0.12	4.60 ± 0.30	*	4.25 ± 0.11	0.00 ± 8.00	16.70 ± 1.81	0.58 ± 0.08
96	25	72.54	-165.75	0.67 ± 0.05	6.28 ± 0.08	5.29 ± 0.36	5.66 ± 1.30	3.37 ± 0.15	19.55 ± 1.37	29.53 ± 3.20	0.62 ± 0.08
96	40	72.54	-165.75	0.65 ± 0.03	6.37 ± 0.21	5.88 ± 0.41	4.13 ± 0.95	4.42 ± 0.19	31.91 ± 2.20	28.27 ± 3.13	0.58 ± 0.08
104	15	71.59	-166.38	0.67 ± 0.06	3.00 ± 0.05	5.19 ± 0.35	4.10 ± 0.94	3.24 ± 0.12	5.58 ± 0.45	13.44 ± 1.45	0.52 ± 0.07
104	20	71.59	-166.38	0.65 ± 0.06	3.76 ± 0.07	5.15 ± 0.34	3.83 ± 0.88	5.23 ± 0.23	4.89 ± 0.34	13.42 ± 1.45	0.51 ± 0.07
104	25	71.59	-166.38	0.68 ± 0.03	3.22 ± 0.07	5.25 ± 0.38	2.52 ± 0.58	3.35 ± 0.09	4.05 ± 0.32	12.79 ± 1.39	0.49 ± 0.07
104	30	71.59	-166.38	0.70 ± 0.06	3.43 ± 0.08	4.72 ± 0.31	3.39 ± 0.78	3.51 ± 0.11	4.37 ± 0.31	12.87 ± 1.39	0.50 ± 0.07
104	40	71.59	-166.38	0.70 ± 0.06	3.72 ± 0.08	5.24 ± 0.35	0.28 ± 0.07	3.77 ± 0.12	8.83 ± 0.62	16.30 ± 1.77	0.52 ± 0.07
106	15	71.68	-165.98	0.66 ± 0.06	3.15 ± 0.05	4.87 ± 0.33	5.03 ± 0.16	3.30 ± 0.08	4.78 ± 0.36	12.47 ± 1.35	0.51 ± 0.07
106	20	71.68	-165.98	0.70 ± 0.06	3.10 ± 0.05	5.19 ± 0.35	4.28 ± 0.98	3.49 ± 0.44	4.79 ± 0.34	14.48 ± 1.21	0.46 ± 0.04
107	15	71.68	-165.78	0.67 ± 0.07	2.94 ± 0.11	5.13 ± 0.34	3.70 ± 0.85	3.64 ± 0.41	3.92 ± 0.28	15.07 ± 1.26	0.46 ± 0.04
107	20	71.68	-165.78	0.66 ± 0.06	2.96 ± 0.13	5.00 ± 0.33	4.59 ± 1.06	4.23 ± 0.50	10.20 ± 0.74	14.85 ± 1.23	0.48 ± 0.04
107	30	71.68	-165.78	0.69 ± 0.06	2.93 ± 0.06	5.14 ± 0.34	4.55 ± 0.13	3.32 ± 0.37	3.96 ± 0.29	14.62 ± 1.23	0.43 ± 0.03
107	40	71.68	-165.78	0.79 ± 0.06	5.62 ± 0.09	7.19 ± 0.47	3.60 ± 0.10	4.46 ± 0.58	16.09 ± 1.15	28.78 ± 2.39	0.55 ± 0.04
112	15	71.15	-165.69	0.68 ± 0.06	3.93 ± 0.08	5.04 ± 0.37	3.78 ± 0.87	4.07 ± 0.57	5.71 ± 0.41	21.27 ± 1.78	0.43 ± 0.03
112	25	71.15	-165.69	0.65 ± 0.05	3.59 ± 0.09	5.03 ± 0.33	2.98 ± 0.04	3.96 ± 0.49	6.81 ± 0.49	20.91 ± 1.76	0.43 ± 0.03
112	35	71.15	-165.69	0.65 ± 0.06	5.25 ± 0.04	4.85 ± 0.32	0.66 ± 0.15	6.15 ± 0.67	10.04 ± 0.73	24.58 ± 2.04	0.46 ± 0.04

120	15	70.70	-165.55	0.46 ± 0.01	3.49 ± 0.12	5.61 ± 0.62	2.61 ± 0.31	*	36.16 ± 2.59	12.82 ± 1.08	0.31 ± 0.02
120	25	70.70	-165.55	0.47 ± 0.04	3.80 ± 0.07	5.64 ± 0.14	3.35 ± 0.40	1.81 ± 0.23	4.79 ± 0.34	13.61 ± 1.14	0.33 ± 0.03
120	35	70.70	-165.55	0.46 ± 0.02	4.61 ± 0.09	5.63 ± 0.19	0.28 ± 0.03	2.01 ± 0.29	4.87 ± 0.35	14.52 ± 0.47	0.33 ± 0.03
124	15	70.34	-164.29	0.56 ± 0.01	2.97 ± 0.06	7.07 ± 0.18	5.58 ± 0.08	5.05 ± 0.57	3.57 ± 0.26	8.32 ± 0.24	0.38 ± 0.03
124	25	70.34	-164.29	0.53 ± 0.02	2.76 ± 0.05	6.87 ± 0.10	2.42 ± 0.28	2.13 ± 0.24	3.74 ± 0.27	8.79 ± 0.25	0.39 ± 0.03
124	35	70.34	-164.29	0.60 ± 0.02	4.34 ± 0.05	7.18 ± 0.16	2.95 ± 0.35	2.70 ± 0.31	5.24 ± 0.38	14.26 ± 0.40	0.41 ± 0.03
127	12	70.09	-163.36	0.32 ± 0.02	46.33 ± 0.66	8.31 ± 0.19	3.92 ± 0.45	3.57 ± 0.40	8.88 ± 0.64	59.64 ± 1.71	0.61 ± 0.05
127	20	70.09	-163.36	0.44 ± 0.01	7.28 ± 0.16	6.78 ± 0.19	0.77 ± 0.09	2.70 ± 0.37	6.13 ± 0.45	13.18 ± 0.37	0.40 ± 0.03
137	12	69.95	-167.00	0.11 ± 0.00	2.34 ± 0.05	3.95 ± 0.15	4.49 ± 0.54	0.91 ± 0.05	3.01 ± 0.21	7.39 ± 0.80	0.33 ± 0.04
151	15	70.48	-167.02	0.36 ± 0.01	3.19 ± 0.06	5.79 ± 0.16	4.75 ± 0.11	3.13 ± 0.22	2.88 ± 0.25	7.60 ± 0.82	0.38 ± 0.05
151	25	70.48	-167.02	0.35 ± 0.00	3.10 ± 0.05	5.62 ± 0.15	4.10 ± 0.47	1.41 ± 0.06	2.83 ± 0.23	7.91 ± 0.86	0.38 ± 0.05
152	15	70.69	-165.90	0.41 ± 0.01	4.26 ± 0.09	5.58 ± 0.18	3.18 ± 0.37	2.18 ± 0.14	3.55 ± 0.28	8.45 ± 0.92	0.36 ± 0.05
152	30	70.69	-165.90	0.34 ± 0.01	3.11 ± 0.10	5.49 ± 0.16	3.57 ± 0.42	1.33 ± 0.08	2.51 ± 0.24	8.10 ± 0.89	0.34 ± 0.05
156	15	70.70	-167.20	0.21 ± 0.01	2.66 ± 0.08	4.87 ± 0.12	3.93 ± 0.46	1.81 ± 0.12	5.90 ± 0.42	3.38 ± 0.37	0.32 ± 0.04
156	25	70.70	-167.20	0.17 ± 0.00	2.39 ± 0.04	5.01 ± 0.18	5.16 ± 0.15	0.75 ± 0.06	8.05 ± 0.56	2.94 ± 0.32	0.30 ± 0.04
160	15	70.71	-168.52	0.58 ± 0.02	3.48 ± 0.06	*	8.79 ± 0.18	2.89 ± 0.10	37.82 ± 2.60	13.32 ± 1.44	0.40 ± 0.05
168	15	71.76	-168.73	0.68 ± 0.05	4.46 ± 0.09	*	*	7.19 ± 0.33	0.00 ± 6.55	15.57 ± 1.69	0.52 ± 0.07
168	25	71.76	-168.73	0.68 ± 0.05	3.25 ± 0.06	7.29 ± 0.21	7.63 ± 0.22	4.05 ± 0.07	37.57 ± 2.63	14.70 ± 1.59	0.50 ± 0.07
168	40	71.76	-168.73	0.70 ± 0.05	4.22 ± 0.13	7.13 ± 0.18	5.48 ± 0.63	3.72 ± 0.14	23.05 ± 1.59	22.59 ± 2.48	0.56 ± 0.08
175	15	72.56	-168.78	0.66 ± 0.05	3.10 ± 0.06	6.55 ± 0.20	5.64 ± 0.66	3.32 ± 0.12	43.91 ± 3.02	19.80 ± 2.15	0.56 ± 0.08
175	30	72.56	-168.78	0.65 ± 0.01	2.96 ± 0.06	6.18 ± 0.09	4.82 ± 0.56	2.98 ± 0.09	21.03 ± 1.45	18.86 ± 2.04	0.57 ± 0.08
175	40	72.56	-168.78	0.68 ± 0.06	3.95 ± 0.06	6.53 ± 0.11	4.60 ± 0.10	3.24 ± 0.14	16.26 ± 1.11	23.93 ± 2.59	0.59 ± 0.08
175	50	72.56	-168.78	0.74 ± 0.06	6.20 ± 0.10	6.63 ± 0.22	4.25 ± 0.49	3.97 ± 0.11	14.69 ± 1.03	40.19 ± 4.36	0.65 ± 0.09
178	15	72.35	-167.82	0.71 ± 0.05	3.41 ± 0.06	7.47 ± 0.83	*	3.40 ± 0.45	70.09 ± 5.00	10.52 ± 0.88	0.44 ± 0.03
188	15	71.67	-164.02	0.73 ± 0.02	4.28 ± 0.06	*	8.14 ± 0.75	6.06 ± 0.71	*	10.90 ± 0.31	0.43 ± 0.03
188	25	71.67	-164.02	0.67 ± 0.05	4.53 ± 0.10	7.27 ± 0.80	6.31 0.74	4.34 ± 0.59	83.05 ± 5.93	9.94 ± 0.83	0.45 ± 0.04
188	35	71.67	-164.02	0.74 ± 0.06	11.05 ± 0.16	7.68 ± 0.11	6.18 0.72	3.96 ± 0.40	62.44 ± 4.45	32.27 ± 0.92	0.54 ± 0.04
192	15	71.57	-165.47	0.70 ± 0.05	2.98 ± 0.07	7.52 ± 0.82	9.77 1.13	3.85 ± 0.46	37.71 ± 2.69	12.96 ± 0.42	0.42 ± 0.03
192	25	71.57	-165.47	0.68 ± 0.05	2.59 ± 0.05	7.23 ± 0.25	6.79 0.79	3.78 ± 0.41	27.40 ± 1.95	11.50 ± 0.35	0.40 ± 0.03
192	35	71.57	-165.47	0.71 ± 0.06	2.91 ± 0.04	6.70 ± 0.07	5.43 ± 0.63	3.91 ± 0.45	25.47 ± 1.82	15.23 ± 0.44	0.44 ± 0.03
201	15	71.20	-167.93	0.32 ± 0.01	2.44 ± 0.04	5.17 ± 0.12	4.75 ± 0.55	1.56 ± 0.22	15.37 ± 1.10	5.11 ± 0.15	0.27 ± 0.02
201	25	71.20	-167.93	0.37 ± 0.01	2.48 ± 0.03	5.63 ± 0.07	4.04 ± 0.47	1.70 ± 0.21	11.64 ± 0.84	5.63 ± 0.16	0.30 ± 0.02
201	35	71.20	-167.93	0.56 ± 0.02	3.14 ± 0.05	6.08 ± 0.06	4.46 ± 0.53	2.79 ± 0.34	14.17 ± 1.01	12.61 ± 0.36	0.38 ± 0.03
201	45	71.20	-167.93	0.60 ± 0.01	3.16 ± 0.06	6.35 ± 0.15	5.76 ± 0.68	2.91 ± 0.36	16.94 ± 1.22	15.85 ± 0.47	0.41 ± 0.03
205	15	71.58	-167.88	0.66 ± 0.05	3.06 ± 0.07	7.59 ± 0.83	5.61 ± 0.66	3.94 ± 0.47	18.19 ± 1.30	15.72 ± 0.47	0.47 ± 0.04
205	25	71.58	-167.88	0.66 ± 0.05	2.72 ± 0.07	6.80 ± 0.47	5.42 ± 0.56	3.35 ± 0.27	14.51 ± 1.04	13.02 ± 0.37	0.44 ± 0.03
205	40	71.58	-167.88	0.69 ± 0.05	2.76 ± 0.04	6.63 ± 0.14	5.12 ± 0.53	3.65 ± 0.49	16.54 ± 1.18	12.67 ± 0.36	0.43 ± 0.03

209	15	71.64	-165.54	0.67 ± 0.05	2.54 ± 0.03	6.56 ± 0.42	3.32 ± 0.35	3.70 ± 0.50	15.99 ± 1.16	10.63 ± 0.30	0.39 ± 0.03
209	25	71.64	-165.54	0.67 ± 0.05	2.90 ± 0.06	6.28 ± 0.44	4.96 ± 0.51	3.13 ± 0.36	14.29 ± 1.02	8.78 ± 0.25	0.39 ± 0.03
209	35	71.64	-165.54	0.70 ± 0.05	3.09 ± 0.15	6.36 ± 0.60	5.06 ± 0.52	3.93 ± 0.31	27.60 ± 2.21	14.98 ± 1.61	0.52 ± 0.05
215	15	71.40	-167.31	0.24 ± 0.02	4.08 ± 0.36	5.11 ± 0.46	4.05 ± 0.42	1.48 ± 0.12	18.67 ± 1.51	3.77 ± 0.42	0.34 ± 0.03
215	25	71.40	-167.31	0.28 ± 0.02	3.23 ± 0.16	4.79 ± 0.46	5.01 ± 0.51	1.27 ± 0.10	20.72 ± 1.79	3.85 ± 0.41	0.40 ± 0.04
215	35	71.40	-167.31	0.50 ± 0.03	5.92 ± 0.28	5.90 ± 0.39	0.22 ± 0.03	2.35 ± 0.19	16.88 ± 1.36	10.85 ± 1.17	0.54 ± 0.05
221	15	71.25	-167.96	0.17 ± 0.01	6.07 ± 0.31	3.75 ± 0.36	6.35 ± 0.65	2.56 ± 0.22	19.09 ± 1.74	3.43 ± 0.37	0.29 ± 0.03
221	25	71.25	-167.96	0.22 ± 0.01	5.14 ± 0.23	5.15 ± 0.47	4.69 ± 0.48	1.51 ± 0.13	20.61 ± 1.70	4.03 ± 0.43	0.40 ± 0.03

*Not determined or contaminated

Table S 3.2: Analyzed reference seawater D1 and standard deviation and the respective consensus value

	SAFe D1 n= 12 (nM)	SAFe consensus Value (nM)
Cd	0.942 ± 0.017	0.991 ± 0.031
Fe	0.677 ± 0.053	0.670 ± 0.040
Ni	8.320 ± 0.236	8.580 ± 0.260
Cu	2.079 ± 0.033	2.270 ± 0.110
Zn	7.386 ± 0.461	7.400 ± 0.350
Pb	0.028 ± 0.003	0.028 ± 0.003
Mn	0.352 ± 0.036	0.350 ± 0.050
Co	0.047 ± 0.004	0.045 ± 0.005

Table S 3.3 : Long-lived radium activities in surface waters of the Bering Sea (Fish Ra 1-3) and Chukchi Sea.

Station	Collection date	Latitude	Longitude	Ra-226 (dpm 100 L^{-1})	Ra-228 (dpm 100 L^{-1})	AR
FISH Ra 1	May 14 2014	56.65	-166.41	4.75 ± 0.41	1.64 ± 0.10	0.35
FISH Ra 2	May 14 2014	58.20	-166.12	6.39 ± 0.56	6.38 ± 0.32	1.00
FISH Ra 3	May 15 2014	63.52	-168.40	6.79 ± 0.58	11.83 ± 0.56	1.74
8	May 16 2014	65.72	-168.84	5.07 ± 0.43	4.49 ± 0.22	0.89
9	May 17 2014	67.67	-166.94	7.05 ± 0.61	6.69 ± 0.32	0.95
23	May 19 2014	70.62	-165.20	4.68 ± 0.41	7.38 ± 0.35	1.58
27	May 19 2014	70.27	-163.87	5.81 ± 0.50	12.01 ± 0.57	2.07
29	May 20 2014	70.25	-163.24	5.82 ± 0.68	14.42 ± 0.87	2.48
32	May 22 2014	70.66	-164.13	7.84 ± 0.67	12.81 ± 0.60	1.63
33	May 22 2014	70.83	-165.33	4.94 ± 0.42	7.45 ± 0.35	1.51
35	May 23 2015	70.91	-164.99	4.88 ± 0.42	9.54 ± 0.45	1.95
36	May 23 2014	71.05	-164.99	5.14 ± 0.44	10.57 ± 0.50	2.05
38	May 23 2014	71.41	-164.43	5.20 ± 0.45	9.97 ± 0.47	1.92
40	May 23 2014	71.53	-164.24	4.77 ± 0.57	9.47 ± 0.66	1.99
46	May 24 2014	72.02	-166.06	8.02 ± 0.69	18.59 ± 0.88	2.32
49	May 24 2014	72.36	-166.28	5.74 ± 0.49	13.84 ± 0.66	2.41
51	May 25 2014	72.56	-166.41	6.53 ± 0.56	15.07 ± 0.71	2.31
53	May 25 2014	72.74	-166.72	5.49 ± 0.47	11.98 ± 0.57	2.18
56	May 26 2014	72.80	-167.78	5.81 ± 0.50	12.25 ± 0.58	2.11
59	May 26 2014	72.44	-168.25	5.44 ± 0.47	12.31 ± 0.58	2.26
64	May 27 2014	72.16	-166.61	7.07 ± 0.61	16.28 ± 0.77	2.30
68	May 27 2014	72.09	-167.36	8.88 ± 0.77	21.01 ± 1.00	2.37
70	May 28 2014	72.07	-163.55	6.86 ± 0.59	17.39 ± 0.83	2.54
75	May 29 2014	72.27	-162.44	8.98 ± 0.78	22.24 ± 1.06	2.48
77	May 29 2014	72.59	-162.82	9.20 ± 0.80	17.86 ± 0.85	1.94
79	May 29 2014	72.85	-163.12	7.28 ± 0.63	18.12 ± 0.86	2.49
81	May 30 2014	73.08	-162.77	7.44 ± 0.65	8.36 ± 0.39	1.12
96	Jun 02 2014	72.55	-165.76	8.57 ± 0.74	19.89 ± 0.95	2.32
99*	Jun 02 2014	71.93	-166.35	8.78 ± 0.77	18.05 ± 0.87	2.06
99	Jun 02 2014	71.93	-166.35	8.94 ± 0.70	18.30 ± 0.81	2.05
104	Jun 04 2014	71.59	-166.38	8.70 ± 0.75	17.43 ± 0.83	2.00
106	Jun 05 2014	71.68	-165.98	8.93 ± 0.77	18.87 ± 0.90	2.11
107	Jun 06 2014	71.68	-165.78	8.70 ± 0.75	18.58 ± 0.88	2.14
112	Jun 07 2014	71.15	-165.77	10.90 ± 0.94	19.23 ± 0.91	1.76
124	Jun 08 2014	70.34	-164.29	7.68 ± 0.66	16.87 ± 0.80	2.20
127	Jun 08 2014	70.09	-163.36	8.85 ± 0.77	24.42 ± 1.16	2.76
133	Jun 09 2014	69.96	-165.47	7.79 ± 0.67	17.19 ± 0.82	2.21
137	Jun 09 2014	69.95	-167.00	5.84 ± 0.50	11.45 ± 0.54	1.96

142	Jun 09 2014	69.85	-168.68	7.77	±	0.67	12.22	±	0.58	1.57
143	Jun 10 2014	69.94	-168.93	8.90	±	0.77	14.53	±	0.69	1.63
146	Jun 10 2014	69.94	-167.78	8.62	±	0.74	13.79	±	0.65	1.60
148	Jun 10 2014	70.08	-167.06	8.98	±	0.78	17.46	±	0.83	1.94
152	Jun 11 2014	70.69	-165.90	8.02	±	0.69	10.51	±	0.50	1.31
156	Jun 11 2014	70.70	-167.20	9.41	±	0.81	15.58	±	0.74	1.65
160	Jun 11 2014	70.71	-168.51	8.59	±	0.74	13.19	±	0.63	1.54
162	Jun 12 2014	70.94	-168.78	7.53	±	0.65	15.16	±	0.72	2.01
168	Jun 12 2014	71.76	-168.73	6.11	±	0.53	12.43	±	0.59	2.03
173	Jun 13 2014	72.29	-168.84	8.72	±	0.75	19.00	±	0.90	2.18
175	Jun 13 2014	72.56	-168.78	10.28	±	0.89	22.20	±	1.06	2.16
178*	Jun 13 2014	72.36	-167.82	10.16	±	0.88	20.85	±	0.99	2.05
178	Jun 13 2014	72.36	-167.82	10.09	±	0.87	20.46	±	0.97	2.03
182	Jun 14 2014	72.08	-166.28	8.62	±	0.75	19.16	±	0.91	2.22
188	Jun 14 2014	71.67	-164.02	8.41	±	0.73	18.59	±	0.88	2.21
192	Jun 15 2014	71.57	-165.47	9.06	±	0.78	18.83	±	0.89	2.08
196*	Jun 15 2014	71.61	-166.05	10.05	±	0.87	16.87	±	0.80	1.68
196	Jun 15 2014	71.61	-166.05	9.23	±	0.80	15.82	±	0.75	1.71
209*	Jun 18 2014	71.62	-165.55	9.08	±	0.79	18.13	±	0.86	2.00
209	Jun 18 2014	71.62	-165.55	9.12	±	0.73	18.21	±	0.89	2.00
215	Jun 18 2014	71.40	-167.31	9.03	±	0.78	13.21	±	0.63	1.46
221	Jun 19 2014	71.25	-167.96	8.31	±	0.72	16.03	±	0.76	1.93
223	Jun 19 2014	70.98	-167.19	10.45	±	0.91	21.43	±	1.02	2.05

*Water sample collected from the CTD in order to compare with the sample water collected from the intake line.

Table S 3.4: Leached fiber blanks and detector backgrounds. The ash residue of some sample fibers was measured after leaching ("leached-ashed fibers") to evaluate the completeness of the leaching procedure. The last column corresponds to the Ra activity in leached-ashed fiber relative to the original sample (%).

Isotope	Peak	Background (cpm)	blank fibers (cpm)	leached-ashed fibers (cpm)	Residual activity in the leached-ashed fiber (%)
^{226}Ra	^{214}Pb	0.01 ± 0.005	0.03 ± 0.007	0.08 ± 0.02	5.6 ± 0.3
	^{214}Bi	0.01 ± 0.004	0.01 ± 0.007	0.04 ± 0.03	3.6 ± 0.5
^{228}Ra	^{228}Ac	0.009 ± 0.003	0.02 ± 0.005	0.03 ± 0.01	6.6 ± 1.4

Table S 3.5: The variance and coefficients of the principal components.

	Eigenvalue	Percentage of Variance	Cumulative		Coefficients of PC1	Coefficients of PC2	Coefficients of PC3
1	6.45	49.58%	49.58%	Cd	0.37	0.10	-0.10
2	2.57	19.76%	69.34%	Fe	0.20	-0.32	0.31
3	1.49	11.49%	80.83%	Ni	0.28	0.24	0.30
4	0.76	5.83%	86.66%	Cu	0.06	0.35	0.31
5	0.72	5.50%	92.16%	Zn	0.28	0.28	0.03
6	0.38	2.94%	95.10%	Pb	0.13	0.36	0.44
7	0.28	2.13%	97.23%	Mn	0.31	-0.27	-0.08
8	0.14	1.08%	98.31%	Co	0.26	-0.38	0.25
9	0.13	0.99%	99.30%	NH_4	0.25	-0.40	-0.15
10	0.06	0.47%	99.77%	PO_4	0.37	0.08	-0.23
11	0.02	0.14%	99.92%	Si	0.35	0.14	-0.26
12	0.01	0.05%	99.96%	NO_3-	0.31	0.23	-0.36
13	0.005	0.04%	100%	AR	0.23	-0.21	0.41

4 Unprecedented Fe delivery by the River Congo to the South Atlantic Gyre

Lúcia H. Vieira[1], Stephan Krisch[1], Mark J. Hopwood[1], Aaron J. Beck[1], Jan Scholten[2], Volker Liebetrau[1] and Eric P. Achterberg[1]

Submitted to *Nature Geoscience*

1 Marine Biogeochemistry Division, GEOMAR Helmholtz Centre for Ocean Research Kiel, Kiel 24148, Germany

2 Institute of Geosciences, Christian-Albrecht University Kiel, Kiel 24118, Germany

Abstract

Rivers are a major supplier of particulate and dissolved material to the ocean, but their role as a source of bio-essential dissolved iron (dFe) is thought to be limited due to rapid, efficient Fe removal during estuarine mixing. Here, we use trace element and radium isotope data to show that the influence of the River Congo on surface ocean Fe concentrations can be traced over 1000 km from the Congo outflow. Due to an unusual combination of high Fe input into the Congo-shelf-zone and rapid lateral transport into the South Atlantic, the Congo plume constitutes an exceptionally large offshore dFe flux of $5.8 \pm 2.1 \times 10^{8}$ mol yr^{-1}. This corresponds to 40% of the dFe atmospheric input into the entire South Atlantic Ocean and makes a higher contribution to marine dFe availability than any other river system. Congo dFe outflow is therefore likely responsible for the relief of Fe-limitation of phytoplankton growth observed across this oligotrophic region of the South Atlantic Gyre.

4.1 Introduction

Elevated dissolved trace element (dTE; defined by < 0.2 μm filtration) concentrations in coastal regions are derived from riverine inputs (Buck et al., 2007; Figuères et al., 1978), benthic pore-water and re-suspended sediment supply (Elrod et al., 2004), atmospheric deposition (Jickells, 1995) and submarine groundwater discharge (SGD) (Windom et al., 2006). Whilst riverine fluxes of dTEs into the ocean are significant, estuarine processes remove a high, but variable, fraction of riverine dFe. Typically 90-99% of dFe is removed at low salinity in estuaries due to the rapid aggregation of Fe and organic species with increasing ionic strength (Boyle et al., 1977), with further removal by biological uptake and scavenging in estuarine and shelf regions (Birchill et al., 2019). Whilst riverine Fe concentrations are 3-5 orders of magnitude greater than those in seawater (Gaillardet et al., 2013), rivers provide only ~3% of the new Fe delivered annually to the oceans (Raiswell and Canfield, 2012). Consequently, there is typically limited potential for river-derived Fe to directly affect productivity in offshore ocean regions where Fe often limits, or co-limits, primary production (Browning et al., 2017).

The Congo is the second largest river on Earth by discharge volume (Hopkins et al., 2013), and is the only major river to discharge into an eastern boundary ocean region with a narrow shelf (Stramma and England, 1999), producing a unique near-equatorial river plume (Hopkins et al., 2013). Although the Congo is an important source of freshwater to the SE Atlantic (Eisma and van Bennekom, 1978), little is known about associated TE fluxes and their influence on SE Atlantic productivity. In November-December 2015, the GEOTRACES cruise GA08 proceeded along the SW African shelf to determine the lateral extent of

chemical enrichment from the Congo plume. Here we use a conservative terrigenous tracer, the naturally occurring radium isotopes (^{228}Ra and ^{224}Ra), in combination with TE distributions to derive TE fluxes from the Congo plume into the South Atlantic. Radium isotopes are produced by sedimentary thorium decay, released from river plumes and shelf sediments, and then transported to the open ocean by turbulent mixing and advection. In seawater, only mixing and decay processes control the Ra distribution.

4.2 Methods

4.2.1 Sample collection and analysis

Surface seawater samples (3 m) for Ra isotopes and dissolved Fe (dFe) analyses were collected onboard R/V Meteor during the GEOTRACES GA08 cruise in the Southern Atlantic between 22 November and 27 December 2015 (Fig. 4.1).

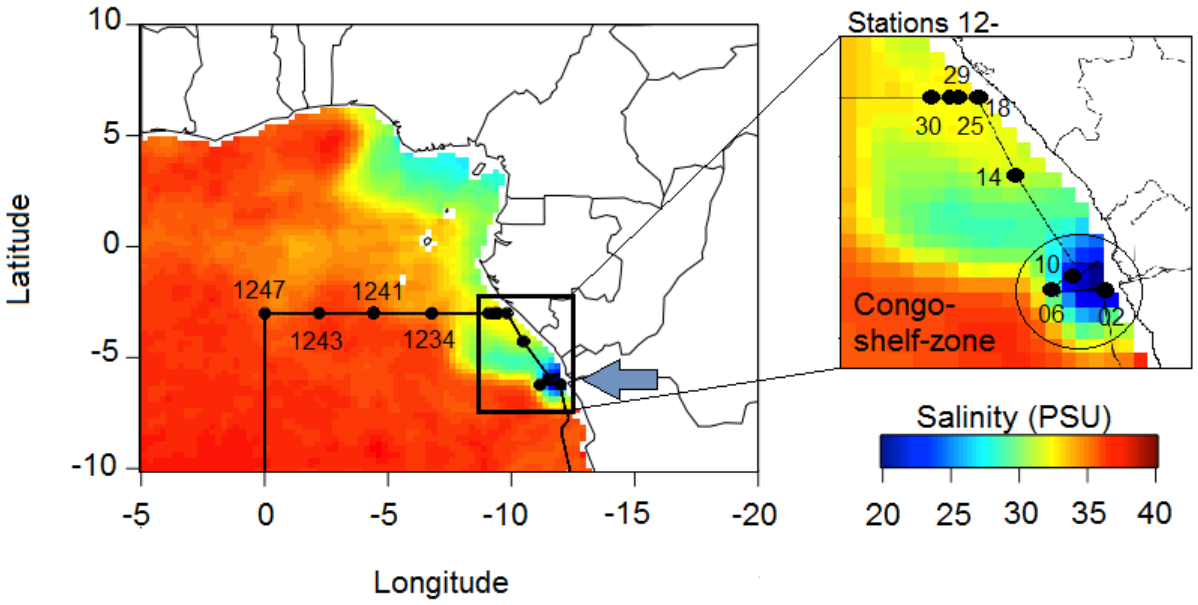

Figure 4.1: Satellite-derived surface seawater salinity (from 25th December 2015 to 1st January 2016) during GEOTRACES cruise GA08 with the ^{228}Ra stations sampled along the Congo River plume. Arrow indicates the Congo River mouth. Inset provides a detailed view of stations along the coastal transect, and circled stations represent the Congo-shelf-zone (see text). Offshore plume is shown in detail in the inset and extends along the 3°S transect (1218-1247) (data from https://opendap.jpl.nasa.gov/).

4.2.1.1 Radium isotopes

Surface samples (3 m) were collected by pumping ca. 250 L of seawater into a barrel. Seawater was then filtered through MnO_2-impregnated acrylic fiber (Mn-fibers) at a flow rate <1 L min^{-1} to quantitatively extract Ra isotopes. Next, the Mn-fibers were rinsed and air (partially) dried. Activities of ^{224}Ra were determined using four Ra delayed coincidence counters (RaDeCC) (Moore and Arnold, 1996). The fibers were counted onboard and then recounted six weeks later in order to determine ^{224}Ra in excess of ^{228}Th (^{224}Ra $_{ex}$). RaDeCC counters were calibrated with International Atomic Energy Agency (IAEA) reference solutions (Scholten et al., 2010).

After measurement of ^{224}Ra, fibers were ashed and subsequently leached in order to determine the activities of long-lived Ra (^{228}Ra and ^{226}Ra) isotopes using a high-purity, well-type germanium (HPGe) gamma spectrometer. The fibers were ashed twice at 600° C for 16 h, leached in 3.5 M Hydroxylamine and concentrated HCl followed by co-precipitation with $BaSO_4$. The precipitate was then sealed in 1 mL vials and analyzed after at least 3 weeks to allow ^{222}Rn to reach equilibrium with its parent ^{226}Ra. Radium-226 activities were determined using the ^{214}Pb peak (352 keV) and the ^{214}Bi peak (609 keV). ^{228}Ra activities were determined using the ^{228}Ac peaks (338 keV and 911 keV). Sample counting efficiencies were determined by spiking Mn-fibers with known amounts of ^{228}Ra and ^{226}Ra, and processing similar to samples. Sample activities were corrected for detector background counts and fiber blank activities. Ra reference solution was provided by the IAEA had a reported activity accuracy of 6% for ^{226}Ra and 5% for ^{228}Ra. Measured precisions for ^{228}Ra and ^{226}Ra was ~ 5% (1-σ). These levels of accuracy and precision lead to an uncertainty on the sample activities of <10%.

4.2.1.2 Trace elements

Surface trace element sampling was conducted using a tow fish deployed alongside the ship at about 3 – 4 m depth. Seawater was collected in a shipboard clean laboratory container and stored in acid-cleaned low-density polyethylene (LDPE) 125 mL bottles. Samples for dissolved trace elements (dTE) were collected using a cartridge filter (0.8/0.2 µm, Acropak 500 – PALL). All seawater samples were acidified onboard with ultra-clean HCl (UpA grade, Romil) to pH 1.9. Freshwater River Congo samples were collected at three time-points (April, July, and October 2017), retained for analysis of dFe after syringe filtration (0.20 µm,

Millipore), and acidified as per seawater. Samples in the concentration range below 20 nM dFe/dMn were measured following Rapp et al. (2017). Samples with higher concentrations were analyzed by inductively coupled plasma-mass spectrometry (ICP-MS) after dilution with ultra-pure 1 M HNO_3 (Romil SpA grade, sub-boiled), and calibration by standard addition. The accuracy and precision of measurements were evaluated by analysis of SAFe S, SAFe D2, and CASS6 reference seawater (table S 4.2).

4.2.2 Radium-228 inventory and TE flux estimates

4.2.2.1 The Congo-shelf-zone

The ^{228}Ra Congo-shelf-endmember was determined by the average ^{228}Ra activities (14.5 ± 3.5 dpm 100 L^{-1}; Table 4.1) of samples with salinity less than 32 PSU, which best reflect river influenced waters in the Congo-shelf-zone. We estimated the ^{228}Ra inventory (I_{228}) in the surface water of our Congo-shelf-endmember as 3.7 ± 0.4 x 10^9 atoms m^{-2} by considering a plume thickness of 5 m in the Congo-shelf-zone (see Figure S 4.1 - supplementary material) and assuming a uniform ^{228}Ra distribution within this plume thickness. Radium-228 flux from the Congo-shelf-zone was determined using the Ra inventory of our Congo-shelf-endmember and the residence time of the waters in the Congo-shelf-zone (Flux ^{228}Ra = inventory / residence time). A residence time of 3 days (Eisma and van Bennekom, 1978) is consistent with the Congo discharge volume required to produce the observed salinity within the plume region (Bowden, 1980). As our Congo-shelf-endmember is ~100 km away from the river mouth, the area of our sampling region was considered as a square of 100 x 100 km (whenever referring to the Congo-shelf-zone). Taking the Ra at the lowest measured salinities (S<32) as representative of the entire Congo river mouth zone probably represents a

lower estimate of the true inventory because activities are likely higher at mid-salinities nearer to the river mouth and shoreline (Fig. S 4.2). Note that the regional satellite-derived salinity in Figure 4.1 does not correspond directly with measured salinity for the Ra samples in the Congo-shelf-zone (~30 PSU).

Because dFe, dMn, and dCo in our study appear to have a source similar to Ra, the ^{228}Ra flux was used to determine the fluxes of these TE in the Congo-shelf-zone, by multiplying the ^{228}Ra flux in this region by the averaged ratio between dTE concentrations (Table 4.1) observed in samples with lowest measured salinity (i.e., <29 PSU; TE Congo-shelf-endmember) and the ^{228}Ra Congo-shelf-endmember (dTE/^{228}Ra). Samples with salinity <29 represent intermediate TE endmembers that reflect mixing between the river and seawater (S>33 PSU). Ra and TE sampling locations do not coincide exactly, as unlike for Ra samples, TE samples were collected using a tow fish, i.e., while the R/V Metor was sailing.

4.2.2.2 The off-shelf transect (3°S)

The residence time of 7 ± 2 days at the start of the off-shelf transect (3°S; between st.1218 and the station at the shelf-break st.1229) was determined using the ^{224}Ra/^{228}Ra ratios as per Moore, (2004). We used the ^{224}Ra/^{228}Ra ratio at st.1218 as our initial ratio. ^{224}Ra was detectable over the next 40 km at the next 2 stations along this transect (st.1229). Once Ra isotopes are released into the water column, their activities decrease with increasing distance from the source as a result of dilution and radioactive decay. Both isotopes are affected by dilution, but radioactive decay is negligible for ^{228}Ra ($T_{1/2}$ = 5.8 yr) over short distances, so changes in the ^{224}Ra/^{228}Ra ratio reflect the time elapsed since the water was isolated from the source. Strong density stratification isolates the freshwater plume from bottom waters, so

surface waters are unlikely to be affected by additional Ra input. Therefore, the residence time (T) can be derived as:

$$T = \ln\left[\frac{(^{224}Ra/^{228}Ra)_i}{(^{224}Ra/^{228}Ra)_o}\right] \times \frac{1}{\lambda_{224}} \qquad \text{(Equation 4.1)}$$

where $(^{224}Ra/^{228}Ra)_i$ is the initial ratio at st.1218, $(^{224}Ra/^{228}Ra)_o$ is the ratio observed away from the source (offshore) at station 1229, and λ_{224} is the decay constant of ^{224}Ra.

Previous studies have combined the ^{228}Ra flux with water column dissolved trace elements to ^{228}Ra ratios (TE/ ^{228}Ra) in order to quantify the shelf-ocean input rates (Charette et al., 2016; Sanial et al., 2018). We propose the use of this approach to estimate the fluxes of TE (dFe, dMn, and dCo) from the Congo River plume to the Atlantic Ocean following Charette et al. (2016).

$$\text{Flux dTE} = \text{Flux Ra} \times \left[\frac{dTE_{shelf} - dTE_{offshelf}}{Ra_{shelf} - Ra_{offshelf}}\right] \qquad \text{(Equation 4.2)}$$

where $dTE_{\text{-shelf}}$ and $^{228}Ra_{\text{-shelf}}$ are the average concentrations of the dTE and ^{228}Ra activities in surface waters over the shelf (between st.1218 and the station at the shelf-break st.1229), respectively; and $dTE_{\text{-off-shelf}}$ and $^{228}Ra_{\text{-off-shelf}}$ are the dTE concentration and ^{228}Ra activities in surface waters of the open ocean station (st. 1234). Note that a diffusion-dominated system between the stations 1218 and 1234 was observed as indicated by a linear gradient in both dFe and ^{228}Ra distributions. The dTE/Ra ratios are presented in Table 4.1.

4.3 Results and Discussion

4.3.1 Trace element and Radium distributions in the Congo-shelf-zone and offshore plume

On the shelf where Congo waters first encounter the Atlantic Ocean, hereafter the "Congo-shelf-zone", the mean dFe concentrations was ~15% of the Congo River concentration. About 50-85% of river-derived dFe is removed from solution at low salinities (0-5) in the Congo estuary, with the greatest removal in large size fractions (Figuères et al., 1978). Mean dFe concentration in the River Congo freshwater was 7380 ± 3150 nM, similar to previous measurements (~9000 nM) (Figuères et al., 1978). Extrapolating the linear regression line of dFe vs. salinity in the Congo-shelf-zone (Fig. 4.2A) to zero salinity indicates an effective zero-salinity-endmember concentration of 3480 ± 550 nM (R^2 = 0.75), indicating that only ~50% of dFe is removed, consistent with prior work (Figuères et al., 1978), but yet limited removal compared to other river systems (90-99%) (Figuères et al., 1978; Boyle et al., 1977). Slow removal of Fe in some estuaries (Powell and Wilson-Finelli, 2003) has been attributed to stabilization of the dFe pool by organic material, making the dFe pool resistant to flocculation (Krachler et al., 2005). Alternatively, sources of Fe other than river-water may simply offset the loss from estuarine mixing. Indeed, similar ^{228}Ra and other TE enrichments over the Congo-shelf-zone (Fig. 4.2B; Fig. S 4.3) suggest they have a common source, most likely from shelf-sediments (Elrod et al., 2004; Elderfield and Hepworth, 1975; Lohan and Bruland, 2008) or submarine groundwater discharge (SGD) (Windom, et al., 2006) indicating that the apparently low removal primarily reflects additional sources of dFe rather than stabilization of the river dFe.

Covariation of dissolved manganese (dMn) and cobalt (dCo) with salinity indicate an effective-zero-salinity-endmember higher than measured in the river (Table 4.1), indicating non-conservative inputs relative to simple mixing of river and seawater (Fig. S 4.3). An additional TE source in the Congo-shelf-zone is also evident in the lower Fe:Mn (6.3 ± 6.0) and Fe:Co (525 ± 490) ratios compared to those in river water (Fe:Mn = 71.2 ± 37.5; Fe:Co = 4290 ± 2345).

The enhanced signatures of ^{228}Ra and TEs in the Congo River plume can be traced off-shelf at 3°S over 1000 km from the Congo River mouth (Fig. 4.2C). Benthic input supplies ^{228}Ra and TEs between the river mouth and Congo-shelf-zone (here considered 10000 km^2 plume area; Methods), but the shallow Congo River plume is isolated from the seafloor off-shelf (Hopkins et al., 2013). Indeed, a conservative ^{228}Ra mixing behavior (Fig 4.2B) indicates no additional ^{228}Ra inputs beyond the Congo-shelf-zone, and similarity between the ^{228}Ra and TE distributions with salinity (Fig. 4.2C-D, Fig. S 4.3) indicates that the plume forms the only major source of Ra and TEs in this region. Salinity increased offshore along the 3°S transect, with occasional fresher 'pockets' coincident with elevated ^{228}Ra and TE concentrations (e.g., at 1100 km; Fig. 4.2C-D). These freshwater 'pockets' likely come from filaments, meanders, or eddies originating near the Congo River mouth (Vangriesheim et al., 2009; Palma and Matano, 2017), which can transport elevated Ra and TE concentrations. The linear ^{228}Ra gradient with distance beyond 360 km offshore (R^2 0.91) (Fig. S 4.4) indicate that the ^{228}Ra distribution is controlled by eddy diffusion near the shelf-break (Moore, 2000 a). Beyond the shelf-break, there appears a break in the slope of ^{228}Ra versus distance, likely caused by offshore advection.

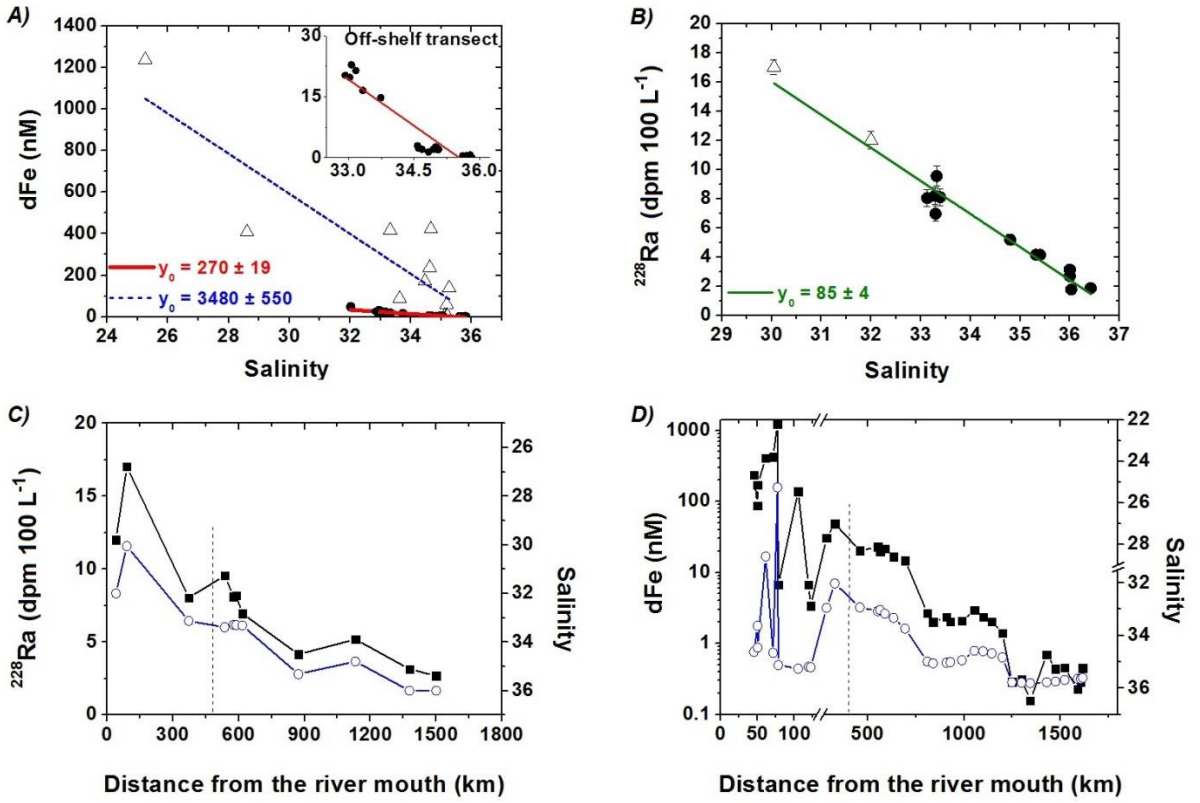

Figure 4.2: (A) and (B): Mixing diagram between River and open ocean waters from the Congo-shelf-zone to the end of the 3°S transect (st.1202-1247) for dFe and ^{228}Ra concentrations, respectively. Open triangles represent the samples collected in the Congo-shelf-zone and circles represent the samples in the off-shelf 3°S transect. Dashed blue line in A represents the regression line for the Congo-shelf-zone, and the red line represents linear regression for the off-shelf-transect. Intercepts are represented as y_0 and considered as the effective-zero-salinity-endmembers. Inset in A is an expanded version of the off-shelf-transect. The regression line for ^{228}Ra (green line in B) includes all data. (C) and (D): ^{228}Ra, dFe (note log scale) (solid black squares), and inverse salinity distributions (open circles) in plume surface waters from the Congo-shelf-zone to the end of the 3°S transect (st.1202-1247). Dashed vertical lines in C and D represent the beginning of the off-shelf transect at 3°S.

The effective-zero-salinity-endmember concentration for Fe was 90% lower for the off-shelf samples compared with the Congo-shelf-zone samples (270 vs. 3480 nM; Fig. 4.2A), indicating substantial removal of Fe along the Congo plume at distances <400 km from the river mouth. Nevertheless, elevated dFe is still observed at the start of the off-shelf transect (~25 nM; Fig. 4.3), despite major Fe removal in the initial outflow of the Congo plume.

Dissolved-Fe concentrations in other shelf systems decline sharply at the shelf-break to less than 1 nM (Wu and Luther, 1996; Rijkenberg et al., 2012) and thus the influence of major rivers (e.g. the Amazon) on surface ocean Fe concentrations is limited (Rijkenberg et al., 2014). Unlike other major river systems, however, the Congo River plume carries elevated dFe concentrations (20-30 nM) up to 600 km from the river mouth (Fig. 4.3). Dissolved-Fe concentrations of ~15 nM were observed up to 100 km beyond the shelf-break and remained >2 nM for 500 km beyond the shelf-break. These features indicate a sustained Fe flux into the South Atlantic Gyre where Fe limitation or co-limitation of primary production has been observed (Browning et al., 2017).

4.3.2 Radium-228 and TE fluxes within the Congo-shelf-zone

Ra isotopes were used to quantify the TE fluxes for (i) the Congo-shelf-zone, where additional TE and Ra inputs created an intermediate endmember that mixed approximately conservatively along the Congo plume (Fig. 4.2A-B), and (ii) the 3°S off-shelf, where there were no additional TE and Ra inputs.

The highest ^{228}Ra activities (^{224}Ra = 8.15 dpm 100 L^{-1}; ^{228}Ra = 17.2 dpm 100 L^{-1}) was found at the lowest observed salinity (S = 30, 100 km from the river mouth; Fig. 4.2B). At salinity 30, all surface-associated Ra from river particles is desorbed (Key et al., 1985; Elsinger and Moore, 1984; Li et al., 1977) (Fig. S 4.2); therefore, the ^{228}Ra Congo-shelf-endmember (Methods) includes all dissolved ^{228}Ra derived from: (i) desorption from river-borne particles; (ii) river dissolved phase; and (iii) shelf sediments near the river mouth. The water residence time in the Congo-shelf-zone is approximately 3 days (Eisma and van Bennekom, 1978; Bowden, 1980). Assuming steady state and negligible loss by decay, the residence time

and ^{228}Ra inventory in the Congo-shelf-zone (Methods), indicate a ^{228}Ra flux to this region of 3.9 ± 0.4 x 10^{11} atoms m^{-2} yr^{-1}, or ~3.9 ± 0.4 x 10^{21} atoms yr^{-1} when scaled to the approximate 10000 km^2 plume area.

Conservative mixing between the Congo-shelf-endmember and offshore waters (Fig. 4.2B) gives a ^{228}Ra effective-zero-salinity-endmember activity of 85 ± 4 dpm 100 L^{-1}. Together with the river discharge (1.3 x 10^{12} m^3 yr^{-1}) (Milliman and Farnsworth, 2011), this suggests a fluvial Ra flux of 4.8 ± 0.3 x 10^{21} atoms yr^{-1}, which is similar to the ^{228}Ra flux estimated for the Congo-shelf-zone (3.9 ± 0.4 x 10^{21} atoms yr^{-1}). If this Ra flux derives solely from the river, the effective-zero-salinity-endmember and actual river activities must be similar.

Radium-228 data is not available for the Congo River, but global rivers activities are generally less than 20 dpm 100 L^{-1} (McKee, 2008) (Fig. S 4.2). Assuming the Congo is similar to other major rivers (<20 dpm 100 L^{-1}), the average Congo river discharge (Milliman and Farnsworth, 2011) would supply maximum 2.6 x 10^{14} dpm yr^{-1}, or ~ 10 x 10^{20} atoms yr^{-1} of dissolved ^{228}Ra. Desorption of surface-bound Ra from river-borne particles generally supplies <2 dpm g^{-1} (Moore and Shaw, 2008). The Congo suspended sediment load is 43 Mt yr^{-1} (Milliman and Farnsworth, 2011), so desorption can supply no more than ~3.75 x 10^{20} atoms yr^{-1}, or an equivalent dissolved ^{228}Ra activity of 6 dpm 100 L^{-1}. Thus, the supply of ^{228}Ra from the Congo River itself is approximately 1.4 x 10^{21} atoms yr^{-1}, or only ~30-35% of the flux into the Congo-shelf-zone. If the remainder was supplied by benthic diffusion, it would represent a flux on the order of 400 x 10^9 atoms m^{-2} yr^{-1}, nearly four-fold higher than the maximum reported globally (Moore et al., 2008). This suggests that either (i) the dissolved ^{228}Ra activity in the Congo River is exceptionally high compared to other large

rivers (~79 dpm 100 L^{-1}, vs <20 dpm 100 L^{-1} elsewhere); (ii) ^{228}Ra diffusion from shelf sediments in this region is anomalously high compared to other regions globally; or (iii) there is another source of Ra such as submarine groundwater discharge (Moore, 1996; Rodellas et al., 2015).

Radium-228 and TEs have a common source in the estuarine mixing zone up to our Congo-shelf-endmember, and combining the ^{228}Ra flux and concentration ratios of TE:^{228}Ra (Methods) for the Congo-shelf-zone provides dFe flux (dFe-$Flux_{\text{-Congo-shelf}}$) of 5.6 ± 4.2 x 10^5 µmol m^{-2} yr^{-1} (5.6 ± 4.2 x 10^9 mol yr^{-1}), dMn $Flux_{\text{-Congo-shelf}}$ of 4.4 ± 0.7 x 10^8 mol yr^{-1}; and dCo-$Flux_{\text{-Congo-shelf}}$ of 5.3 ± 0.8 x 10^6 mol yr^{-1} (Table 4.1).

4.3.3 Radium-228 and TE off-shelf fluxes along 3° S transect

The shelf width at 3°S is 70 km, giving an offshore ^{228}Ra inventory within this plume cross-section of 2.6 ± 0.2 x 10^{13} atoms m^{-2}. With a residence of 7 ± 2 days (Methods), a ^{228}Ra input from the Congo plume into the open Atlantic Ocean is 1.4 ± 0.4 x 10^{15} atoms m^{-2} yr^{-1}, or assuming a plume thickness of 15 m (Fig. S 4.1), 22 ± 6.2 x 10^{15} atoms yr^{-1} m-$shoreline^{-1}$. Satellite-derived surface salinity at 3°S (Fig. S 4.5) indicates a shoreline plume width of ~300 km, so the total offshore ^{228}Ra flux is 6.2 ± 2.0 x 10^{21} atoms yr^{-1}. Within uncertainties, this flux matches that estimated for the Congo-shelf-zone (3.9 ± 0.4 x 10^{21} atoms yr^{-1}), consistent with the observed conservative mixing behavior of ^{228}Ra in the plume. The flux represents 4% of previous estimates of total annual ^{228}Ra input into the Atlantic Ocean (Moore et al., 2008).

Table 4.1: Radium-228 and trace element fluxes

	Congo River [a]	**Congo-shelf-zone [b]**	**Off-shelf transect (3°S) [b]**
^{228}Ra-Flux (atoms yr^{-1})	4.8 ± 0.4 x 10^{21}	3.9 ± 0.4 x 10^{21}	6.2 ± 2.0 x 10^{21}
dFe-Flux (mol yr^{-1})	9.6 ± 4.1 x 10^{9}	5.6 ± 4.2 x 10^{9}	5.8 ± 2.1 x 10^{8}
dMn-Flux (mol yr^{-1})	1.3 ± 0.4 x 10^{8}	4.4 ± 0.7 x 10^{8}	3.1 ± 1.5 x 10^{8}
dCo-Flux (mol yr^{-1})	2.2 ± 0.8 x 10^{6}	5.3 ± 0.8 x 10^{6}	4.6 ± 1.8 x 10^{6}
dFe/^{228}Ra gradient (pmol atoms^{-1})	-	1.45 ± 1.0	0.09 ± 0.02
dMn/^{228}Ra gradient (pmol atoms^{-1})	-	0.11 ± 0.01	0.05 ± 0.02
dCo/^{228}Ra gradient (fmol atoms^{-1})	-	1.4 ± 0.2	0.7 ± 0.2
Average ^{228}Ra activity (dpm 100 L^{-1})	-	14.5 ± 3.5	8.62 ± 0.86
Average dFe concentration (nM)	7380 ± 3150	920 ± 670	20.9 ± 1.67
Average dMn concentration (nM)	105 ± 30	73 ± 4.0	14.7 ± 4.48
Average dCo concentration (nM)	1.72 ± 0.59	0.88 ± 0.05	0.20 ± 0.03

[a] Trace element (TE) fluxes from the Congo River were determined using the measured TE concentration in the River Congo (Supp. Material. Table S 4.1) and river discharge reported in Milliman and Farnsworth (2011). Radium-228 flux from the Congo River was estimated by extrapolating the regression line to zero salinity (Fig. 4.2B) and multiplying the intercept by the river discharge.

[b] See methods for details on TE and ^{228}Ra concentrations and fluxes in the Congo-shelf-zone and off-shelf transect.

Tracer-estimated fluxes in dynamic cross-shelf regions are complicated by mesoscale features like eddies (Palma and Matano, 2017), which may influence TE and Ra distributions. Nevertheless, our data unambiguously indicate that the Congo plume is a dominant regional source of Fe, Mn, and Co to the South Atlantic Gyre. The similarity between the TE and ^{228}Ra distributions suggests that the fluxes scale proportionally (Charette et al., 2016). Given a Fe:^{228}Ra ratio of 0.09 pmol atoms^{-1}, the off-shelf dFe-Flux from the Congo River plume into the South Atlantic Ocean is 5.8 ± 2.1 x 10^{8} mol yr^{-1} (or 130 ± 45 mol m^{-2} yr^{-1}), which represents approximately 40% of the total dFe atmospheric deposition into the entire South Atlantic Ocean (Duce and Tindale, 1991). The similarity between the dMn and dCo fluxes in the Congo-shelf-zone and in the off-shelf transect (Table 4.1) is

consistent with their conservative behavior along the Congo River plume, likely because of slow Mn and Co oxidation (Sunda and Huntsman, 1988; Moffett and Ho, 1996) and Mn photo-reduction in surface waters (Sunda et al., 1983), which keeps Mn in solution and facilitates its transport to the open ocean.

The enhanced dFe flux from the Congo, relative to other rivers, into the South Atlantic may result from stabilization by organic ligands (Spencer et al., 2012). However, elevated dissolved organic carbon (DOC) concentrations are commonly found in many major river systems (Sholkovitz et al., 1978; Benner and Opsahl, 2001), and dFe removal in the Congo estuary has been explicitly demonstrated (Figuères et al., 1978). Therefore high DOC alone cannot explain the unique dFe distribution observed along the Congo plume. Near-conservative behavior of Fe has however been found in some estuaries with rapid flushing (Mayer, 1982). Indeed, rapid lateral advection appears to enhance TE transport from the Congo compared with other rivers (Fig. 4.3). A similar feature has been reported in the Arctic Ocean, where rapid transport of river-derived terrestrial materials, including carbon and TEs, through the Transpolar Drift leads to nanomolar TE concentrations in the central Arctic (Rijkenberg et al., 2018).

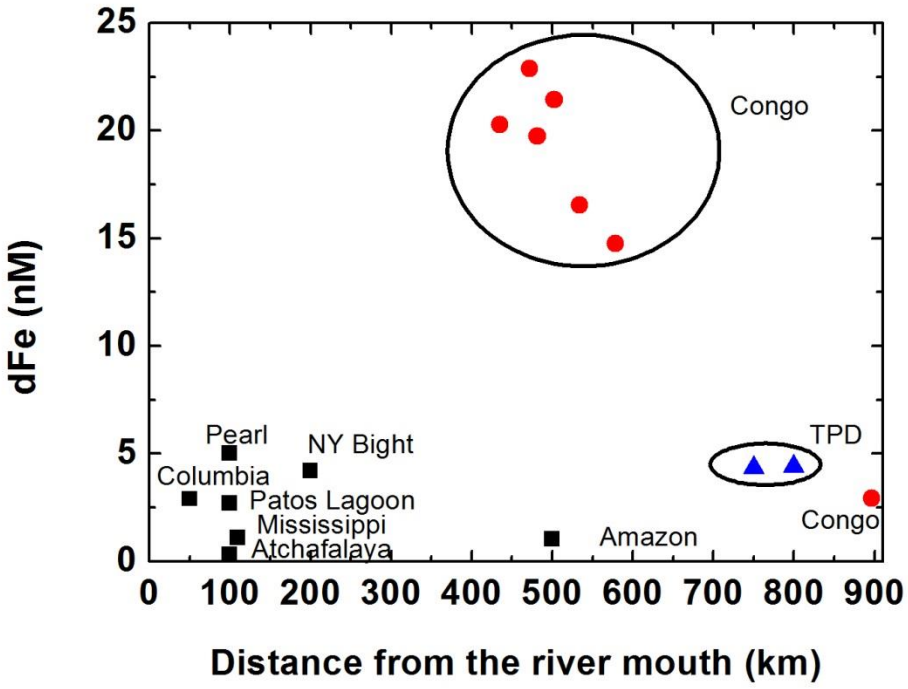

Figure 4.3: Comparison of dFe concentrations vs. distance from the river mouth in other riverine systems (Rijkenberg et al., 2014; Joung and Shiller, 2016; Symes and Kester, 1985; Windom et al., 2006; Zhang et al., 2019; Buck et al., 2007; Rijkenberg et al., 2018). TPD indicates Transpolar Drift, and NY Bight indicates New York Bight.

4.4 Conclusion

The elevated dFe export observed in our study appears to impact phytoplankton in the South Atlantic Gyre. Primary production across extensive regions of the SE Atlantic is proximally limited, or co-limited by the availability of the micronutrients Fe and Co due to limited atmospheric supply beyond the equatorial dust-belt (Browning et al., 2017). However, primary productivity within the offshore region in the current study was instead found to be limited by nitrogen availability (Browning et al., 2017), likely due to the large TE input from the Congo plume. Changes to the spatial orientation of the plume due to shifts in wind patterns or changing freshwater discharge may therefore directly affect TE supply and thus

offshore primary production within the South Atlantic Gyre. Wind speeds are likely to decrease in the Congo region over the coming century (Mcinnes et al., 2011) and future reduction in Atlantic thermohaline circulation is projected to further alter prevailing wind patterns in the intertropical convergence zone (Zhang and Delworth, 2005; Dong and Sutton, 2002). On a decadal timescale, total annual rainfall across the Congo River Basin is not expected to change significantly, but an amplification of the seasonal variability of Congo River runoff is predicted (Hänsler et al., 2013). Whilst the Congo basin is understudied due to geopolitical instability, there is thus clear potential for changes in Congo runoff to affect nutrient availability and marine primary production downstream of the Congo-shelf zone.

Acknowledgments

We thank the captain and crew of the RV Meteor M121 cruise/ GEOTRACES GA08 section and the chief scientist M. Frank for cruise support. We thank S. Koesling, P. Lodeiro and C. Schlosser for their assistance in sample collection on the GA08 expedition and Thomas Browning for the assistance with satellite data. We thank Mr. Bomba Sangolay from the National Institute of Fisheries Research (Instituto Nacional de Investigação Pesqueira, Luanda, Angola) for collection of samples in the Congo River. Lúcia H. Vieira received a doctoral scholarship from the Conselho Nacional de Desenvolvimento Científico e Tecnológico (CNPq - grant number 239548/2013-2), Brazil. The cruise was funded by the Deutsche Forschungsgemeinschaft (DFG).

Author contributions

Lúcia H. Vieira carried out the sampling, analyzed the radium samples, and wrote the first draft of the manuscript. Stephan Krisch and Mark J. Hopwood analyzed GA08 trace element samples. **Lúcia H. Vieira** calculated the trace element fluxes after detailed discussions with Aaron. J. Beck and Mark J. Hopwood. Volker Liebetrau provided analytical assistance for Ra analysis. Eric.P. Achterberg and Jan Scholten designed the GA08 study. All authors gave detailed comments on a later version of the manuscript.

4.5 Supplementary Material

Throughout the SE Atlantic region, Congo River waters are confined to the upper layers, which are decoupled from bottom influence (Yankovsky and Chapman,1997; Hopkins et al., 2013). Proceeding downstream within the Congo River estuary, the bathymetry drops abruptly to 100 m depth due to the presence of a deep canyon at the river mouth which exerts a strong influence on the hydrography of the plume and ensures its detachment from shelf sediments (Jansen et al., 1984). Seasonal variations in wind direction and intensity strongly affect the Congo River plume dispersion (Signorini et al., 1999; Denamiel et al., 2013) as well as the complex circulation within the SE Atlantic Ocean (Stramma and Scott, 1999). Congo River plume dynamics have not been thoroughly investigated and models concerning its off-shelf distribution are not entirely consistent (Denamiel et al., 2013, Vic et al., 2014, Nof et al., 2012; Palma and Matano, 2017). Some studies suggest that the typical orientation is west-north-west, due to a combination of the unique geomorphology of the Congo River estuary, ocean currents and wind patterns (Hopkins et al., 2013; Denamiel et al., 2013; Eisma and van Bennekom, 1978). A more recent study however suggests that the near-equatorial river discharge of the Congo River generates a β-plume and is characterized by a train of eddies propagating westward (Palma and Matano, 2017).

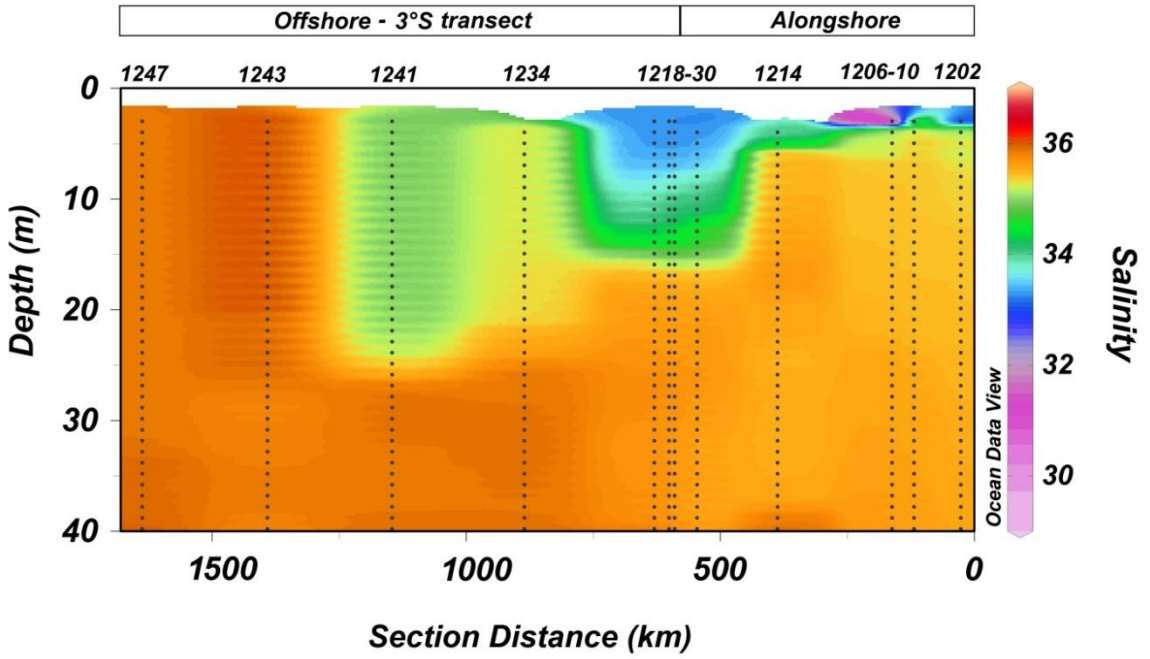

Figure S 4.1: Salinity profiles within the Congo River plume. Numbers on the top represent the stations sampled during this study (see Fig. 4.1 in the main text).

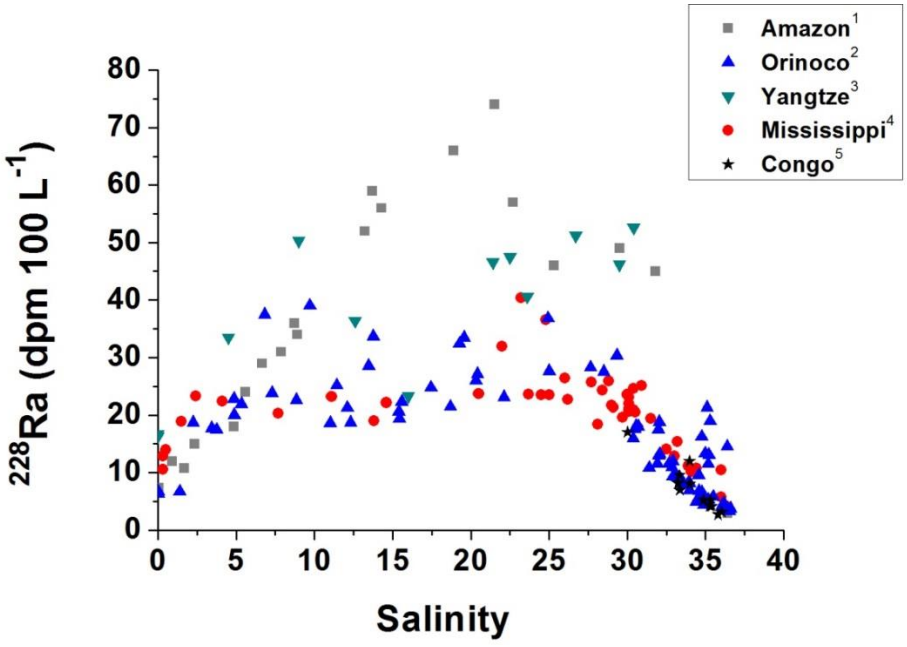

Figure S 4.2: Radium-228 activities across the estuarine salinity gradient in the Amazon[1], Orinoco[2], Yangtze[3], Mississippi[4] estuaries and this study[5]. River endmembers range between 3.2 to 16.3 dpm 100 L^{-1}, with non-conservative input at mid-salinity. [1] Key et al., 1985; [2] Moore and Todd, 1993; [3] Elsinger and Moore, 1984; [4] Krest et al.,1999.

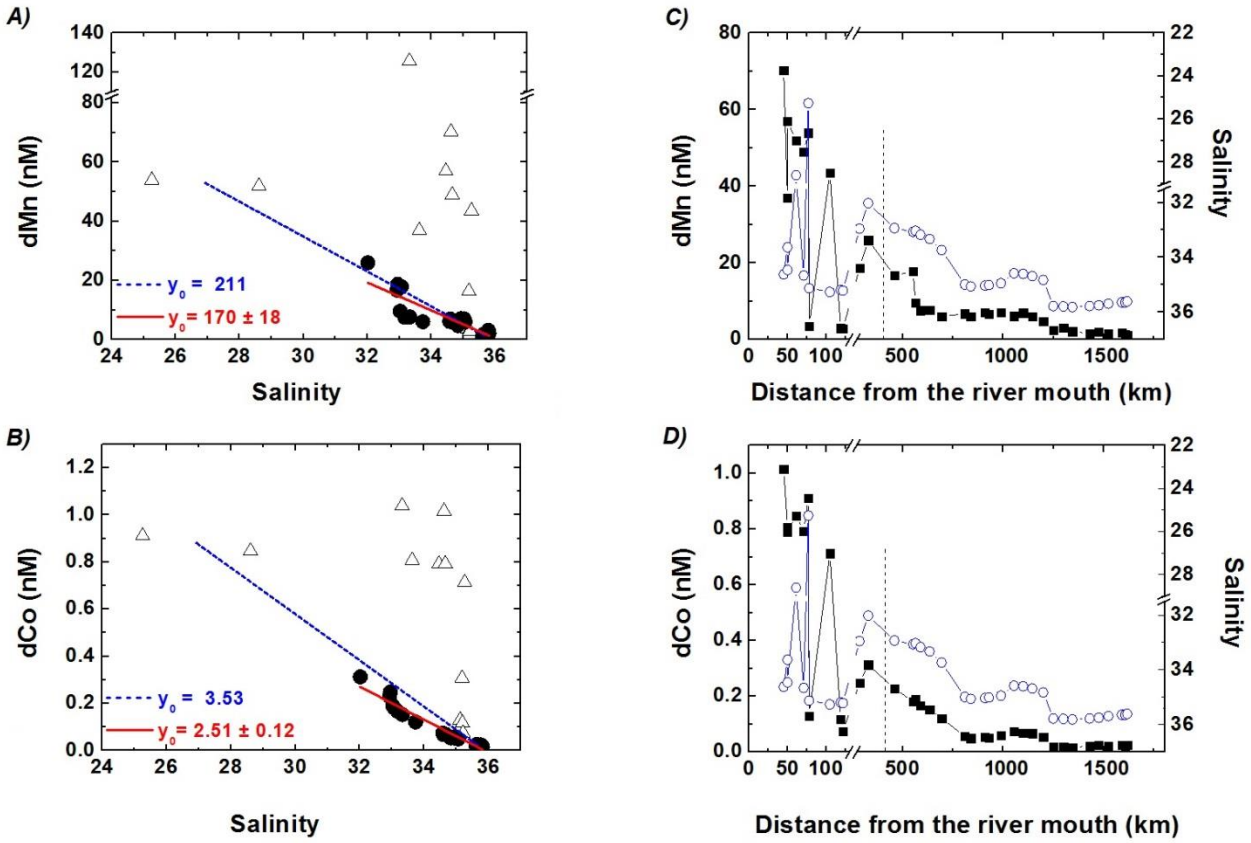

Figure S 4.3: (A) and (B): Mixing diagram between River and open ocean waters from the Congo-shelf-zone to the end of the 3°S transect (st.1202-1247) for dMn and dCo concentrations, respectively. Open triangles represent the samples collected in the Congo-shelf-zones and circles represent the samples in the off-shelf transect. Dashed blue lines represent conservative mixing between freshwater and seawater, which connect two points that represent the lowest salinity (average of the samples with salinity < 29) and highest salinity (average of the samples with salinity > 36) measured during our whole study. Solid red line represents the linear regression for samples in the off-shelf transect (for TE); their intercept values (y_0) area notated. (C) and (D): dMn and dCo concentrations (solid black squares), and inverse salinity distributions (open blue circles) in surface waters from the Congo River-shelf-zone to the end of the 3°S transect (st.1202-1247), respectively. Dashed vertical lines in C and D represent the beginning of the off-shelf transect at 3°S.

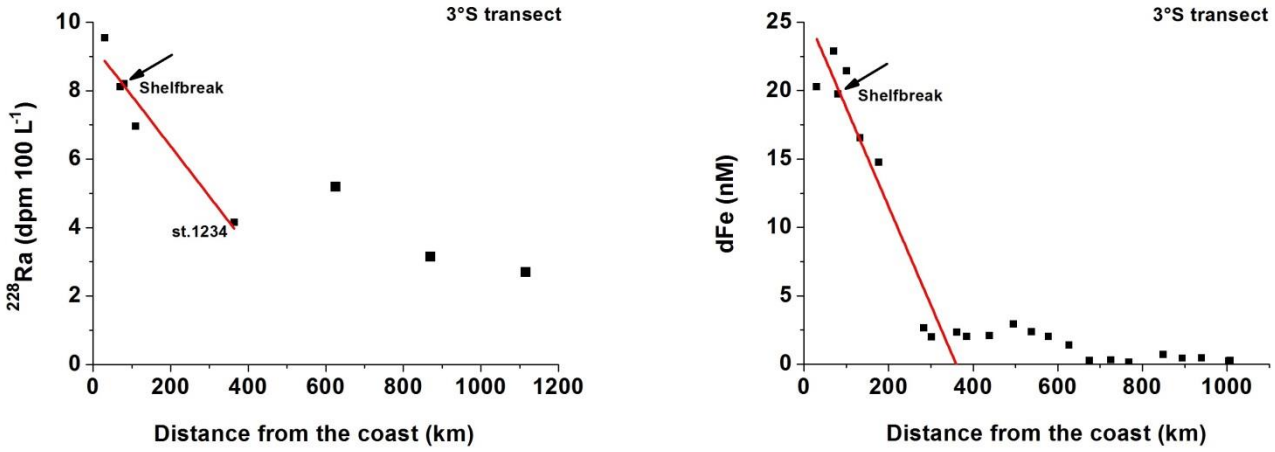

Figure S 4.4: Radium-228 and dFe distributions in surface waters of the 3°S transect. Red lines represent the linear fit in the inner 360 km of the 3°S transect, and arrows represent the location of the shelf-break.

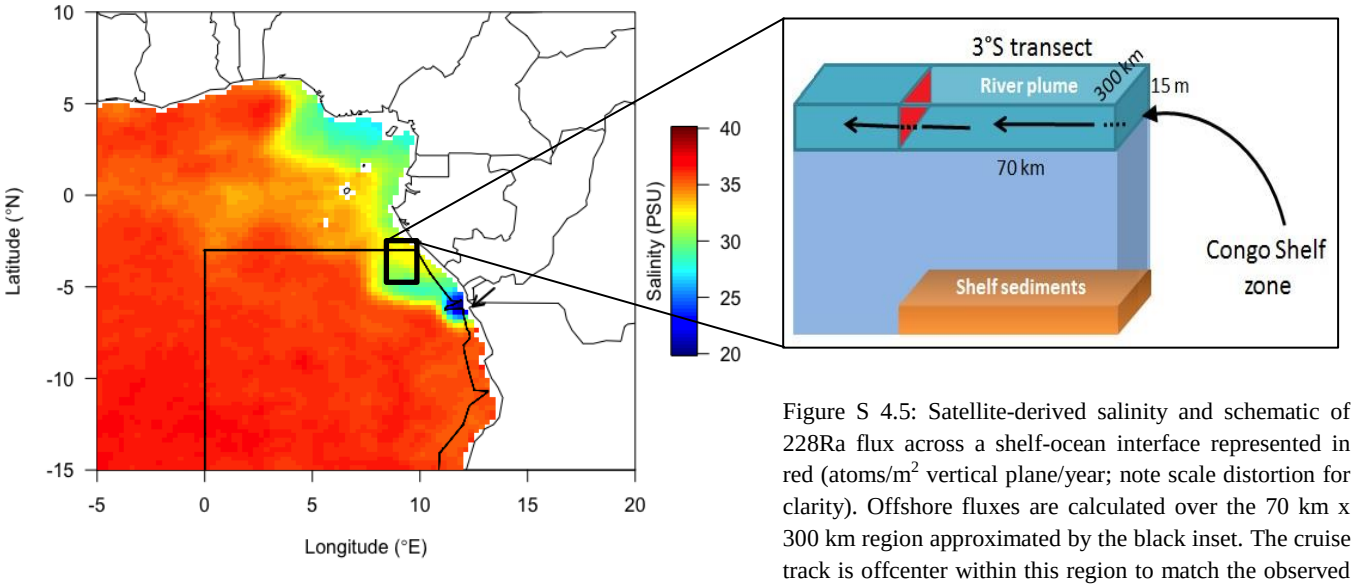

Figure S 4.5: Satellite-derived salinity and schematic of 228Ra flux across a shelf-ocean interface represented in red (atoms/m^2 vertical plane/year; note scale distortion for clarity). Offshore fluxes are calculated over the 70 km x 300 km region approximated by the black inset. The cruise track is offcenter within this region to match the observed plume distribution.

Table S 4.1: Trace element concentrations measured in the Congo River at 6°027 S, 12°603 E.

Collection date	dFe (nM)	dMn (nM)	dCo (nM)	TdFe (nM)	TdMn (nM)	TdCo (nM)
04.05.2017	10827 ± 416	138 ± 4.2	2.4 ± 0.0	17016 ± 877	138 ± 4.21	2.4 ± 0.0
22.07.2017	4638 ± 219	76 ± 4.1	1.2 ± 0.2	19975 ± 1290	250 ± 12	3.6 ± 0.1
08.10.2017	6689 ± 771	97 ± 8.4	1.5 ± 0.4	11046 ± 266	266 ± 17	3.3 ± 0.1

Table S 4.2: Values for TE analyses for SAFe S, D2 and CASS6 Certificate Reference Material (CRM)

	TEs	**Consensus value (nM)**	**Reported value (nM)**
SAFe S [a]	dMn	0.790 ± 0.060	0.860 ± 0.099 (n = 2)
	dFe	0.093 ± 0.008	0.106 ± 0.013 (n = 2)
	dCo	0.005 ± 0.001	0.004 ± 0.002 (n = 2)
CASS6 [b]	dMn	40.51 ± 2.23	42.8 ± 0.76 (n = 3)
	dFe	27.97 ± 2.19	26.79 ± 2.75 (n = 3)
SAFe D2 [a]	dCo	0.046 ± 0.003	0.054 ± 0.004 (n = 2)

[a] Bruland K.W., 2009. GEOTRACES and SAFe Intercalibrations, Consensus Values for the GEOTRACES 2008 and SAFe Reference Samples. In: http://es.ucsc.edu/~kbruland/GeotracesSaFe/kwbGeotracesSaFe.html (accessed 05 March 2019). SAFe S and D2 were determined via pre-concentration follow by ICPMS analysis.

[b] In: https://www.nrc-cnrc.gc.ca/eng/solutions/advisory/crm/certificates/cass_6.html (accessed 05 March 2019). CASS6 were determined by isotope dilution alongside high TE samples (> 20 nM Fe)

Table S 4.3: Analytical Blanks (n = 30)

	TEs	**Value (pM)**
System Blank (SeaFAST & ICP-MS)	dMn	9 ± 4
	dFe	61 ± 24
	dCo	1.9 ± 1
Buffer Blank	dMn	42 ± 15
	dFe	102 ± 53
	dCo	2.6 ± 2

5 Forcing factors for Ra isotope distributions in the southeast Atlantic Ocean

Lúcia H. Vieira[1], Aaron J. Beck[1], Mark J. Hopwood[1], Jan Scholten[2], Volker Liebetrau[1] and Eric P. Achterberg[1]

To be submitted

1 Marine Biogeochemistry Division, GEOMAR Helmholtz Centre for Ocean Research Kiel, Kiel 24148, Germany

2 Institute of Geosciences, Christian-Albrecht University Kiel, Kiel 24118, Germany

Abstract

The southeast (SE) Atlantic Ocean is strongly influenced by boundary inputs of terrestrially derived material, including the discharge of the world's second largest river (Congo River), and benthic fluxes related to the Benguela Upwelling system and its associated oxygen minimum zone (OMZ). This study used naturally occurring Ra isotopes (^{226}Ra, ^{228}Ra, ^{224}Ra, and ^{223}Ra) as tracers of shelf sediment and river water inputs into the South Atlantic in order to quantify the relative importance of these ocean boundary processes in different regions of the SE Atlantic. Fluxes from the Congo-Angola shelf sediments (Flux $Ra_{\text{-Congo}}$ = 2.9 - 4.8 x 10^9 atoms m^{-2} yr^{-1}) were of the same order of magnitude than those in the Benguela region (Flux $Ra_{\text{-Benguela}}$ = 5.5 - 9.2 x 10^9 atoms m^{-2} yr^{-1}), and in agreement with reported values in the East Pacific Ocean and Southern California (USA), for example. In addition, all four Ra isotopes and Fe (II) in bottom waters may indicate oxygen deficient submarine groundwater discharge (SGD) along the Namibian shelf. The magnitude of this feature, with Fe (II) concentrations >200 nM indicates that it may play a major role in Ra and trace element (TE) distributions in the SE Atlantic. The influence of the Congo River was reflected in elevated ^{228}Ra and ^{226}Ra activities in its extensive surface plume extending up to 1000 km from the river mouth. The ^{224}Ra to ^{228}Ra ratios indicated that the plume transport along the coast was at a speed of 0.30 ± 0.04 m s^{-1}. In addition to these strong coastal influences, northward flowing subantarctic waters in the Benguela region appeared to drive a large variability of ^{226}Ra to silicate (Si) ratios between the northern and southern portion of our study domain.

5.1 Introduction

The southeast (SE) Atlantic Ocean features an important eastern boundary ocean region that is influenced by the discharge of the world's second largest river and the Benguela Upwelling system. The Benguela Upwelling system is one of the four major global eastern boundary upwelling systems, in addition to those found off the coasts of California, Peru, Chile, and northwest Africa. Wind-driven offshore Ekman surface water drift in these regions results in the upwelling of nutrient-rich deep waters facilitating primary productivity in shelf waters. However, this intense productivity also leads to the formation of extensive oxygen minimum zones (OMZs) due to the resultant sinking, and remineralization of particulate organic matter. The SE Atlantic shelf region therefore constitutes a region of particularly active TE exchange at its boundaries, with pronounced TE inputs expected from the atmosphere (Southern African dust plume) (e.g., Prospero et al., 2002; Mahowald et al., 2005), OMZ overridden shelf sediments from the continental margins (e.g., Elrod et al., 2004; Chase et al., 2007; Moore, 1969), and the Congo River (Figuères et al., 1978; chapter 4). The Congo River is the only major river in the world discharging into an eastern boundary region and plays a significant role in delivering radium (Ra) isotopes and trace elements (TEs) into the SE Atlantic Ocean (see chapter 4).

The naturally occurring isotopes of Ra present a range of half-lives (^{226}Ra, $T_{1/2}$=1600 y; ^{228}Ra, $T_{1/2}$= 5.75 y; ^{223}Ra, $T_{1/2}$=11.4 d; ^{224}Ra, $T_{1/2}$= 3.66 d), and have relative conservative behaviors in the oceans, and therefore are applied as geochemical tracers in oceanographic studies (e.g., Moore, 2000 a, 2000 b; Charette et al., 2001; Chung, 1980; Sarmiento, 1982; Moore and Dymond, 1991). Radium isotopes are more soluble in seawater in contrast to their

parent thorium isotopes, and diffusion from marine sediments and inputs from rivers are major Ra sources to the oceans (Kaufman et al., 1973; Moore, 1969). Previous studies in the Atlantic Ocean have reported average ^{226}Ra activities in the offshore surface waters of ca. 7.8 dpm 100 L^{-1} (Broecker et al., 1976), with increasing activities towards Antarctica coinciding with increasing nutrient concentrations, such as silicate (Ku and Lin, 1976; Hanfland, 2002). The nutrient-like depth profiles of ^{226}Ra, and the similarities between ^{226}Ra and silicate (Si) distributions in the ocean, led scientists to propose that biogeochemical processes such as phytoplankton uptake, particularly tests of siliceous phytoplankton, and particle scavenging, play a role in the oceanic ^{226}Ra cycle (Broecker et al., 1967; Ku et al., 1970; Ku and Lin, 1976). Enhanced ^{228}Ra activities are typically observed in surface waters relative to intermediate and deep waters, due to inputs from continental margins (shelf and slope sediments, rivers and submarine groundwater discharge (SGD) (e.g., Li et al., 1980; Charette et al., 2015). Yet, as the mean half-life of ^{228}Ra is much shorter (5.75 y) than that of vertical ocean mixing, little ^{228}Ra penetrates into the intermediate ocean (Moore, 1972).

Radium-228 inventories were determined in the upper 1000 m of the Atlantic Ocean using data obtained in the period 1981 to 1989 as part of the Transient Tracers in the Ocean (TTO) program (Moore et al., 2008). This allowed the estimation of total fluxes of SGD to the Atlantic Ocean. Stations were grouped within 15° ×15° boxes and ^{228}Ra data from 0-1000 m used to estimate the ^{228}Ra inventory in each box. Charette et al. (2015) used the same technique to determine the ^{228}Ra inventory in each 15° × 15° box from 15° to 45°N in the North Atlantic Ocean, and by comparison with the inventories derived from the TTO program, showed that the ^{228}Ra inventory is at steady state on a time scale of ~30 years in the

North Atlantic. However, no such temporal comparison has, to date, been conducted in the South Atlantic region described herein.

GEOTRACES cruise GA08 to the SE Atlantic Ocean was conducted to investigate the sources, sinks, and biogeochemical cycling of TEs in this region. As Ra isotopes are powerful tracers of inputs of TEs to the oceans and their off-shelf transport (Sanial et al., 2018; Dulaiova et al., 2009; Charette et al., 2016), here we report the overall distributions of Ra isotopes related to dominant boundary sources and biogeochemical and physical processes in the SE Atlantic. Significant features investigated within this region include: (i) the Benguela Current as the eastern boundary of the South Atlantic subtropical gyre; (ii) the Angola-Benguela Front; (iii) wind-driven coastal upwelling; (iv) oxygen minimum zone (OMZ); and (v) the Congo River plume. In this way, our study demonstrates how Ra isotopes can be applied to improve our understanding of these biogeochemical processes and helps subsequent quantification of TE fluxes from these boundaries, and therefore fulfill a major goal of the international GEOTRACES program.

5.2 Methods

The GEOTRACES section GA08 occurred from 22 November to 27 December 2015. The distributions of Ra isotopes were determined in shallow shelf waters (N-S section, Fig. 5.1) of the: (i) Angola Basin; and (ii) northernmost Cape Basin. These sections were complemented by two E-W sections perpendicular to the coast at 3°S (referred to here as 'the Congo-Angola region') and at ~29°S (referred to here as 'the Benguela region').

5.2.1 Sample collection and analysis

Approximately 250 L of surface seawater (~3 m depth) was filtered through MnO_2-impregnated acrylic fiber (Mn-fibers) at a flow rate <1 L min^{-1} to quantitatively extract Ra isotopes. In addition, 5 in-situ Stand-Alone Pumping Systems (Challenger Oceanic) were used to collect depth profiles of dissolved Ra isotopes, deployed at 100 m, 200 m, 300-400 m, 500-650 m, and 1000-1250 m depths. For this, seawater (~1000 L) was pumped by the SAPS through a membrane filter (1 μm pore size, polycarbonate; Whatman) to collect suspended particles, and the filtrate passed through a cartridge filled with MnO_2 coated fiber (Mn-cartridge) to extract the Ra isotopes (Henderson et al., 2013). Before pump deployments, the Mn-cartridges were cut in half (~15 cm each piece), and a plastic spring was placed below each Mn-cartridge inside the holder. A Ra extraction efficiency on the Mn-cartridges of 65% ± 12% was determined by (i) co-precipitation of a sample (1 L) with $BaSO_4$ (Moore et al., 1985) and subsequent analysis in a high purity, well-type germanium detector (HPGe; Canberra, EGPC 150) for an interrupted period of 55 days; and (ii) placement of two cartridges in series on an in-situ pump at certain stations (chapter 2).

Surface Ra samples were collected at all stations (Fig. 5.1). Vertical profiles of Ra were obtained at all stations along the Congo-Angola transect, the 29°S transect, and the Namibian shelf between stations 1316 and 1331. After collection, the Mn-fibers and Mn-cartridges were rinsed with Ra-free tap water and partially dried using compressed air. Radium-223 and ^{224}Ra activities in the Mn-fibers and Mn-cartridges were determined using four Ra Delayed Coincidence Counters (RaDeCC) (Moore and Arnold, 1996). The first measurements were performed onboard and the samples were then recounted after 6 weeks in order to determine

^{224}Ra in excess with ^{228}Th (^{224}Ra $_{ex)}$ (^{223}Ra were not corrected for ^{227}Ac). The RaDeCC counters were calibrated by measuring reference solutions containing known activities of ^{224}Ra adsorbed on columns of acrylic-MnO_2 fibers (Scholten et al., 2010).

After the measurements of ^{223}Ra and ^{224}Ra, the fibers and cartridges were ashed and subsequently leached in order to determine the activities of long-lived Ra (^{228}Ra and ^{226}Ra) using the HPGe gamma spectrometer. Ashing was conducted at 600°C for around 16 h with a subsequent chemical leach followed by co-precipitation of Ra with $BaSO_4$ (Moore et al., 1985) (see more details in chapter 2). The precipitate was stored in 1 mL vials, tightly closed with Parafilm and analyzed after at least 3 weeks to allow ^{222}Rn to achieve equilibration with its parent ^{226}Ra. Radium-226 activities were determined using the ^{214}Pb peak (352 keV) and ^{214}Bi peak (609 keV), while ^{228}Ra activities were determined using the ^{228}Ac peaks (338 keV and 911 keV). The detector efficiency was determined by spiking Mn-fibers and Mn-cartridges with known amounts of ^{228}Ra and ^{226}Ra, ashing, leaching and measurement in the gamma spectrometer as per the samples. Activities of the sample were corrected for detector background counts and fiber blank activities. The Ra reference solution was provided by the International Atomic Energy Agency (IAEA) and had a reported activity accuracy of 6% for ^{226}Ra and 5% for ^{228}Ra. Measured precisions for ^{228}Ra and ^{226}Ra was ~ 5%; i.e., these levels of accuracy and precision lead to an uncertainty on the sample activities of <10%.

For trace element clean sample collection, Ocean Test Equipment samplers mounted on a powder coated sampling rosette with a Kevlar conducting cable were deployed complying with GEOTRACES specifications for trace metal work. After conducting profiles, samplers were carried into an over-pressured trace element sampling container on deck equipped with

an air filtration system. Samplers were over-pressured (0.2 atm N_2) and subsamples for Fe (II) (unfiltered) and dissolved Fe (dFe) collected within 2 h of arrival on deck using flow-through 0.8/0.2 µm filters (Acropack 500). Low-density polyethylene (LDPE) bottles (125 mL) for dFe samples were pre-cleaned according to GEOTRACES protocol (1 week in Mucasol detergent, 1 week in 1.2 M HCl, 1 week in 1.2 M HNO_3, with 3 de-ionized water rinses after each stage). Opaque LDPE bottles for Fe (II) were prepared similarly and filled with no headspace. After collection, dFe samples were acidified by addition of HCl (UPA grade, ROMIL) to pH <2.0. Fe (II) samples were analyzed at sea within 1 h of sample collection using a dual Fe (II)/H_2O_2 luminol flow injection analysis system (Jones et al., 2013) exactly as per Hopwood et al. (2017). Fe (II) analysis was calibrated daily by standard additions of 0.2-20 nM, with standard additions made to both aged surface and aged sub-surface waters. Dissolved trace element concentrations were determined after >6-month storage at pH 1.9 via ICPMS after offline pre-concentration using a SEAFAST trace element pre-concentration system exactly as per Rapp et al. (2017). Macronutrient samples were collected unfiltered from OTE samplers into 30 mL LDPE bottles which were rinsed once prior to filling and then refrigerated until analysis. The analysis was conducted at sea via an autoanalyzer (Hansen and Koroleff, (1999) with daily analysis of a certified reference solution.

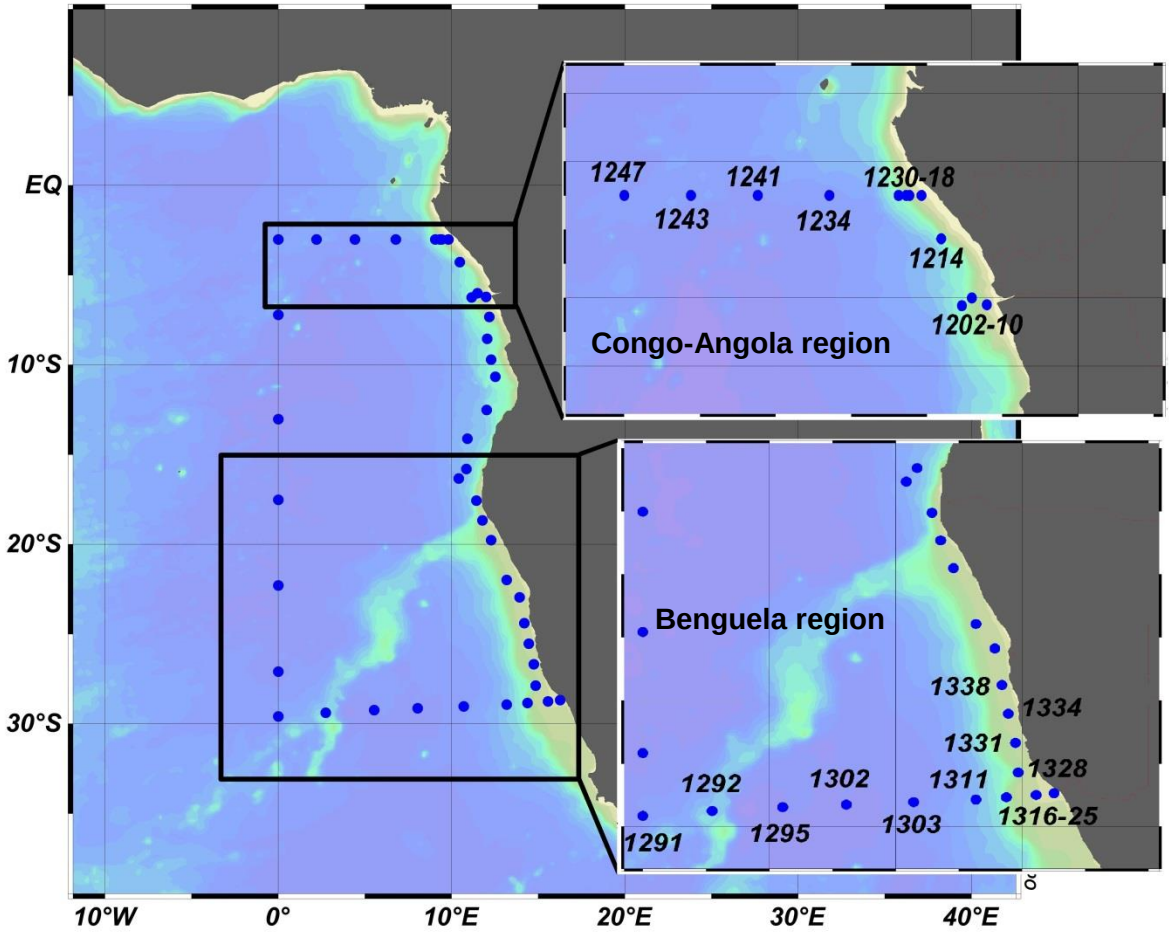

Figure 5.1: Study region with sampling stations in the SE Atlantic Ocean during the GEOTRACES GA08 section cruise. In-set provides detailed view of stations discussed in this chapter.

5.3 Results and Discussion

5.3.1 Shelves, slopes, and abyssal sediments as sources of Ra isotopes

The Congo River plume determines the Ra isotope distributions in surface waters of the Congo-Angola region (Fig. 5.2), as discussed later. Yet, in subsurface waters up to <300 m (σ_0 < 26.75), elevated ^{228}Ra activities (>1 dpm 100 L^{-1}) were also observed, relative to

intermediate waters (< 0.6 dpm 100 L^{-1}). This feature was also observed in the Benguela region (Fig. 5.2) suggesting a source mechanism unrelated to riverine inputs. Enhanced ^{228}Ra activities observed in the upper 300 m that extends >1000 km from the African continental margin may indicate lateral transport along isopycnal surfaces with Ra derived from shelf and slope sediments (hereafter, shelf ^{228}Ra plume).

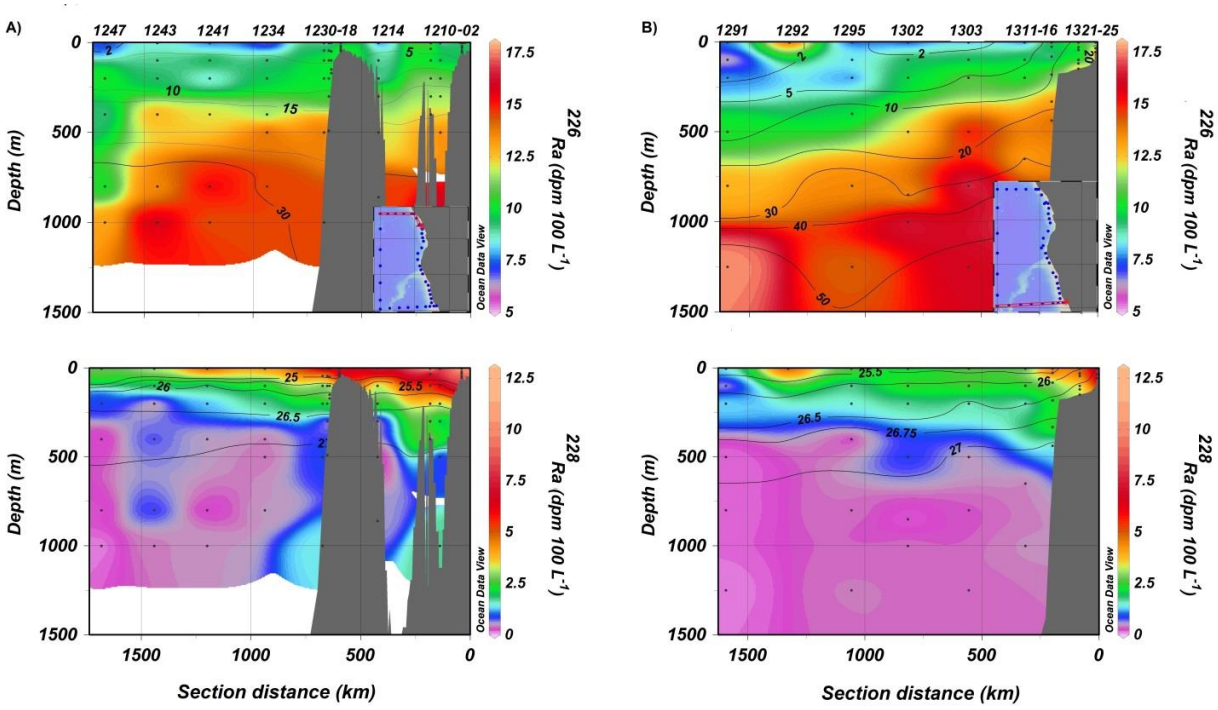

Figure 5.2: Radium-226 and ^{228}Ra distributions (dpm 100 L^{-1}) along the A) Congo-Angola region (stations along the shore and the 3°S transect) and B) Benguela region along the ~29°S. Iso-contours represent silicate concentrations and the potential density anomaly σ_0 (kg m^{-3}) for ^{226}Ra and ^{228}Ra distributions, respectively.

Radium-228 inventories for each station along the 3°S and 29°S transects were calculated by linear interpolation of datapoints between (i) the surface and <300 m; and (ii) the surface and 1000-1250 m. The average ^{228}Ra inventories (*I*) for <300 m (σ_0 < 26.75), were about 1.2 x 10^{10} atoms m^{-2} for the Congo-Angola region (3°S transect; from st.1218 to st.1247) and 2.5 x 10^{10} atoms m-^{2} for the Benguela region (29°S transect; from st.1325 to st.1291). We

excluded the surface waters of the Congo River plume from these calculations, as we here focus on ^{228}Ra inputs from the shelf and slope sediments into the Atlantic Ocean. The Ra flux from the Congo River plume is presented in chapter 4. In order to determine the ^{228}Ra fluxes (Flux Ra) from the shelf sediments in both regions, ^{228}Ra activities were corrected for the intermediate water background activities (Sanial et al., 2018) derived from the average ^{228}Ra activities between 400 m and 1000-1250 m across the 3°S and 29°S transects. Thus, the ^{228}Ra supply rate from the shelves would be balanced by losses due to transport and radioactive decay (λ) along both transects, and can be determined as:

$$\text{Flux Ra} = I \left[\lambda + \frac{1}{\tau}\right] \qquad \text{(Equation 5.1)}$$

The transport loss of ^{228}Ra is estimated by dividing the inventory of ^{228}Ra (I) in the upper 300 m (σ_0 < 26.75) by the residence time (τ) of the water within this layer (equation 5.1). Considering that the water residence time within the thermocline (<300 m depth, corresponding to the depth of the observed ^{228}Ra shelf plume) in the SE South Atlantic ranges between 4 to 10 years (Gordon and Bosley, 1991), ^{228}Ra fluxes from the Congo-Angola shelf (Flux Ra $_{\text{Congo}}$) ranged between 2.9 x 10^9 atoms m^{-2} $yr^{-1}$and 4.8 x 10^9 atoms m^{-2} yr^{-1}, while ^{228}Ra input from the Benguela shelf (Flux Ra $_{\text{Benguela}}$) were somewhat higher varying from 5.5 x 10^9 atoms m^{-2} $yr^{-1}$to 9.2 x 10^9 atoms m^{-2} yr^{-1}, but of the same order of magnitude. The calculated ^{228}Ra fluxes from shelf sediments are comparable with reported ^{228}Ra inputs from continental shelves. For example, in the eastern tropical South Pacific Ocean, the ^{228}Ra fluxes from the slope and shelf sediments were respectively 3.8 x 10^9 atoms m^{-2} yr^{-1} and 6.0 x 10^9 atoms m^{-2} yr-1 (Sanial et al., 2018); also similar to those found in San Pedro (5.2 x 10^9 atoms m^{-2} yr^{-1}) and San Nicolas (11 x 10^9 atoms m^{-2} yr^{-1}) on the Southern

California (USA) (Hammond, et al., 1990), but an order of magnitude lower than the shelf ^{228}Ra fluxes in Western North Atlantic Ocean (~57 x 10^9 atoms m^{-2} yr^{-1}) (Kwon et al., 2014; Charette et al., 2016) and in the Chukchi Sea (54 x 10^9 atoms m^{-2} yr^{-1}) (Vieira et al., 2019).

Our inventory of ^{228}Ra between the surface and 1250 m depth in the box corresponding to the Congo-Angola (4.2 ± 2.0 x 10^{10} atoms m^{-2}) and the Benguela (3.4 ± 0.9 x 10^{10} atoms m^{-2}) regions are somewhat higher than those presented by Moore et al. (2008) for the same regions (i.e., 3.0 x 10^{10} atoms m^{-2} and 1.6 x 10^{10} atoms m^{-2}, respectively). However, in the Congo-Angola region, the inventories from TTO and GA08 are not statistically different (at $p < 0.01$; t-test; 1σ), suggesting that ^{228}Ra may have also been at steady state for about 3 decades in that region. In contrast, the inventories between the two programs are significantly different in the Benguela region. This suggests that ^{228}Ra fluxes in the Benguela region may have increased over the last 30 years, which implies that ^{228}Ra is not at steady state. Another possible cause for the difference is that the TTO samples were collected farther offshore. Our inventory was determined using a long transect of 10 stations including five along the shelf, while the Moore et al. (2008) inventory was based on only three stations as far as ~ 1600 km from the coast. Our most open ocean station (st.1291) showed a ^{228}Ra profile that was similar to from the same site in the TTO program.

During the GA08 cruise, Ra isotopes were sampled in bottom waters at 10 m, 50 m, 100 m and 300 m above the seafloor (stations 1247, 1295, and 1303). The average ^{226}Ra activity near the seafloor was 19.4 dpm 100 L^{-1}, consistent with reported values (19-21 dpm 100 L^{-1}) for bottom waters in the SE Atlantic Ocean (Broecker et al., 1976). Our highest ^{226}Ra activity (24.5 ± 2.5 dpm 100 L^{-1}) was observed at 4418 m (st.1303) in the Benguela region (Fig. 5.3)

and was three-fold higher than for surface waters (7.8 ± 0.8 dpm 100 L^{-1}). The enhanced ^{228}Ra, $^{224}Ra_{ex}$ and ^{223}Ra activities observed in the first 100 m above the seafloor (Fig. 5.3) are likely due to abyssal sediment inputs. Enhanced suspended particulate loads in the near-bottom nepheloid layer were observed, particularly at station 1295, indicated by turbidity measurements (Fig. 5.3).

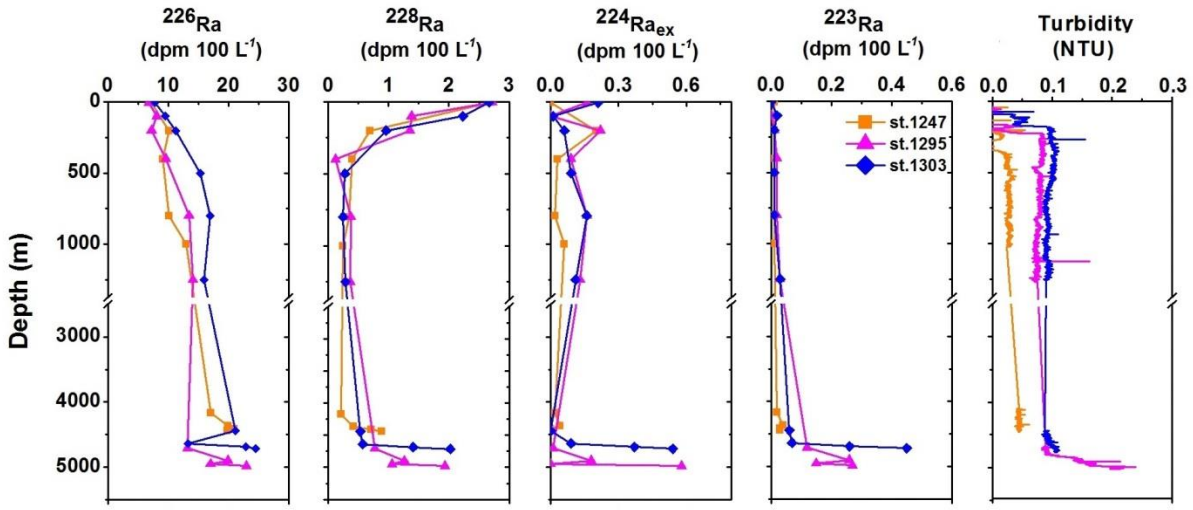

Figure 5.3: Distributions of the Ra isotopes and turbidity in the water column of stations 1247 (orange squares), 1295 (pink triangles) and 1303 (blue diamonds).

5.3.2 The Angola-Benguela front, upwelling, OMZ, and SGD along the African coast

Along the Benguela shelf (considered here as south of 15°S on Fig. 5.1), surface Ra activities were quite variable. The activities of $^{224}Ra_{ex}$ and ^{228}Ra varied by an order of magnitude from 0.95 ± 0.04 dpm 100 L^{-1} to 0.10 ± 0.04 dpm 100 $L^{-1}$and 12.0 ± 0.8 to 1.3 ± 0.1 dpm 100 L^{-1}, respectively, with the highest activities of both isotopes found in the freshest waters (salinity = 34.7) at the most southern station (st.1325). Surface ^{226}Ra activities were quite variable ranging between 8.0 ± 0.8 and 15.2 ± 0.5 dpm 100 L^{-1}.

The ^{228}Ra to ^{226}Ra ratio is a useful tracer when comparing water bodies (e.g., Moore, 1986; Moore, 2000 a, 2000 b; Moore and Todd, 1993). The cold and nutrient-rich northward flow of the Benguela Current usually meets the nutrient-poor and warm southward propagating waters of the Angola Current at the so-called Angola–Benguela front (ABF) at approximately 15°-17°S (Nelson and Hutchings, 1983; Lass et al., 2000). The ABF is also noticeable in the ^{228}Ra/^{226}Ra distributions where two mixing lines meet (Fig. 5.4), indicating two different water masses on the north and south side of this transect. This observation indicates that rapid mixing is controlling the distribution of Ra in this region. The three blue points that fall off the line on Fig 5.4 (i.e. st.1325, st.1331, and st.1334) may reflect waters with different sources. The colder, fresher and nutrient-rich waters of stations 1331 and 1334 suggest stronger influence of upwelling. On the other hand, the enhanced ^{228}Ra surface activities at the shallow station 1325 (~60 m deep) may suggest input from the highly Ra enriched bottom waters, as discussed later. The high ^{228}Ra/^{226}Ra ratios found in the northern station on the Angola shelf (red line in Figure 5.4) may reflect influences of the Congo River, as part of the Congo River discharge may be carried southward by the Angola Current during summer months (Tchipalanga et al., 2018).

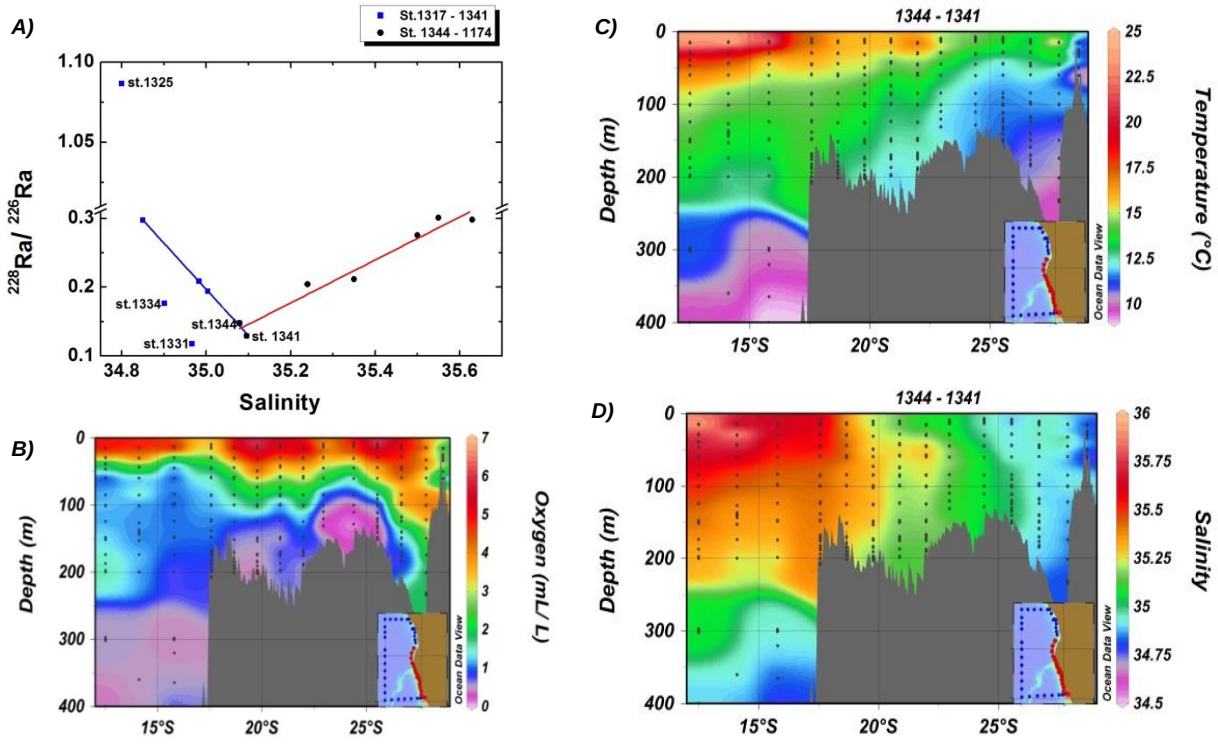

Figure 5.4: $^{228}Ra/^{226}Ra$ activity ratios plotted against salinity (R^2= 0.96) along the Angola-Namibia shelf region (A); oxygen (B), temperature (C) and salinity (D) distributions along the Angola-Namibia shelf zone

Prevailing southeasterly trade winds in the Benguela region drive an offshore surface water drift resulting in strong upwelling of cold and nutrient-rich waters originating from depths which roughly correspond to the South Atlantic Central Water (Shannon, 1985; Lutjeharms and Valentine, 1987). This upwelling can clearly be observed in the ^{226}Ra distribution (Fig. 5.2). The mean ^{226}Ra activity in the East South Atlantic Central Water (ESACW; ~300-500 m deep) was 11.2 ± 1.8 dpm 100 L^{-1}, which corresponds to that found in surface waters off Namibia (11.3 ± 2.0 dpm 100 L^{-1}). The same feature can be observed in the temperature (Fig. 5.4 C), Si (Fig. 5.7), density, and salinity distributions. The permanent upwelling that occurs in this region is linked to the development of the OMZ, as the nutrient-rich upwelled waters

result in an increase in primary productivity and the sinking particulate organic matter consequently induces pronounced oxygen depletion in subsurface shelf waters and sediments.

Furthermore, the Ra enrichment (e.g. ^{226}Ra) in the water column may be related to TE cycling within the OMZ along the Namibia coast. Todd et al. (1988) reported that the ^{226}Ra maxima in the permanent anoxic waters of the Framvaren Fjord in Norway was associated with particulate iron (Fe)-manganese (Mn)- oxyhydroxide cycling in the water. Reduced Mn (Mn (II)) and Fe (Fe (II)) diffuse upwards from the anoxic sediments into overlying waters where they are subsequently precipitated as Mn (IV) and Fe (III) particulate phases, which scavenge ^{226}Ra. Oxidized colloidal Fe and Mn, and particulate Fe oxyhydroxide and Mn-oxides upon settling through the oxic-anoxic interface of the water column re-dissolve in the reducing zone, releasing Fe, Mn, and the radionuclides back into solution, which could potentially contribute for example to the observed maxima in ^{226}Ra (e.g. 21.8 dpm 100 L^{-1} at 100 m of st.1328; Fig. 5.5).

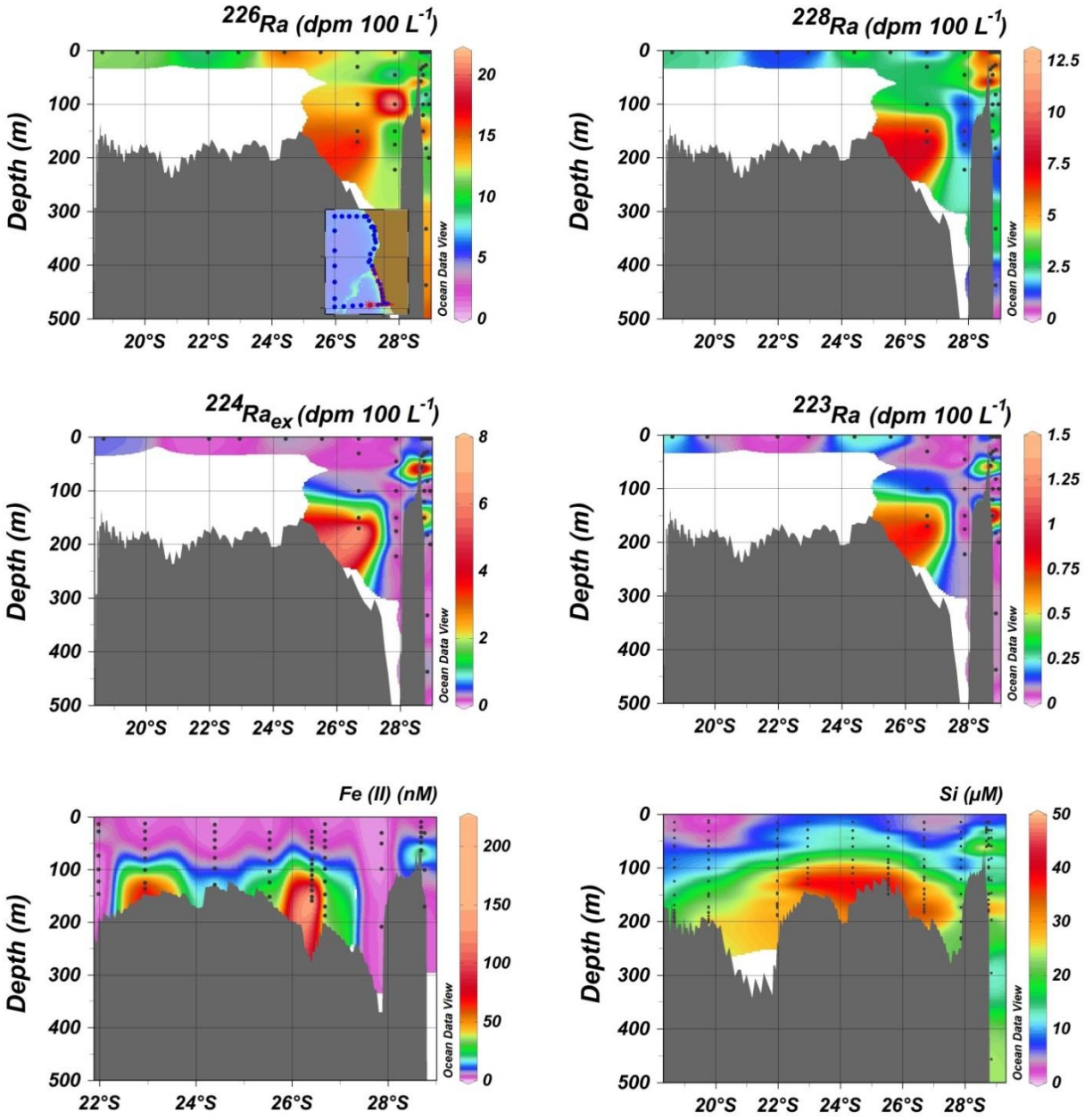

Figure 5.5: Radium isotope, Fe (II) and Si distributions along the Namibian coast. Radium vertical profiles comprise stations from 1325 to 1331.

Near-bottom Ra activities and Si concentrations were enhanced on the Namibian shelf (Fig. 5.5). Radium-224 was enriched by over an order of magnitude compared to surface waters, while ^{228}Ra and ^{226}Ra were enriched by factors of 2 to 6, likely due sedimentary inputs. Similarly, enhanced Fe (II) concentrations of 222 nM were observed in bottom waters of the shelf stations (Fig. 5.5), with coinciding distributions of the four Ra isotopes and Si distributions. Such an Fe (II) distribution provides unambiguous evidence of a large sedimentary Fe source associated with reducing conditions. The resolution of Si and Fe (II) data is higher than for Ra isotopes, and it is plausible that the activities of Ra isotopes might have been higher still at stations with Fe (II) and Si maxima. High concentrations of Si close to the seafloor indicate silica dissolution, which may potentially release ^{226}Ra into the water column. Along the Namibian coast, a belt of anoxic and organic-rich diatom mud has been reported in shelf sediments, composed of organic matter, diatomaceous silica, calcium carbonate, and phosphorite (Calvert and Price, 1983). This type of sediment is expected to form a source of ^{226}Ra, but not ^{228}Ra or ^{224}Ra (Moore and Shaw, 1998). A submarine fluid input as a unique source of Ra, Fe (II) and Si, such as (anoxic) SGD, could potentially explain the enrichment of all four Ra isotopes (Fig. 5.5). Inputs from SGD along the Namibian coast have already been postulated (Emeis et al., 2004).

Seasonal occurrence of H_2S-rich waters occurs occasionally during austral summer along the Namibian coast (e.g., Copenhagen, 1934; Mohrholz et al., 2008; Ohde and Mohrholz, 2011). Emeis et al. (2004) hypothesized that the sporadic H_2S eruptions on the Namibian shelf, which can occur after periods of inland rains (Weeks et al. 2004), could be explained by SGD. The Kuiseb River is reported to disappear into the Great Namib Desert dunes before reaching the sea, but may continue underground through drowned valleys, filled with alluvial

sediments, transmitting a hydraulic pressure signal of a rising water table after rain storms. This signal could trigger the release of trapped gasses in the organic-rich coastal sediments (Emeis et al., 2004). H_2S and reduced metals in the SGD form a potential source of reducing fluids to coastal waters that could prolong the duration and strength of the anoxic events in this region. However, rainfall in Namibia is highly variable both spatially and temporally (Eckardt et al., 2013). Although studies have suggested that annual rainfall did not show a clear trend over the last 30 years (Fauchereau et al., 2003; Morishima and Akasaka, 2010), dry periods in Namibia have become longer and more intense (Morishima and Akasaka, 2010), and rainfall variability has increased with an increase in heavy rainfall (Lu et al., 2016). Changes in the precipitation regimes in Namibia induced by climate change may therefore alter the SGD inputs along the coast leading to a change in the intensity of H_2S events and Ra, Fe (II) and Si release into the water column.

5.3.3 The influence of Subantarctic waters on ^{226}Ra distributions

Along the coast of the Benguela region, the activities of the long-lived Ra isotopes were elevated relative to offshore waters (mean ^{226}Ra = 11.1 ± 2.0 dpm 100 L^{-1}), likely due to the influence of the ^{226}Ra enriched Antarctic waters (Ku and Lin, 1976) and upwelled waters off the Namibian coast. Subantarctic waters in the Benguela region may drive the large variability of ^{226}Ra and Si ratios between the northern and southern portion of our study domain. ^{226}Ra showed a nutrient-like profile and strongly correlated with Si (Fig. 5.6), as also reported by e.g., Chung (1980), Moore and Dymond (1991), Ku and Lin (1976), Ku et al. (1970), Broecker et al. (1967), Charette et al. (2015), and Hanfland (2002). We here present the first ^{226}Ra and Si correlation for the South Atlantic Ocean between 100-1250 m (Fig. 5.6)

and compare this with the historical open ocean Ra and Si distributions in the Atlantic Ocean. In the current study, a ^{226}Ra/Si slope of 0.11 dpm 100 L^{-1} μM^{-1} observed in the Benguela region was almost 2-fold lower than observed further north in the Congo-Angola basin (0.21 dpm 100 L^{-1} μM^{-1}) (with Si concentrations > 5µM). The ^{226}Ra to Si ratio in Antarctic waters is reported to be 0.07 dpm 100 L^{-1} μM^{-1} (Ku and Lin, 1976; Hanfland, 2002), while in the North Atlantic, this ratio is two and three times steeper (0.24 dpm 100 L^{-1} μM^{-1}) than that observed in the Benguela and Antarctic regions (Charette et al., 2015). Thus, the ^{226}Ra and Si ratios not only appear to vary significantly between ocean basins (Li et al., 1973; Chung, 1980), a strong variability is also observed across the Atlantic Ocean. It has been suggested that the northward increase in ^{226}Ra/Si ratios in the Atlantic intermediate water may be the result of the mixing of water mass with different^{226}Ra and Si signatures, such as that between the upper North Atlantic Deep Water (uNADW), depleted in Si but enriched in ^{226}Ra (i.e. high ^{226}Ra/Si) with the Antarctic Intermediate Water (AAIW) with lower ^{226}Ra/Si ratios (Charette et al., 2015; Broecker et al., 1967). Indeed, the different ^{226}Ra and Si ratios in the northern and southern regions of our study appear to be more related to the large variability in the Si concentrations within the same water masses across the South Atlantic Ocean (Fig. 5.7). The variability may be defined by the concentrations of preformed nutrient of the waters derived from the surface Southern Ocean, which feed into the main thermocline of the Atlantic Ocean (Sarmiento et al., 2007).

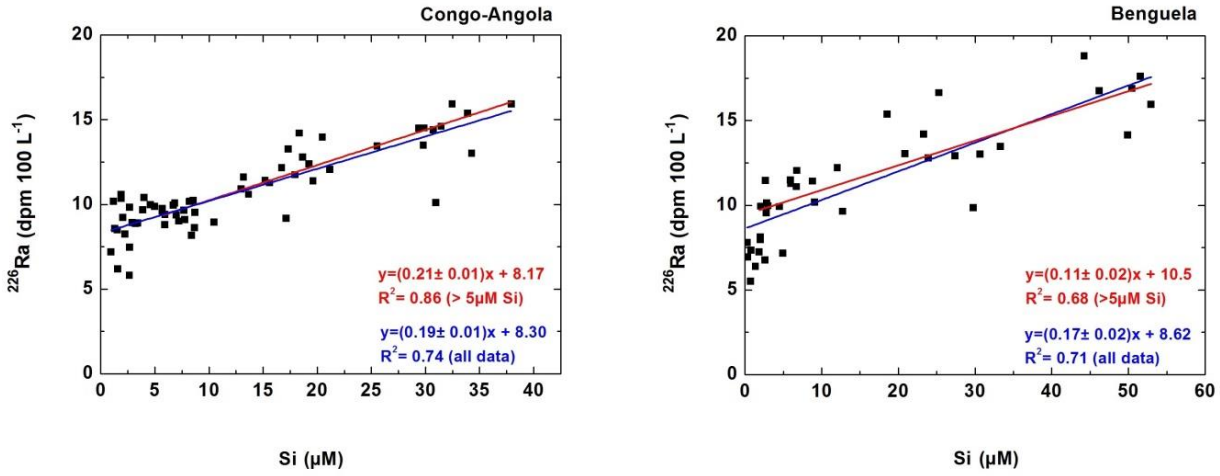

Figure 5.6: Radium-226 and Si relationships during the GEOTRACES GA08 cruise in the Congo-Angola (3°S transect) and Benguela regions (29°S transect). Blue lines represent the ^{226}Ra/Si correlation within all samples, while red lines are for samples with silicate higher than 5 µM.

In contrast to the Congo-Angola basin, Si is depleted in a greater water depth interval in the Benguela region (up to a 500 m thick layer) (Fig. 5.7). Using data from the GEOSECS program, van Bennekom and Berger. (1984) suggested that, in the upper water column of the Angola Basin (100-400 m), the increase from south to north of dissolved Si due to in situ regeneration was 50 g m^{-2}. Below 900 m however, our deep-water-Si concentrations are higher by a factor of 2 or 3 in the Benguela region relative to the same water depths in the Congo-Angola basin (Fig. 5.7); water mass analysis suggests that the waters below 900 m correspond to a mixture of AAIW and uNADW in both regions (σ_0 ~ 27.4). The difference in Si concentration within this layer may be due to the influence of the Si enriched waters from the Subantarctic Zone, and as it flows northward from the source region, its Si concentration may decrease as it mixes with Si poorer water from the north. This could explain the lower ^{226}Ra/Si ratio observed with increasing latitude. The ^{226}Ra to Si ratios in surface waters appear more variable, likely because the concentration of both ^{226}Ra and Si in surface waters (Si < 5µM) are affected by uptake and scavenging processes that occur at different rates.

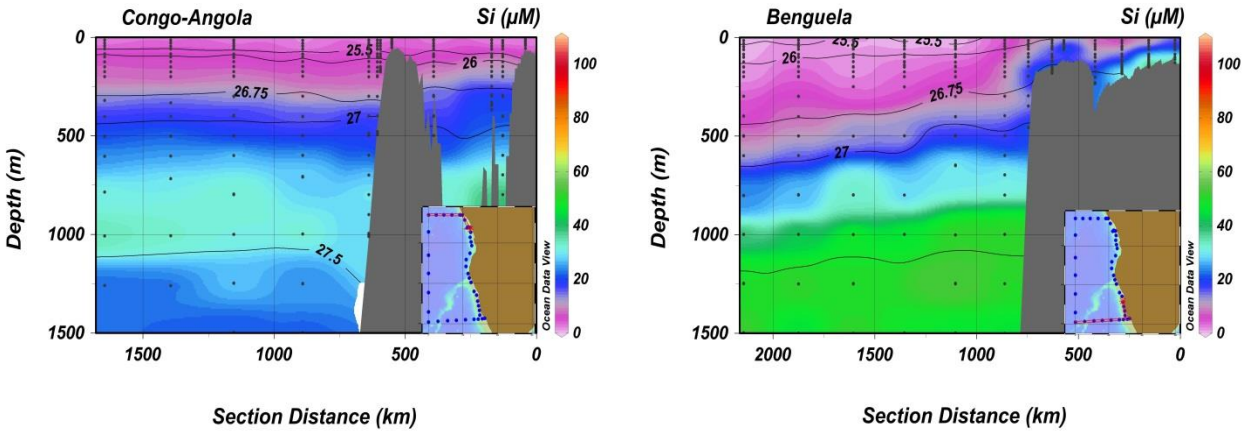

Figure 5.7: Silicate distribution in the first 1500 m in the Congo-Angola and Benguela regions. Iso-contours represent potential density anomaly σ_0 (kg m^{-3}).

5.3.4 The influence of the River Congo on Ra isotope distributions in the SE Atlantic

Activities of ^{226}Ra and ^{228}Ra were elevated in coastal surface waters of the Congo-Angola region (mean = 8.3 ± 2.3 dpm 100 L^{-1} and 8.81 ± 3.83 dpm 100 L^{-1}, respectively) due to the influence of the Congo River. The Congo River plume forms a buoyant low salinity surface outflow of up to 15 m deep (Yankovsky and Chapman, 1997; Hopkins et al., 2013). The Ra distribution indicates that the Congo plume can be traced in the offshore region (3°S transect; Fig. 5.1) up to ~ 1000 km from its mouth (st.1241) (e.g., 5.2 dpm 100 L^{-1}; Fig. 5.2). The presence of enhanced ^{228}Ra signatures in surface waters several hundreds of km offshore suggests rapid horizontal transport of the river plume. The highest Ra activities (^{224}Ra = 8.15 dpm 100 L^{-1}; ^{223}Ra = 0.97 dpm 100 L^{-1}; ^{228}Ra = 17.0 dpm 100 L^{-1}; and ^{226}Ra = 13.5 dpm 100 L^{-1}) were observed in surface waters of station 1210 at the edge of the shelf (Fig. 5.2) and at the observed lowest salinity (S = 30). In the northward extension of the plume, that follows the Congo River canyon nearshore (st.1214), the long-lived Ra activities in surface waters decreased by a factor of 2 with distance from st.1210 (^{228}Ra: ~ 8.04 dpm 100 L^{-1}; ^{226}Ra ~

7.33 dpm 100 L^{-1}), while the short-lived Ra decreased by an order of magnitude (^{224}Ra ~ 0.74 dpm 100 L^{-1}; ^{223}Ra ~ 0.17 dpm 100 L^{-1}). Radium activities decrease with increasing distance from the source, due to dilution, mixing and radioactive decay. If both the ^{224}Ra and ^{228}Ra activities are above their limit of detection at a certain distance from the Congo mouth, and ^{224}Ra/^{228}Ra ratios have the same source and no additional sources of Ra exist along the plume length, then the apparent age (T) of waters at st.1214 in comparison to the shelf-edge st.1210 can be derived following Moore (2000 b):

$$T = \ln\left[\frac{(^{224}Ra/^{228}Ra)_i}{(^{224}Ra/^{228}Ra)_o}\right] \times \frac{1}{\lambda_{224}} \qquad \text{(Equation 5.2)}$$

where $(^{224}Ra/^{228}Ra)_i$ is the initial ratio at st.1210, $(^{224}Ra/^{228}Ra)_o$ is the ratio observed away from the source (offshore) at station 1214, and λ_{224} is the decay constant of ^{224}Ra. Sediment inputs to surface waters between st.1210 and st.1214 are unlikely due to the vertical stratification resulting from strong density gradients between the surface Congo plume and deeper waters, and also due to the abrupt drop of the bathymetry to 1500 m between the stations (Fig. 5.2). In this way, the apparent age of the water mass above the canyon is ~ 9 days, which indicates that the plume following the Congo River canyon flows along the coast at 0.30 ± 0.04 m s^{-1}.

A decrease of ^{228}Ra with salinity in surface waters indicated a conservative mixing between the river plume and Atlantic waters (Fig. 5.8; Vieira et al., in review). Thus, a simple mixing model between ocean and rivers waters can be constructed using ^{228}Ra distributions and salinity. Using this approach, we are able to derive the ^{228}Ra content on a fraction of river or

Atlantic water and plot the non-conservative ^{228}Ra ($^{228}Ra_{non\text{-}cons}$) distribution (Moore et al., 1995).

$$^{228}Ra_{non\text{-}cons} = {}^{228}Ra_M - (^{228}Ra_{es}\ f_{es}) - (^{228}Ra_O\ f_O) \qquad \text{(Equation 5.3)}$$

where f_O and f_{es} are the fractions of the ocean and estuary, respectively, determined by the salinity endmembers; $^{228}Ra_O$ and $^{228}Ra_{es}$ are the ^{228}Ra activity in the ocean and Congo-shelf-endmember (st.1210), respectively; and $^{228}Ra_M$ is the ^{228}Ra activity measured in a sample. The ocean endmembers for ^{228}Ra (2.00 ± 0.4) and salinity (36.4) were determined from the average of ^{228}Ra activities and salinities in open ocean surface waters of the meridional transect of the GA08 cruise.

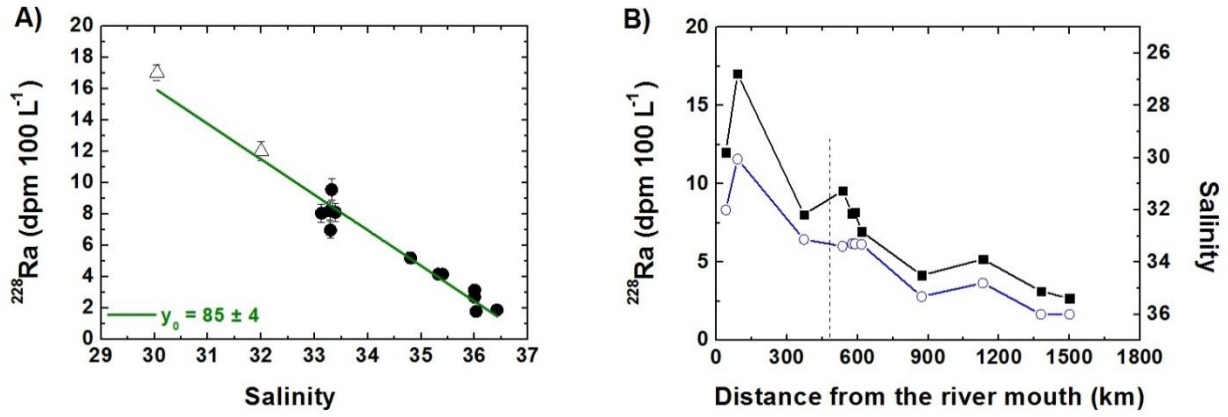

Figure 5.8: (A): River and open ocean waters mixing diagram. (B) ^{228}Ra (black squares) and salinity (blue open circles) distributions in surface waters from st.1202 to the end of the 3°S transect (st.1247). Note inverse salinity scale. This figure is based on Figure 4.2 of chapter 4.

Figure 5.8 indicates that all surface samples fall on or close to the conservative mixing line; in addition, all $^{228}Ra_{non\text{-}cons}$ values in equation 5.1 were ≤ 0, suggesting no additional Ra inputs. This indicates that the Congo River plume is the major source of ^{228}Ra to surface waters of that region, as also reported in chapter 4. The offshore stations at around 500 km

from the Congo River mouth (e.g. st.1230) showed 83% of their surface layers consisted of open ocean waters, while the river-derived ^{228}Ra (^{228}Ra $_{R}$) was greater than 70%. Moreover, the dilution did not appear to be homogeneously distributed and pockets of freshwater were observed along the 3°S transect with high ^{228}Ra activities at ~1000 km from the Congo outflow (Fig.5.8). The freshwater pockets, possibly originating from filaments, meanders, or eddies from the river mouth (Vangriesheim et al., 2009), were composed for 75% of ocean water and > 83% of river-derived ^{228}Ra (e.g. st.1241).

5.4 Conclusion

Ra isotope distributions in the SE Atlantic Ocean show evidence of significant inputs from the Congo River waters and the continental shelf of southwest Africa, an eastern boundary region influenced by the Benguela Upwelling system and an OMZ. In the Benguela region, mixing occurs rapidly; the mixing pattern is consistent with the Angola – Benguela front, and the dispersion of the currents matches the trends we see in the ^{228}Ra/^{226}Ra ratios. Ra sources and behavior in the Benguela OMZ, as enhanced Ra isotopes and Fe (II) and Si concentrations were observed in bottom waters along the Namibian shelf, suggest silica dissolution, input of anoxic SGD, or that Ra can participate in the TE cycles within the OMZ, where reductive dissolution of Fe-Mn oxyhydroxides may remobilize Ra in this region.

Our results show an increase in ^{228}Ra inventories along the Benguela region (< 15°S) relative to that reported during the TTO program in the late 1980s. Possible causes include the closer proximity of our stations to the shelf influenced zone, compared to the (offshore) TTO stations; or variations in the ^{228}Ra input to the Benguela zone, suggesting that ^{228}Ra may not be in steady state in this region. Shelf-fluxes of ^{228}Ra in this region (5.6×10^9 to 9.4×10^9

atoms m^{-2} yr^{-1}) are not significantly different than that from the Congo-Angola shelf (2.5 x 10^9 to 4.1 x 10^9 atoms m^{-2} yr^{-1}). If, as suggested by Ra, Fe, and Si distributions, sporadic SGD varying in intensity, space and time, may affect TE, Si and Ra distribution and export to the South Atlantic.

Acknowledgments

We thank the captain and crew of the RV Meteor M121 cruise/ GEOTRACES GA08 section; S. Koesling, P. Lodeiro and C. Schlosser for cruise support. Lúcia H. Vieira received a doctoral scholarship from the Conselho Nacional de Desenvolvimento Científico e Tecnológico (CNPq - grant number 239548/2013-2), Brazil.

Author contributions

Lúcia H. Vieira carried out the sampling, analyzed the radium samples, and wrote the first draft of the manuscript. Mark J. Hopwood analyzed Fe (II) samples. **Lúcia H. Vieira** calculated the radium fluxes after detailed discussion with Aaron. J. Beck. Volker Liebetrau provided analytical assistance for Ra analysis. Eric.P. Achterberg and Jan Scholten designed the GA08 study.

6 Conclusions and future directions

The major aim of this study was to identify boundary sources and sinks of TEs, and quantify land-ocean exchange rates of these elements, in order to better understand their biogeochemical cycling in the ocean and how their sources and cycling might respond to future climate change. Using Ra isotopes, I determined boundary TE fluxes from two regions that constrain the major TE sources: (i) a broad ice-covered Arctic shelf region; (ii) an eastern boundary system off the western African coast, influenced by the discharge of the world's second largest river and the Benguela Upwelling system in the southern portion of the study domain.

In chapter 3, the first TE data on the Chukchi Sea shelf collected during spring is presented. The Chukchi Sea is not only one of the most productive Arctic shelf seas (Hill and Cota, 2005), but has crucial importance on delivering TEs and other shelf-derived materials to the Arctic Ocean. Thus, in this chapter, I investigated the dissolved and total dissolvable TE (Cd, Fe, Ni, Cu, Zn, Pb, Mn, and Co) distributions in the Chukchi Sea during spring, and applied ^{228}Ra as tracer of benthic TE inputs in the Chukchi Sea shelf and the subsequent dFe flux to the Arctic Ocean. I showed that convective mixing induced by ice formation during spring led to extremely high TE concentrations over the shelf. Sediment resuspension events caused by mixing processes played a major role in buffering dFe released from shelf sediments, as sediment particles likely scavenged dFe and formed labile particulate phases. Nonetheless, regardless of TE removal processes, this study showed that elevated benthic TE inputs and subsequent geochemical enrichment of the Pacific-origin waters on the Chukchi shelf

provided suitable conditions for phytoplankton blooms. In addition, 10-25% of dFe produced over the shelf is transported to the central Arctic, indicating the importance of the Chukchi Sea shelf as one of the major sources of TEs that sustains the Arctic primary productivity. Therefore, changes in the Bering and Chukchi Seas will have significant impacts on the biogeochemical cycles of the Arctic Ocean.

Some key indicators of major climate changes in the Chukchi Sea are becoming evident, including reduced ice cover (Shimada et al., 2006), an increase in primary productivity (Arrigo et al., 2008) and an increase in the Pacific water inflow from the Bering Strait to the Arctic (Woodgate et al., 2018). The increase in primary productivity, and subsequent increase of carbon export, is projected to enhance denitrification rates in the sediments (Arrigo et al., 2008), favoring TE reduction and increasing benthic TE diffusive release. In addition, changes in denitrification rates may further diminish nitrate concentrations in the already nitrate depleted waters transported from the Arctic Ocean to North Atlantic (Arrigo et al., 2008) lowering the N:P ratio of the overflow waters from the Arctic to the North Atlantic. As N_2-fixation is favored in waters with a low N:P ratio, an increase of N_2 fixation in the North Atlantic is expected (Yamamoto-Kawai et al., 2006); the question whether the waters transported from the Arctic to the North Atlantic would contain enough Fe to sustain such enhanced N_2-fixation (Arrigo et al., 2008) remains unanswered. Therefore, similar to this study, further work focused on identifying Fe sources and quantifying its subsequent input to the Arctic basin is urgently needed.

In the current study, ^{228}Ra fluxes from the Chukchi Sea sediments were within the largest reported globally. Radium-228 activities I found during spring were 2-fold higher than

previously reported during the summer months, indicating that seasonal variability of Ra, and possibly TE, over the Chukchi Sea shelf may be of crucial importance to understand the influence of the shelves on the chemical budget of the Arctic Ocean. However, the reason why ^{228}Ra is higher during spring is unclear. Recently, Kipp et al. (2018) showed that the levels of ^{228}Ra in the central Arctic have increased by a factor of 2 over the past 10 years, due to an increase of benthic ^{228}Ra fluxes from the Arctic shelves. They hypothesized that longer open water season allows more wind-driven mixing, which likely drives the increase in ^{228}Ra fluxes. They also suggested that this may be the case for other shelf-derived materials such as TEs. These changes may be altering the influence of the shelves on the chemical budgets and biogeochemical cycles in the Arctic Ocean, with subsequent effects on the primary productivity of the Arctic and Atlantic Oceans. As the extensive continental shelves cover about one-third of the Arctic Ocean, an important next step is to conduct continued measurements of TEs and Ra on the Arctic shelves and in the basins, in order to elucidate temporal trends and evaluate the consequences of climate change on the shelf TE supply to the Arctic Ocean.

Chapter 4 and 5 focused on the boundary processes that control the distribution of Ra and TEs in the Southeast Atlantic Ocean. In chapter 4, I used ^{228}Ra as a geochemical tracer to track the horizontal TE (dFe, dCo, and dMn) dispersions of the Congo River plume and to quantify the input rates of these elements from the River Congo into the South Atlantic Gyre. The results of this study indicated limited removal of dFe on the shelf linked to the Congo River outflow (called throughout this thesis "Congo-shelf-zone"). As strong dFe removal (50-85%) has been demonstrated within low salinity (0-5) of the Congo estuary waters (Figuères et al., 1978), I concluded that the dFe removal within the Congo estuary is

balanced by dFe inputs into the Congo-shelf-zone. The constrained river inputs for dissolved and desorbed Ra fractions do not supply the amount of Ra required to maintain the Ra inventory observed in the Congo-shelf-zone. Based on the principle that Ra and TEs have common sources (see chapter 1), I suggested that indeed there must be a significant, 'missing' Ra and TE source between the river and the Congo-shelf-zone, which may be SGD. Although shelf inputs increased ^{228}Ra and TE concentrations in the Congo-shelf-zone, the lower salinity in surface waters isolated the plume from the seafloor influences due to the density gradient once the plume was removed from the Congo-shelf-zone. Thus, proceeding along the river plume pathway in the off-shelf transect (3°S), the linear decrease of ^{228}Ra with salinity in surface waters indicated a conservative mixing between the river plume and Atlantic waters, and the similarity between the ^{228}Ra and TE distributions with salinity indicated that the plume was the only major source of Ra and TEs in offshore region. Combining the ^{228}Ra fluxes with the distributions of dissolved TEs, I could provide the first estimate of Ra-derived TE fluxes from a river plume into the ocean. Thus, I showed that the presence of TEs and ^{228}Ra in surface waters several hundreds of kilometer off-shelf indicating rapid horizontal mixing of the river plume, which consequently influences the delivery of high levels of TEs from the Congo River outflow into the Southeast Atlantic Ocean, a reportedly oligotrophic region (Browning et al., 2017). Indeed, primary productivity within the offshore region of the current study was not Fe-limited; instead the region was limited by nitrogen availability (Browning et al., 2017). This led to the conclusion that the large TE input from the Congo River plume relieves micro-nutrient limitation (Fe and Co) (Browning et al., 2017) and potentially increases N_2 fixation in the eastern South Atlantic Gyre. Changes in the Congo runoff regime, as well as the surface ocean circulation patterns

driven by winds, will therefore potentially alter the magnitude of TE fluxes and consequently affect the primary productivity in the Southeast Atlantic Ocean.

Signorini et al. (1999) reported that seasonal variations of the wind and the river discharge can strongly affect the Congo River plume dispersion, as well as the complex ocean circulation within the SE Atlantic Ocean (Stramma and Schott 1999). Although in the near future the Congo River Basin (catchment) might not experience significant changes in the annual total precipitation in response to a changing climate, more intense rainfall is likely to occur during the African wet season (Hänsler et al., 2013); hence intensifying the seasonal and interannual variability of Congo River runoff (Alsdorf et al., 2016). In addition, it has been suggested that the Congo Basin is very sensitive to changes in potential evapotranspiration, which may affect the total Congo runoff (Tshimanga and Hughes, 2012). Due to rising temperatures, evaporation is likely to increase, and a reduction of more than 10% of the total Congo runoff is predicted (Tshimanga and Hughes, 2012), which will potentially decrease the TE delivery to the Atlantic Ocean. Moreover, changes in atmospheric-ocean interactions, Sea Surface Temperatures, wind patterns, and the location of the Inter-Tropical Convergence Zone may have profound impacts on the hydrological conditions of the Congo River Basin (Balas et al., 2007; Farnsworth et al., 2011; Poccard et al., 2000). However, little is still known about the hydrological response of the Congo River to future changes in climate, due to a lack of experimental research in the Congo Basin; in addition, projected changes in this region may not be completely consistent, due to the usage of different hydrological models and climate scenarios (Hänsler et al., 2013). Therefore, continued river discharge data has to be collected to improve our knowledge of the long-term changes of the Congo River Basin hydrology. Additional TE and Ra sampling in the Congo

River itself and in the Southeast Atlantic would also aid prediction of how changes in river water chemistry and its plume will affect TE distributions and consequently primary production in the South Atlantic Gyre.

In chapter 5, the impacts of the main sources and geochemical processes on the distribution of Ra in the Southeast Atlantic Ocean are discussed. As such, Ra isotope distributions were presented along two East-West sections (3°S and 29°S) in the SE Atlantic Ocean and in shelf waters along the western African coast. The study region constrains the boundaries of 3 major oceans such as Atlantic, Indian, and Southern Oceans, in addition to the major TE and Ra sources such as a river (Congo River) and a large continental shelf influenced by the Benguela Upwelling system and oxygen minimum zone. In this chapter, I presented the correlations between ^{226}Ra and Si in the Southeast Atlantic. Although the coupling between ^{226}Ra and Si cycles in the oceans has been well established, their relationship in the Southeast Atlantic is for the first time presented during this study. I showed that there is a strong variability in the ^{226}Ra and Si correlations (up to 1000 m depth) across the Atlantic Basin. The ^{226}Ra/Si ratios increased significantly with increasing latitude, likely due to the influence of the Si-enriched subantarctic waters that supply nutrients into the thermocline of the Atlantic Ocean. Whilst the distribution of ^{226}Ra reflects the properties of the major water masses present in the study region, ^{228}Ra is a tracer of continental sources in the upper ocean. As such, ^{228}Ra was enriched in the first 250-300 m over the entire 3°S and 29°S transects, indicating strong shelf influences over 1000 km in the SE Atlantic Ocean. Similar fluxes were observed in the Benguela (29°S) and the Congo-Angola region (3°S) with reported values in the East Pacific Ocean and Southern California coast (USA).

The ^{228}Ra inventories along the 3°S and 29°S transects were determined and compared to historical ^{228}Ra inventories in that region (Moore et al., 2008). I showed that the inventories seem to have increased over the past 30 years in the southern transect (29°S). The reason for the observed increase could be because the current study may have more efficiently captured the influence of the shelf, as more samples were collected in this undersampled region, or ^{228}Ra is not at steady state in this region, and fluxes from the continental shelf may have increased over last 3 decades. The later hypothesis indicates that increased shelf fluxes may not only affect Ra isotopes but also other shelf-derived TEs. In addition, increased Ra isotopes (and Fe (II)) concentrations were observed in the oxygen minimum zone of the Benguela region, which may be explained by inputs from additional Ra sources, such as the reducing shelf sediments as a result of silica dissolution, or SGD along the Namibian shelf. Studies have suggested that rainfall episodes in the Namibian coastal hinterland could further lead to a subterranean aquifer recharge and its subsequent discharge as SGD into the Namibian coast; such process may be related to the nearshore hydrogen sulfide (H_2S) eruptions observed off Namibia (Emeis et al.; 2004; Weeks et al., 2004) and may therefore influence the duration and extent of the hypoxia events in this region. The sporadic H_2S events appear to be more frequent and longer lasting than previously thought, and simple upward advection during the upwelling may not be sufficient to explain the range of H_2S events observed (Weeks et al., 2004). This may also support the idea of the existence of SGD. However, in order to make predictions on how the Benguela system will change in the future relative to Ra and TE fluxes to the Atlantic Ocean, we must test if (i) the hypothesis of SGD is true, and for that, Ra isotopes are powerful tools (Moore et al., 1996) (ii) the correlation and lag between rainfall episodes and aquifer recharge-discharge. Although

studies have investigated the macro-nutrient inputs from SGD (e.g., Valiela et al., 1990; Wang et al., 2018), little is known about the SGD supply of the bio-essential TEs (Windom et al., 2006). Paired studies of TEs and Ra in this region should certainly continue to improve our knowledge of the driving factors for their observed distributions, and how these distributions can be altered with climate-induced changes in this system.

In summary, this Ph.D. thesis had an original multidisciplinary approach which showed that the quantification of TEs from continental margins, such as from shelf sediments and rivers, is vital to provide constraints on the TEs biogeochemical cycling in the oceans. Thus, this study has shown how Ra isotopes can be used to identify TE sources and quantify TE supply rates to the oceans, hence improving our capability to constrain the ocean boundary TE inputs and to evaluate how this TE supply may change in response to future changes in climate. Future research should therefore continue to focus on identifying Ra sources and quantifying their fluxes in diverse ocean environments in order to improve their applicability as tracers in oceanographic studies.

References

Aagaard, K., Coachman K. L., Carmack E. C., 1981. On the halocline of the Arctic Ocean. Deep Sea Res., Part A, 28, 529-545.

Aagaard, K., Carmack, E.C., 1989. The role of sea ice and other fresh water in the Arctic circulation. Journal of Geophysical Research 94, 14485–14498.

Achterberg, E. P., Holland, T. W., Bowie, A. R., Mantoura, R. F., Worsfold, P. J., 2001. Determination of Iron In Seawater. Analytica Chimica Acta, 442(1), 1–14.

Achterberg, E.P., Moore, C.M., Henson, S.A., Steigenberger, S., Stohl, A., Eckhardt, S., Avendano, L.C., Cassidy, M., Hembury, D., Klar, J.K., Lucas, M.I., Macey, A.I., Marsay, C.M., Ryan-Keogh, T.J., 2013. Natural iron fertilization by the Eyjafjallajökull volcanic eruption. Geophys. Res. Lett. 40, 1–6.

Aguilar-Islas, A., Bruland, K., 2006. Dissolved manganese and silicic acid in the Columbia River plume, Marine Cheimistry 101, 233–247.

Aguilar-Islas, A. M., Hurst, M.P., Buck, K.N., Sohst, B., Smith, G. J., Lohan, M. C., Bruland, K. W., 2007. Micro- and macronutrients in the southeastern Bering Sea: insight into iron-replete and iron-depleted regimes. Progr. Oceanogr. 73, 99–126.

Aguilar-Islas, A. M., Rember, R. D., Mordy, C. W., Wu, J., 2008. Sea ice-derived dissolved iron and its potential influence on the spring algal bloom in the Bering Sea, Geophys. Res. Lett., 35, L24601.

Aguilar-Islas, A. M., Rember, R., Nishino, S., Kikuchi, T., Itoh, M., 2013. Partitioning and lateral transport of iron to the Canada Basin. Polar Science, 7(2), 82–99.

Alsdorf, D., Beighley, E., Laraque, A., Lee, H., Tshimanga, R., O'Loughlin, F., Mahé, G., Dinga, B., Moukandi, G., Spencer, R.G.M., 2016. Opportunities for hydrologic

research in the Congo Basin. Rev. Geophys. 54, 378–409.

Arrigo, K. R., van Dijken G. L., Pabi, S., 2008. Impact of a shrinking Arctic ice cover on marine primary production. Geophys. Res. Lett., 35, L19603.

Arrigo, K. R., van Dijken, G. L., 2015. Continued increases in Arctic Ocean primary production. Progress in Oceanography, 136, 60-70.

Arrigo, K. R., Mills, M. M., van Dijken, G. L., Lowry, K. E., Pickart, R. S., Schlitzer, R., 2017. Late Spring Nitrate Distributions Beneath the Ice-Covered Northeastern Chukchi Shelf, Journal of Geophysical Research: Biogeosciences, 95(17), 18, 163–9.

Balas, N., Nicholson, E.S., Klotter, D., 2007. The relationship of rainfall variability in West Central Africa to sea-surface temperature fluctuations. Int. J. Climatol. 27, 1335–1349.

Baskaran, M., Naidu, A. S., 1995. 210Pb-derived chronology and the fluxes of 210Pb and 137 Cs isotopes into continental shelf sediments, East Chukchi Sea, Alaskan Arctic. Geochimica et Cosmochimica Acta, 59(21), 4435–4448.

Benner, R., Opsahl, S., 2001. Molecular indicators of the sources and transformations of dissolved organic matter in the Mississippi river plume. Org. Geochem. 32, 597–611.

Biller, D. V., Bruland, K. W., 2013. Source and distribution of Mn, Fe, Co, Ni, Cu, Zn, and Cd relative to macronutrients along the central California coast during the spring and summer upwelling season. Marine Chemistry, 155, 50-70.

Birchill, A.J., Hartner, N.T., Kunde, K., Siemering, B., Daniels, C., González-Santana, D., Milne, A., Ussher, S.J., Worsfold, P.J., Leopold, K., Painter, S.C., Lohan, M.C., 2019. The eastern extent of seasonal iron limitation in the high latitude North Atlantic Ocean. Sci. Rep. 9, 1–12.

Bourdon, B., Henderson, G. M., Lundstrom, C. C., Turner S., 2003. Uranium-series geochemistry. Reviews in Mineralogy and Geochemistry, 52, 656 pp.

Bourquin, M., van Beek, P., Reyss, J.L., Riotte, J., Freydier, R., 2011. Determination of 226Ra concentrations in seawater and suspended particles (NW Pacific) using MC-ICP-MS. Mar. Chem. 126, 132–138.

Bowden, K., 1980. Physical factors: salinity, temperature, circulation and mixing processes, in: Olausson, E., Cato, I. (Eds.), Chemistry and Biogeochemistry of Estuaries. John Wiley & Sons, Chichester, 38-68 pp.

Boyd, P.W., Ibisanmi, E., Sander, S.G., Hunter, K.A., Jackson, G.A., 2010. Remineralization of upper ocean particles: implications for iron biogeochemistry. Limnol. Oceanogr. 55, 1271–1288.

Boyle, E., Edmond, I.M., 1975. Copper in surface waters south of New Zealand. Nature 253, 107-109.

Boyle, E. A., Edmond, J. M., Sholkovitz, E. R. , 1977. The mechanism of iron removal in estuaries. Geochim. Cosmochim. Acta 41, 1313–1324.

Braga, E.S., Andrié, C., Bourlès, B., Vangriesheim, A., Baurand, F., Chuchla, R., 2004. Congo River signature and deep circulation in the eastern Guinea Basin. Deep. Res. Part I Oceanogr. Res. Pap. 51, 1057–1073.

Breitbarth, E., Achterberg, E.P., Ardelan, M.V., Baker, A. R., Bucciarelli, E., Chever, F., Croot, P.L., Duggen, S., Gledhill, M., Hassellov, M., Hassler, C., Hoffmann, L.J., Hunter, K. a., Hutchins, D. a., Ingri, J., Jickells, T., Lohan, M.C., Nielsdottir, M.C., Sarthou, G., Schoemann, V., Trapp, J.M., Turner, D.R., Ye, Y., 2010. Iron biogeochemistry across marine systems - progress from the past decade. Biogeosciences 7, 1075–1097.

Broecker, W.S., Li, Y.H., Cromwell, J., 1967. Radium-226 and radon-222: concentration in atlantic and pacific oceans. Science 158, 1307–10.

Broecker, W. S., Goddard, J., Sarmiento, J. L., 1976. The distribution of ^{226}Ra in the Atlantic Ocean. Earth and Planetary Science Letters 32, 220-235.

Brown, Z. W., Casciotti, K. L., Pickart, R. S., Swift, J. H., Arrigo, K. R., 2015. Aspects of the marine nitrogen cycle of the Chukchi Sea shelf and Canada Basin. Deep-Sea Research Part II: Topical Studies in Oceanography, 118, 73–87.

Browning, T.J., Achterberg, E.P., Rapp, I., Engel, A., Bertrand, E.M., Tagliabue, A., Moore, C.M., 2017. Nutrient co-limitation at the boundary of an oceanic gyre. Nature 551, 242–246.

Bruland, K.W., 1980. Oceanographic Distributions of Cadmium, Zinc, Nickel, and Copper in the North Pacific. Earth and Planetary Science Letters 47, 176-198.

Bruland, K. W., Lohan M. C., 2003. Controls on trace metals in seawater, in: Elderfield, H. (Eds.), The Oceans and Marine Geochemistry. Treatise on Geochemistry, Amsterdam, vol. 6, 23–47 pp.

Bruland K.W., 2009. GEOTRACES and SAFe Intercalibrations, Consensus Values for the GEOTRACES 2008 and SAFe Reference Samples. http://es.ucsc.edu/~kbruland/GeotracesSaFe/kwbGeotracesSaFe.html (Last access: April 2019).

Bruland, K. W., Middag, R., Lohan, M. C., 2014. Controls of Trace Metals in Seawater, in, Holland, H. D., Turekian, K. K. (Eds.), Treatise on Geochemistry, 2nd Ed., Elsevier, Oxford, 19-51 pp.

Buck, K.N., Lohan, M.C., Berger, C.J.M., Bruland, K.W., 2007. Dissolved iron speciation in two distinct river plumes and an estuary: Implications for riverine iron supply. Limnol. Oceanogr. 52, 843–855.

Buesseler, K.O., 1998. The decoupling of production and particulate export in the surface ocean. Global Biogeochem. Cycles 12, 297-310.

Burnett, W.C., Bokuniewicz, H., Huettel, M., Moore, W.S., Taniguchi, M., 2003. Groundwater and pore water inputs to the coastal zone. Biogeochemistry 66, 3–33.

Burnett,W.C., Aggarwal, P.K., Bokuniewicz, H., Cable, J.E., Charette, M.A., Kontar, E., Krupa, S., Kulkarni, K.M., Loveless, A., Moore, W.S., Oberdorfer, J.A., Oliveira, J., Ozyurt, N., Povinec, P., Privitera, A.M.G., Rajar, R., Ramessur, R.T., Scholten, J., Stieglitz, T., Taniguchi, M., Turner, J.V., 2006. Quantifying submarine groundwater discharge in the coastal zone via multiple methods. Sci. Total Environ. 367, 498–543.

Cai, W.-J., Wang, Y., Krest, J., Moore, W.S., 2003. The geochemistry of dissolved inorganic carbon in a surficial groundwater aquifer in North Inlet, South Carolina, and the carbon fluxes to the coastal ocean. Geochim. Cosmochim. Acta 67, 631–639.

Calvert, S.E., Price, N.B., 1983. Geochemistry of Namibian Shelf Sediments. In: Thiede, J., Suess, E. (Eds.), Coastal upwelling, its sediment record. Plenum Press, New York, 337–375 pp.

Carroll, J., Falkner, K. K., Brown, T., Moore, W. S., 1993. The role of the Ganges-Brahmaputra mixing zone in supplying barium and ^{226}Ra to the Bay of Bengal. Geochim. Cosmochim. Acta 57, 2981–2990.

Charette, M.A., Buesseler, K.O., Andrews, J.E., 2001. Utility of radium isotopes for evaluating the input and transport of groundwater-derived nitrogen to a cape cod estuary. Limnol. Oceanogr. 46, 465–470.

Charette, M. A., Gonneea, M. E., Morris, P. J., Statham, P., Fones, G., Planquette, H., Salter, I., Garabato, A. N., 2007. Radium isotopes as tracers of iron sources fuelling a Southern Ocean phytoplankton bloom. Deep-Sea Research II, 54, 1989–1998.

Charette, M.A., Morris, P.J., Henderson, P.B., Moore, W.S., 2015. Radium isotope distributions during the US GEOTRACES North Atlantic cruises. Mar. Chem. 177 (Part 1), 184–195.

Charette, M.A., Lam, P.J., Lohan, M.C., Kwon, E.Y., Hatje, V., Jeandel, C., Shiller, A.M., Cutter, G.A., Thomas, A., Boyd, P.W., Homoky, W.B., Milne, A., Thomas, H., Anderson, P.S., Porcelli, D., Tanaka, T., Geibert, W., Dehairs, F., Garcia-Orellana, J., 2016. Coastal ocean and shelf-sea biogeochemical cycling of trace elements and isotopes : lessons learned from GEOTRACES. Phil.Trans.R.Soc.A 374: 20160076, 1–19.

Chase, Z., Strutton, P.G., Hales, B., 2007. Iron links river runoff and shelf width to phytoplankton biomass along the U.S. West Coast. Geophys. Res. Lett. 34, 10–13.

Chester, R., Jickells, T., 2012. Marine Geochemistry, 3rd Ed. Wiley-Blackwell, Oxford.

Chung, Y., Craig, H., 1980. ^{226}Ra in the Pacific Ocean. Earth Planet. Sci. Lett. 49 (2), 267–292.

Chung, Y., 1980. Radium–barium–silica correlations and a two-dimensional radium model for the world ocean. Earth Planet. Sci. Lett. 49 (2), 309–318.

Cid, A.P., Urushihara, S., Minami, T., Norisuye, K., Sohrin, Y., 2011. Stoichiometry among bioactive trace metals in seawater on the Bering Sea shelf. J. Oceanogr. 67 (6), 747–764.

Cid, A.P., Nakatsuka, S., Sohrin, Y., 2012. Stoichiometry among bioactive trace metals in the Chukchi and Beaufort Seas. J. Oceanogr. 68 (6), 985–1001.

Clark, I., 2015. Groundwater geochemistry and isotopes. CRC Press, Boca Raton, FL.

Coachman, L.K., Aagaard, K., Tripp, R.B., 1975. Bering Strait: The Regional Physical Oceanography. University of Washington Press, Seattle.

Cochran J. K., 1980. The flux of 226Ra from deep-sea sediments. Earth Planet. Sci. Lett. 49, 381–392.

Cochran, J. K., 1984. The fates of uranium and thorium decay series nuclides in the estuarine environment, in: Kennedy, V. S. (Ed.), The Estuary as a Filter. Academic Press, NewYork, 179–220 pp.

Cochran, J. K., S. Krishnaswami., 1980. Radium, thorium, uranium and ^{210}Pb in deep-sea sediments and sediment pore waters from the North Equatorial Pacific. American Journal of Science, 280, 849–889.

Connelly, T.L., Baer, S.E., Cooper, J.T., Bronk, D.A.,Wawrik, B., 2014. Urea uptake and carbon fixation by marine pelagic bacteria and archaea during the Arctic summer and winter seasons. Appl. Environ. Microbiol. 80 (19), 6013–6022.

Cooper, L. W., Whitledge, T. E., Grebmeier, J. M., Weingartner, T., 1997. The nutrient, salinity, and stable oxygen isotope composition of Bering and Chukchi Sea waters. Journal of Geophysical Research, 102(C6), 12563–12573.

Copenhagen, W. J., 1934. Sulfur as a factor in the corrosion of iron and steel structures in the sea. Trans. R. Soc. S. Afr., 22, 103–127.

Corlett, W.B., Pickart, R.S., 2017. The Chukchi slope current. Prog. Oceanogr. 153, 50–65.

Crotwell, A. M., Moore, W. S., 2003. Nutrient and Radium and Fluxes from Submarine and Groundwater Discharge to Port Royal Sound, South Carolina, Aquat. Geochem., 9, 191–208.

Cullen, J. T., 2006. On the nonlinear relationship between dissolved cadmium and phosphate in the modern global ocean: could chronic iron limitation of phytoplankton growth cause the kink? Limnol Oceanogr 51:1369–1380.

Dale, A. W., Nickelsen, L., Scholz, F., Hensen, C., Oschlies, A., Wallmann. K., 2015. A revised global estimate of dissolved iron fluxes from marine sediments. Glob. Biogeochem. Cycles 29, 691–707.

de Jong, J., Schoemann, V., Lannuzel, D., Tison, J.-L., Mattielli, N., 2008. High-accuracy

determination of iron in seawater by isotope dilution multiple collector inductively coupled plasma mass spectrometry (ID-MC-ICP-MS) using nitrilotriacetic acid chelating resin for pre-concentration and matrix separation, Anal. Chim. Acta, 623, 126–139.

Denamiel, C., Budgell, W. P., Toumi, R., 2013. The congo river plume: Impact of the forcing on the far-field and near-field dynamics. J. Geophys. Res. Ocean. 118, 964–989.

Dong, B.-W., Sutton, R.T., 2002. Adjustment of the coupled ocean-atmosphere system to a sudden change in the Thermohaline Circulation. Geophys. Res. Lett. 29, 18-1-18–4.

Duce, R. A., Tindale, N. W., 1991. Atmospheric transport of iron and its deposition in the ocean. Limnol. Oceanogr. 36, 1715–1726.

Duce, R.A., Liss, P.S., Merrill, J.T., Atlas, E.L., Buat-Menard, P., Hicks, B.B., Miller, J.M., Prospero, J.M., Arimoto, R., Church, T.M., Ellis, W., Galloway, J.N., Hansen, L., Jickells, T.D., Knap, A.H., Reinhardt, K.H., Schneider, B., Soudine, A., Tokos, J.J., Tsunogai, S., Wollast, R., Zhou, M., 1991. The atmospheric input of trace species to the world ocean. Glob. Biogeochem. Cycles 5, 193–259.

Dulaiova, H., Ardelan, M. V., Henderson, P.B., Charette, M.A., 2009. Shelf-derived iron inputs drive biological productivity in the southern Drake Passage. Global Biogeochem. Cycles 23, 1–14.

Eckardt, F., Soderberg, K., Coop, L., Muller, A., Vickery, K., Grandin, R., Jack, C., Kapalanga, T., Henschel, J., 2013. The nature of moisture at Gobabeb, in thecentral Namib Desert. J. Arid Environ. 93, 7–19.

Eicken, H., Gradinger, R., Gaylord, A., Mahoney, A., Rigor, I., Melling, H., 2005. Sediment transport by sea ice in the Chukchi and Beaufort Seas: Increasing importance due to changing ice conditions? Deep-Sea Research Part II, 52(24–26), 3281–3302.

Eisma, D., van Bennekom, A.J., 1978. The Zaire river and estuary and the Zaire outflow in

the Atlantic Ocean. Netherlands J. Sea Res. 12, 255–272.

Elderfield, H., Hepworth, A., 1975. Diagenesis, metals and pollution in estuaries. Mar. Pollut. Bull. 6, 85–87.

Elrod, V. A., Berelson, W. M., Coale, K. H., Johnson, K. S., 2004. The flux of iron from continental shelf sediments: A missing source for global budgets, Geophys. Res. Lett., 31, L12307.

Elsinger, R.J., Moore, W.S., 1980. 226Ra behavior in the Pee Dee River-Winyah Bay estuary. Earth Planet. Sci. Lett. 48, 239–249.

Elsinger, R. J., Moore, W. S.. 1984. ^{226}Ra and ^{228}Ra in the mixing zones of the Pee Dee River-Winyah Bay, Yangtze River and Delaware Bay Estuaries. Estuar. Coast. Shelf Sci. 18, 601–613.

Emeis, K.C., Brüchert, V., Currie, B., Endler, R., Ferdelman, T., Kiessling, A., Leipe, T., Noli-Peard, K., Struck, U., Vogt, T., 2004. Shallow gas in shelf sediments of the Namibian coastal upwelling ecosystem. Cont. Shelf Res. 24, 627–642.

Farnsworth, A., White, E., Williams, R.J.C., Black, E., Kniveton, R.D., 2011. Understanding the large scale driving mechanisms of rainfall variability over Central Africa. Adv. Global Change Res. 3, 101–122.

Fauchereau, N., Trzaska, S., Rouault, M. Richard, Y., 2003. Rainfall variability and changes in Southern Africa during the 20th century in the global warming context. *Natural Hazards*, 29: 139-154.

Figuères, G., Martin, J.M., Meybeck, M., 1978. Iron behaviour in the Zaire estuary. Netherlands J. Sea Res. 12, 338–344.

Foster, D.A., Staubwasser, M., Henderson, G.M., 2004. 226Ra and Ba concentrations in the Ross Sea measured with multicollector ICP mass spectrometry. Mar. Chem. 87, 59–71. https://doi.org/10.1016/j.marchem.2004.02.003

Gaillardet, J., Viers, J., Dupré, B., 2003. Trace Elements in River Waters, in: Drever, J. I. (Ed.), Surface and Groundwater Weathering and Soils. Elsevier-Pergamon, Oxford, 225-272 pp.

Garcia-Solsona, E., Garcia-Orellana, J., Masqué, P., Dulaiova, H., 2008. Uncertainties associated with 223Ra and 224Ra measurements in water via a Delayed Coincidence Counter (RaDeCC). Mar. Chem. 109, 198–219.

Garzoli, S.L., Gordon, A.L., 1996. Origins and variability of the Bengela Current. J. Geophys. Res. 101, 897–906.

Geibert, W., Rodellas, V., Annett, A., van Beek, P., Garcia-Orellana, J., Hsieh, Y.-T., Masque, P., 2013. 226 Ra determination via the rate of 222 Rn ingrowth with the Radium Delayed Coincidence Counter (RaDeCC). Limnol. Oceanogr. Methods 11, 594–603.

Gordon, A.L., Bosley, K.T., 1991. Cyclonic gyre in the tropical South Atlantic. Deep Sea Res. Part A. Oceanogr. Res. Pap. 38, S323–S343.

Grebmeier, J. M., Cooper, L. W., Feder, H. W., Sirenko, B. I., 2006. Ecosystem dynamics of the Pacific-influenced Northern Bering and Chukchi Seas in the Amerasian Arctic, Prog. Oceanogr., 71(2–4), 331–361.

Gustafsson, O., Widerlund, A., Andersson, P. S., Ingri, J., Roos, P., Ledin, A, 2000. Colloid dynamics and transport of major elements through a boreal river - brackish bay mixing zone. Marine Chemistry, 71(1), 1–21 pp.

Hammond, D.E., Marton, R.A., Berelson, W.M., Ku, T.-L., 1990. Radium 228 distribution and mixing in San Nicolas and San Pedro Basins, southern California Borderland. J. Geophys. Res. 95 (C3), 3321–3335

Hänsler, A., Saeed, F., Jacob, D., 2013. Assessment of projected climate change signals over central Africa based on a multitude of global and regional climate projections. In: Haensler A, Jacob, D., Kabat, P., Ludwig, F. (Eds.), Climate change scenarios for

the Congo basin, climate service center, Climate Service Centre Report No. 11, Hamburg, Germany, 210 pp.

Hancock, G. J., Webster, I. T., Ford, P. W., Moore, W. S., 2000. Using Ra isotopes to examine transport processes controlling benthic fluxes into a shallow estuarine lagoon, Geochim. Cosmochim. Ac., 64, 3685–3699.

Hancock, G. J.,Webster, I. T., Stieglitz, T. C., 2006. Horizontal mixing of Great Barrier Reefwaters: Offshore diffusivity determined from radium isotope distribution, J. Geophys. Res., 111, 1–14.

Hanfand, C., 2002. Radium-226 and Radium-228 in the Atlantic Sector of the Southern Ocean. PhD Thesis, Alfred Wegener Institute, Bremerhaven Allemagne.

Hansen, H. P., Koroleff, F., 1999. Determination of nutrients, in Grasshoff, K., Kremling, K., Ehrhardt, M. (Eds.), Methods of seawater analysis. Wiley-VCH Verlag GmbH, Weinheim, 159–228 pp.

Heggie D., 1982. Copper in surface waters of the Bering Sea. Geochim Cosmochim Acta 46:1301–1306.

Heggie, D., Lewis, T., 1984. Cobalt in pore waters of marine sediments. Nature 311: 453–455

Henderson, P.B., Morris, P.J., Moore, W.S., Charette, M.A., 2013. Methodological advances for measuring low-level radium isotopes in seawater. J. Radioanal. Nucl. Chem. 296, 357–362.

Hill, V., Cota G., 2005. Spatial patterns of primary production on the shelf, slope and basin of the western Arctic in 202, Deep Sea Res. Part II, 52, 3344–3354.

Hinzman, L. D., Bettez, N. D., Bolton, W. R., Chapin, F. S., Dyurgerov, M. B., Fastie, C. L., Griffith, B., Hollister, R. D., Hope, A., Huntington, H. P., Jensen, A. M., Jia, G. J., Jorgenson, T., Kane, D. L., Klein, D. R., Kofinas, G., Lynch, A. H., Lloyd, A. H.,

McGuire, A. D., Nelson, F. E., Oechel, W. C., Osterkamp, T. E., Racine, C. H., Romanovsky, V. E., Stone, R. S., Stow, D. A., Sturm, M. Tweedie, C. E., Vourlitis, G. L., Walker, M. D., Walker, D. A., Webber, P. J., Welker, J. M., Winker, K. S., Yoshikawa, K., 2005. Evidence and implications of recent climate change in Northern Alaska and other Arctic regions. Climatic Change, 72(3), 251–298.

Homoky, W.B., Severmann, S., McManus, J., Berelson, W.M., Riedel, T.E., Statham, P.J., Mills, R.A., 2012. Dissolved oxygen and suspended particles regulate the benthic flux of iron from continental margins. Marine Chemistry, 134–135, 59–70.

Homoky, W.B., Weber, T., Berelson, W.M., Conway, T.M., Henderson, G.M., van Hulten, M., Jeandel, C., Severmann, S., Tagliabue, A., 2016. Quantifying trace element and isotope fluxes at the ocean–sediment boundary: a review, Philosophical Transactions of the Royal Society A: Mathematical, Physical and Engineering Sciences, 374(2081): 20160246.

Hong, H.S., Kester, D. R., 1985. Chemical forms of iron in the Connecticut River estuary. Estuar. Coast. Shelf Sci., 21 (4), 449-459.

Hopkins, J., Lucas, M., Dufau, C., Sutton, M., Stum, J., Lauret, O., Channelliere, C., 2013. Detection and variability of the Congo River plume from satellite derived sea surface temperature, salinity, ocean colour and sea level. Remote Sens. Environ., 139, 365–385.

Hopwood, M., Rapp, I., Schlosser, C., Achterberg, E. P., 2017. Hydrogen peroxide in deep waters from the Mediterranean Sea, South Atlantic and South Pacific Oceans. Scientific Reports, 7: 43436.

Hsieh Y. Te, Geibert, W., van-Beek, P., Stahl, H., Aleynik, D., Henderson, G. M., 2013. Using the radium quartet (228Ra, 226Ra, 224Ra, and 223Ra) to estimate water mixing and radium inputs in Loch Etive, Scotland. Limnology and Oceanography, 58(3), 1089–1102.

Hsieh, Y. T., Henderson, G. M., 2011. Precise measurement of Ra-228/Ra-226 ratios and Ra concentrations in seawater samples by multi-collector ICP mass spectrometry. J. Anal. Atom. Spectrom. 26:1338-1346.

Hunt, G.L., Blanchard, A.L., Boveng, P., Dalpadado, P., Drinkwater, K.F., Eisner, L., Hopcroft, R.R., Kovacs, K.M., Norcross, B.L., Renaud, P., Reigstad, M., Renner, M., Skjoldal, H.R., Whitehouse, A., Woodgate, R.A., 2013. The Barents and Chukchi Seas: Comparison of two Arctic shelf ecosystems. J. Mar. Syst. 109–110.

Hurst, M.P., Aguilar-Islas, A.M., Bruland, K.W., 2010. Iron in the southeastern Bering Sea: elevated leachable particulate Fe in shelf bottom waters as an important source for surface waters. Continental Shelf Research 30, 467-480.

Iken, K., Bluhm, B., Dunton, K., 2010. Benthic food-web structure under differing water mass properties in the southern Chukchi Sea. Deep-Sea Research Part II: Topical Studies in Oceanography, 57(1–2), 71–85.

Ivanovich, M., Harmon, R. S., 1992. Uranium-series Disequilibrium: Applications to Earth, Marine, and Environmental Sciences. Clarendon Press, Oxford.

Jansen, J. H. F., Giresse, P., Moguedet, G., 1984. Structural and sedimentary geology of the Congo and Southern Gabon continental shelf; a seismic and acoustic reflection survey. Netherlands J. Sea Res. 17, 364–384.

Jickells, T., 1995. Atmospheric inputs of metals and nutrients to the oceans: their magnitude and effects. Mar. Chem. 48, 199–214.

Jickells, T.D., Baker, A.R., Brooks, N., Liss, P.S., An, Z.S., Cao, J.J., Andersen, K.K., Bergametti, C., Boyd, P.W., Hunter, K.A., Duce, R.A., Kawahata, H., Kubilay, N., LaRoche, J., Mahowald, N., Prospero, J.M., Ridgwell, A.J., Tegen, I., Torres, R., 2005. Global iron connections between desert dust, ocean biogeochemistry, and climate. Science (80), 308, 67–71.

Johnson, K.S., Chavez, F.P., Friederich, G.E., 1999. Continental-shelf sediment as a primary source of iron for coastal phytoplankton. Nature 398, 697–700.

Jones, E. P., Anderson, L. G., 1986. On the origin of the chemical properties of the Arctic Ocean halocline. J. Geophys. Res., 91, 10,759–10,767.

Jones, M. R., Nightingale, P. D., Turner, S. M., Liss, P. S., 2013. Adaptation of a load-inject valve for a flow injection chemiluminescence system enabling dual-reagent injection enhances understanding of environmental Fenton chemistry. Anal. Chim. Acta 796, 55–60.

Joung, D.J., Shiller, A.M., 2016. Temporal and spatial variations of dissolved and colloidal trace elements in Louisiana Shelf waters. Mar. Chem. 181, 25–43.

Kadko, D., 1996. Radioisotopic studies of submarine hydrothermal vents. Rev. Geophys. 34, 349–366.

Kadko, D., Moore, W., 1988. Radiochemical constraints on the crustal residence time of submarine hydrothermal fluids: Endeavour Ridge. Geochim. Cosmochim. Acta 52, 659–668.

Kadko, D., Muench, R., 2005. Evaluation of shelf-basin interaction in the western Arctic by us of short-lived radium isotopes: The importance of mesoscale processes, Deep Sea Res., Part II, 52, 3227–3244.

Kaufman, A., Trier, R. M., Broecker, W. S., Feely, H. W., 1973. Distribution of ^{228}Ra in the world ocean. Journal of Geophysical Research, 78, 8827 -8848.

Key, R. M., Brewer, R. L., Stockwell, J. H., Guinasso Jr., N. L., and Schink, D. R., 1979. Some improved techniques for measuring radon and radium in marine sediments and in seawater. Marine Chemistry, 7(3):251-264.

Key, R.M., Stallard, R.F., Moore, W.S., Sarmiento, J.L., 1985. Distribution and Flux of ^{226}Ra and ^{228}Ra in the Amazon River Estuary. J. Geophys. Res. 90, 6995–7004.

Kim, G., Burnett, W. C., Dulaiova, H., Swarzenski, P. W., Moore, W. S., 2001. Measurement of 224Ra and 226Ra Activities in Natural Waters Using a Radon-in-Air Monitor. Environmental Science & Technology, 35(23):4680-4683.

Kipp, L.E., Charette, M. A., Moore, W. S., Henderson, P. B., Rigor, I. G., 2018. Increased fluxes of shelf-derived materials to the central Arctic Ocean. Sci. Adv. 4, eaao1302.

Klunder, M. B., Bauch, D., Laan, P., de Baar, H. J. W., van Heuven, S., Ober, S., 2012a. Dissolved iron in the Arctic shelf seas and surface waters of the central Arctic Ocean: Impact of Arctic river water and ice-melt, J. Geophys. Res., 117, C01027.

Klunder, M. B., Laan, P., Middag, R., de Baar, H. J. W., Bakker, K., 2012b. Dissolved iron in the Arctic Ocean: Important role of hydrothermal sources, shelf input and scavenging removal, J. Geophys. Res., 117, C04014.

Koczy, F. F., 1958. Natural radium as a tracer in the ocean, in: Proceedings of the Second U.S. Internation Conference on Peaceful Uses of Atomic Energy, 18, 351–357.

Kondo, Y., Obata, H., Hioki, N., Ooki, A., Nishino, S., Kikuchi, T., Kuma, K., 2016. Transport of trace metals (Mn, Fe, Ni, Zn and Cd) in the western Arctic Ocean (Chukchi Sea and Canada Basin) in late summer 2012. Deep Sea Research Part I: Oceanographic Research Papers, 116, 236–252.

Knauss, K.G., Ku, T.-L., Moore, W.S., 1978. Radium and thorium isotopes in the surface waters of the East Pacific and coastal Southern California. Earth Planet. Sci. Lett. 39, 235-249.

Krachler, R., Jirsa, F., Ayromlou, S., 2005. Factors influencing the dissolved iron input by river water to the open ocean. Biogeosciences 2, 311–315.

Krest, J. M., Moore, W. S., Rama., 1999. ^{226}Ra and ^{228}Ra in the mixing zones of the Mississippi and Atchafalaya rivers: Indicators of groundwater input. Mar. Chem. 64, 129–152.

Krishnaswami, S., Cochran, J. K., 2008. U-Th Series Nuclides in Aquatic Systems, vol 13. Elsevier, Amsterdam.

Ku, T. L., Li, Y. H., Mathieu, G. G., Wong, H. K., 1970. Radium in the Indian-Antarctic Ocean south of Australia. Journal of Geophysical Research 75(27), 5286-5292.

Ku, T. L., Lin, M. C., 1976. ^{226}Ra distribution in the Antarctic Ocean. Earth and Planetary Science Letters 32(2), 236-248

Ku, T. L., Luo, S., 1994. New appraisal of Radium-226 as a large-scale oceanic mixing tracer. J. Geophys. Res. 99, 10255-10273

Ku, T. L., Luo, S., 2008. Ocean Circulation/Mixing Studies with Decay-Series Isotopes, in: Krishnaswami, S., Cochran, J. K. (Eds), Radioactivity in the Environment, vol. 13, Elsevier, Amsterdam, 307–344 pp.

Kwon, E. Y., Kim, G., Primeau, F., Moore, W. S., Cho, H. M., DeVries, T., Sarmiento, J. L., Charette, M. A., Cho, Y. K., 2014. Global estimate of submarine groundwater discharge based on an observationally constrained radium isotope model. Geophysical Research Letters 41(23), 2014GL061574.

Landing, W. M., Bruland K. W., 1987. The contrasting biogeochemistry of manganese and iron in the Pacific ocean. Geochimica et Cosmochimica Acta, 51, 29–43.

Langmuir, D.,, Herman, J.,1980. The mobility of Th in natural waters at low temperatures. Geochimica et Cosmochimica Acta, 44, 1753–1766.

Lannuzel, D., Schoemann, V., de Jong, J., Tison, J.L., Chou, L., 2007. Distribution and biogeochemical behaviour of iron in the East Antarctic sea ice. Marine Chemistry. 106, 18–32.

Lass, H. U., Schmidt, M., Mohrholz, V., Nausch, G., 2000. Hydrographic and current measurements in the area of the Angola-Benguela Front. Journal of Physical Oceanography, 30, 2589-2609.

Lepore, K., Moran, S.B., Smith, J.N., 2009. 210Pb as a tracer of shelf-basin transport and sediment focusing in the Chukchi Sea. Deep. Res. Part II Top. Stud. Oceanogr. 56, 1305–1315.

Levy, D. M., Moore, W. S. 1985. Ra-224 in continental shelf waters, Earth Planet. Sci. Lett. 73, 226-230.

Li, Q., Chen, M., Jia, R., Zeng, J., Lin, H., Zheng, M., Qiu, Y., 2017. Transit time of river water in the Bering and Chukchi Seas estimated from δ 18O and radium isotopes. Progress in Oceanography 159, 115-129.

Li, Y. H., Ku, T. L., Mathieu, G. G., Wolgemuth, K., 1973. Barium in the Antarctic Ocean and implications regarding the marine geochemistry of Ba and226Ra, Earth Planet. Sc. Lett., 19, 352–358.

Li, Y.H., Mathieu, G., Biscaye, P., Simpson, H.J., 1977. The flux of ^{226}Ra from estuarine and continental shelf sediments. Earth Planet. Sci. Lett. 37, 237–241.

Li, Y-H., Feely, H. W., Santschi, P. H., 1979. 228Th-228Ra radioactive disequilibrium in the New York Bight and its implications for coastal pollution, Earth Planet. Sci. Lett., 42, 13-26.

Li, Y.-H., Feely, H. W., Toggweiler, J. R., 1980. ^{228}Ra and ^{228}Th concentrations in GEOSECS Atlantic surface waters. Deep Sea Research Part I : Oceanographic Research Papers 27A, 545-555.

Libes, S.M., 2009. Introduction to marine biogeochemistry, 2nd Ed. Academic Press, Elsevier, Amsterdam.

Lohan, M.C., Bruland, K.W., 2008. Elevated Fe (II) and dissolved Fe in hypoxic shelf waters off Oregon and Washington: An enhanced source of iron to coastal upwelling regimes. Environmental Science & Technology, 42(17): 6462-6468.

Loose, B., Kelly, R. P., Bigdeli, A., Williams, W., Krishfield, R., Rutgers van der Loeff, M., Moran, S. B., 2017. How well does wind speed predict air-sea gas transfer in the sea ice zone? A synthesis of radon deficit profiles in the upper water column of the Arctic Ocean, J. Geophys. Res. Oceans, 122, 3696–3714

Lowry, K. E., Pickart, R. S., Selz, V., Mills, M. M., Pacini, A., Lewis, K. M., Joy-Warren, H. L., Nobre, C., van Dijken, G. L., Grondin, P-L., Ferland, J., Arrigo, K. R., 2018. Under-ice phytoplankton blooms inhibited by spring convective mixing in refreezing leads. Journal of Geophysical Research: Oceans, 123, 90–109.

Lu, X., Wang, L., Pan, M., Kaseke, K. F., Li, B., 2016. A multi-scale analysis of Namibian rainfall over the recent decade – comparing TMPA satellite estimates and ground observations. Journal of Hydrology: Regional Studies, 8, 59-68.

Lutjeharms, J.R.E., Valentine, H.R., 1987. Water types and volumetric considerations of the South-East Atlantic upwelling regime. South African J. Mar. Sci. 5, 63–71.

Macias, D., Garcia-Gorriz, E., Piroddi, C., Stips, A., 2014. Biogeochemical control of marine productivity in the Mediterranean Sea during the last 50years. Glob. Biogeochem. Cycles 28, 897-907.

McManus J., Berelson, W. M., Severmann, S., Johnson, K. S., Hammond, D. E., Roy, M., Coale, K. H., 2012. Benthic manganese fluxes along the Oregon-California continental shelf and slope. Cont. Shelf Res. 43, 71–85.

Mahowald, N.M., Baker, A.R., Bergametti, G., Brooks, N., Duce, R.A., Jickells, T.D., Kubilay, N., Prospero, J.M., Tegen, I., 2005. Atmospheric global dust cycle and iron inputs to the ocean. Global Biogeochem. Cycles 19, GB4025.

Maring, H.B., Duce, R.A., 1990. The Impact of Atmospheric Aerosols on Trace Metal Chemistry In Open Ocean Surface Seawater 3. Lead. J. Geophys. Res. 95, 5341–5347.

Mathis, J. T., Pickart, R. S., Hansell, D. A., Kadko, D., Bates, N. R., 2007. Eddy transport of

organic carbon and nutrients from the Chukchi Shelf: Impact on the upper halocline of the western Arctic Ocean. Journal of Geophysical Research: Oceans, 112(5), 1–14.

Mathis, J.T., Grebmeier, J.M., Hansell, D.A., Hopcroft, R.R., Kirchman, D., Lee, S.H., Moran, S.B., Bates, N. R., VanLaningham, S., Cross, J. N, Cai W-J., 2014. Carbon Biogeochemistry of the Western Arctic: Production, Export and Ocean Acidification. In: Grebmeier J. M., Maslowski, W. (Eds.), The Pacific Arctic Region. Springer, Dordrecht, 223-268 pp.

Mayer, L.M., 1982. Retention of riverine iron in estuaries. Geochim. Cosmochim. Acta 46, 1003–1009.

Mcinnes, K.L., Erwin, T.A., Bathols, J.M., 2011. Global Climate Model projected changes in 10 m wind speed and direction due to anthropogenic climate change. Atmos. Sci. Lett. 12, 325–333.

McKee, B.A., 2008. U- and Th-Series Nuclides in Estuarine Environments. In: Krishnaswami, S., Cochran J. K., (Eds.), U–Th Series Nuclides in Aquatic Systems, vol 13. Elsevier, Amsterdam, 193-225 pp.

Measures, C.I., 1999. The role of entrained sediments in sea ice in the distribution of aluminium and iron in the surface waters of the Arctic Ocean. Marine Chemistry. 68, 59–70.

Michel, C., Ingram, R. G., Harris, L. R., 2006. Variability in oceanographic and ecological processes in the Canadian Arctic Archipelago, Progress in Oceanography, 71(2–4), 379–401.

Michel, J., Moore, W.S., King, P.T., 1981. γ-ray Spectrometry for Determination of Radium-228 and Radium-226 in Natural Waters. Anal. Chem., 53, 1885-1889.

Milliman, J.D., Farnsworth, K.L., 2011. River discharge to the coastal ocean: A global synthesis. Cambridge University Press, New York.

Mills, M.M., Brown, Z.W., Lowry, K.E., van Dijken, G.L., Becker, S., Pal, S., Benitez-Nelson, C.R., Downer, M.M., Strong, A.L., Swift, J.H., Pickart, R.S., Arrigo, K.R., 2015. Impacts of low phytoplankton NO_3-: PO_4^{3-} utilization ratios over the Chukchi Shelf, Arctic Ocean. Deep. Res. Part II Top. Stud. Oceanogr. 118, 105–121.

Milne, A., Landing, W., Bizimis, M., Morton, P., 2010. Determination of Mn, Fe, Co, Ni, Cu, Zn, Cd and Pb in seawater using high resolution magnetic sector inductively coupled mass spectrometry (HR-ICP-MS). Anal. Chim. Acta 665, 200–207.

Milne, A., Schlosser, C., Wake, B. D., Achterberg, E. P., Chance, R., Baker, A. R., Forryan, A., Lohan M. C., 2017. Particulate phases are key in controlling dissolved iron concentrations in the (sub)tropical North Atlantic, Geophysical Research Letters., 44, 2377–2387.

Moffett, J.W., Ho, J., 1996. Oxidation of cobalt and manganese in seawater via a common microbially catalyzed pathway. Geochim. Cosmochim. Acta 60, 3415–3424.

Mohrholz, V., Bartholomae, C.H., van der Plas, A.K., Lass, H.U., 2008. The seasonal variability of the northern Benguela undercurrent and its relation to the oxygen budget on the shelf. Cont. Shelf Res. 28, 424–441.

Moore, C.M., Mills, M.M., Arrigo, K.R., Berman-Frank, I., Bopp, L., Boyd, P.W., Galbraith, E.D., Geider, R.J., Guieu, C., Jaccard, S.L., Jickells, T.D., La Roche, J., Lenton, T.M., Mahowald, N.M., Marañón, E., Marinov, I., Moore, G.W.K., Nakatsuka, T., Oschlies, A., Saito, M.A., Thingstad, T.F., Tsuda, A., Ulloa, O., 2013. Processes and patterns of oceanic nutrient limitation. Nat. Geosci. 6, 701–710.

Moore, R. M., Lowings, M. G., Tan, F. C., 1983. Geochemical profiles in the central Arctic Ocean: Their relationship to freezing and shallow circulation. J. Geophys. Res., 88, 2667–2674.

Moore, R. M., 1983. The relationship between distributions of dissolved cadmium, iron and aluminium and hydrography in the central Arctic Ocean, in: Wong, C.S., Boyle, E.,

Bruland K.W., Burton J.D., Goldberg E.D. (Eds.), Trace Metals in Sea Water. NATO Conference Series (IV Marine Sciences), vol 9. Springer, Boston, 131–142 pp.

Moore, W. S., 1969. Oceanic concentrations of ^{228}Radium. Earth and Planetary Science Letters 6(6), 437- 446.

Moore, W.S., 1972. Ra-228 - application to thermocline mixing studies. Earth Planet. Sci. Lett.16 (3),421–446.

Moore, W.S., 1976. Sampling 228Ra in the deep ocean. Deep. Res. 23, 647–651.

Moore, W.S., Key, R.M., Sarmiento, J.L., 1985. Techniques for precise mapping of Ra-226 and Ra-228 in the Ocean. J. Geophys. Res. 90, 6983–6994.

Moore, W.S., 1986. Tracing the Amazon Component of Surface Atlantic Water Using ^{228}Ra, Salinity and Silica. J. Geophys. Res. 91, 2574–2580.

Moore, W.S., 1987. Radium 228 in the South Atlantic Bight. Journal of Geophysical Research: Oceans, 92(C5), 5177–5190.

Moore, W.S., Dymond, J., 1991. Fluxes of ^{226}Ra and barium in the Pacific Ocean: The importance of boundary processes. Earth Planet. Sci. Lett. 107, 55–68.

Moore, W. S., Todd, J. F., 1993. Radium isotopes in the Orinoco Estuary and eastern Caribbean Sea. J. Geophys. Res. 98, 2233–2244.

Moore, W.S., Astwood, H., Lindstrom, C., 1995. Radium isotopes in coastal waters on the Amazon shelf. Geochim. Cosmochim. Acta 59 (20), 4285–4298.

Moore, W.S., Arnold, R., 1996. Measurement of 223Ra and 224Ra in coastal waters using a delayed coincidence counter. J. Geophys. Res. 101, 1321–1329.

Moore, W.S., 1996. Using the radium quartet for evaluating groundwater input and water exchange in salt marshes. Geochim. Cosmochim. Acta 60, 4645–4652.

Moore, W.S., Demaster, D.J., Smoak, J.M., Mckee, B.A., Swarzenski$, P.W., 1996. Radionuclide tracers of sediment-water interactions on the Amazon shelf. Cont. Shelf. Research 16, 645–665.

Moore, W.S., Shaw, T.J., 1998. Chemical signals from submarine fluid advection onto the continental shelf. J. Geophys. Res. 103, 543–552.

Moore, W.S., 2000 a. Determining coastal mixing rates using radium isotopes. Cont. Shelf Res. 20, 1993–2007.

Moore, W.S., 2000 b. Ages of continental shelf waters determined from $^{223}Ra/^{224}Ra$. Journal Geophysical Research 105, 22,117-122,122.

Moore, W.S., 2004. Ages of continental shelf waters determined from 223Ra and 224Ra. J. Geophys. Res. Ocean. 105, 22117–22122.

Moore, W.S., 2008. Fifteen years experience in measuring 224Ra and 223Ra by delayed-coincidence counting. Mar. Chem. 109, 188–197.

Moore, W.S., Sarmiento, J.L., Key, R.M., 2008. Submarine groundwater discharge revealed by 228Ra distribution in the upper Atlantic Ocean. Nat. Geosci. 1, 309–311.

Moore, W.S., Shaw, T.J., 2008. Fluxes and behavior of radium isotopes, barium, and uranium in seven Southeastern US rivers and estuaries. Marine Chemistry. 108, 236–254.

Moore, W.S., Cai, P., 2013. Calibration of RaDeCC systems for 223Ra measurements. Marine Chemistry. 156, 130–137.

Morel, F.M.M., Price, N.M., 2003. The Biogeochemical Cycles of Trace Metals in the Oceans. Science (80-.). 300, 944–947.

Morishima, W., Akasaka, I., 2010. Seasonal trends of rainfall and surface temperature over Southern Africa. African Study Monographs, Suppl.40: 67-76.

Nakayama, Y., Fujita, S., Kuma, K., Shimada, K., 2011. Iron and humic-type fluorescent dissolved organic matter in the Chukchi Sea and Canada Basin of the western Arctic Ocean. J. Geophys. Res. 116, C07031.

National Snow & Ice Data Center (NSIDC). https://nsidc.org/data (accessed 14 May 2018).

Nelson, G., Hutchings, L., 1983. The Benguela upwelling area. Progress in Oceanography 12, 333–356.

Noble, A. E., Echegoyen-Sanz, Y., Boyle, E. A., Ohnemus, D. C., Lam, P. J., Kayser, R., Reuer, M., Wu, J., Smethie, W., 2015. Dynamic variability of dissolved Pb and Pb isotope composition from the U.S. North Atlantic GEOTRACES transect. Deep-Sea Research Part II: Topical Studies in Oceanography, 116, 208–225.

Nof, D., Pichevin, T., Sprintall, J., 2002. "Teddies" and the Origin of the Leeuwin Current. J. Phys. Oceanogr. 32, 2571–2588.

Nozaki, Y., Zhang, J., Takeda, A., 1997. ^{210}Pb and ^{210}Po in the equatorial Pacific and the Bering Sea: The effects of biological productivity and boundary scavenging. Deep. Res. Part II Top. Stud. Oceanogr. 44, 2203-2220.

Ohde, T., Mohrholz, V., 2011. Interannual variability of sulphur plumes off the Namibian coast. Int. J. Remote Sens. 32 (24), 9327–9342.

Okubo, T., Furuyama, K., Sakanoue, M., 1979. Distribution of radium-228 in surface seawater of the east Indian Ocean. Geochem. J. 13, 201-206.

Osterkamp, T.E., 2007. The recent warming of permafrost in Alaska. Glob. Planet. Change 49, 187–202.

Pacini, A., Pickart, R. S., Moore, G. W. K., Våge, K., 2016. Hydrographic structure and modification of Pacific winter water on the Chukchi Sea shelf in late spring, Eos, Transactions American Geophysical Union, Abstract H14B-1406.

Palma, E.D., Matano, R.P., 2017. Journal of Geophysical Research : Oceans An idealized study of near equatorial river plumes. J. Geophys. Res. Ocean. 122, 3599–3620.

Peckham, S.D., Manley, W.F., Dyurgerov, M., Syvitski, J.P.M., 2001. Modeling Coastal Erosion Near Barrow, Alaska. Arct. Coast. Dyn. Rep. an Int. Work. Potsdam 26-30 Novemb. 3, 46–47.

Peterson, B. J., Holmes, R. M., McClelland, J.W., Vörösmarty C. J., Lammers, R. B., Shiklomanov A. I., Shiklomanov, I. A., Rahmstorf, S., 2002. Increasing river discharge to the Arctic Ocean, Science 298, 2171–2173.

Poccard, I., Janicot, S., Camberlin, P., 2000. Comparison of rainfall structures between NCEP/NCAR reanalyses and observed data over tropical Africa. Clim. Dyn. 16, 897–915.

Powell, R.T., Wilson-Finelli, A., 2003. Importance of organic Fe complexing ligands in the Mississippi River plume. Estuar. Coast. Shelf Sci. 58, 757–763.

Prospero, J.M., Ginoux, P., Torres, O., Nicholson, S.E., Gill, T.E., 2002. Environmental characterization of global sources of atmospheric soil dust identified with the Nimbus 7 Total Ozone Mapping Spectrometer (TOMS) absorbing aerosol product. Rev. Geophys. 40, 1–31.

Raiswell, R., Canfield, D. E., 2012. The Iron Biogeochemical Cycle Past and Present, Geochemical Perspectives, 1, 1-220.

Rama, Moore, W. S., 1996. Using the radium quartet for evaluating groundwater input and water exchange in salt marshes, Geochim. Cosmochim. Ac., 60, 4645–4652.

Rapp, I., Schlosser, C., Rusiecka, D., Gledhill, M., Achterberg, E. P., 2017. Automated preconcentration of Fe, Zn, Cu, Ni, Cd, Pb, Co, and Mn in seawater with analysis using high-resolution sector field inductively-coupled plasma mass spectrometry. Analytica Chimica Acta, 976, 1–13.

Reid, D.F., Moore, W.S., Sackett, W.M., 1979. Temporal variation of 228Ra in the near-surface Gulf of Mexico. Earth Planet. Sci. Lett. 43, 227–236.

Resing, J.A., Sedwick, P.N., German, C.R., Jenkins, W.J., Moffett, J.W., Sohst, B.M., Tagliabue, A., 2015. Basin-scale transport of hydrothermal dissolved metals across the South Pacific Ocean. Nature 523, 200–203.

Reyss, J.-L., Schmidt, S., Legeleux, F., Bonte, P., 1995. Large, low background well-type detectors for measurements of environ- mental radioactivity. Nucl. Inst. Meth. A 357, 391–397.

Rijkenberg, M.J.A., Steigenberger, S., Powell, C.F., Van Haren, H., Patey, M.D., Baker, A.R., Achterberg, E.P., 2012. Fluxes and distribution of dissolved iron in the eastern (sub-) tropical North Atlantic Ocean. Global Biogeochem. Cycles 26.

Rijkenberg, M.J.A., Middag, R., Laan, P., Gerringa, L.J.A., Van Aken, H.M., Schoemann, V., De Jong, J.T.M., De Baar, H.J.W., 2014. The distribution of dissolved iron in the West Atlantic Ocean. PLoS One 9, 1–14.

Rijkenberg, M.J.A., Slagter, H.A., Rutgers van der Loeff, M., van Ooijen, J., Gerringa, L.J.A., 2018. Dissolved Fe in the Deep and Upper Arctic Ocean With a Focus on Fe Limitation in the Nansen Basin. Front. Mar. Sci. 5, 1–14.

Rodellas, V., Garcia-Orellana, J., Masqué, P., Font-Muñoz, J.S., 2015. The influence of sediment sources on radium-derived estimates of Submarine Groundwater Discharge. Mar. Chem. 171, 107–117.

Rodellas, V., Garcia-Orellana, J., Trezzi, G., Masqué, P., Stieglitz, T.C., Bokuniewicz, H., Cochran, J.K., Berdalet, E., 2017. Using the radium quartet to quantify submarine groundwater discharge and porewater exchange. Geochim. Cosmochim. Acta 196, 58–73.

Romanovsky, V. E., Burgess, M., Smith, S., Yoshikawa, K., Brown, J., 2002. Permafrost temperature records: Indicators of climate change, Eos 83(50), 589/593–594.

Roy, E. Le, Sanial, V., Charette, M.A., Beek, P. Van, Lacan, F., Henderson, P.B., Souhaut, M., García-ibáñez, M.I., 2018. The 226Ra-Ba relationship in the North Atlantic during GEOTRACES-GA01. Biogeosciences 15, 3027–3048.

Rusiecka, D., Gledhill, M., Milne, A., Achterberg, E. P., Annett, A. L., Atkinson, S., Birchill, A., Karstensen, J., Lohan, M., Mariez, C., Middag, R., Rolison, J. M., Tanhua, T., Ussher, S., Connelly., D., 2018. Anthropogenic signatures of lead in the Northeast Atlantic. Geophysical Research Letters, 45, 2734 – 2743.

Rutgers van der Loeff M. M., Anderson L. G., Hall P. O. J., Iverfeldt A., Josefson A. B., Sundby B., Westerlund S. F. G., 1984. The asphyxiation technique: an approach to distinguish- ing between molecular diffusion and biologically mediated transport at the sediment-water interface. Limnol. Oceanogr. 29, 675–686.

Rutgers van der Loeff, M., Key, R. M., Scholten, J., Bauch, D., Michel, A., 1995. 228Ra as a tracer for shelf water in the Arctic Ocean. Deep Sea Res. Part II Top. Stud. Oceanogr. 42, 1533–1553.

Rutgers van der Loeff, M.M., Cai, P., Stimac, I., Bauch, D., Hanfland, C., Roeske, T., Moran, S.B., 2012. Shelf-basin exchange times of Arctic surface waters estimated from 228Th/228Ra disequilibrium. J. Geophys. Res. Ocean. 117.

Sanial, V., Kipp, L. E., Henderson, P. B., van Beek, P., Reyss, J. L., Hammond, D. E., Hawco, N. J., Saito, M.A., Resing, J.A., Sedwick, P., Moore, W.S., Charette, M. A., 2018. Radium-228 as a tracer of dissolved trace element inputs from the Peruvian continental margin. Marine Chemistry, 201, 20–34.

Santschi, P. H., Li, Y.-H., Bell, J., 1979. Natural radionuclides in the water of Narragansett Bay, Earth Planet. Sc. Lett., 45, 201–213.

Sarmiento, J.L., Rooth, C.G.H., Broecker, W.S., 1982. Radium 228 as a tracer of basin wide processes in the abyssal ocean. J. Geophys. Res. 87 (C12), 9694–9698.

Sarmiento, J.L., Thiele, G., Key, R.M., Moore, W.S., 1990. Oxygen and nitrate new

production and remineralization in the North-Atlantic subtropical gyre. J. Geophys. Res. Oceans 95 (C10), 18303–18315

Sarmiento, J.L., Simeon, J., Gnanadesikan, A., Gruber, N., Key, R.M., Schlitzer, R., 2007. Deep ocean biogeochemistry of silicic acid and nitrate. Global Biogeochem. Cycles 21, 1–16.

Serreze, M. C., Holland, M. M., Stroeve, J., 2007. Perspectives on the Arctic's shrinking sea-ice cover. Science 315, 1533–1536.

Schlitzer, R., Anderson, R. F., Masferrer Dodas, E, et al., 2018. The GEOTRACES Intermediate Data Product 2017, Chem. Geol. 210-223.

Shannon, L. V., 1985. The Benguela ecosystem. 1. Evolution of the Benguela, physical features and processes, in: Barnes M (Ed.), Oceanography and Marine Biology: An Annual Review, 23. Aberdeen University Press, Aberdeen, 105-182 pp.

Shannon L.V., Nelson G., 1996. The Benguela: large scale features and processes and system variability, in: Wefer, G., Berger, W.H., Siedler, G., Webb, D.J. (Eds.), The South Atlantic: past and present circulation. Springer, Berlin, 163-210 pp.

Shaw, T.J., Moore, W.S., Kloepfer, J., Sochaski, M.A., 1998. The flux of barium to the coastal waters of the southeastern United States: the importance of submarine groundwater discharge. Geochim. Cosmochim. Acta 62, 3047–3052

Shimada, K., Kamoshida, T., Itoh, M., Nishino, S., Carmack, E., McLaughlin, F., Zimmermann, S., Proshutinsky, A., 2006. Pacific Ocean inflow: Influence on catastrophic reduction of sea ice cover in the Arctic Ocean. Geophysical Research Letters 33, L08605.

Scholten, J.C., Pham, M.K., Blinova, O., Charette, M.A., Dulaiova, H., Eriksson, M., 2010. Preparation of Mn-fiber standards for the efficiency calibration of the delayed coincidence counting system (RaDeCC). Marine Chemistry. 121, 206–214.

Sholkovitz, E. R., Boyle, E. A., Price, N. B., 1978. The removal of dissolved humic acids and iron during estuarine mixing. Earth Planet. Sci. Lett. 40, 130–136.

Siedlecki, S. A., Mahadevan, A., Archer, D. E., 2012. Mechanism for export of sediment-derived iron in an upwelling regime. Geophys. Res. Lett., 39, L03601.

Signorini, S. R., Murtugudde, R. G., McClain, C. R., Christian, J. R., Picaut, J., Busalacchi, A. J., 1999. Biological and physical signatures in the tropical and subtropical Atlantic, J. Geophys. Res., 104(C8), 18,367–18,382.

Spencer, R.G.M., Hernes, P.J., Aufdenkampe, A.K., Baker, A., Gulliver, P., Stubbins, A., Aiken, G.R., Dyda, R.Y., Butler, K.D., Mwamba, V.L., Mangangu, A.M., Wabakanghanzi, J.N., Six, J., 2012. An initial investigation into the organic matter biogeochemistry of the Congo River. Geochim. Cosmochim. Acta 84, 614–627.

Spencer, R.G.M., Stubbins, A., Gaillardet, J., 2014. Geochemistry of the Congo River, Estuary and Plume, in: Bianchi, T.S., Allison, M.A., Cai, W.J. (Eds.), Biogeochemical Dynamics at Major River–Coastal Interfaces Linkages with Global Change. Cambridge University Press, Cambridge, 3–18 pp.

Springer, A. M., McRoy, C. P., Flint, M. V., 1996. The Bering Sea Green Belt: shelf-edge processes and ecosystem production. Fish Oceanogr 5, 205–223.

Stabeno, P. J., Schumacher, J. D., Davis R. F., Napp J. M., 1998. Under-ice observations of water column temperature, salinity and spring phytoplankton dynamics: Eastern Bering Sea shelf. Journal of Marine Research, 56, 239–255.

Stabeno, P.J., Danielson, S., Kachel, D., Kachel, N.B., Mordy, C.W., 2016. Currents and transport on the Eastern Bering Sea shelf: An integration of over 20 years of data. Deep Sea Res. Part II Top. Stud. Oceanogr. 134, 13–29.

Stabeno, P., Kachel, N., Ladd, C., Woodgate, R., 2018. Flow Patterns in the Eastern Chukchi Sea: 2010–2015. J. Geophys. Res. Ocean. 123, 1177–1195.

Stramma, L., Peterson, R., 1989. Geostrophic transport in the Benguela Current region. J. Phys. Oceanogr. 19, 1440–1448.

Stramma, L., England, M. H., 1999. On the water masses and mean circulation Atlantic Ocean. J. Geophys. Res. 104, 20,863-20,883.

Stramma, L., Schott, F., 1999. The mean flow field of the tropical Atlantic Ocean. Deep. Res. 46, 279–303.

Stumm, W., Morgan, J.J., 1981. Aquatic Chemistry: An Introduction Emphasizing Chemical Equilibria in Natural Waters. 2nd Ed. John Wiley & Sons Ltd., New York.

Stumm, W., Morgan, J.J., 1995. Aquatic Chemistry: Chemical Equilibria and Rates in Natural Waters. John Wiley & Sons, New York.

Sunda, W.G., Huntsman, S.A., Harvey, G.R., 1983. Photoreduction of manganese oxides in seawater and its geochemical and biological implications. Nature 301, 234–236.

Sunda, W. G., Huntsman S. A., 1988. Effect of sunlight on redox cycles of manganese in the southwestern Sargasso Sea. Deep-Sea Res. 35:1297-1317.

Symes, J.L., Kester, D.R., 1985. The distribution of iron in the Northwest Atlantic. Marine Chemistry 17, 57–74.

Tagliabue A, Aumont O, Bopp L., 2014. The impact of different external sources of iron on the global carbon cycle. Geophys. Res. Lett. 41, 920–926.

Tanaka, T., Yasuda, I., Kuma, K., Nishioka, J., 2015. Evaluation of the biogeochemical impact of iron-rich shelf water to the Green Belt in the southeastern Bering Sea. Continental Shelf Research, 143, 130-138.

Tang, J., Johannesson, K. H., 2006. Controls on the geochemistry of rare earth elements along a groundwater flow path in the Carrizo Sand aquifer, Texas, USA. Chem. Geol. 225, 156–171.

Taniguchi M, Uchida S, Kinoshita M., 2003. Periodical changes of submarine fluid discharge from a deep seafloor, Suiyo Sea Mountain, Japan. Geophys. Res. Lett. 30.

Taylor, R.L., Semeniuk, D.M., Payne, C.D., Zhou, J., Tremblay, J.É., Cullen, J.T., Maldonado, M.T., 2013. Colimitation by light, nitrate, and iron in the Beaufort Sea in late summer. J. Geophys. Res. Ocean. 118, 3260–3277.

Tchipalanga, P., Dengler, M., Brandt, P., Kopte, R., Macuéria, M., Coelho, P., Ostrowski, M., Keenlyside, N.S., 2018. Eastern Boundary Circulation and Hydrography Off Angola: Building Angolan Oceanographic Capacities. Bull. Am. Meteorol. Soc. 99, 1589–1605.

Thuróczy, C. E., Gerringa, L. J. A. Klunder, M., Laan, P., de Baar, H. J. W., 2011. Distinct trends in the speciation of iron between the shallow shelf seas and the deep basins of the Arctic Ocean, J. Geophys. Res. Ocean. 116, C10009.

Todd, J. F., Elsinger, R. J., Moore, W. S., 1988. The distributions of uranium, radium and thorium isotopes in two anoxic fjords: Framvaren Fjord (Norway) and Saanich Inlet (British Columbia). Marine Chemistry 23, 393–415.

Tovar-Sánchez, A., Duarte, C.M., Alonso, J.C., Lacorte, S., Tauler, R., Galban-Malagón, C., 2010. Impacts of metals and nutrients released from melting multiyear Arctic sea ice. J. Geophys. Res. Ocean. 115, 1–7.

Tovar-Sánchez, A., Basterretxea, G., Ben Omar, M., Jordi, A., Sánchez-Quiles, D., Makhani, M., Mouna, D., Muya, C., Anglès, S., 2016. Nutrients, trace metals and B-vitamin composition of the Moulouya River: A major North African river discharging into the Mediterranean Sea. Estuar. Coast. Shelf Sci. 176, 47–57.

Trefry, J. H., Trocine, R. P., Cooper, L. W., Dunton, K. H., 2014. Trace metals and organic carbon in sediments of the northeastern Chukchi Sea. Deep Sea Res. Part II Top. Stud. Oceanogr. 102, 18–31.

Tshimanga, R.M., Hughes, D.A., 2012. Climate change and impacts on the hydrology of the

Congo Basin: The case of the northern sub-basins of the Oubangui and Sangha Rivers. Phys. Chem. Earth 50–52, 72–83.

Valiela, I., Costa, J., Foreman, K., Teal, J. M., Howes, B., Aubrey, D., 1990. Transport of groundwater-borne nutrients from watersheds and their effects on coastal waters. Biogeochemistry 10, 177–197.

van Beek, P., François, R., Conte, M., Reyss, J. L., Souhaut, M., Charette, M., 2007. $^{228}Ra/^{226}Ra$ and $^{226}Ra/Ba$ ratios to track barite formation and transport in the water column. Geochimica et Cosmochimica Acta 71(1), 71-86.

van Beek, P., Souhaut, M., Reyss, J.-L., 2010. Measuring the radium quartet (228Ra, 226Ra, 224Ra, 223Ra) in seawater samples using gamma spectrometry. Journal of Environmental Radioactivity, 101 (7):521-529.

van Bennekom, A.J., Berger, G.W., 1984. Hydrography and silica budget of the Angola Basin. Netherlands J. Sea Res. 17, 149–200.

van der Merwe, P., Lannuzel, D., Bowie, A.R., Mancuso Nichols, C.A., Meiners, K.M., 2011. Iron fractionation in pack and fast ice in East Antarctica: Temporal decoupling between the release of dissolved and particulate iron during spring melt. Deep. Res. Part II Top. Stud. Oceanogr. 58, 1222–1236

Vandenhove, H., Verrezen, F., Landa, E. R., 2010. Radium, in: Atwood D. (Ed.), Radionuclides in the Environment. Wiley, Chichester, 97–108.

Vangriesheim, A., Pierre, C., Aminot, A., Metzl, N., Baurand, F., Caprais, J.C., 2009. The influence of Congo River discharges in the surface and deep layers of the Gulf of Guinea. Deep. Res. Part II Top. Stud. Oceanogr. 56, 2183–2196.

Varga, Z., 2008. Ultratrace-level radium-226 determination in seawater samples by isotope dilution inductively coupled plasma mass spectrometry. Anal. Bioanal. Chem. 390, 511–519

Vieira, L.H., Achterberg, E.P., Scholten, J., Beck, A.J., Liebetrau, V., Mills, M.M., Arrigo, K.R., 2019. Benthic fluxes of trace metals in the Chukchi Sea and their transport into the Arctic Ocean. Marine Chemistry. 208, 43–55.

Vic, C., Berger, H., Tréguier, A.-M., Couvelard, X., 2014. Dynamics of an Equatorial River Plume: Theory and Numerical Experiments Applied to the Congo Plume Case. J. Phys. Oceanogr. 44, 980-994.

Walsh, J. J., McRoy, C. P., Coachman, L. K., Goering, J. J., Nihoul, J. J., Whitledge, T. E., Blackburn, T. H., Parker, P. L., Wirick, C. D., Shuert, P. G., Grebmeier, J. M., Springer, A. M., Tripp, R. D., Hansell, D. A., Djenidi, S., Deleersnijder, E., Henriksen, K., Lund, B. A., Andersen, P., Müller-Karger, F. E., Dean, K., 1989. Carbon and nitrogen cycling within the Bering/Chukchi Seas: source regions for organic matter effecting AOU demands of the Arctic Ocean. Progr. Oceanogr. 22, 277–359.

Walvoord, M. A., Striegl, R. G., 2007. Increased groundwater to stream discharge from permafrost thawing in the Yukon River basin: Potential impacts on lateral export of carbon and nitrogen. Geophys. Res. Lett., 34, L12402.

Wang, D., Henrichs, S.M., Guo, L., 2006. Distributions of nutrients, dissolved organic carbon, and carbohydrates in the western Arctic Ocean. Cont. Shelf Res. 26 (14), 1654–1667.

Wang, S.L., Chen, C.T.A., Huang, T.H., Tseng, H.C., Lui, H.K., Peng, T.R., Kandasamy, S., Zhang, J., Yang, L., Gao, X., Lou, J.Y., Kuo, F.W., Chen, X.G., Ye, Y., Lin, Y.J., 2018. Submarine Groundwater Discharge helps making nearshore waters heterotrophic. Sci. Rep. 8, 1–10.

Webster I. T., Hancock G. J., Murray A. S., 1995. Modelling the effect of salinity on radium desorption from sediments. Geochim. Cosmochim. Acta 59, 2469–2476.

Weeks, S.J., Currie, B., Bakun, A., Peard, K.R., 2004. Hydrogen sulphide eruptions in the Atlantic Ocean off southern Africa: Implications of a new view based on SeaWiFS satellite imagery. Deep. Res. Part I Oceanogr. Res. Pap. 51, 153–172.

Weingartner, T., Aagaard, K., Woodgate, R., Danielson, S., Sasaki, Y., Cavalieri, D., 2005. Circulation on the north central Chukchi Sea shelf. Deep-Sea Res. II 52, 3150–3174.

Windom, H. L., Moore, W. S., Niencheski, L. F. H., Jahnke, R.A., 2006. Submarine groundwater discharge: A large, previously unrecognized source of dissolved iron to the South Atlantic Ocean. Marine Chemistry 102, 252–266.

Woodgate, R. A., Aagaard, K., Swift, J. H., Falkner, K. K., Smethie,W. M. J., 2005. Pacific ventilation of the Arctic Ocean's lower halocline by upwelling and diapycnal mixing over the continental margin. Geophys. Res. Lett. 32, L18609.

Woodgate R. A., Aagaard K., 2005. Revising the Bering Strait freshwater flux into the Arctic Ocean. Geophys. Res. Lett., 32, L02602.

Woodgate, R. A., 2018. Increases in the Pacific inflow to the Arctic from 1990 to 2015, and insights into seasonal trends and driving mechanisms from year-round Bering Strait mooring data. Progress in Oceanography 160, 124-154.

Wu, J., Luther, G.W., 1996. Spatial and temporal distribution of iron in the surface water of the northwestern Atlantic Ocean. Geochim. Cosmochim. Acta 60, 2729–2741.

Yamamoto-Kawai, M., Carmack, E., McLaughlin, F., 2006. Nitrogen balance and Arctic throughflow, Nature 443, 43.

Yang, D., Kane, D. L., Hinzman, L. D., Zhang, X., Zhang, T., Ye, H., 2002. Siberian Lena River hydrologic regime and recent change. J. Geophys. Res. 107(D23), 4694.

Yang, D., Marsh, P., Ge, S., 2014. Heat flux calculations for Mackenzie and Yukon Rivers. Polar Science, 8(3), 232–241.

Yankovsky, A., Chapman, D., 1997: A simple theory for the fate of buoyant coastal discharges. J. Phys. Oceanogr., 27, 1386–1401.

Zhang, R., Delworth, T.L., 2005. Simulated tropical response to a substantial weakening of the Atlantic thermohaline circulation. J. Clim. 18, 1853–1860.

Zhang, R., Zhu, X., Yang, C., Ye, L., Zhang, G., Ren, J., Wu, Y., Liu, S., Zhang, J., Zhou, M., 2019. Distribution of dissolved iron in the Pearl River (Zhujiang) Estuary and the northern continental slope of the South China Sea. Deep. Res. Part II Top. Stud. Oceanogr.

Statement of declaration

I, Lúcia Helena Vieira, hereby declare that I have written this Ph.D. thesis independently, under compliance of the rules for good scientific practice of the German Research Foundation. I declare that I have used only the sources, the data and the support that I have clearly mentioned. Moreover, I assure that this Ph.D. thesis has not been submitted for the conferral of a degree elsewhere, and that none of my academic degrees has ever been withdrawn. Published or submitted for publication manuscripts are identified at the relevant places.

Lúcia Helena Vieira Kiel, 20.05.2019